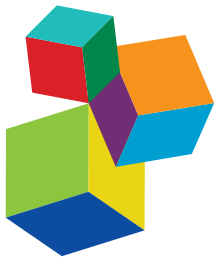


IMPROVING THE UNDERSTANDING OF KINETIC PROCESSES IN SOLAR WIND AND MAGNETOSPHERE: FROM CLUSTER TO MMS

EDITED BY: Antonella Greco, Benoit Lavraud, Denise Perrone and
Alexandros Chasapis

PUBLISHED IN: Frontiers in Astronomy and Space Sciences and Frontiers in Physics



Frontiers eBook Copyright Statement

The copyright in the text of individual articles in this eBook is the property of their respective authors or their respective institutions or funders. The copyright in graphics and images within each article may be subject to copyright of other parties. In both cases this is subject to a license granted to Frontiers.

The compilation of articles constituting this eBook is the property of Frontiers.

Each article within this eBook, and the eBook itself, are published under the most recent version of the Creative Commons CC-BY licence. The version current at the date of publication of this eBook is CC-BY 4.0. If the CC-BY licence is updated, the licence granted by Frontiers is automatically updated to the new version.

When exercising any right under the CC-BY licence, Frontiers must be attributed as the original publisher of the article or eBook, as applicable.

Authors have the responsibility of ensuring that any graphics or other materials which are the property of others may be included in the CC-BY licence, but this should be checked before relying on the CC-BY licence to reproduce those materials. Any copyright notices relating to those materials must be complied with.

Copyright and source acknowledgement notices may not be removed and must be displayed in any copy, derivative work or partial copy which includes the elements in question.

All copyright, and all rights therein, are protected by national and international copyright laws. The above represents a summary only. For further information please read Frontiers' Conditions for Website Use and Copyright Statement, and the applicable CC-BY licence.

ISSN 1664-8714

ISBN 978-2-88966-241-8

DOI 10.3389/978-2-88966-241-8

About Frontiers

Frontiers is more than just an open-access publisher of scholarly articles: it is a pioneering approach to the world of academia, radically improving the way scholarly research is managed. The grand vision of Frontiers is a world where all people have an equal opportunity to seek, share and generate knowledge. Frontiers provides immediate and permanent online open access to all its publications, but this alone is not enough to realize our grand goals.

Frontiers Journal Series

The Frontiers Journal Series is a multi-tier and interdisciplinary set of open-access, online journals, promising a paradigm shift from the current review, selection and dissemination processes in academic publishing. All Frontiers journals are driven by researchers for researchers; therefore, they constitute a service to the scholarly community. At the same time, the Frontiers Journal Series operates on a revolutionary invention, the tiered publishing system, initially addressing specific communities of scholars, and gradually climbing up to broader public understanding, thus serving the interests of the lay society, too.

Dedication to Quality

Each Frontiers article is a landmark of the highest quality, thanks to genuinely collaborative interactions between authors and review editors, who include some of the world's best academicians. Research must be certified by peers before entering a stream of knowledge that may eventually reach the public - and shape society; therefore, Frontiers only applies the most rigorous and unbiased reviews. Frontiers revolutionizes research publishing by freely delivering the most outstanding research, evaluated with no bias from both the academic and social point of view. By applying the most advanced information technologies, Frontiers is catapulting scholarly publishing into a new generation.

What are Frontiers Research Topics?

Frontiers Research Topics are very popular trademarks of the Frontiers Journals Series: they are collections of at least ten articles, all centered on a particular subject. With their unique mix of varied contributions from Original Research to Review Articles, Frontiers Research Topics unify the most influential researchers, the latest key findings and historical advances in a hot research area! Find out more on how to host your own Frontiers Research Topic or contribute to one as an author by contacting the Frontiers Editorial Office: frontiersin.org/about/contact

IMPROVING THE UNDERSTANDING OF KINETIC PROCESSES IN SOLAR WIND AND MAGNETOSPHERE: FROM CLUSTER TO MMS

Topic Editors:

Antonella Greco, Università della Calabria, Italy

Benoit Lavraud, UMR5277 Institut de recherche en astrophysique et planétologie (IRAP), France

Denise Perrone, Italian Space Agency (ASI), Italy

Alexandros Chasapis, University of Delaware, United States

Citation: Greco, A., Lavraud, B., Perrone, D., Chasapis, A., eds. (2021). Improving the Understanding of Kinetic Processes in Solar Wind and Magnetosphere: From CLUSTER to MMS. Lausanne: Frontiers Media SA. doi: 10.3389/978-2-88966-241-8

Table of Contents

- 04 Editorial: Improving the Understanding of Kinetic Processes in Solar Wind and Magnetosphere: From CLUSTER to Magnetospheric Multiscale Mission**
Improving the Understanding of Kinetic Processes in Solar Wind and Magnetosphere: From CLUSTER to Magnetospheric Multiscale Mission
Antonella Greco, Denise Perrone, Benoit Lavraud and Alexandros Chasapis
- 08 Sign Singularity of the Local Energy Transfer in Space Plasma Turbulence**
Luca Sorriso-Valvo, Gaetano De Vita, Federico Fraternali, Alexandre Gurchumelia, Silvia Perri, Giuseppina Nigro, Filomena Catapano, Alessandro Retinò, Christopher H. K. Chen, Emiliya Yordanova, Oreste Pezzi, Khatuna Chargazia, Oleg Kharshiladze, Diana Kvaratskhelia, Christian L. Vásconez, Raffaele Marino, Olivier Le Contel, Barbara Giles, Thomas E. Moore, Roy B. Torbert and James L. Burch
- 19 Energy Conversion at Kinetic Scales in the Turbulent Magnetosheath**
Zoltán Vörös, Emiliya Yordanova, Yuri V. Khotyaintsev, Ali Varsani and Yasuhito Narita
- 28 Kinetic Plasma Turbulence: Recent Insights and Open Questions From 3D3V Simulations**
Silvio Sergio Cerri, Daniel Grošelj and Luca Franci
- 39 Collisionless Magnetic Reconnection and Waves: Progress Review**
Yuri V. Khotyaintsev, Daniel B. Graham, Cecilia Norgren and Andris Vaivads
- 59 Anisotropy of the Spectral Index in Ion Scale Compressible Turbulence: MMS Observations in the Magnetosheath**
Owen Wyn Roberts, Yasuhito Narita, Rumi Nakamura, Zoltán Vörös and Daniel Gershman
- 75 Discovery of an Electron Gyroradius Scale Current Layer: Its Relevance to Magnetic Fusion Energy, Earth's Magnetosphere, and Sunspots**
Jaeyoung Park, Giovanni Lapenta, Diego Gonzalez-Herrero and Nicholas A. Krall
- 89 Cluster and MMS Simultaneous Observations of Magnetosheath High Speed Jets and Their Impact on the Magnetopause**
C. Philippe Escoubet, K.-J. Hwang, S. Toledo-Redondo, L. Turc, S. E. Haaland, N. Aunai, J. Dargent, Jonathan P. Eastwood, R. C. Fear, H. Fu, K. J. Genestreti, Daniel B. Graham, Yu V. Khotyaintsev, G. Lapenta, Benoit Lavraud, C. Norgren, D. G. Sibeck, A. Varsani, J. Berchem, A. P. Dimmock, G. Paschmann, M. Dunlop, Y. V. Bogdanova, Owen Roberts, H. Laakso, Arnaud Masson, M. G. G. T. Taylor, P. Kajdič, C. Carr, I. Dandouras, A. Fazakerley, R. Nakamura, Jim L. Burch, B. L. Giles, C. Pollock, C. T. Russell and R. B. Torbert
- 110 Current Sheet Statistics in the Magnetosheath**
Emiliya Yordanova, Zoltán Vörös, Savvas Raptis and Tomas Karlsson
- 121 Magnetic Field Turbulence in the Solar Wind at Sub-ion Scales: In Situ Observations and Numerical Simulations**
L. Matteini, L. Franci, O. Alexandrova, C. Lacombe, S. Landi, P. Hellinger, E. Papini and A. Verdini



Editorial: Improving the Understanding of Kinetic Processes in Solar Wind and Magnetosphere: From CLUSTER to Magnetospheric Multiscale Mission

Antonella Greco^{1*}, **Denise Perrone**², **Benoit Lavraud**³ and **Alexandros Chasapis**⁴

¹Dipartimento di Fisica, Università Della Calabria, Rende, Italy, ²ASI—Italian Space Agency, Rome, Italy, ³IRAP—Institut de Recherche en Astrophysique et Planétologie, Toulouse, France, ⁴Laboratory for Atmospheric and Space Physics, University of Colorado, Boulder, CO, USA

Keywords: plasma turbulence, magnetic reconnection, waves, instabilities, dissipation mechanisms, kinetic plasma processes, *in situ* observations, numerical simulations

Editorial on the Research Topic

Improving the Understanding of Kinetic Processes in Solar Wind and Magnetosphere: From CLUSTER to Magnetospheric Multiscale Mission

The most common matter state in the Universe is plasma (Krall and Trivelpiece, 1986). In the Heliosphere, these plasmas are almost collisionless, magnetized, and quasi-neutral and can mimic a large number of astrophysical plasmas that can only be observed remotely, e.g., the interstellar medium, astrophysical shocks and jets, accretion disks, cluster of galaxies etc.

Single-point space missions have described many properties of near-Earth and heliospheric plasmas by using both *in situ* measurements and remote sensing observations. From the first observations by the *Mariner* mission of turbulent solar wind flow (Neugebauer and Snyder, 1966; Neugebauer and Snyder, 1967), and the first computing of power spectra of alfvénic fluctuations (Coleman, 1968), or pioneering observations of large-scale magnetic structures (Burlaga et al., 1977) from the *Explorer 43* mission, both making single space observations, the community has advanced a lot in knowledge of plasma phenomena.

However, analyses of space plasma using *in situ* data from single spacecraft suffer from a spatio-temporal ambiguity, viz., the difficulty of disentangling temporal and spatial variations. This issue is acute for magnetofluid turbulence in the solar wind where it is very difficult to deduce the three-dimensional properties of the turbulent fluctuations from single spacecraft data (Goldstein et al., 2015). A full and realistic description of our plasma environment requires measurements able to determine the three-dimensional, time-dependent features observed in this turbulent system. Indeed, only multi-spacecraft observations are able to exhibit a connection between space and time: the same physical observables are measured not only at different points in space but also at different instants in time. *Cluster* was the first mission (Escoubet et al., 1997; Escoubet et al., 2001), and until data began to flow from the *Magnetospheric Multiscale Mission* (MMS), it was the only mission designed to describe the three-dimensional structure of plasma phenomena in geospace. To achieve this, *Cluster*, launched in the summer of 2000 and currently still in operation, consists of four identical spacecraft flying in a tetrahedral configuration, thereby making it possible to distinguish between spatial and temporal variations.

Beyond detailed analysis of the electromagnetic field and plasma characteristics, thanks to the robust experiments on board the four spacecraft, the goal of the *Cluster* mission has been to

OPEN ACCESS

Edited and reviewed by:

Rudolf Von Steiger,
University of Bern, Switzerland

*Correspondence:

Antonella Greco
antonella.greco@fis.unical.it

Received: 07 April 2020

Accepted: 29 September 2020

Published: 30 October 2020

Citation:

Greco A, Perrone D, Lavraud B and Chasapis A (2020) Editorial: Improving the Understanding of Kinetic Processes in Solar Wind and Magnetosphere: From CLUSTER to Magnetospheric Multiscale Mission. *Front. Astron. Space Sci.* 7:549935.
doi: 10.3389/fspas.2020.549935

exploit multi-point observations to compute spatial gradients. The curlometer analysis technique (Dunlop et al., 1988; Dunlop et al., 2002a; Dunlop and Eastwood, 2008) allows a direct estimation of the total current density from $\nabla \times \mathbf{B}$, using high-resolution magnetic field measurements. The same technique can be applied to velocity field measurements, i.e., $\nabla \times \mathbf{V}$, to resolve flow vorticity (Chanteur, 1998; Harvey, 1998). Therefore, *Cluster* has contributed to determine currents and vorticity in various regions of the Earth's magnetosphere (Dunlop et al., 2016), such as in the magnetotail (see, e.g., Runov et al., 2006; Nakamura et al., 2008; Shen et al., 2008; Narita et al., 2013), in the magnetopause (see, e.g., Dunlop and Balogh, 2005; Panov et al., 2006), in the inner magnetosphere (see, e.g., Vallat et al., 2005; Shen et al., 2014), as well as in the solar wind (see, e.g., Eastwood et al., 2002; Gurgiolo et al., 2010).

Four-spacecraft measurements have been also used to estimate the normal and the speed of a discontinuity (Russell et al., 1983; Dunlop et al., 2002b), by using the so-called timing method. Recently, the timing method has been used to study structures at ion scales in the solar wind turbulence (Perrone et al., 2016; Perrone et al., 2017). Further, measurements from the four satellites, in the appropriate configuration, have allowed to calculate the dispersion relation of several waves ubiquitous in the geospace environment (Narita et al., 2003; Narita and Glassmeier, 2005) by using the wave telescope or k-filtering technique (Pinçon and Lefèuvre, 1991; Motschmann et al., 1996; Glassmeier et al., 2001; Glassmeier, 2003).

Cluster observations have been also used to study turbulence of the plasma which surrounds our local geospace environment. In particular, turbulence correlation scales have been estimated in both Earth's plasmashell (Vörös et al., 2005; Weygand et al., 2005) and solar wind (Matthaeus et al., 2005; Weygand et al., 2007). Moreover, for the first time, it has been possible to describe the three-dimensional properties of the inertial range of interplanetary turbulence at ion scales (Narita et al., 2011a; Narita et al., 2011b), where intermittency starts to manifest itself. Further, thanks to high-resolution magnetic field data, *Cluster* has allowed to study turbulence toward electron scales in the solar wind (Alexandrova et al., 2009; Sahraoui et al., 2009), where dissipation should take place.

Finally, *Cluster* data have elucidated aspects of reconnection that occurs in the solar wind, magnetosheath, and magnetosphere. For example, multi-point measurements allowed to unambiguously determine the characteristics of the near-Earth's reconnection line on the ion scale (Runov et al., 2003), and to lead to a significant progress in understanding the microphysics of this processes, revealing the subsequent both adiabatic and non-adiabatic particle energization (Retinò et al., 2007; Sundkvist et al., 2007).

In March of 2015, the MMS, consisting of four identical spacecraft, similar to *Cluster*, was launched, providing multi-point measurements in near-Earth space (Burch et al., 2016a). The spacecraft are flying at significantly smaller separations, down to ~ 5 km, while the instruments are providing high-time resolution plasma data, as well as three-dimensional

electric field measurements, allowing for an unprecedented investigation of kinetic processes. The MMS instruments are able directly to observe the electron diffusion region at the Earth's magnetopause and magnetotail, thus adding critical insight into the physics of magnetic reconnection (Burch et al., 2016b; Torbert et al., 2018). MMS observations enabled the study of the statistical properties of turbulence and the associated energy cascade in near-Earth space from the inertial range down to proton and electron scales (Bandyopadhyay et al., 2018; Chhiber et al., 2018). Intermittent structures at kinetic scales have been identified, revealing the existence of electron-scale current sheets, similar to what was previously observed at ion scales (Greco et al., 2016; Yordanova et al., 2016). Furthermore, MMS makes it possible to resolve electron-scale regions of active magnetic reconnection, while more recent studies have investigated their role in kinetic-scale turbulence (Phan et al., 2018; Stawarz et al., 2019), providing new insight into the dissipative processes at kinetic scales. The novel measurements lead to the developments of new techniques that examine the complex structure of the plasma velocity distribution functions, shedding a new light into the kinetic physics behind turbulent dissipation (Servidio et al., 2017).

The main motivation in organizing this special issue in Frontiers of Astronomy and Space Sciences, twenty years after the first multi-point observations, is to give an overview of the achievements in the understanding of kinetic processes in both the Earth's magnetosphere and the solar wind as well as to present the current efforts of the scientific community in this field. This special issue collects mainly papers on observations in turbulent space plasmas. Contributions from numerical studies are also present to support the observational evidences and improve the understanding of turbulent collisionless plasmas.

AUTHOR CONTRIBUTIONS

All authors listed have made a substantial, direct and intellectual contribution to the work, and approved it for publication. In detail, AG wrote the initial draft. DP added several paragraphs. BL gave comments, and AC took the final look.

FUNDING

AC was supported in part by the NASA MMS project, and the NASA Grant No. 80NSSC19K1469.

ACKNOWLEDGMENTS

The authors would like to acknowledge all the contributors to this research topic. The authors would like to thank the *Cluster* experiment teams for making available their data and recognize the tremendous effort in developing and operating the MMS spacecraft and instruments.

REFERENCES

- Alexandrova, O., Saur, J., Lacombe, C., Mangeney, A., Mitchell, J., Schwartz, S. J., et al. (2009). Universality of solar-wind turbulent spectrum from MHD to electron scales. *Phys. Rev. Lett.* 103 (16), 165003. doi:10.1103/PhysRevLett.103.165003
- Bandyopadhyay, R., Chasapis, A., Chhiber, R., Parashar, T. N., Matthaeus, W. H., Shay, M. A., et al. (2018). Incompressive energy transfer in the earth's magnetosheath: magnetospheric multiscale observations. *Astrophys. J.* 866, 106. doi:10.3847/1538-4357/aade04
- Burch, J. L., Moore, T. E., Torbert, R. B., and Giles, B. L. (2016a). Magnetospheric multiscale overview and science objectives. *Space Sci. Rev.* 199, 5–21. doi:10.1007/s11214-015-0164-9
- Burch, J. L., Torbert, R. B., Phan, T. D., Chen, L.-J., Moore, T. E., Ergun, R. E., et al. (2016b). Electron-scale measurements of magnetic reconnection in space. *Science* 352 (6290), aaf2939. doi:10.1126/science.aaf2939
- Burlaga, L. F., Lemaire, J. F., and Turner, J. M. (1977). Interplanetary current sheets at 1 AU. *J. Geophys. Res.* 82 (22), 3191–3200. doi:10.1029/JA082i022p03191
- Chanteur, G. (1998). "Spatial interpolation for four spacecraft: theory," in *Analysis methods for multi-spacecraft data*. Editors G. Paschmann and P. W. Daly. ISSI Scientific Reports Series, (Bern: ESA/ISSI), Chap. 14, Vol. 1, 371–394, ISBN 1608-280X.
- Chhiber, R., Chasapis, A., and Bandyopadhyay, R. (2018). Higher-order turbulence statistics in the earth's magnetosheath and the solar wind using magnetospheric multiscale observations. *J. Geophys. Res. Space Phys.* 123 (12), 9941–9954. doi:10.1029/2018JA025768
- Coleman, P. J. (1968). Turbulence, viscosity, and dissipation in the solar-wind plasma. *Astrophys. J.* 153, 371–388. doi:10.1086/149674
- Dunlop, M. W., Balogh, A., Glassmeier, K.-H., and Robert, P. (2002a). Four-point Cluster application of magnetic field analysis tools: the curlometer. *J. Geophys. Res.* 107 (A11), 1384. doi:10.1029/2001JA005088
- Dunlop, M. W., Balogh, A., and Glassmeier, K.-H. (2002b). Four-point Cluster application of magnetic field analysis tools: the discontinuity analyzer. *J. Geophys. Res.* 107 (A11), 1385. doi:10.1029/2001JA005089
- Dunlop, M. W., and Balogh, A. (2005). Magnetopause current as seen by Cluster. *Ann. Geophys.* 23 (3), 901–907. doi:10.5194/angeo-23-901-2005
- Dunlop, M. W., and Eastwood, J. P. (2008). "The curlometer and other gradient based methods," in *Multi-spacecraft analysis methods revisited*. Editors G. Paschmann and P. W. Daly. ISSI Scientific Reports Series, (ESA/ISSI), 17–26, ISBN 987-92-9221-937-6.
- Dunlop, M. W., Haaland, S., Escoubet, P.-C., and Dong, X.-C. (2016). Commentary on accessing 3-D currents in space: experiences from Cluster. *J. Geophys. Res.* 121, 7881–7886. doi:10.1002/2016JA022668
- Dunlop, M. W., Southwood, D. J., Glassmeier, K.-H., and Neubauer, F. M. (1988). Analysis of multipoint magnetometer data. *Adv. Space Res.* 8 (9–10), 273–277. doi:10.1016/0273-1177(88)90141-X
- Dunlop, M. W., Yang, J.-Y., Yang, Y.-Y., Xiong, C., Lühr, H., Bogdanova, Y. V., et al. (2015). Simultaneous field-aligned currents at Swarm and Cluster satellites. *Geophys. Res. Lett.* 42 (10), 3683–3691. doi:10.1002/2015GL063738
- Eastwood, J. P., Balogh, A., Dunlop, M. W., and Smith, C. W. (2002). Cluster observations of the heliospheric current sheet and an associated magnetic flux rope and comparisons with ACE. *J. Geophys. Res.* 107 (A11), 1365. doi:10.1029/2001JA009158
- Escoubet, C. P., Fehringer, M., and Goldstein, M. (2001). Introduction: the cluster mission. *Ann. Geophys.* 19, 1197–1200. doi:10.5194/angeo-19-1197-2001
- Escoubet, C. P., Schmidt, R., and Goldstein, M. L. (1997). Cluster—science and mission overview. *Space Sci. Rev.* 79, 11–32. doi:10.1023/A:1004923124586
- Forsyth, C., Lester, M., Cowley, S. W. H., Dandouras, I., Fazakerley, A. N., Fear, R. C., et al. (2008). Observed tail current systems associated with bursty bulk flows and auroral streamers during a period of multiple substorms. *Ann. Geophys.* 26 (1), 167–184. doi:10.5194/angeo-26-167-2008
- Glassmeier, K.-H. (2003). Correction to 'Cluster as a wave telescope-first results from the fluxgate magnetometer. *Ann. Geophys.* (21), 1071.
- Glassmeier, K.-H., Motschmann, U., Dunlop, M., Balogh, A., Acuña, M. H., Carr, C., et al. (2001). Cluster as a wave telescope-first results from the fluxgate magnetometer. *Ann. Geophys.* 19 (10), 1439–1447. doi:10.5194/angeo-19-1439-2001
- Goldstein, M.-L., Escoubet, P., Hwahn, K.-J., Wendel, D. E., Viñas, A.-F., Fung, S. F., et al. (2015). Multipoint observations of plasma phenomena made in space by Cluster. *J. Plasma Phys.* 81 (2), 325810301. doi:10.1017/S0022377815000185
- Greco, A., Perri, S., Servidio, S., Yordanova, E., and Veltri, P. (2016). The complex structure of magnetic field discontinuities in the turbulent solar wind. *Astrophys. J. Lett.* 823 (2), L39. doi:10.3847/2041-8205/823/2/L39
- Gurgiolo, C., Goldstein, M. L., Viñas, A. F., and Fazakerley, A. N. (2010). First measurements of electron vorticity in the foreshock and solar wind. *Ann. Geophys.* 28 (12), 2187–2200. doi:10.5194/angeo-28-2187-2010
- Harvey, C. C. (1998). "Spatial gradients and the volumetric tensor," in *Analysis methods for multi-spacecraft data*. Editors G. Paschmann and P. W. Daly (Bern), Chap. 12, 307–322, ISSI Scientific Report SR-001.
- Krall, N. A., and Trivelpiece, A. W. (1986). *Principles of plasma physics*. San Francisco Press.
- Matthaeus, W. H., Dasso, S., Weygand, J. M., Milano, L. J., Smith, C. W., and Kivelson, M. G. (2005). Spatial correlation of solar-wind turbulence from two-point measurements. *Phys. Rev. Lett.* 95 (23), 231101. doi:10.1103/PhysRevLett.95.231101
- Motschmann, U., Woodward, T. I., Glassmeier, K. H., Southwood, D. J., and Pinçon, J. L. (1996). Wavelength and direction filtering by magnetic measurements at satellite arrays: generalized minimum variance analysis. *J. Geophys. Res.* 101 (A3), 4961. doi:10.1029/95JA03471
- Nakamura, R., Baumjohann, W., Fujimoto, M., Asano, Y., Runov, A., Owen, C. J., et al. (2008). Cluster observations of an ion-scale current sheet in the magnetotail under the presence of a guide field. *J. Geophys. Res.* 113 (A7), A07S16. doi:10.1029/2007JA012760
- Narita, Y., and Glassmeier, K.-H. (2005). Dispersion analysis of low-frequency waves through the terrestrial bow shock. *J. Geophys. Res.* 110 (A12), A12215. doi:10.1029/2005JA011256
- Narita, Y., Glassmeier, K.-H., Goldstein, M. L., Motschmann, U., and Sahraoui, F. (2011a). Three-dimensional spatial structures of solar wind turbulence from 10 000-km to 100-km scales. *Ann. Geophys.* 29 (10), 1731–1738. doi:10.5194/angeo-29-1731-2011
- Narita, Y., Glassmeier, K.-H., Sahraoui, F., and Goldstein, M. L. (2011b). Wave-vector dependence of magnetic-turbulence spectra in the solar wind. *Phys. Rev. Lett.* 104 (17), 171101. doi:10.1103/PhysRevLett.104.171101
- Narita, Y., Glassmeier, K.-H., Schäfer, S., Motschmann, U., Sauer, K., Dandouras, I., et al. (2003). Dispersion analysis of ULF waves in the foreshock using Cluster data and the wave telescope technique. *Geophys. Res. Lett.* 30 (13), 1710. doi:10.1029/2003GL017432
- Narita, Y., Nakamura, R., and Baumjohann, W. (2013). Cluster as current sheet surveyor in the magnetotail. *Ann. Geophys.* 31, 1605–1610. doi:10.5194/angeo-31-1605-2013
- Neugebauer, M., and Snyder, C. W. (1966). Mariner 2 observations of the solar wind: 1. average properties. *J. Geophys. Res.* 71, 4469–4484. doi:10.1029/JZ071i019p04469
- Neugebauer, M., and Snyder, C. W. (1967). Mariner 2 observations of the solar wind: 2. relation of plasma properties to the magnetic field. *J. Geophys. Res.* 72, 1823–1828. doi:10.1029/JZ072i007p01823
- Panov, E., Büchner, J., Fränz, M., Korth, A., Khotyaintsev, Y., Nikutowski, B., et al. (2006). CLUSTER spacecraft observation of a thin current sheet at the Earth's magnetopause. *Adv. Space Res.* 37 (7), 1363–1372. doi:10.1029/2006GL026556
- Perrone, D., Alexandrova, O., Mangeney, A., Maksimovic, M., Lacombe, C., Rakoto, V., et al. (2016). Compressive coherent structures at ion scales in the slow solar wind. *Astrophys. J.* 826, 196. doi:10.3847/0004-637X/826/2/196
- Perrone, D., Alexandrova, O., Roberts, O. W., Lion, S., Lacombe, C., Walsh, A., et al. (2017). Coherent structures at ion scales in fast solar wind: cluster observations. *Astrophys. J.* 849, 49. doi:10.3847/1538-4357/aa9022
- Phan, T. D., Eastwood, J. P., Shay, M. A., Drake, J. F., Sonnerup, B. U. Ö., Fujimoto, M., et al. (2018). Electron magnetic reconnection without ion coupling in Earth's turbulent magnetosheath. *Nature* 557, 202–206. doi:10.1038/s41586-018-0091-5
- Pinçon, J. L., and Lefèuvre, F. (1991). Local characterization of homogeneous turbulence in a space plasma from simultaneous measurements of field components at several points in space. *J. Geophys. Res.* 96 (1), 1789–1802. doi:10.1029/90JA02183

- Retinò, A., Sundkvist, D., Vaivads, A., Mozer, F., André, M., and Owen, C. J. (2007). *In situ* evidence of magnetic reconnection in turbulent plasma. *Nature Phys.* 3 (4), 236–238. doi:10.1038/nphys574
- Runov, A., Nakamura, R., Baumjohann, W., Treumann, R. A., Zhang, T. L., Volwerk, M., et al. (2003). Current sheet structure near magnetic X-line observed by Cluster. *Geophys. Res. Lett.* 30 (11), 1579. doi:10.1029/2002GL016730
- Runov, A., Nakamura, R., and Baumjohann, W. (2006). Multi-point study of the magnetotail current sheet. *Adv. Space Res.* 38 (1), 85–92. doi:10.1016/j.asr.2004.09.024
- Russell, C. T., Mellott, M. M., Smith, E. J., and King, J. H. (1983). Multiple spacecraft observations of interplanetary shocks: four spacecraft determination of shock normals. *J. Geophys. Res.* 88 (A6), 4739. doi:10.1029/JA088iA06p04739
- Sahraoui, F., Goldstein, M. L., Robert, P., and Khotyaintsev, Yu. V. (2009). Evidence of a cascade and dissipation of solar-wind turbulence at the electron gyroscale. *Phys. Rev. Lett.* 102 (23), 231102. doi:10.1103/PhysRevLett.102.231102
- Servidio, S., Chasapis, A., Matthaeus, W. H., Perrone, D., Valentini, F., Parashar, T. N., et al. (2017). Magnetospheric multiscale observation of plasma velocity-space cascade: hermite representation and theory. *Phys. Rev. Lett.* 119 (20), 205101. doi:10.1103/PhysRevLett.119.205101
- Shen, C., Rong, Z. J., Li, X., Dunlop, M., Liu, Z. X., Malova, H. V., et al. (2008). Magnetic configurations of the tilted current sheets in magnetotail. *Ann. Geophys.* 26 (11), 3525. doi:10.5194/angeo-26-3525-2008
- Shen, C., Yang, Y. Y., Rong, Z. J., Li, X., Dunlop, M., Carr, C. M., et al. (2014). Direct calculation of the ring current distribution and magnetic structure seen by Cluster during geomagnetic storms. *J. Geophys. Res.* 119 (4), 2458. doi:10.1002/2013JA019460
- Shi, J. K., Cheng, Z. W., Zhang, T. L., Dunlop, M., Liu, Z. X., Torkar, K., et al. (2010). South-north asymmetry of field-aligned currents in the magnetotail observed by Cluster. *J. Geophys. Res.* 115 (A7), A07228. doi:10.1029/2009JA014446
- Stawarz, J. E., Eastwood, J. P., Phan, T. D., Gingell, I. L., Shay, M. A., Burch, J. L., et al. (2019). Properties of the turbulence associated with electron-only magnetic reconnection in earth's magnetosheath. *Astrophys. J. Lett.* 877 (2), L37. doi:10.3847/2041-8213/ab21c8.
- Sundkvist, D., Retinò, A., Vaivads, A., and Bale, S. D. (2007). Dissipation in turbulent plasma due to reconnection in thin current sheets. *Phys. Rev. Lett.* 99 (2), 025004. doi:10.1103/PhysRevLett.99.025004
- Torbert, R. B., Burch, J. L., Phan, T. D., Hesse, M., Argall, M. R., Shuster, J., et al. (2018). Electron-scale dynamics of the diffusion region during symmetric magnetic reconnection in space. *Science* 362 (6421), 1391–1395. doi:10.1126/science.aat2998
- Turner, A. J., Gogoberidze, G., Chapman, S. C., Hnat, B., and Müller, W.-C. (2011). Nonaxisymmetric anisotropy of solar wind turbulence. *Phys. Rev. Lett.* 107 (9), 095002. doi:10.1103/PhysRevLett.107.095002
- Vörös, Z., Baumjohann, W., Nakamura, R., Runov, A., Volwerk, M., Schwarzl, H., et al. (2005). Dissipation scales in the earth's plasma sheet estimated from Cluster measurements. *Nonlinear Process. Geophys.* 12, 725–732. doi:10.5194/npg-12-725-2005
- Vallat, C., Dandouras, I., Dunlop, M., Balogh, A., Lucek, E., Parks, G. K., et al. (2005). First current density measurements in the ring current region using simultaneous multi-spacecraft CLUSTER-FGM data. *Ann. Geophys.* 23, 1849–1865. doi:10.5194/angeo-23-1849-2005
- Weygand, J. M., Kivelson, M. G., Khurana, K. K., Schwarzl, H. K., Thompson, S. M., McPherron, R. L., et al. (2005). Plasma sheet turbulence observed by Cluster II. *J. Geophys. Res.* 110, A01205. doi:10.1029/2004JA010581
- Weygand, J. M., Matthaeus, W. H., Dasso, S., Kivelson, M. G., and Walker, R. J. (2007). Taylor scale and effective magnetic Reynolds number determination from plasma sheet and solar wind magnetic field fluctuations. *J. Geophys. Res.* 112 (A10), A10201. doi:10.1029/2007JA012486
- Yordanova, E., Vörös, Z., Varsani, A., Graham, D. B., Norgren, C., Khotyaintsev, Y. V., et al. (2016). Electron scale structures and magnetic reconnection signatures in the turbulent magnetosheath. *Geophys. Res. Lett.* 43 (12), 5969–5978. doi:10.1002/2016GL069191

Conflict of Interest: The authors declare that the research was conducted in the absence of any commercial or financial relationships that could be construed as a potential conflict of interest.

Copyright © 2020 Greco, Perrone, Lavraud and Chasapis. This is an open-access article distributed under the terms of the Creative Creative Commons Attribution License (CC BY). The use, distribution or reproduction in other forums is permitted, provided the original author(s) and the copyright owner(s) are credited and that the original publication in this journal is cited, in accordance with accepted academic practice. No use, distribution or reproduction is permitted which does not comply with these terms.



Sign Singularity of the Local Energy Transfer in Space Plasma Turbulence

Luca Sorriso-Valvo^{1,2*}, **Gaetano De Vita**², **Federico Fraternali**³, **Alexandre Guchumelia**⁴, **Silvia Perri**⁵, **Giuseppina Nigro**⁵, **Filomena Catapano**⁶, **Alessandro Retinò**⁷, **Christopher H. K. Chen**⁸, **Emiliya Yordanova**⁹, **Oreste Pezzi**^{10,11}, **Khatuna Chargazia**^{4,12}, **Oleg Kharshiladze**⁴, **Diana Kvaratskhelia**^{4,13}, **Christian L. Vásconez**¹, **Raffaele Marino**¹⁴, **Olivier Le Contel**⁷, **Barbara Giles**¹⁵, **Thomas E. Moore**¹⁵, **Roy B. Torbert**¹⁶ and **James L. Burch**¹⁷

¹ Departamento de Física, Escuela Politécnica Nacional, Quito, Ecuador, ² Istituto per la Scienza e Tecnologia dei Plasmi (ISTP), Consiglio Nazionale delle Ricerche, Bari, Italy, ³ Dipartimento di Scienze Applicate e Tecnologia, Politecnico di Torino, Turin, Italy, ⁴ M. Nodia Institute of Geophysics, Iv. Javakhishvili Tbilisi State University, Tbilisi, Georgia, ⁵ Dipartimento di Fisica, Università della Calabria, Rende, Italy, ⁶ Serco Italia for ESA-ESRIN, Frascati, Italy, ⁷ LPP-CNRS/Ecole Polytechnique/Sorbonne Université, Paris, France, ⁸ School of Physics and Astronomy, Queen Mary University of London, London, United Kingdom, ⁹ Swedish Institute of Space Physics, Uppsala, Sweden, ¹⁰ Gran Sasso Science Institute, L'Aquila, Italy, ¹¹ INFN/Laboratori Nazionali del Gran Sasso, Assergi, Italy, ¹² I. Vekua Institute of Applied Mathematics, Iv. Javakhishvili Tbilisi State University, Tbilisi, Georgia, ¹³ Sokhumi State University, Tbilisi, Georgia, ¹⁴ Laboratoire de Mécanique des Fluides et d'Acoustique, CNRS, École Centrale de Lyon, Université Claude Bernard Lyon, INSA de Lyon, Écully, France, ¹⁵ NASA, Goddard Space Flight Center, Greenbelt, MD, United States, ¹⁶ Space Science Center, University of New Hampshire, Durham, NH, United States, ¹⁷ Southwest Research Institute, San Antonio, TX, United States

OPEN ACCESS

Edited by:

Alexandros Chasapis,
University of Delaware, United States

Reviewed by:

Annick Pouquet,
University of Colorado Boulder,
United States

Wieslaw Marian Macek,
Space Research Center (PAN), Poland

*Correspondence:

Luca Sorriso-Valvo
lucasorriso@gmail.com

Specialty section:

This article was submitted to
Space Physics,
a section of the journal
Frontiers in Physics

Received: 30 May 2019

Accepted: 11 July 2019

Published: 20 August 2019

Citation:

Sorriso-Valvo L, De Vita G, Fraternali F, Guchumelia A, Perri S, Nigro G, Catapano F, Retinò A, Chen CHK, Yordanova E, Pezzi O, Chargazia K, Kharshiladze O, Kvaratskhelia D, Vásconez CL, Marino R, Le Contel O, Giles B, Moore TE, Torbert RB and Burch JL (2019) Sign Singularity of the Local Energy Transfer in Space Plasma Turbulence. *Front. Phys.* 7:108. doi: 10.3389/fphy.2019.00108

In weakly collisional space plasmas, the turbulent cascade provides most of the energy that is dissipated at small scales by various kinetic processes. Understanding the characteristics of such dissipative mechanisms requires the accurate knowledge of the fluctuations that make energy available for conversion at small scales, as different dissipation processes are triggered by fluctuations of a different nature. The scaling properties of different energy channels are estimated here using a proxy of the local energy transfer, based on the third-order moment scaling law for magnetohydrodynamic turbulence. In particular, the sign-singularity analysis was used to explore the scaling properties of the alternating positive-negative energy fluxes, thus providing information on the structure and topology of such fluxes for each of the different type of fluctuations. The results show the highly complex geometrical nature of the flux, and that the local contributions associated with energy and cross-helicity non-linear transfer have similar scaling properties. Consequently, the fractal properties of current and vorticity structures are similar to those of the Alfvénic fluctuations.

Keywords: turbulence, dissipation, space plasmas, magnetosphere, singularity

1. INTRODUCTION

The dynamics of space plasmas is characterized by a broad variety of complex processes that include turbulence, instabilities, and several mechanisms of particle-radiation interaction. Such processes are intrinsically connected across multiple scales. For example, the energy associated with large-scale structures and instabilities is transported toward smaller and smaller scales through a turbulent cascade due to the non-linear interactions among magnetic and velocity fluctuations, throughout the so-called inertial range that may span one to more than three decades in scales [1–3]. When the energy reaches scales of the order of or smaller than the typical ion and electron scales (e.g., the proton Larmor radius or inertial length), a different turbulent cascade occurs [4, 5].

At those scales, weakly collisional plasma kinetic processes arise, such as non-linear damping of waves, kinetic instabilities, particle collisions, and magnetic reconnection, that convert the energy stored in the field fluctuations into particle energization and acceleration, and plasma heating [6–11].

Past theoretical, experimental and numerical attempts to describe these processes have focused mostly on simplified, idealized conditions. However, in recent years there is an increasing interest in their cross-scale, interwoven nature. Multi-spacecraft and high resolution measurements in the solar wind and in the terrestrial magnetosphere [12, 13] have provided evidence of such interconnection [14]. The increasing performance of numerical simulations has also allowed processes on several scales to be examined, and therefore to highlight their relationship [15–24]. Theoretical efforts are also being carried out in order to highlight the specific processes governing the energy exchange between ranges associated to different regimes [25–27]. In this framework, the local, fine-scale details of the turbulent energy cascade acquire new importance, as the specific characteristics of the fluctuations carrying energy to the kinetic scales can be associated with different plasma processes [11, 28, 29].

Recent analysis has revealed that the temperature and energized particles are enhanced in the proximity of current sheets [30–34] or of locations of concentration of turbulent energy [27, 35]. The local, fine details of the energy transfer process in the turbulent cascade may therefore play a fundamental role in the activation of those plasma kinetic processes that are believed to be responsible for energy conversion, usually (and loosely) referred to as dissipation. In numerical simulations specific techniques, mostly based on Fourier-space filtering, have been developed to achieve a detailed description of the energy transfer [36–38]. However, the limitations arising from the one-dimensional nature of spacecraft sampling require the introduction of approximated quantities. A simple example is provided by the normalized magnitude of the small-scale magnetic field fluctuations, basically locating current sheets and similar magnetic structures. Techniques known as local intermittency measure (LIM) [39] and partial variance of increments (PVI) [40] were extensively used in the last decades. A more informative proxy, called local energy transfer (LET), is based on the third-order scaling law for turbulent plasmas [41], and carries information about the nature of the fluctuations transporting the energy to small scales [29]. For example, the use of this proxy allowed the identification of specific ion features, such as beams, where the alignment between small-scale magnetic field and velocity fluctuations was dominating. This suggested non-linear resonance between Alfvénic fluctuations and particles as a possible mechanism for the generation of those beams [29].

In this article, the topological properties of the energy flow channels are examined. Measurements from the solar wind and from different regions of the terrestrial magnetosphere are studied by means of sign-singularity analysis. The results show the presence of interwoven positive-negative energy flux, allowing estimation of the typical fractal dimension of the structures, and eventually the role of their different components,

in the turbulent cascade and, therefore, on feeding small-scale dissipative processes. Section 2 describes the proxy used in this work and the cancelation analysis technique. In section 3 we describe the data used. Section 4 provides a description of the results and the comparison between different data sets. Finally, the results are briefly discussed in section 4.

2. METHODS

2.1. A Proxy of the Local Energy Transfer in Turbulence

The fluctuations observed in magnetohydrodynamic plasma turbulence have been shown to follow the Politano-Pouquet law [41]. This predicts the linear scaling of the mixed third-order moment of the fields fluctuations on the scale, when homogeneity, scale separation, isotropy, and time-stationarity are met. Using the Taylor hypothesis [42, 43] $\mathbf{r} = t\langle \mathbf{v} \rangle$ (necessary to transform space (\mathbf{r}) and time (t) arguments via the bulk speed ($\langle \mathbf{v} \rangle$), the Politano-Pouquet law can be written as:

$$Y(\Delta t) = \langle \Delta v_l (|\Delta \mathbf{v}|^2 + |\Delta \mathbf{b}|^2) - 2\Delta b_l (\Delta \mathbf{v} \cdot \Delta \mathbf{b}) \rangle = -\frac{4}{3} \langle \varepsilon \rangle \Delta t \langle v \rangle. \quad (1)$$

The mixed third-order moment $Y(\Delta t)$ is computed using the increments $\Delta \psi(t, \Delta t) = \psi(t + \Delta t) - \psi(t)$ of a field ψ (either the plasma velocity \mathbf{v} or the magnetic field $\mathbf{b} = \mathbf{B}/\sqrt{4\pi\rho}$ given in velocity units through the mass density ρ) across a temporal scale Δt , the subscript l indicating the longitudinal component, i.e., parallel to the bulk speed. The total energy flux given in Equation (1) is proportional to the mean energy transfer rate $\langle \varepsilon \rangle$. The Politano-Pouquet law describes the scaling of the small imbalance between positive and negative energy flux in the turbulent cascade, and is associated with the scale-dependent intrinsic asymmetry (skewness) of the turbulent fluctuations [1, 41]. The linear scaling (1) was robustly observed in numerical simulations [44–46], in the solar wind plasma [47–51], and in the terrestrial magnetosheath [52–54]. In order to attempt a description of the local energy flux from space data time series, the law (1) can be revisited without computing the average, thus giving a time series of the heuristic proxy of the local energy transfer rates (LET) at a given scale Δt , which can be estimated by computing the quantity:

$$\varepsilon^\pm(t, \Delta t) = -\frac{3}{4} \frac{\Delta v_l (|\Delta \mathbf{v}|^2 + |\Delta \mathbf{b}|^2) - 2\Delta b_l (\Delta \mathbf{v} \cdot \Delta \mathbf{b})}{\Delta t \langle v \rangle}. \quad (2)$$

This procedure neglects several contributions to the scaling, which in (1) are suppressed by averaging over a large sample, and therefore provides only a rough approximation of the actual local energy transfer rate [38, 55]. However, because of the intrinsic difficulty in estimating the neglected terms from one-dimensional data, this proxy can be used as a first degree approximation in space plasmas time series. The LET was previously used to determine heating regions in the interplanetary plasma [27] and on kinetic numerical simulations [35, 37].

The LET is composed of two additive terms, one associated with the magnetic and kinetic energy advected by the velocity

fluctuations, $\varepsilon_e = -3/(4\Delta t \langle v \rangle)[\Delta v_l(\Delta \mathbf{v}^2 + \Delta \mathbf{b}^2)]$, and the other with the cross-helicity coupled to the longitudinal magnetic fluctuations, $\varepsilon_c = -3/(4\Delta t \langle v \rangle)[-2\Delta b_l(\Delta \mathbf{v} \cdot \Delta \mathbf{b})]$ [27]. Such separation has been used to identify regions dominated by current and vorticity structures from regions dominated by coupled, Alfvénic fluctuations in the terrestrial magnetospheric boundary layer, revealing the presence of ion beams mostly associated with the small-scale Alfvénic fluctuations, and thus indicating a possible mechanism for the transfer of the turbulent energy to the particles [29]. Since the LET, as well as its two separated components, are signed quantities, it may be interesting to explore the scaling properties of the mixing of the positive and negative parts of the turbulent cascade. These may be related to the direction of the energy flow, although this interpretation is not supported by theoretical evidence. Moreover, unlike in the averaged Politano-Pouquet law, decoupling the sign dependence on scale and position is not trivial for the local proxy. Therefore, caution should be used in evaluating the physical meaning of the sign. However, it could still be associated to injection or removal of energy from specific locations and scales. It has been shown both in MHD [56] and in hydrodynamic flows [57] that a selective filter of the triads carrying the energy throughout the inertial range, as well as the absence of resonant triads in the anisotropic case in the presence of rotation and stratification [58], may lead to the modulation of an inverse cascade in fully developed three-dimensional turbulence. It would be thus interesting to investigate the nature of the sign of the local energy dissipation obtained with the proxy proposed here also by the implementation of shell models [59, 60].

Preliminary comparison between the proxy and more comprehensive estimates of the local energy transfer rate, performed using three-dimensional MHD numerical simulations [38], suggests good qualitative agreement (not shown) in terms of location of the larger transfer regions, although there are some discrepancies in the magnitude and fluctuation of the signed transfers that may relate to the approximated and unfiltered nature of the LET. For the purposes of this study, the proxy does not necessarily need to fully capture the turbulent energy flux, as it is rather related to the specific features of the plasma and field fluctuations that contribute to the actual energy flux.

The complexity of the energy flow across scales might carry information about the topology of the small-scale structures, and also specifically for their energy or cross-helicity contributions. This information can be useful to determine which dissipative processes are selectively activated by the turbulent cascade. In this work, we aim at providing such information, that will be obtained by means of the cancelation analysis, which is briefly described in the following section.

2.2. Sign Singularity and Cancelation Analysis

The properties of chaotic flows can be described through the singularity analysis of the field [61]. In particular, if a given field changes sign on arbitrarily small scale, its measure is called

sign singular [61]. The quantitative description of this singularity is important for the description of the topological properties (e.g., fractal dimension, filling factor...) of sign-defined (smooth) coherent structures, such as the ones emerging in intermittent, turbulent flows. A standard technique to estimate sign singularity is provided by the cancelation analysis, previously used to describe the scaling properties of MHD, Hall-MHD, and Vlasov-Maxwell turbulence in numerical simulations [44, 62–65] and in the current helicity in solar photospheric active regions [66–69].

Given a scalar field $f(\mathbf{r})$ with zero mean, defined on a d -dimensional domain $Q(L)$ of size L , its signed measure can be defined as the normalized field integrated over scale dependent subsets $Q(l) \subset Q(L)$ of size l ,

$$\mu(l) = \frac{\int_{Q(l)} d\mathbf{r} f(\mathbf{r})}{\int_{Q(L)} d\mathbf{r} |f(\mathbf{r})|}.$$

A coarse-graining of the domain provides an estimate of the sign-singularity of the measure by means of the scaling exponent κ (also called cancelation exponent) of the cancelation function, which is in turn defined as $\chi(l) = \sum_{Q_i(l)} |\mu_i(l)| \sim l^{-\kappa}$, the sum being intended over all disjoint subsets $Q_i(l)$ fully covering the domain $Q(L)$. In a chaotic field, positive and negative fluctuations cancel each other if the integral is performed over large subsets, resulting in a small signed measure at large scales. However, if the integration subset has the typical size of the smooth structures, cancelations are reduced and the signed measure is relatively larger. The scaling law of the cancelation function, as described by the cancelation exponent, can thus provide information on the field cancelations across the scales. Some specific values of the cancelation exponent can help to interpret the results. If the field is smooth, then the cancelation function does not depend on the scale, and $\kappa = 0$. If the field is homogeneous with random discontinuities, then cancelations are enhanced and $\kappa = d/2$. Values in between these two examples indicate the coexistence of random fluctuations and smooth structures, whose fractal dimension D is thus given by $\kappa = (d - D)/2$ [44]. The fractal dimension D provides information about the space filling and complexity of the structures carrying the energy to small scales, and might be related to the efficiency of the transport mechanism. In this study we will make use of κ and D as parameters to describe the topological properties of the different turbulent energy channels, and compare the results for the interplanetary space and the magnetosphere.

3. DATA

In order to study the cancelation properties of the local energy transfer rate proxy LET, and of its two components, we have selected two magnetospheric plasma intervals measured by the Magnetospheric Multiscale mission (MMS) [13], which provides data at high cadence, and one longer interval of fast solar wind measured by the Wind spacecraft [70].

The first sample, labeled as MMS-KH, was recorded on September 8, 2015 between 10:07:04 and 11:25:34 UTC, while MMS was in the dusk-side magnetopause, moving across a portion of plasma dominated by the Kelvin-Helmholtz instability

(KH) formed at the boundary between the magnetosheath and the magnetosphere. The interval was extensively studied in the past, showing the presence of strong turbulence and intermittency [71]. The MMS spacecraft performed multiple crossings of the KH boundary, resulting in the alternate sampling of plasma from the magnetosheath and from the magnetospheric boundary layer. The boundary crossings between the two regions are clearly highlighted by sharp transitions of the plasma parameters, so that it is easy to separate them. In this work, we have accurately selected 53 short intervals (ranging one to ten minutes) that are purely immersed in the magnetospheric boundary layer (based on plasma temperature and density), rejecting magnetosheath and transition regions. This allows some degree of homogeneity of the sample, necessary for statistical analysis.

The second magnetospheric interval, named MMS-MS, was selected in the turbulent magnetosheath region under quasi-parallel bow shock geometry on November 30, 2015, between 00:21 and 00:26 UTC. This 5-minute interval is characterized by intense fluctuations in all plasma and field parameters and by the presence of small scale magnetic structures. Some of these have been studied in detail, and various kinetic processes, such as local electron acceleration and magnetic reconnection at thin current sheets have been observed [72–74].

For both MMS intervals, the magnetic field data with sampling frequency 1 kHz used here are a merged product [75] from the burst mode flux gate (FGM) [76] and search coil (SCM) [77] instruments on MMS. The ion moments come from the fast plasma instrument (FPI) [78] at a sampling rate of 150 ms.

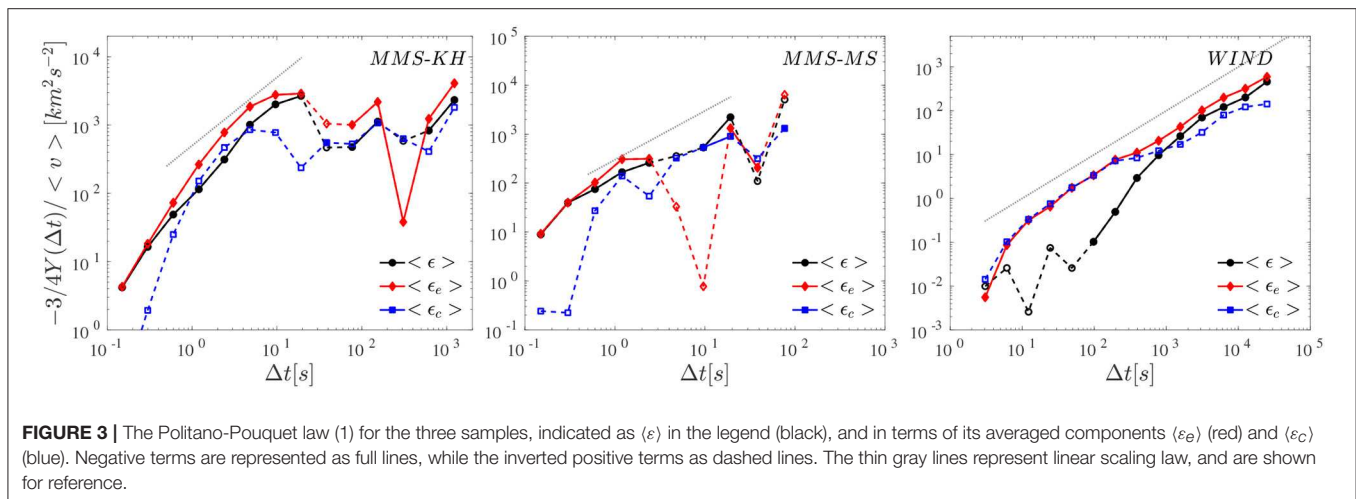
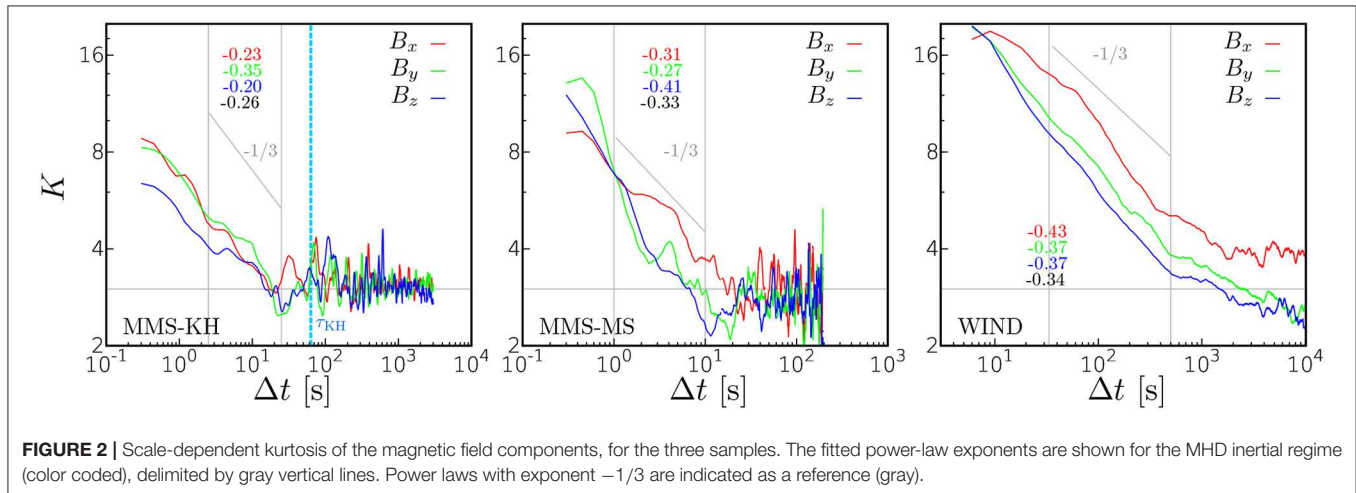
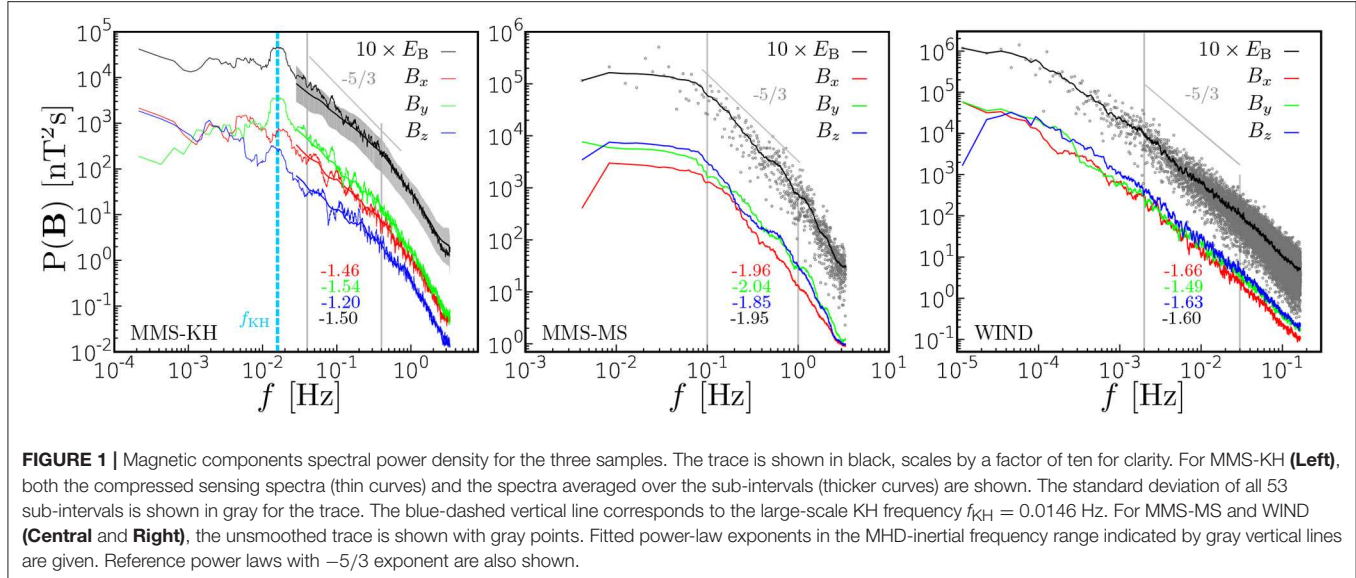
Finally, in order to compare the magnetospheric results with the solar wind, we have also studied the cancelation properties of the proxy LET using one sample of fast solar wind measured by the Wind spacecraft [70], labeled as WIND. The data interval consists of 6 days when Wind was in a fast stream during days 14 to 19 of 2008, and is the same interval as studied in Wicks et al. [79]. The data from the magnetic field instrument MFI [80] and plasma instrument 3DP [81] at 3 s cadence were used, with the magnetic field converted to Alfvén units using the kinetic normalization described in Chen et al. [82]. The average conditions during the interval were a solar wind speed of 660 km/s, magnetic field strength $B = 4.4$ nT, density 2.4 cm^{-3} and proton beta $\beta_p = 1.2$, typical for the fast solar wind.

The three intervals are characterized by variable levels of magnetic fluctuations. As shown in **Figure 1**, all three intervals present a reasonably well defined power-law spectral scaling range. For the WIND and MMS-KH intervals, the spectra are close to the Kolmogorov prediction, with scaling exponents $\sim -5/3$ compatible with the standard values for MHD turbulence. The MMS-KH data shows slightly shallower spectra, but still in the standard range of observation of turbulent space plasmas. Note that the power spectra in these data were obtained using the compressed sensing technique described in Fraternale et al. [83]. The magnetosheath interval, MMS-MS, has less defined power-law scaling, possibly because of its short duration, and the scaling exponent is ~ -2 (see the fitted exponents inside each panel frame), suggesting the presence of uncorrelated structures. This is typical of the highly fluctuating magnetosheath magnetic

field, and indicates a relatively less developed turbulence. In the magnetosheath flanks, Kolmogorov-type power spectra can be observed in the MHD range [84, 85]. However, in the region closer to the subsolar point, where MMS orbit lies during this particular event, the plasma is highly compressed and closely confined between the bow shock and the magnetopause. The solar wind turbulence, once modified and shuffled by the bow shock crossing, does not have enough space and time to reach a fully developed state, because of the close proximity of the two large boundaries. This results in the observed steeper spectral exponents. Note that in the present sample the typical ion frequencies are of the order of 1.3 Hz, which exclude the possibility that the observed scaling range is in the kinetic regime [4].

The formation of small-scale structures, typical of intermittency, is evidenced by the (roughly) power-law increase toward the small scales of the normalized fourth order moment (kurtosis) of the magnetic fluctuations, $K_i(\Delta t) = \langle \Delta B_i^4 \rangle / \langle \Delta B_i^2 \rangle^2$ (**Figure 2**), the subscript i indicating the component x , y , or z . Note that the Gaussian value $K = 3$ is observed for scales larger than the estimated inertial range (right gray vertical line). The Power-law decrease with the scale is a direct consequence of the structure function scaling in turbulent fields. The fitted scaling exponents are indicated in each panel, and are proportional to the degree of intermittency of the system [86]. For the solar wind data, where the turbulence is more developed, the power-law behavior is more evident. Both the exponents and the small-scale magnitude of the kurtosis are in agreement with typical values for fast solar wind [3]. A shorter, less defined power-law scaling range, with slightly smaller scaling exponents, is observed in MMS-KH and MMS-MS data, suggesting a less developed intermittency in the younger turbulence of the shocked plasma. Similar results (not shown) were obtained through the standard analysis of the anomalous scaling of the structure functions [1], fitted to a p -model [87], in the extended self-similarity approach [88]. After averaging over the three components (no major differences were observed), the magnetic field intermittency parameters p are 0.67, 0.79, and 0.82 for the MMS-KH, MMS-MS, and WIND samples respectively (p lies in the interval [0.5, 1], with $p = 0.5$ indicating absence of intermittency). These results show the strongly intermittent nature of the WIND sample, the slightly less intermittent MMS-SH sample, and the weakly intermittent nature of the MMS-KH sample.

Finally, the Politano-Pouquet law (1) can be estimated in the samples under study, both in terms of total energy transfer $\langle \varepsilon \rangle$, and in terms of the averaged components $\langle \varepsilon_e \rangle$ and $\langle \varepsilon_c \rangle$. The resulting scaling functions are shown in **Figure 3** for the three intervals. None of the observed cases display a clear linear scaling. This might be due to the violation of the several requirements necessary for the Politano-Pouquet law to hold (e.g., incompressibility, isotropy, stationarity, large Reynolds number), to the presence of large-scale features advected by the flowing plasma, or simply to the lack of statistical convergence of the third-order moment, due to intrinsic finite-size limitation of space data. The challenging observation of the linear law in solar wind was already noticed using Ulysses data [48, 89].



In the MMS-KH data a power-law scaling slightly different from the expected linear relation is suggested. In WIND, there is evidence of linear scaling of the two components separately, while their combination does not display the predicted linear dependence. In the MMS-MS sample, the third-order moment and its components experience multiple sign inversions, possibly due to the finite size sample and to the expected poorly developed turbulence, evidenced by the steeper magnetic spectral exponent, as discussed above.

The intervals used in this work appear thus characterized, to different degrees, by the presence of an inertial range of turbulent, intermittent fluctuations, with a roughly defined energy cascade leading to the formation of small-scale structures.

4. RESULTS

From the MMS and WIND measurements described above, we have computed the LET, examples of which are shown in **Figure 4**. In this work we will use the LET at scale of 1.2 s, which is still inside and near the bottom of the MHD inertial range, where the Politano-Pouquet law is valid [29]. The proxy has the typical behavior of intermittent dissipation in turbulence [1], with the presence of intense bursts of energy flux alternating with quieter regions. The cancellation analysis described in section 2 was then performed on the signed fields ε , ε_e , and ε_c , as obtained from the different data sets considered for this study. A range of time-scale separations within the inertial range was considered, so that we have estimates of the LET for different scales Δt within the turbulent cascade.

Top panels of **Figure 5** shows three examples of scaling of the cancellation function $\chi(l)$ for the LET proxy ε , computed using the field fluctuations at a scale Δt near the bottom of the inertial range, as indicated in each figure. Each example refers to one of the three data sets studied in this paper. Power-law scaling can be easily identified in a region roughly corresponding to the respective inertial range of MHD turbulence (see **Figure 1** for comparison). In the WIND data, a possible secondary power-law scaling is observed in the large-scale range $\Delta t \gtrsim 10$ m, where spectra usually decay as $1/f$ (see in **Figure 1** the large-scale spectral break at $f \simeq 0.002$ Hz) [3]. On the other hand, the higher resolution of MMS data allows to highlight the presence of scaling in the ion range of scales (i.e., for $\Delta t \lesssim 1$ s, compatible with the spectral break visible near 1 Hz in **Figure 1**), where a different type of cascade may take place [4, 71, 84]. However, the scaling in this range should be studied in the framework of ion plasma physics, for example by including the Hall-MHD corrections to the Politano-Pouquet law [46, 55]. This is left for future study. The cancellation functions have been fitted to power laws in the inertial range for all samples, and additionally in the $1/f$ scaling range for the solar wind data, providing the cancellation exponents κ , and thus the corresponding fractal dimensions $D = d - 2\kappa$ (in this case $d = 1$, so that the values of $D = 1$ would indicate smooth, space-filling structures). Their values are indicated in the figure for some selected examples. A similar behavior was robustly observed for all samples and all LET components, and at all scales

Δt within the inertial range, so that it is possible to compare the cancellation properties of the LET in the different cases. In the MMS-KH interval (left panel), the cancellation exponents near the end of the inertial range ($\Delta t = 1.2$ s) is $\kappa \sim 1/3$ for the three variables, a value indicating high complexity. This corresponds to fractal dimension of the order of $D \sim 0.33$, which is indicative of highly fragmented structures. In the magnetosheath sample MMS-MS (central panel), at the same scale the exponent is closer to $\kappa \sim 1/2$, which is usually representative of random sign alternation, or absence of smooth, persistent structures of that scale. This is in agreement with the observed steep spectrum, indicative of the presence of weakly correlated discontinuities (or structures), and with the large kurtosis of this sample, which accounts for the broad presence of such structures. In the fast solar wind sample measured by Wind, the scaling exponent of the total energy transfer proxy near the bottom of the inertial range ($\Delta t = 6$ s) is $\kappa \sim 1/4$, which corresponds to the presence of structures of fractal dimension $D \sim 0.5$. This is in agreement with the typical observation of disrupted current sheets of solar wind intermittent turbulence [63], and confirms the fact that the turbulence is well developed in this fast wind stream, with strong intermittency. For the same interval, in the $1/f$ range of scales, a different fit of the cancellation function provides $\kappa \sim 1/2$, in excellent agreement with the uncorrelated nature of the Alfvénic fluctuations observed at such scales [3].

Further information can be gained by observing the scale dependence of the cancellation exponent (or the corresponding fractal dimension). This can be obtained using the LET proxy estimated at different scales, using increments of the fields on variable scales Δt . Thus, for each scale, the LET and its components provide scale-dependent, local estimates of the turbulent energy flow. Results of cancellation analysis are collected in the bottom panels of **Figure 5**, where the cancellation exponent κ is shown for the three samples, and for the three variables. For all samples, at scales larger than the correlation scale (roughly 10 s for both MMS samples [29, 71] and about 30 s for WIND, as evident from the spectrum and from the kurtosis) the cancellation exponent is $\kappa \lesssim 0.1$ (or $D \gtrsim 0.8$) for all fields, as expected for smooth, space-filling fluctuations. As the scale decreases, all samples display an increase of complexity, in a scale range roughly corresponding to the inertial range, where the intermittent structures are generated. Finally, a plateau or saturation seems to take place at or near the ion-scale spectral break. This could indicate that the intermittent structures have reached their stable geometry. However, this effect could also be due to the MHD nature of the LET proxies, which might be unable to properly capture further fragmentation of the fluctuations. The study of the ion range with the appropriate variable is left for future work.

In the MMS-KH interval (left panel), the increase of complexity toward small scales is smooth and power-law like, and extends to the whole inertial range. The non-linear cascade and the complex entanglement of positive and negative energy flux (proxies of the direct and inverse cascade, respectively) is thus beautifully captured by the LET in this sample. In the inertial range, all three variables (different lines) have similar exponents.

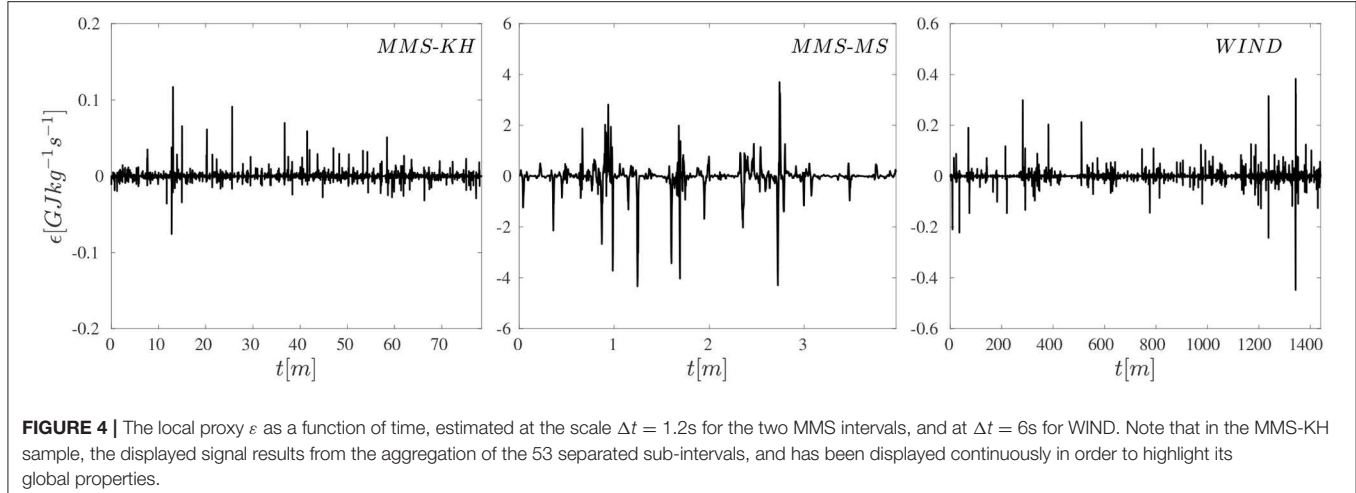


FIGURE 4 | The local proxy ϵ as a function of time, estimated at the scale $\Delta t = 1.2\text{s}$ for the two MMS intervals, and at $\Delta t = 6\text{s}$ for WIND. Note that in the MMS-KH sample, the displayed signal results from the aggregation of the 53 separated sub-intervals, and has been displayed continuously in order to highlight its global properties.

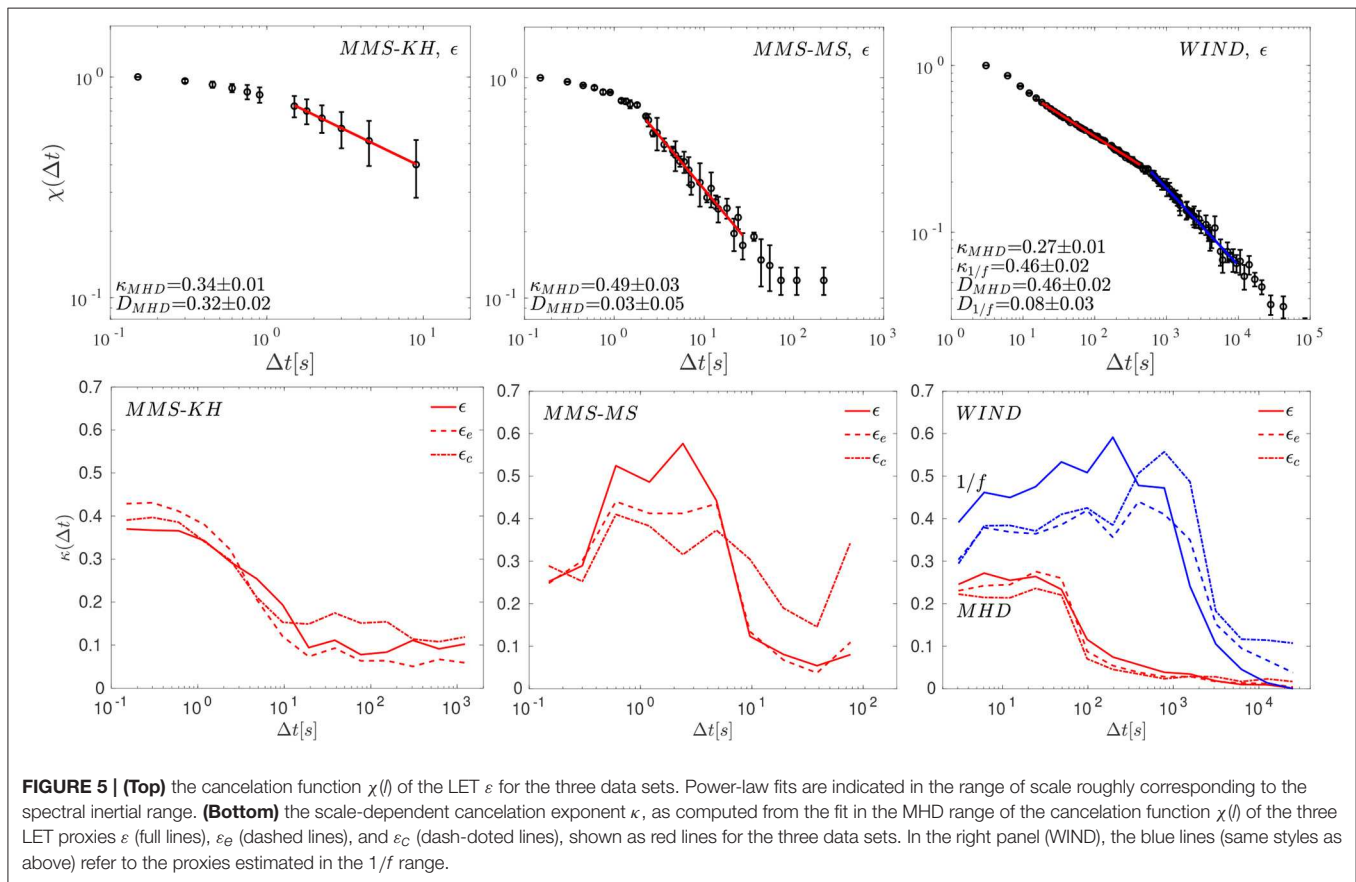


FIGURE 5 | (Top) the cancellation function $\chi(l)$ of the LET ϵ for the three data sets. Power-law fits are indicated in the range of scale roughly corresponding to the spectral inertial range. **(Bottom)** the scale-dependent cancellation exponent κ , as computed from the fit in the MHD range of the cancellation function $\chi(l)$ of the three LET proxies ϵ (full lines), ϵ_e (dashed lines), and ϵ_c (dash-dotted lines), shown as red lines for the three data sets. In the right panel (WIND), the blue lines (same styles as above) refer to the proxies estimated in the $1/f$ range.

The cross-helicity component ϵ_c seems to provide slightly larger exponents than the energy component ϵ_e , suggesting that the energy transfer associated with current and vorticity structures occurs in a slightly smaller fraction of the volume (smaller fractal dimension).

As for the KH interval, the WIND cancellation exponents obtained in the MHD range present similar exponents for the three MHD variables throughout the whole range of scales,

indicating that the alternation of positive and negative energy flow is similar for the three proxies. This could be an indication of well developed turbulence, where a sufficient equilibrium between the competing terms in the cascade has been reached. The growth of the complexity roughly follows a power-law scaling, which confirms the excellent scaling properties of this sample, and that the LET proxies capture the sign complexity of the energy cascade.

From the bottom panels of **Figure 5**, it is evident that the overall behavior described above is roughly coherent for the WIND (in the MHD range) and MMS-KH samples. This suggest the universality of the turbulent cascade mechanism, at least with respect to the sign-singularity properties, or, equivalently, to the fractal properties of the structures responsible for the energy transfer. The similarity is also corresponding to the presence of well-developed Kolmogorov spectra for both samples (see **Figure 1**), and to the power-law scaling of the kurtosis describing intermittency. In particular, the small-scale limiting values of κ are larger for the MMS-KH sample than for WIND, in agreement with the more developed intermittency highlighted by the kurtosis and structure function analysis.

In the magnetosheath data, the increase of complexity of the positive-negative alternation for the total and structure-related proxies is sharper, less defined, and is observed right at the beginning of the spectral power-law range. The overall behavior is different for the three proxies, with the total energy reaching a value of the exponent corresponding to uncorrelated, random fluctuations, while both components reach slightly smaller κ . Some degree of correlation is thus present in these two proxies, indicating the presence of extremely fragmented current, vorticity, and Alfvénic structures, whose superposition results in uncorrelated energy flux. The magnetosheath sample is thus probably characterized by less developed turbulence, corresponding to the steeper spectrum, and by the presence of small-scale structures, in agreement with the large kurtosis.

Finally, in the WIND 1/f range, there is a similar trend as in the MMS-MS data, with smooth fluctuations at large scale, but the increase to uncorrelated, random values occurs sharply at the top of the inertial range, so that the energy flow associated with large-scale fluctuations clearly does not contribute to the energy cascade, as expected.

DISCUSSION

The nature of the turbulent energy cascade has been analyzed in three samples of space plasmas by means of cancelation analysis applied to heuristic proxies of the local energy transfer. The analysis provided information on the sign alternation of the local mixed third-order fluctuations, which may be related to the fractal properties of the associated energy transfer and thus to small-scale dissipative processes. In two samples, namely in the solar wind and in the KH instability at the magnetospheric boundary layer, the turbulent cascade is well described by the proxies, and cancelation analysis captures the increasing complexity of the alternating positive and negative fluctuations. In these two samples, the energy is transferred to small scales eventually generating disrupted current and vorticity structures, as well as Alfvénic structures. The fractal dimension of these structures, obtained from the cancelation exponents, is indicative

of a strong concentration of energy within a small fraction of the volume, typical of intermittency. The cancelation analysis of the magnetosheath sample studied in this work, on the contrary, provides an overall lower complexity estimate, which suggests the presence of less evolved turbulence, and lack of formation of well-structured energy channels. This is in agreement with the steeper spectrum and the more irregular Politano-Pouquet scaling law.

These results help to characterize the fluctuations that carry energy to smaller scales and provide the input or trigger for the activation of kinetic, dissipative processes in the small-scale range [11, 28, 29]. Moreover, the estimated one-dimensional projected fractal dimension provides information on the topology of the different types of fluctuations, namely of the current sheets, vorticity structures and Alfvénic fluctuations, that play an important role in the dissipation of the turbulence.

DATA AVAILABILITY

MMS data are available at the MMS Science Data Center (<https://lasp.colorado.edu/mms/sdc/public/>). Wind data are available at CDAWeb (<https://cdaweb.gsfc.nasa.gov>).

AUTHOR CONTRIBUTIONS

LS-V designed and performed data analysis. GD, FF, GN, AG, KC, OK, DK, RM, and CV performed data analysis. FC, EY, SP, CC, OP, and AR selected and prepared the data. BG, TM, RT, and JB provided the data. All authors contributed to writing the article and interpreting the results of the data analysis.

FUNDING

LS-V and CV were supported by EPN Internal Project PII-DFIS-2019-01. FF was supported by grant FOIFLUT 37/17/F/AR-B. EY was supported by the Swedish Contingency Agency, grant 2016-2102. CC was supported by STFC Ernest Rutherford Fellowship ST/N003748/2. AG, KC, OK, DK, and LS-V have received support from the Shota Rustaveli National Science Foundation Project No FR17_279. SP has received funding from the European Unions Horizon 2020 Research and Innovation programme under grant agreement No 776262 (AIDA, www.aida-space.eu). The French LPP involvement for the SCM instrument on MMS was supported by CNRS and CNES.

ACKNOWLEDGMENTS

We acknowledge useful discussions with Denis Kuzzay, Lorenzo Matteini, and Olga Alexandrova. FF acknowledges HPC@POLITO for computational resources.

REFERENCES

1. Frisch UP. *Turbulence: the legacy of A.N. Kolmogorov*. Cambridge: Cambridge University Press (1995).

2. Marsch E, Tu CY. Intermittency, non-Gaussian statistics and fractal scaling of MHD fluctuations in the solar wind. *Nonlinear Process Geophys.* (1997) **4**:101.
3. Bruno R, Carbone V. The solar wind as a turbulence laboratory. *Liv Rev Solar Phys.* (2013) **10**:1. doi: 10.12942/lrsp-2013-2

4. Macek WM, Krasińska A, Silveira MVD, Sibeck DG, Wawrzaszek A, Burch JL, et al. Magnetospheric multiscale observations of turbulence in the magnetosheath on kinetic scales. *Astrophys J Lett.* (2018) **864**:L29. doi: 10.3847/2041-8213/aad9a8
5. Chen CHK, Boldyrev S. Nature of kinetic scale turbulence in the earth's magnetosheath. *Astrophys J Lett.* (2017) **842**:122. doi: 10.3847/1538-4357/aa74e0
6. Salem CS, Howes GG, Sundkvist D, Bale SD, Chaston CC, Chen CHK, et al. Identification of kinetic Alfvén wave turbulence in the solar wind. *Astrophys J Lett.* (2012) **745**:L9. doi: 10.1088/2041-8205/745/1/L9
7. Chang CS, Gary SP, Wang J. Whistler turbulence forward cascade versus inverse cascade: three-dimensional particle-in-cell simulations. *Astrophys J.* (2015) **800**:87. doi: 10.1088/0004-637X/800/2/87
8. Chen CHK. Recent progress in astrophysical plasma turbulence from solar wind observations. *J Plasma Phys.* (2016) **82**:535820602. doi: 10.1017/S0022377816001124
9. Pezzi O, Valentini F, Veltri P. Collisional relaxation of fine velocity structures in plasmas. *Phys Rev Lett.* (2016) **116**:145001. doi: 10.1103/PhysRevLett.116.145001
10. Pezzi O. Solar wind collisional heating. *J Plasma Phys.* (2017) **83**:555830301. doi: 10.1017/S0022377817000368
11. Chen CHK, Klein KG, Howes GG. Evidence for electron Landau damping in space plasma turbulence. *Nat Commun.* (2019) **10**:740. doi: 10.1038/s41467-019-10843-3
12. Escoubet CP, Fehringer M, Goldstein M. The Cluster mission. *Ann Geophys.* (2001) **19**:1197. doi: 10.5194/angeo-19-1197-2001
13. Burch JL, Moore TE, Torbert RB, Giles BL. Magnetospheric multiscale overview and science objectives. *Space Sci Rev.* (2016) **199**:5. doi: 10.1007/978-94-024-0861-4-2
14. Greco A, Perri S, Servidio S, Yordanova E, Veltri P. The complex structure of magnetic field discontinuities in the turbulent solar wind. *Astrophys J Lett.* (2016) **823**:L39. doi: 10.3847/2041-8205/823/2/L39
15. Karimabadi H, Roytershteyn V, Wan M, Matthaeus WH, Daughton W, Wu P, et al. Coherent structures, intermittent turbulence, and dissipation in high-temperature plasmas. *Phys Plasmas.* (2013) **20**:012303. doi: 10.1063/1.4773205
16. Valentini F, Servidio S, Perrone D, Califano F, Matthaeus WH, Veltri P. Hybrid vlasov-maxwell simulations of two-dimensional turbulence in plasmas. *Phys Plasmas.* (2014) **21**:082307. doi: 10.1063/1.4893301
17. Franci L, Verdini A, Matteini L, Landi S, Hellinger P. Solar wind turbulence from MHD to sub-ion scales: high-resolution hybrid simulations. *Astrophys J Lett.* (2015) **804**:L39. doi: 10.1088/2041-8205/804/2/L39
18. Servidio S, Valentini F, Perrone D, Greco A, Califano F, Matthaeus WH, et al. A kinetic model of plasma turbulence. *J Plasma Phys.* (2015) **81**:325810107. doi: 10.1017/S0022377814000841
19. Valentini F, Perrone D, Stabile S, Pezzi O, Servidio S, De Marco R, et al. Differential kinetic dynamics and heating of ions in the turbulent solar wind. *N J Phys.* (2016) **18**:125001. doi: 10.1088/1367-2630/18/12/125001
20. Cerri SS, Servidio S, Califano F. Kinetic cascade in solar-wind turbulence: 3D3V hybrid-kinetic simulations with electron inertia. *Astrophys J.* (2017) **846**:L18. doi: 10.3847/2041-8213/aa87b0
21. Groselj D, Cerri SS, Navarro AB, Willmott C, Told D, Loureiro NL, et al. Fully kinetic versus reduced-kinetic modeling of collisionless plasma turbulence. *Astrophys J.* (2017) **847**:28. doi: 10.3847/1538-4357/aa894d
22. Franci L, Landi S, Verdini A, Matteini L, Hellinger P. Solar wind turbulent cascade from MHD to sub-ion scales: large-size 3D hybrid particle-in-cell simulations. *Astrophys J.* (2018) **853**:26. doi: 10.3847/1538-4357/aaa3e8
23. Pezzi O, Servidio S, Perrone D, Valentini F, Sorriso-Valvo L, Greco A, et al. Velocity-space cascade in magnetized plasmas: numerical simulations. *Phys Plasmas.* (2018) **25**:060704. doi: 10.1063/1.5027685
24. Perrone D, Passot T, Laveder D, Valentini F, Sulem PL, Zouganelis I, et al. Fluid simulations of plasma turbulence at ion scales: comparison with Vlasov-Maxwell simulations. *Phys Plasmas.* (2018) **25**:052302. doi: 10.1063/1.5026656
25. Schekochihin AA, Parker JT, Highcock EG, Dellar PJ, Dorland W, Hammett GW. Phase mixing versus nonlinear advection in drift-kinetic plasma turbulence. *J Plasma Phys.* (2016) **82**: 905820212. doi: 10.1017/S0022377816000374
26. Servidio S, Chasapis A, Matthaeus WH, Perrone D, Valentini F, Parashar TN, et al. Magnetospheric multiscale observation of plasma velocity-space cascade: hermite representation and theory. *Phys Rev Lett.* (2017) **119**:205101. doi: 10.1103/PhysRevLett.119.205101
27. Sorriso-Valvo L, Carbone F, Perri S, Greco A, Marino R, Bruno R. On the statistical properties of turbulent energy transfer rate in the inner heliosphere. *Solar Phys.* (2018) **293**:10. doi: 10.1007/s11207-017-1229-6
28. Klein KG, Howes GG. Measuring collisionless damping in heliospheric plasmas using field-particle correlations. *Astrophys J Lett.* (2016) **826**:L30. doi: 10.3847/2041-8205/826/2/L30
29. Sorriso-Valvo L, Catapano F, Retinò A, Le Contel O, Perrone D, Roberts OW, et al. Turbulence-driven ion beams in the magnetospheric Kelvin-Helmholtz instability. *Phys Rev Lett.* (2019) **122**:035102. doi: 10.1103/PhysRevLett.122.035102
30. Osman KT, Matthaeus WH, Hnat B, Chapman SC. Kinetic signatures and intermittent turbulence in the solar wind plasma. *Phys Rev Lett.* (2012) **108**:261103. doi: 10.1103/PhysRevLett.108.261103
31. Servidio S, Valentini F, Califano F, Veltri P. Local kinetic effects in two-dimensional plasma turbulence. *Phys Rev Lett.* (2012) **108**:045001. doi: 10.1103/PhysRevLett.108.045001
32. Vásconez CL, Pucci F, Valentini F, Servidio S, Matthaeus WH, Malara F. Kinetic Alfvén wave generation by large-scale phase mixing. *Astrophys J.* (2015) **815**:1. doi: 10.1088/0004-637X/815/1/1
33. Pucci F, Vásconez CL, Pezzi O, Servidio S, Valentini F, Matthaeus WH, et al. From Alfvén waves to kinetic Alfvén waves in an inhomogeneous equilibrium structure. *J Geophys Res Space Phys.* (2016) **121**:1024. doi: 10.1002/2015JA022216
34. Valentini F, Vásconez CL, Pezzi O, Servidio S, Malara F, Pucci F. Transition to kinetic turbulence at proton scales driven by large-amplitude kinetic Alfvén fluctuations. *Astronomy Astrophys.* (2017) **599**:A8. doi: 10.1051/0004-6361/201629240
35. Sorriso-Valvo L, Perrone D, Pezzi O, Valentini F, Servidio S, Zouganelis I, et al. Local energy transfer rate and kinetic processes: the fate of turbulent energy in two-dimensional hybrid Vlasov-Maxwell numerical simulations. *J Plasma Phys.* (2018) **84**:725840201. doi: 10.1017/S002237781800302
36. Camporeale E, Sorriso-Valvo L, Califano F, Retinò A. Coherent structures and spectral energy transfer in turbulent plasma: a space-filter approach. *Phys Rev Lett.* (2018) **120**:125101. doi: 10.1103/PhysRevLett.120.125101
37. Yang Y, Wan M, Matthaeus WH, Sorriso-Valvo L, Parashar TN, Lu Q, et al. Scale dependence of energy transfer in turbulent plasma. *Month Not R Astronom Soc.* (2019) **482**:4933. doi: 10.1093/mnras/sty2977
38. Kuzzay D, Alexandrova O, Matteini L. Local approach to the study of energy transfers in incompressible magnetohydrodynamic turbulence. *Phys Rev E.* (2019) **99**:053202. doi: 10.1103/PhysRevE.99.053202
39. Farge M. Wavelet transforms and their applications to turbulence. *Ann Rev Fluid Mech.* (1992) **24**:395.
40. Greco A, Chuychai P, Matthaeus WH, Servidio S, Dimitruk P. Intermittent MHD structures and classical discontinuities. *Geophys Res Lett.* (2008) **35**:L19111. doi: 10.1029/2008GL035454
41. Politano H, Pouquet A. Dynamical length scales for turbulent magnetized flows. *Geophys Res Lett.* (1998) **25**:273.
42. Peyret R, Taylor TD. *Computational Methods for Fluid Flow*. New York, NY: Springer (1986).
43. Perri S, Servidio S, Vaivads A, Valentini F. Numerical study on the validity of the Taylor hypothesis in space plasmas. *Astrophys J Suppl Ser.* (2017) **231**:4. doi: 10.3847/1538-4365/aa755a
44. Sorriso-Valvo L, Carbone V, Noullez A, Politano H, Pouquet A, Veltri P. Analysis of cancellation in two-dimensional magnetohydrodynamic turbulence. *Phys Plasmas.* (2002) **9**:89. doi: 10.1063/1.1420738
45. Andrés N, Galtier S, Sahraoui F. Exact law for homogeneous compressible Hall magnetohydrodynamics turbulence. *Physical Review E.* (2018) **97**:013204. doi: 10.1103/PhysRevE.97.013204
46. Ferrand R, Galtier S, Sahraoui F, Meyrand R, Andrés N, Banerjee S. On exact laws in incompressible Hall magnetohydrodynamic turbulence. *arXiv.* (2019) arXiv:1905.06110v1.

47. MacBride BT, Forman MA, Smith CW. Turbulence and third moment of fluctuations: kolmogorov's 4/5 law and its MHD analogues in the solar wind. In: Fleck B, Zurbuchen TH, Lacoste H, editors. *Solar Wind 11/SOHO 16, Connecting Sun and Heliosphere*. Noordwijk: ESA Special Publication (2005). p. 613.
48. Sorriso-Valvo L, Marino R, Carbone V, Noullez A, Lepreti F, Veltri P, et al. Observation of inertial energy cascade in interplanetary space plasma. *Phys Rev Lett.* (2007) **99**:115001. doi: 10.1103/PhysRevLett.99.115001
49. Marino R, Sorriso-Valvo L, Carbone V, Noullez A, Bruno R, Bavassano B. Heating the solar wind by a magnetohydrodynamic turbulent energy cascade. *Astrophys J Lett.* (2008) **667**:L71. doi: 10.1086/587957
50. Coburn JT, Smith CW, Vasquez BJ, Stawarz JE, Forman MA. The turbulent cascade and proton heating in the solar wind during solar minimum. *Astrophys J.* (2012) **754**:93. doi: 10.1088/0004-637X/754/2/93
51. Banerjee S, Hadid LZ, Sahraoui F, Galtier S. Scaling of compressible magnetohydrodynamic turbulence in the fast solar wind. *Astrophys J Lett.* (2016) **829**:L27. doi: 10.3847/2041-8205/829/2/L27
52. Hadid LZ, Sahraoui F, Galtier S, Huang SY. Compressible magnetohydrodynamic turbulence in the Earth's magnetosheath: estimation of the energy cascade rate using *in situ* spacecraft data. *Phys Rev Lett.* (2018) **120**:055102. doi: 10.1103/PhysRevLett.120.055102
53. Bandyopadhyay R, Chasapis A, Chhiber R, Parashar TN, Maruca BA, Matthaeus WH, et al. Solar wind turbulence studies using MMS fast plasma investigation data. *Astrophys J.* (2018) **866**:81. doi: 10.3847/1538-4357/aade93
54. Bandyopadhyay R, Chasapis A, Chhiber R, Parashar TN, Matthaeus WH, Shay MA, et al. Incompressible energy transfer in the Earth's magnetosheath: magnetospheric multiscale observations. *Astrophys J.* (2018) **866**:106. doi: 10.3847/1538-4357/aade04
55. Hellinger P, Verdini A, Landi S, Franci L, Matteini L, von Kármán. Howarth equation for hall magnetohydrodynamics: hybrid simulations. *Astrophys J Lett.* (2018) **857**:L19. doi: 10.3847/2041-8213/aae06
56. Deblliquy O, Verma MK, Carati D. Energy fluxes and shell-to-shell transfers in three-dimensional decaying magnetohydrodynamic turbulence. *Phys Plasmas.* (2005) **12**:042309. doi: 10.1063/1.187996
57. Sahoo G, Biferale L. Disentangling the triadic interactions in Navier-Stokes equations. *Eur Phys J E.* (2015) **38**:114. doi: 10.1140/epje/i2015-1-5114-4
58. Marino R, Mininni PD, Rosenberg D, Pouquet A. Inverse cascades in rotating stratified turbulence: fast growth of large scales. *Europhys Lett.* (2013) **102**:44006. doi: 10.1209/0295-5075/102/44006
59. Verma MK, Roberts DA, Goldstein ML, Ghosh S, Stribling WT. A numerical study of the nonlinear cascade of energy in magnetohydrodynamic turbulence. *J Geophys Res.* (1996) **101**:21619.
60. Dar G, Verma MK, Eswaran V. Energy transfer in two-dimensional magnetohydrodynamic turbulence: formalism and numerical results. *Physica D.* (2001) **157**:207. doi: 10.1016/S0167-2789(01)00307-4
61. Ott E, Du Y, Sreenivasan KR, Juneja A, Suri AK. Sign-singular measures: fast magnetic dynamos, and high-Reynolds-number fluid turbulence. *Phys Rev Lett.* (1992) **69**:2654.
62. Graham J, Mininni PD, Pouquet A. Cancellation exponent and multifractal structure in two-dimensional magnetohydrodynamics: direct numerical simulations and Lagrangian averaged modeling. *Phys Rev E.* (2005) **72**:045301. doi: 10.1103/PhysRevE.72.045301
63. Martin LN, De Vita G, Sorriso-Valvo L, Dimitruk P, Nigro G, Primavera L, et al. Cancellation properties in Hall magnetohydrodynamics with a strong guide magnetic field. *Phys Rev E.* (2013) **88**:063107. doi: 10.1103/PhysRevE.88.063107
64. De Vita G, Sorriso-Valvo L, Valentini F, Servidio S, Primavera L, Carbone V, et al. Analysis of cancellation exponents in two-dimensional Vlasov turbulence. *Phys Plasmas.* (2014) **21**:072315. doi: 10.1063/1.4891339
65. Gingell I, Sorriso-Valvo L, Burgess D, De Vita G, Matteini L. Three-dimensional simulations of sheared current sheets: transition to turbulence? *J Plasma Phys.* (2017) **83**:705830104. doi: 10.1017/S0022377817000058
66. Abramenko V, Yurchyshyn VB, Carbone V. Sign-singularity of the current helicity in solar active regions. *Solar Phys.* (1998) **178**:35.
67. Sorriso-Valvo L, Carbone V, Veltri P, Abramenko V, Noullez A, Politano H, et al. Topological changes of the photospheric magnetic field inside active regions: a prelude to flares? *Planet Space Sci.* (2004) **52**:937. doi: 10.1016/j.pss.2004.02.006
68. Sorriso-Valvo L, De Vita G, Kazachenko MD, Krucker S, Primavera L, Servidio S, et al. Sign singularity and flares in solar active region NOAA 11158. *Astrophys J.* (2015) **801**:36. doi: 10.1088/0004-637X/801/1/36
69. De Vita G, Vecchio A, Sorriso-Valvo L, Briand C, Primavera L, Servidio S, et al. Cancellation analysis of current density in solar active region NOAA10019. *J Space Weather Space Clim.* (2015) **5**:A28. doi: 10.1051/swsc/2015029
70. Acuña MH, Ogilvie KW, Baker DN, Curtis SA, Fairfield DH, Mish WH. The global geospace science program and its investigations. *Space Sci Rev.* (1995) **71**:5.
71. Stawarz JE, Eriksson S, Wilder FD, Ergun RE, Schwartz SJ, Pouquet A, et al. Observations of turbulence in a Kelvin' Helmholtz event on 8 September 2015 by the Magnetospheric Multiscale mission. *J Geophys Res Space Phys.* (2016) **121**:11021. doi: 10.1002/2016JA023458
72. Eriksson S, Lavraud B, Wilder FD, Stawarz JE, Giles BL, Burch JL, et al. Magnetospheric Multiscale observations of magnetic reconnection associated with Kelvin' Helmholtz waves. *Geophys Res Lett.* (2016) **43**:5606. doi: 10.1002/2016GL068783
73. Yordanova E, Vörös Z, Varsani A, Graham DB, Norgren C, Khotyaintsev YuV, et al. Electron scale structures and magnetic reconnection signatures in the turbulent magnetosheath. *Geophys Res Lett.* (2016) **43**:5969. doi: 10.1002/2016GL069191
74. Vörös Z, Yordanova E, Varsani A, Genestreti KJ, Khotyaintsev YuV, Li W, et al. MMS Observation of magnetic reconnection in the turbulent magnetosheath. *J Geophys Res Space Phys.* (2017) **122**:11442. doi: 10.1002/2017JA024535
75. Fischer D, Magnes W, Hagen C, Dors I, Chutter MW, Needell J, et al. Optimized merging of search coil and fluxgate data for MMS. *Geoscient Instr Methods Data Syst.* (2016) **5**:521. doi: 10.5194/gi-5-21-2016
76. Russell CT, Anderson BJ, Baumjohann W, Bromund KR, Dearborn D, Fischer D, et al. The magnetospheric multiscale magnetometers. *Space Sci Rev.* (2016) **199**:189. doi: 10.1007/s11214-014-0057-3
77. Le Contel O, Leroy P, Roux A, Coillot C, Alison D, Bouabdellah A, et al. The search-coil magnetometer for MMS. *Space Sci Rev.* (2016) **199**:257. doi: 10.1007/978-94-024-0861-4-9
78. Pollock C, Moore T, Jacques A, Burch J, Gliese U, Saito Y, et al. Fast plasma investigation for magnetospheric multiscale. *Space Sci Rev.* (2016) **199**:331. doi: 10.1007/s11214-016-0245-4
79. Wicks RT, Mallet A, Horbury TS, Chen CH, Schekochihin AA, Mitchell JJ. Alignment and scaling of large-scale fluctuations in the solar wind. *Phys Rev Lett.* (2013) **110**:025003. doi: 10.1103/PhysRevLett.110.025003
80. Lepping RP, Acuña MH, Burlaga LF, Farrell WM, Slavin JA, Schatten KH, et al. The WIND magnetic field investigation. *Space Sci Rev.* (1995) **71**:207.
81. Lin RP, Anderson KA, Ashford S, Carlson C, Curtis D, Ergun R, et al. A three-dimensional plasma and energetic particle investigation for the wind spacecraft. *Space Sci Rev.* (1995) **71**:125.
82. Chen CHK, Bale SD, Salem CS, Maruca BA. Residual energy spectrum of solar wind turbulence. *Astrophys J.* (2013) **770**:125. doi: 10.1088/0004-637X/770/2/125
83. Fraternali F, Pogorelov NV, Richardson JD, Tordella D. Magnetic turbulence spectra and intermittency in the heliosheath and in the local interstellar medium. *Astrophys J.* (2018) **872**:40. doi: 10.3847/1538-4357/aaf30
84. Alexandrova O, Lacombe C, Mangeney A. Spectra and anisotropy of magnetic fluctuations in the Earth's magnetosheath: Cluster observations. *Ann Geophys.* (2008) **26**:3585. doi: 10.5194/angeo-26-3585-2008

85. Huang SY, Hadid LZ, Sahraoui F, Yuan ZG, Deng XH. On the existence of the kolmogorov inertial range in the terrestrial magnetosheath turbulence. *Astrophys J Lett.* (2017) **836**:L10. doi: 10.3847/2041-8213/836/1/L10
86. Carbone F, Sorriso-Valvo L. Experimental analysis of intermittency in electrohydrodynamic instability. *Eur Phys J E.* (2014) **37**:61. doi: 10.1140/epje/i2014-14061-x
87. Meneveau C, Sreenivasan KR. Simple multifractal cascade model for fully developed turbulence. *Phys Rev Lett.* (1987) **59**:1424.
88. Benzi R, Ciliberto S, Tripiccione R, Baudet C, Massaioli F, Succi S. Extended self-similarity in turbulent flows. *Phys Rev E.* (1993) **48**:R29.
89. Marino R, Sorriso-Valvo L, D'Amicis R, Carbone V, Bruno R, Veltri P. On the occurrence of the third-order scaling in high latitude solar wind. *Astrophys J.* (2012) **750**:41. doi: 10.1088/0004-637X/750/1/41

Conflict of Interest Statement: The authors declare that the research was conducted in the absence of any commercial or financial relationships that could be construed as a potential conflict of interest.

Copyright © 2019 Sorriso-Valvo, De Vita, Fraternale, Gurchumelia, Perri, Nigro, Catapano, Retinò, Chen, Yordanova, Pezzi, Chargazia, Kharshiladze, Kvaratskhelia, Vásconez, Marino, Le Contel, Giles, Moore, Torbert and Burch. This is an open-access article distributed under the terms of the Creative Commons Attribution License (CC BY). The use, distribution or reproduction in other forums is permitted, provided the original author(s) and the copyright owner(s) are credited and that the original publication in this journal is cited, in accordance with accepted academic practice. No use, distribution or reproduction is permitted which does not comply with these terms.



Energy Conversion at Kinetic Scales in the Turbulent Magnetosheath

Zoltán Vörös^{1,2*}, Emiliya Yordanova³, Yuri V. Khotyaintsev³, Ali Varsani¹ and Yasuhito Narita¹

¹ Space Research Institute, Austrian Academy of Sciences, Graz, Austria, ² Geodetic and Geophysical Institute, Hungarian Academy of Sciences, Sopron, Hungary, ³ Swedish Institute of Space Physics, Uppsala, Sweden

OPEN ACCESS

Edited by:

Antonella Greco,
Department of Physics, University of
Calabria, Italy

Reviewed by:

Yan Yang,
Southern University of Science and
Technology, China
Anton Artemyev,
Space Research Institute (RAS),
Russia

*Correspondence:

Zoltán Vörös
zoltan.voeroes@oeaw.ac.at

Specialty section:

This article was submitted to
Space Physics,
a section of the journal
*Frontiers in Astronomy and Space
Sciences*

Received: 30 June 2019

Accepted: 30 August 2019

Published: 13 September 2019

Citation:

Vörös Z, Yordanova E,
Khotyaintsev YV, Varsani A and
Narita Y (2019) Energy Conversion at
Kinetic Scales in the Turbulent
Magnetosheath.
Front. Astron. Space Sci. 6:60.
doi: 10.3389/fspas.2019.00060

The process of conversion or dissipation of energy in nearly collisionless turbulent space plasma, is yet to be fully understood. The existing models offer different energy dissipation mechanisms which are based on wave particle interactions or non-resonant stochastic heating. There are other mechanisms of irreversible processes in space. For example, turbulence generated coherent structures, e.g., current sheets are ubiquitous in the solar wind and quasi-parallel magnetosheath. Reconnecting current sheets in plasma turbulence are converting magnetic energy to kinetic and thermal energy. It is important to understand how the multiple (reconnecting) current sheets contribute to spatial distribution of turbulent dissipation. However, detailed studies of such complex structures have been possible mainly via event studies in proper coordinate systems, in which the local inflow/outflow, electric and magnetic field directions, and gradients could be studied. Here we statistically investigate different energy exchange/dissipation (EED) measures defined in local magnetic field-aligned coordinates, as well as frame-independent scalars. The presented statistical comparisons based on the unique high-resolution MMS data contribute to better understanding of the plasma heating problem in turbulent space plasmas.

Keywords: plasma turbulence, current sheets, magnetic reconnection, terrestrial magnetosheath, plasma heating

1. INTRODUCTION

Turbulence represents an unsolved problem in classical physics of continuous media (e.g., fluids) characterized by velocity shears, intermittent distribution of kinetic energy over multiple spatial, and temporal scales involving strong non-linear interactions and many (possibly infinite) degrees of freedom (e.g., Frisch, 1995). Natural fluid or gaseous flows have both laminar and turbulent components. Some examples are the atmospheric/oceanic circulation, the blood flow, turbulent river flows, turbulent flows in engineering, industrial and laboratory settings, etc. In natural and artificial flows the turbulence strength usually plays a decisive role determining the overall dynamical behavior of a given system. Turbulence in astrophysical systems is also expected to affect the dynamical behavior of plasmas over multiple scales, for example, modifying transport processes or supporting large-scale instabilities (Brandenburg and Lazarian, 2013). On the Sun, among others, turbulence can play a role in coronal heating, solar wind expansion (Cranmer et al., 2015) and particle acceleration (Vlahos et al., 2019). *In-situ* observations of solar wind fluctuations near the ecliptic and at high latitudes revealed scaling and intermittency features resembling the large-scale properties of hydrodynamic turbulence (Tu and Marsch, 1995; Bruno and Carbone, 2013). Within the terrestrial magnetosphere, because of the limited volumes and boundaries, the large fluid-scale scaling features of turbulent fluctuations might be less accessible

(Vörös et al., 2007). Nevertheless, plasma turbulence in the geospace environment also plays a significant role in plasma transport and energization (Borovsky and Funsten, 2003; Vörös et al., 2006; Zimbardo et al., 2010). Space plasma turbulence significantly differs from neutral fluid turbulence in several aspects. It contains a magnetic field which introduces anisotropies into turbulent fluctuations and it is nearly collisionless. In the absence of collisions the dissipation of energy and heating of plasma is rather different from the collisional dissipation in neutral fluids (Howes et al., 2008; Alexandrova et al., 2013; Parashar et al., 2015). The basically collisionless energy transfer processes at kinetic scales happen through wave-field-fluctuation particle interactions, including Landau damping (Chen et al., 2009; Schekochihin et al., 2009), cyclotron damping (Hollweg and Markovskii, 2002) and stochastic heating (Chandran et al., 2010; Hopcock et al., 2018; Schekochihin et al., 2018). Particle energization and heating can happen at (reconnecting) current sheets (Dmitruk et al., 2004; Retino et al., 2007; Servidio et al., 2009; Osman et al., 2012) generated by turbulence through self-organization (Matthaeus et al., 2015). Current sheets observed in the turbulent solar wind (Greco et al., 2009; Servidio et al., 2011) and in the turbulent magnetosheath downstream of a quasi-parallel shock (Chasapis et al., 2015; Vörös et al., 2016; Stawarz et al., 2019) are ubiquitous.

In this paper, using high-resolution field and plasma data from the Magnetospheric Multi-Scale (MMS) mission we investigate derived energy exchange/dissipation measures at (reconnecting) current sheets in the turbulent quasi-parallel magnetosheath. The paper is organized as follows. Section 2 explains the data and instrumentation and section 3 introduces the EED measures and their time evolution during a more than 4 min long time interval in the turbulent magnetosheath. Section 4 presents a conditional statistics of averaged EED measures for normalized current densities. Section 5 contains the summary and conclusions.

2. DATA AND INSTRUMENTATION

We consider the time interval between 00:21:45 and 00:26:15 UT on November 30, 2015, when the MMS spacecraft were in the strongly compressed quasi-parallel magnetosheath. The MMS fleet was at the GSE position $(9, -3, -0.5) R_E$ in tetrahedron configuration with inner probe separation between 4 and 22 km comparable to the electron and ion inertial lengths of ~ 1 and 20 km, respectively. During the selected time interval the ion and electron moments with time resolution of 150 and 30 ms, respectively, are available from Fast Plasma Investigation (FPI) instrument (Pollock et al., 2016). The electric field data from Electric Double Probes (EDP) instrument are available with time resolution of 8 kHz (Ergun et al., 2016; Lindqvist et al., 2016; Torbert et al., 2016b). The merged digital fluxgate (FGM) (Russell et al., 2016) and search coil (SCM) (Contel et al., 2016) data were developed by using instrument frequency and timing models that were created during the FIELDS integration test campaign (Fischer et al., 2016; Torbert et al., 2016b). The merged magnetic data analyzed here consists of FGM measurements below 4 Hz and data from SCM between 1 Hz and 6 kHz.

Figure 1 contains the field and plasma data for the selected period of time. **Figures 1A,E** show the GSE components of the magnetic field and of the electric field from MMS1 spacecraft. **Figures 1B–D** are quantities calculated from multi-point spacecraft measurement. **Figure 1B** contains the magnetic shear angles θ_{ij} obtained between spacecraft pairs MMS2-1, 3-1, and 4-1. **Figures 1C,D** show the magnitude of the magnetic field curvature (curvB) and curlometer current density (J_{curl}) GSE components, calculated by using the well-known four-point techniques (Dunlop et al., 1988; Chanteur, 1998). The rest of the subplots show electron (**Figures 1F–H**) and ion (**Figures 1I–K**) omnidirectional differential energy flux spectrograms, temperature (including parallel and perpendicular values to the magnetic field) and velocity data, respectively. All parameters show high variability, including the electron and ion energy flux spectrograms. The electron velocity (**Figure 1H**) fluctuates more than the ion velocity (**Figure 1K**), which indicates the presence of electron scale structures in the magnetosheath. The temperature anisotropy is stronger for the electrons (**Figure 1G**) than for the ions (**Figure 1J**), showing preferential electron heating in the parallel direction.

On the X axis of **Figure 1G** four time intervals are highlighted: (a) Quiet interval (after 00:22:18 UT indicated by brown color) when θ_{ij} , curvB, E , and J_{curl} are small, which means that the spacecraft do not cross any current sheets; (b) Time interval 1 (red color), the enhanced currents, magnetic shear and curvature are associated with reconnecting current sheet exhibiting a full set of fluid and kinetic scale signatures of magnetic reconnection (Vörös et al., 2017); (c) Time interval 2 (red color) contains a strong current sheet associated with electron acceleration parallel to the magnetic field, without clear signatures of ongoing reconnection (Eriksson et al., 2016); (d) Time interval 3 (red color), here ion and electron scale signatures of magnetic reconnection (Yordanova et al., 2016). During the studied active time intervals 1–3 localized enhancements of electron and proton temperatures were also observed. From the ion energy flux spectrogram (**Figure 1I**), it is also visible that occasionally the most energetic ions appear first, such dispersed ion can be generated by remote sources (Vörös et al., 2017). Such dispersion features in the electron energy flux spectrogram are not seen (**Figure 1F**). Relative to the currents in the quiet time interval there are multiple enhancements of the current density frequently associated with rotation of the magnetic field and enhanced curvB (**Figures 1B–D**). Therefore, it is meaningful to further investigate how these current structures are associated with energy conversion/dissipation processes.

3. EED (ENERGY EXCHANGE/DISSIPATION) MEASURES

The electron momentum equation in a two-fluid collisionless plasma can be expressed in the form (Gurnett and Bhattacharjee, 2005):

$$\mathbf{E} + \mathbf{V}_e \times \mathbf{B} = -\frac{1}{qN} \nabla \cdot \mathbb{P}_e + \frac{m_e}{qN} \left(\frac{\partial \mathbf{J}}{\partial t} + \nabla \cdot \mathbf{N}(\mathbf{V}_i \mathbf{V}_i - \mathbf{V}_e \mathbf{V}_e) \right) \quad (1)$$

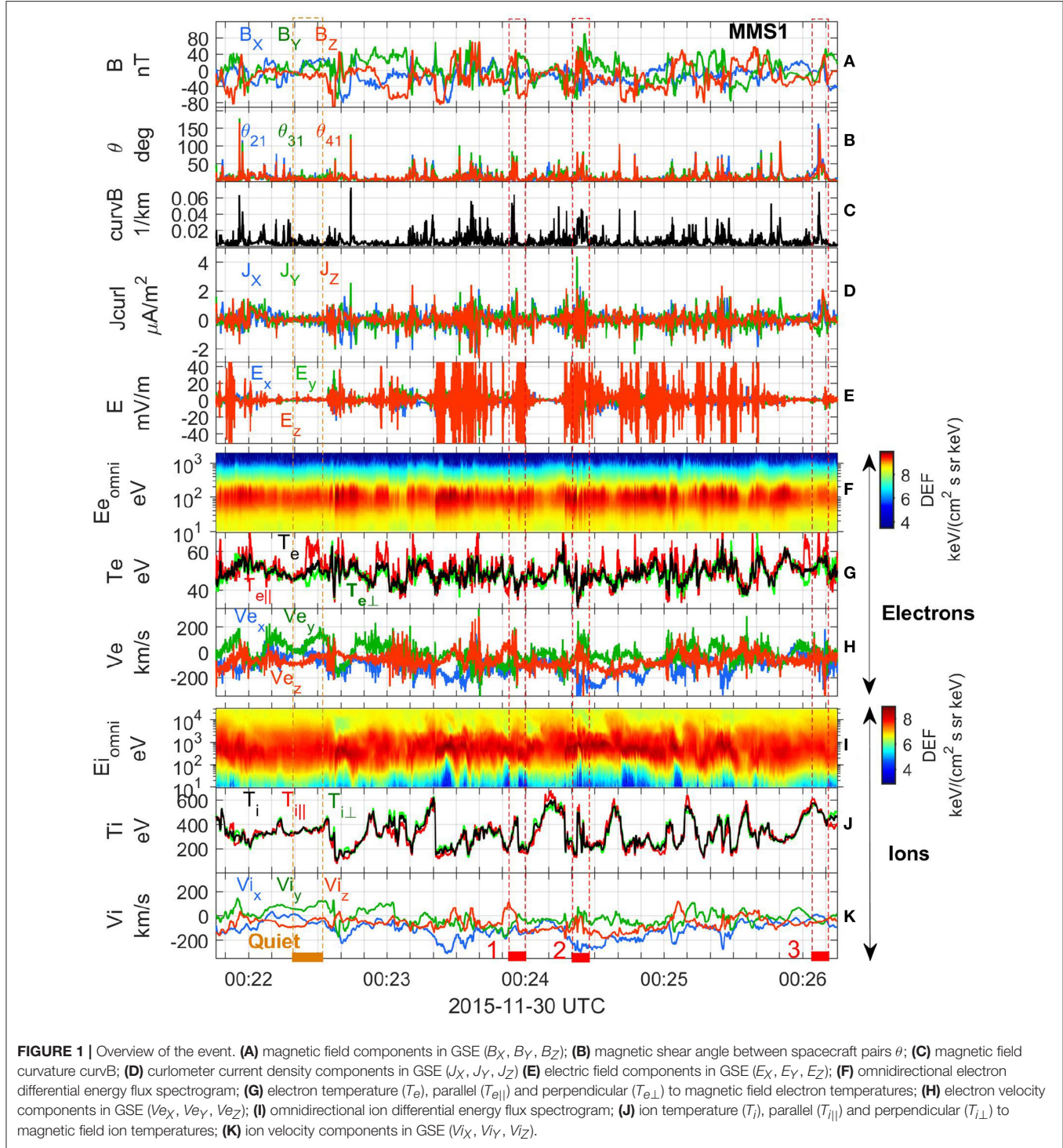


FIGURE 1 | Overview of the event. **(A)** magnetic field components in GSE (B_X , B_Y , B_Z); **(B)** magnetic shear angle between spacecraft pairs θ ; **(C)** magnetic field curvature curvB; **(D)** curlometer current density components in GSE (J_X , J_Y , J_Z) **(E)** electric field components in GSE (E_X , E_Y , E_Z); **(F)** omnidirectional electron differential energy flux spectrogram; **(G)** electron temperature (T_e), parallel ($T_{e||}$) and perpendicular ($T_{e\perp}$) to magnetic field electron temperatures; **(H)** electron velocity components in GSE (V_{eX} , V_{eY} , V_{eZ}); **(I)** omnidirectional ion differential energy flux spectrogram; **(J)** ion temperature (T_i), parallel ($T_{i||}$) and perpendicular ($T_{i\perp}$) to magnetic field ion temperatures; **(K)** ion velocity components in GSE (V_{iX} , V_{iY} , V_{iZ}). **2015-11-30 UTC**

where $\mathbf{E}' = \mathbf{E} + \mathbf{V}_e \times \mathbf{B}$ is the electric field in the moving frame of electrons, \mathbb{P}_e is the electron pressure tensor, N is the plasma density and the last term which is proportional to the mass of electrons (m_e), the electron inertia term, is negligible when the spatial scale lengths are greater than the electron inertial length. Since collisionless reconnection is associated with multi-scale physics, the ion and electron scales

are important in describing the electric fields and currents. In this paper we neglect the last term in Equation (1) and we consider the two remaining terms for constructing the EED measures:

$$\mathbf{J.E}' \quad (2)$$

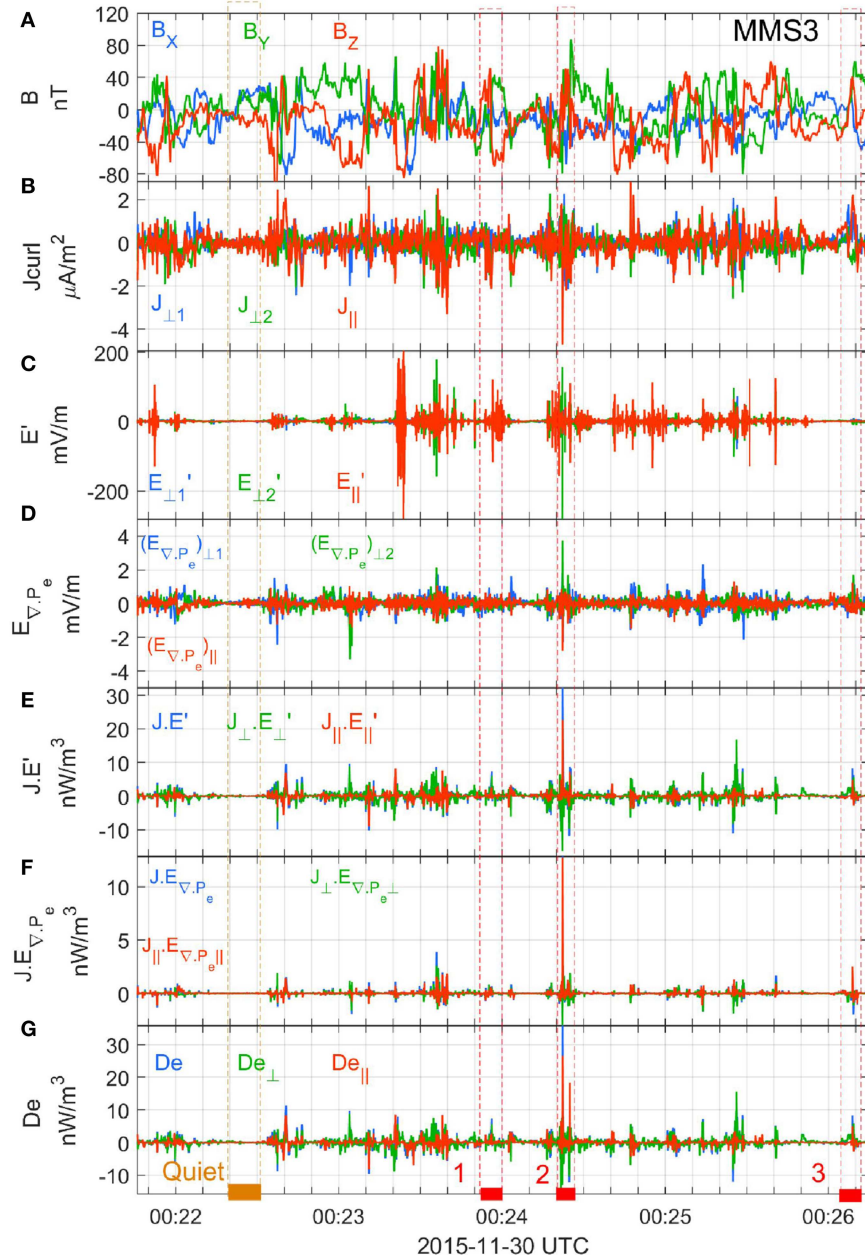


FIGURE 2 | (A) magnetic field components in GSE (B_x , B_y , B_z); **(B)** curlometer current density components in field-aligned (FAC) coordinates ($J_{\perp 1}$, $J_{\perp 2}$, $J_{||}$); **(C)** electric field in the moving electron frame $\mathbf{E}' = \mathbf{E} + \mathbf{V}_e \times \mathbf{B}$ in FAC coordinates; **(D)** electric field calculated from the divergence of electron pressure tensor ($E_{\nabla P_e}$) in FAC coordinates; **(E–G)** EED measures; **(E)** $\mathbf{J} \cdot \mathbf{E}'$ and the perpendicular and parallel products (Equation 2); **(F)** $\mathbf{J} \cdot (-\frac{1}{qN} \nabla \cdot \mathbb{P}_e)$ and the perpendicular and parallel products (Equation 3); **(G)** D_e (Equation 4).

and

$$\mathbf{J} \cdot \mathbf{E}_{\nabla P_e} \equiv \mathbf{J} \cdot \left(-\frac{1}{qN} \nabla \cdot \mathbb{P}_e \right) \quad (3)$$

which correspond to the rate of work done by non-ideal part of electric field on plasma particles. Here $\nabla \cdot \mathbb{P}_e$ was again calculated by using the four-point techniques (Chanteur, 1998). Both quantities are used in studies of energy conversion rates associated with magnetic reconnection (e.g., Burch et al., 2016;

Torbert et al., 2016a). However, the energy exchange processes in turbulent collisionless plasmas can be more complicated. Recent particle-in-cell simulations indicate that the pressure-stress interactions can also channel the energy of turbulent fluid motions to plasma particles and this type of energy transfer is preferentially localized at coherent structures (Yang et al., 2017). A recent study by Chasapis et al. (2018) has suggested that perhaps both channels of energy conversion, the work by electromagnetic fields and the effects of pressure-stress

interactions can be analyzed by using the high resolution MMS data. The pressure-stress interactions describe the transfer of energy from multi-scale fluid motions (possibly via a turbulent cascade) to thermal energy and depend on the pressure tensor and velocity gradients. While this energy conversion channel can also be important in collisionless space plasmas (Chasapis et al., 2018), we believe more studies would be needed to optimize the multi-spacecraft separations to properly estimate the underlying scales and velocity gradients. In this paper the pressure-stress terms are not considered. On the other hand, we also consider the frame independent measure introduced by Zenitani et al. (2011):

$$D_e = \mathbf{J} \cdot \mathbf{E}' - q(N_i - N_e)(\mathbf{V}_e \cdot \mathbf{E}') \quad (4)$$

which is similar to Equation (2), however, Equation (4) contains the additional second term on the right side corresponding to the work associated with the transport of net charge. For the time interval considered here the mean value of this term is ~ 0 nW/m³ with dispersion of ~ 0.7 nW/m³ (not shown). We note that the average values of electron and ion densities are rather high and approximately equal to ~ 100 1/cm³, therefore the plasma moments are well determined.

Figures 2A,B contain the magnetic field and curlometer current density components. In **Figures 2C–G** the non-ideal electric field components and the EED measures (Equations 2–4) are shown. Since the goal is to perform a statistical analysis, the field-aligned coordinate system (FAC) is chosen in which the currents, electric fields and the derived measures are transformed to parallel and two perpendicular components relative to the local mean magnetic field. Before calculating the EED measures the electric fields were filtered using a fourth-order elliptic low-pass filter. This removes the high-frequency part of the electric field fluctuations over 1 Hz which can be associated with electrostatic noise or waves. In this way, also the unpredictable effect of stochastic high-frequency fluctuations of the electric field on the dot products in Equations (2–4) is reduced. Since the field aligned and field perpendicular EED measures can be associated with different physical processes (Ergun et al., 2018), in calculating the dot products the parallel and perpendicular components of currents and electric fields are taken, for example, $J_{||} \cdot E'_{||}$ and $J_{\perp} \cdot E'_{\perp}$. To make the calculations possible for the whole time interval the perpendicular directions 1 and 2 are not distinguished.

Figure 2 demonstrates that during the quiet time interval (after 00:22:18 UT, indicated in **Figure 2G**), in the absence of current structures, the EED measures (**Figures 2E–G**) remain close to zero. The previously reported (reconnecting) current sheet events, time intervals 1,2,3, are all associated with elevated values of EED measures. The largest deviations of the measures are associated with the strongest currents during the event 2.

Figures 3A–C show the histograms of the EED measures, separately for the dot products (blue color), the perpendicular (green color) and the parallel (red color) products, respectively. Data for MMS3 spacecraft are shown. The broader distribution corresponds to $\mathbf{J} \cdot \mathbf{E}'$ as it is larger over the sub-ion scales than

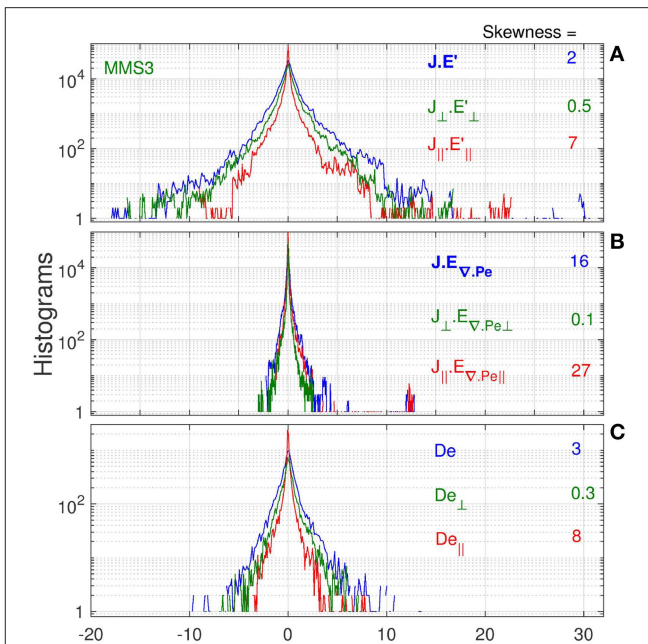


FIGURE 3 | (A–C) Histograms of EED measures and their perpendicular and parallel products from MMS3 sapcecraft; The color coded skewness associated with a histogram is shown for each component on the right.

$\mathbf{J} \cdot \left(-\frac{1}{qN} \nabla \cdot \mathbb{P}_e \right)$ and also it does include some contributions from the fluid scale stresses. For each subplot and product type the skewness of the distributions are shown on the right. The positive skewness means that the distributions have longer tails in positive direction with the meaning that there might exist a net dissipation in the overall energy exchange processes in the turbulent magnetosheath. The largest skewness are associated with EED measures in parallel to magnetic field direction.

4. CONDITIONAL STATISTICS

The goal of the paper is to determine how the local dissipation depends on the strength of the current density in turbulence. To this end we calculated the time averaged EED measures conditioned on current density and normalized to the time averages of the same measure over the whole time interval. In other words, the relative local enhancements of EED measures for certain values of current densities are estimated relative to the background fluctuations of EED measures, for examples $\langle \mathbf{J} \cdot \mathbf{E}' / \mathbf{J} \rangle / \langle \mathbf{J} \cdot \mathbf{E}' \rangle$. These quantities are plotted against the normalized current density $|\mathbf{J}| / |\mathbf{J}|_{rms} \equiv J / J_{rms}$, where J_{rms} is the root mean square. For each EED measure and MMS1–4 spacecraft the parallel (triangles) and the perpendicular components (circles) of the dot products are shown in **Figures 4A–C**. Again, in dependence on J / J_{rms} the measures in parallel direction grow faster. The dependence of normalized EED measures averaged in time and over the spacecraft are shown with thick black lines in each subplot. For comparison, in **Figure 4C** the results from 2.5D PIC (magenta color) and

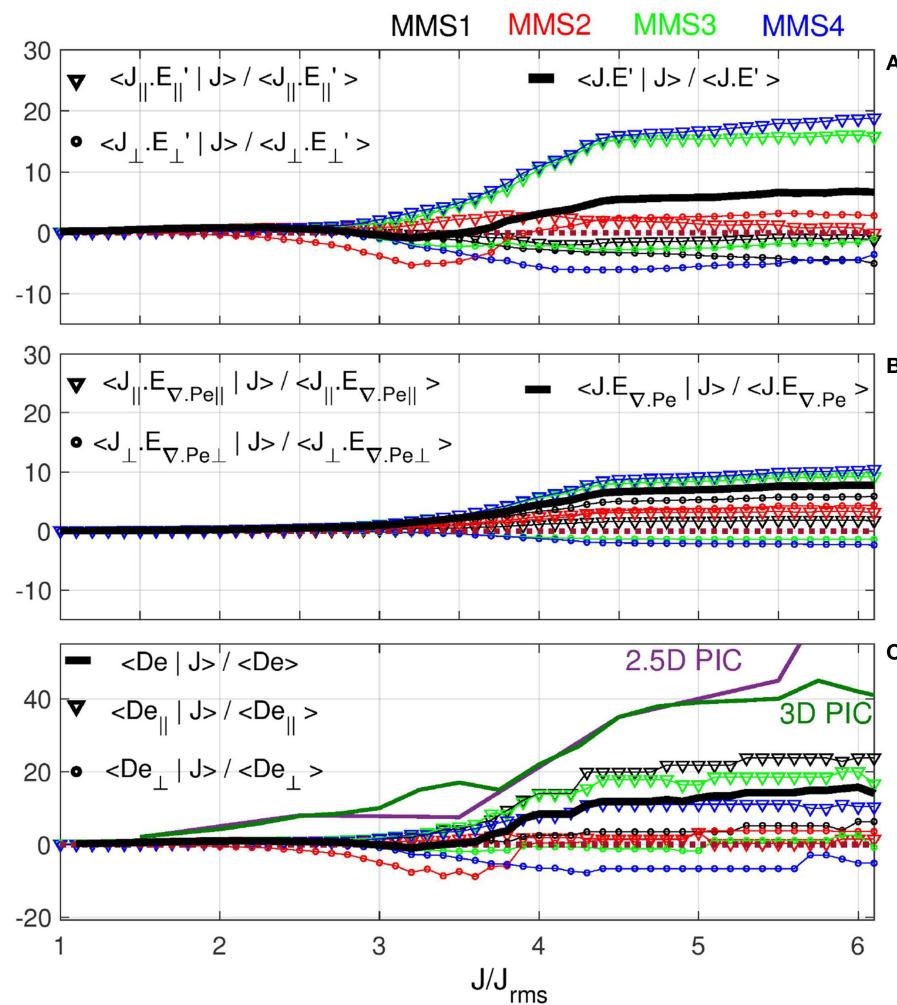


FIGURE 4 | (A–C) Normalized current density J/J_{rms} (rms = root mean square) versus conditional temporal averages of normalized EED measures calculated by conditioning on the values of current density J . The color code in each subplot corresponds to the spacecraft MMS1–4. The triangles show the parallel and the circles the perpendicular products. The thick black lines represent temporal and spatial averages between MMS1–4. In subplot (C) the results from 2.5D and 3D PIC simulations are shown (Wan et al., 2015).

3D PIC (green color) are also shown (Wan et al., 2015). It can be seen that in simulations the normalized conditional average $\langle D_e | J \rangle$ increases faster with J than in the magnetosheath turbulence. However, there is a qualitative agreement, showing that stronger current densities are associated with larger dissipation. This seems to be a valid statement for each EED measure.

In Figure 4 the EED measures start increasing roughly at $J = 3J_{rms}$ and there are significant differences between components and spacecraft. Actually, $J_{rms} \sim 0.6 \mu\text{A}/\text{m}^2$ and for e.g. $4J_{rms}$ the threshold for J is $2.4 \mu\text{A}/\text{m}^2$ which corresponds to only a few current sheets in Figure 2B. For $J = 6J_{rms} = 3.6 \mu\text{A}/\text{m}^2$ it is only one current sheet (event 2 in Figure 2B) which enters into the statistics in Figure 4, therefore the differences between the spacecraft can be understood as due to different crossing geometries across the same event.

5. SUMMARY AND CONCLUSIONS

In this study more than 4 min of high resolution field and plasma data from the MMS spacecraft was analyzed. Although longer time intervals of magnetosheath data were available from the previous missions, the time resolution of the plasma data was not sufficient to study the thin structures generated by turbulence. The measures corresponding to the work done by electric fields ($\mathbf{J} \cdot \mathbf{E}'$ and $\mathbf{J} \cdot (-\frac{1}{qN} \nabla \cdot \mathbb{P}_e)$) and the corrected measure obtained after removing the net charge transport term (D_e), were estimated. The statistical analysis of the temporally and spatially averaged and normalized measures has shown that there is a net irreversible work done by electric fields at current sheets. The averaged $\langle D_e | J \rangle$ increases as the current density increases in qualitative agreement with PIC numerical simulations (Wan et al., 2015). However, the time interval under study is rather short

when currents stronger than $5 - 6J_{rms}$ are considered for statistical analysis.

The relative importance of the terms in Equation (1) and of the EED measures in Equations (2–4) have been studied both numerically and experimentally at reconnecting current sheets (Hesse et al., 2016; Nakamura et al., 2016; Shay et al., 2016; Torbert et al., 2016b; Genestreti et al., 2018). According to these event studies, E' (left hand side of Equation 1) dominates outside the reconnection diffusion region, where both electrons and ions are attached to the magnetic field, and the right hand side of the Equation (1) is negligible. Inside the electron diffusion region, where both ions and electrons are demagnetized, the terms on the right hand side of Equation (1) balance E' and the first term on the right, $(\nabla \cdot P_e)$, is much larger than the second inertial term. However, near the reconnection X-line the inertial term can reach half of the pressure divergence term (Genestreti et al., 2018). Since the probability of crossing multiple reconnection X-lines in the magnetosheath is low, the inertial term can be neglected. On the other hand, in terms of EED measures (Equations 2–4), enhanced energy conversion/dissipation can occur not only within the electron diffusion region, but also at reconnection separatrices (Shay et al., 2016). Obviously, when the focus is on understanding of the statistics of dissipation occurring at multiple current sheets in the turbulent magnetosheath the geometry of crossings or the proper coordinate systems of local current sheets cannot be controlled. Our results show that in the quasi-parallel magnetosheath the electric fields (left and right hand sides of Equation 1) and the EED measures are intermittently enhanced. At the same time $E' \gg E_{\nabla \cdot P_e}$ (**Figures 2C,D**) and except for the current sheet during time interval 2, $J \cdot E' > D_e > J \cdot E_{\nabla \cdot P_e}$ (**Figures 2E–G, 3**). The comparison of histograms in **Figures 3A,C** shows that the distribution of D_e is narrower than the distribution of $J \cdot E'$, moreover, the tails of the histograms are also different. However, the comparison of the averaged and normalized EED measures at current sheets in **Figure 4** shows that, for stronger currents, D_e is slightly larger than $J \cdot E'$. The EED measures with net positive kurtosis (**Figure 3**) and irreversible work at current sheets (**Figure 4**) indicate that the spacecraft are crossing ion-electron scale current structures, reconnecting current sheets or reconnection separatrices in the turbulent magnetosheath. In fact, case studies have already shown that during the time interval 2 the MMS spacecraft touched the outer electron diffusion region (Vörös et al., 2017) and during the time interval 3 MMS went through a reconnection separatrix (Yordanova et al., 2016).

It was also found that during the analyzed time interval dissipation occurred preferentially in parallel direction to the magnetic field. This is seen in **Figure 1G**, where $T_{e\parallel} > T_{e\perp}$, but mainly in **Figures 3, 4**, where the statistics of EED measures is presented. In a similar study by Ergun et al. (2018) it was found that the net dissipation in the Earth's plasma sheet was mainly associated with the perpendicular contribution of $J \cdot E'$ and the parallel part represented merely 20% of dissipation. However, Ergun et al. (2018) did not apply any conditioning on current sheets for their EED measure. Also, on the basis of Cluster observations of magnetic reconnection in the Earth's magnetotail (Fu et al., 2017) found that in terms of $J \cdot E' > 0$

energy dissipation occurred at current filaments, at spiral nulls (O-lines) mainly in perpendicular direction to the magnetic field. However, near radial nulls (X-lines) energy dissipation was surprisingly small. Although in our case the dissipation occurred mainly in the parallel to magnetic field direction, at some MMS spacecraft the EED measures also show net positive dissipation in perpendicular direction as well. Again, in a statistical analysis which includes multiple current sheets the crossings of particular locations of the underlying structures cannot be controlled. Also, the magnetic shear angles ($<180^\circ$) in **Figure 1B** indicate, that at least over the MMS separation distances, the magnetic field associated with the current sheets is not fully antiparallel and significant guide fields can exist. A reconnection event study has shown that the guide field during time interval 1 reached $\sim 20\%$ of the main magnetic field (Vörös et al., 2017). Recently, in a statistical study of magnetic reconnection events in the turbulent magnetosheath, Phan et al. (2018) have shown that out of 34 events 23 were associated with magnetic shear angles $<45^\circ$. We can speculate that in turbulent space plasmas the chaotic motions typically generate current sheets with significant guide fields. Both numerical simulations (Shay et al., 2014) and data analysis (Phan et al., 2013; Wilder et al., 2018) show that a guide field suppresses electron perpendicular heating and supports parallel heating. This could explain our observations of preferred parallel heating and energy conversion at magnetosheath current sheets.

Although our understanding of the energy conversion mechanisms at current sheets has improved over the past years, we are far from seeing the complete picture of the associated turbulent dissipation. We mention here two limiting factors. First, the generating mechanisms of current sheets and the role of velocity gradients needs to be understood better. Second, reconnecting current sheets in 3D turbulence can be associated with electron scale coherent structures, for example, interacting extended flux ropes (Daughton et al., 2011). In both cases the one-scale tetrahedron geometry (Cluster or MMS) appears to be a limiting factor in the observation of real multi-scale 3D processes.

Certainly, further numerical simulations, event studies and statistical analysis of current sheets will be needed to understand better the role of coherent structures in kinetic energy conversions in collisionless turbulent plasmas and their contribution to the total heating of larger plasma volumes.

DATA AVAILABILITY

The datasets analyzed for this study can be found in the MMS science data archive <https://lasp.colorado.edu/mms/sdc/public/>.

AUTHOR CONTRIBUTIONS

ZV and EY analyzed the data and drafted the manuscript. YK, AV, and YN contributed to the interpretation of the analysis and general improvements in the manuscript.

FUNDING

ZV was supported by the Austrian FWF project P28764-N27. EY was supported by the Swedish Civil Contingencies Agency, grant 2016-2102.

REFERENCES

- Alexandrova, O., Chen, C., Sorriso-Valvo, L., Horbury, T., and Bale, S. (2013). Solar wind turbulence and the role of ion instabilities. *Space Sci. Rev.* 178, 101–139. doi: 10.1007/s11214-013-0004-8
- Borovsky, J., and Funsten, H. (2003). Mhd turbulence in the earths plasma sheet: dynamics, dissipation and driving. *J. Geophys. Res.* 108, 1–37. doi: 10.1029/2002JA009625
- Brandenburg, A., and Lazarian, A. (2013). Astrophysical hydromagnetic turbulence. *Space Sci. Rev.* 178, 163–200. doi: 10.1007/s11214-013-0009-3
- Bruno, R., and Carbone, V. (2013). The solar wind as a turbulence laboratory. *Living Rev. Sol. Phys.* 10, 1–208. doi: 10.12942/lrsp-2013-2
- Burch, J. L., Torbert, R. B., Phan, T. D., Chen, L. L., Moore, T. E., Ergun, R. E., et al. (2016). Electron-scale measurements of magnetic reconnection in space. *Science* 352, aaf2939–1–aaf2939–10. doi: 10.1126/science.aaf2939
- Chandran, B., Li, B., Rogers, B., Quataert, E., and Germaschewski, K. (2010). Perpendicular ion heating by low-frequency alfvén wave turbulence in the solar wind. *Astrophys. J.* 720, 503–515. doi: 10.1088/0004-637X/720/1/503
- Chanteur, G. (1998). “Spatial interpolation for four spacecraft: theory,” in *Analysis Methods for Multi-Spacecraft Data*, eds G. Paschmann and P. Daly (Bern; Noordwijk: ISSI/ESA Publications Division), 349–369.
- Chasapis, A., Retino, A., Sahraoui, F., Vaivads, A., Khotyaintsev, Y., Sundkvist, D., et al. (2015). The current sheets and associated electron heating in turbulent space plasma. *Astrophys. J. Lett.* 804, 1–5. doi: 10.1088/2041-8205/804/1/L1
- Chasapis, A., Yang, Y., Matthaeus, W., Parashar, T., Haggerty, C., Burch, J., et al. (2018). Energy conversion and collisionless plasma dissipation channels in the turbulent magnetosheath observed by the magnetospheric multiscale mission. *Astrophys. J.* 862, 1–7. doi: 10.3847/1538-4357/aac775
- Chen, C. H. K., Klein, K. G., and Howes, G. G. (2009). Evidence for electron landau damping in space plasma turbulence. *Nat. Com.* 10, 1–8. doi: 10.1038/s41467-019-08435-3
- Contel, O. L., Leroy, P., Roux, A., Coillot, C., Alison, D., Bouabdellah, A., et al. (2016). The search-coil magnetometer for MMS. *Space Sci. Rev.* 199, 257–282. doi: 10.1007/978-94-024-0861-4-9
- Cranmer, S. R., Asgari-Targhi, M., Miralles, M. P., Raymond, J. C., Strachan, L., Tian, H., et al. (2015). The role of turbulence in coronal heating and solar wind expansion. *Phil. Trans. R. Soc. A* 373, 1–16. doi: 10.1098/rsta.2014.0148
- Daughton, W., Roytershteyn, V., Karimabadi, H., Yin, L., Albright, B., Bergen, B., et al. (2011). Role of electron physics in the development of turbulent magnetic reconnection in collisionless plasmas. *Nat. Phys.* 7, 539–542. doi: 10.1038/nphys1965
- Dmitruk, P., Matthaeus, W., and Seenu, N. (2004). Test particle energization by current sheets and nonuniform fields in magnetohydrodynamic turbulence. *Astrophys. J.* 617, 667–679. doi: 10.1086/425301
- Dunlop, M., Southwood, D., Glassmeier, K., and Neubauer, F. (1988). Analysis of multipoint magnetometer data. *Adv. Space Res.* 8, 273–277. doi: 10.1016/0273-1177(88)90141-X
- Ergun, R., Goodrich, K., Wilder, F., Ahmadi, N., Holmes, J., Eriksson, S., et al. (2018). Magnetic reconnection, turbulence, and particle acceleration: observations in the earths magnetotail. *Geophys. Res. Lett.* 45, 3338–3347. doi: 10.1002/2018GL076993
- Ergun, R., Tucker, S., Westfall, J., Goodrich, K., Malaspina, D., Summers, D., et al. (2016). The axial double probe and fields signal processing for the MMS mission. *Space Sci. Rev.* 199, 167–188. doi: 10.1007/s11214-014-0115-x
- Eriksson, E., Vaivads, A., Graham, D., Khotyaintsev, Y., Yordanova, E., Hietala, H., et al. (2016). Strong current sheet at a magnetosheath jet: kinetic structure and electron acceleration. *J. Geophys. Res. Space Phys.* 121, 9608–9618. doi: 10.1002/2016JA023146
- Fischer, D., Magnes, W., Hagen, C., Dors, I., Chutter, M., Needell, J., et al. (2016). Optimized merging of search coil and fluxgate data for MMS. *Geosci. Instrum. Method. Data Syst.* 5, 521–530. doi: 10.5194/gi-5-521-2016
- Frisch, U. (1995). *Turbulence: The Legacy of A.N. Kolmogorov*. Cambridge: Cambridge University Press.
- Fu, H., Vaivads, A., Khotyaintsev, Y., Andre, M., Cao, J., Olshevsky, V., et al. (2017). Intermittent energy dissipation by turbulent reconnection. *Geophys. Res. Lett.* 44, 37–43. doi: 10.1002/2016GL071787
- Genestreti, K., Varsani, A., Burch, J., Cassak, P., Torbert, R., Nakamura, R., et al. (2018). MMS observation of asymmetric reconnection supported by 3-d electron pressure divergence. *J. Geophys. Res.* 123, 1806–1821. doi: 10.1002/2017JA025019
- Greco, A., Matthaeus, W., Servidio, S., Chuychai, P., and Dmitruk, P. (2009). Statistical analysis of discontinuities in solar wind ace data and comparison with intermittent mhd turbulence. *Astrophys. J.* 691, L111–L114. doi: 10.1088/0004-637X/691/2/L111
- Gurnett, D., and Bhattacharjee, A. (2005). *Introduction to Plasma Physics*. Cambridge: Cambridge University Press.
- Hesse, M., Liu, Y., Chen, L., Bessho, N., Kuznetsova, M., Birn, J., et al. (2016). On the electron diffusion region in asymmetric reconnection with a guide magnetic field. *Geophys. Res. Lett.* 43, 2359–2364. doi: 10.1002/2016GL068373
- Hollweg, J., and Markovskii, S. A. (2002). Cyclotron resonances of ions with obliquely propagating waves in coronal holes and the fast solar wind. *J. Geophys. Res.* 107, 1–7. doi: 10.1029/2001JA000205
- Hopcock, I. W., Chandran, B. D. G., Klein, K. G., Mallet, A., and Verscharen, D. (2018). Stochastic proton heating by kinetic-alfven-wave turbulence in moderately high-beta plasmas. *J. Plasma Phys.* 84, 1–21. doi: 10.1017/S0022377818001277
- Howes, G., Cowley, S., Dorland, W., Hammett, G., Quataert, E., and Schekochihin, A. (2008). A model of turbulence in magnetized plasmas: implications for the dissipation range in the solar wind. *J. Geophys. Res.* 113, 1–24. doi: 10.1029/2007JA012665
- Lindqvist, P., Olsson, G., Torbert, R., King, B., Granoff, M., Rau, D., et al. (2016). The spin-plane double probe electric field instrument for MMS. *Space Sci. Rev.* 199, 137–165. doi: 10.1007/978-94-024-0861-4-6
- Matthaeus, W. H., Wan, M., Servidio, S., Greco, A., Osman, K. T., Oughton, S., et al. (2015). Intermittency, nonlinear dynamics and dissipation in the solar wind and astrophysical plasmas. *Philos. Trans. R. Soc. A* 373, 1–32. doi: 10.1098/rsta.2014.0154
- Nakamura, T., Nakamura, R., and Hasegawa, H. (2016). Spatial dimensions of the electron diffusion region in anti-parallel magnetic reconnection. *Ann. Geophys.* 34, 357–367. doi: 10.5194/angeo-34-357-2016
- Osman, K. T., Matthaeus, W. H., Wan, M., and Rappazzo, A. F. (2012). Intermittency and local heating in the solar wind. *Phys. Rev. Lett.* 108, 261102–1–261102–4. doi: 10.1103/PhysRevLett.108.261102
- Parashar, T., Salem, C., Wicks, R., Karimabadi, H., Gary, S., and Matthaeus, W. (2015). Turbulent dissipation challenge: a community-driven effort. *J. Plasma Phys.* 81, 1–22. doi: 10.1017/S0022377815000860
- Phan, T., Shay, M., Gosling, J., Fujimoto, M., Drake, J., Paschmann, G., and et al. (2013). Electron bulk heating in magnetic reconnection at earths magnetopause: dependence on the inflow alfvén speed and magnetic shear. *Geophys. Res. Lett.* 40, 4475–4480. doi: 10.1002/grl.50917
- Phan, T. D., Eastwood, J. P., Shay, M. A., Drake, J. F., Sonnerup, B., Fujimoto, M., and et al. (2018). Electron magnetic reconnection without ion coupling in earth’s turbulent magnetosheath. *Nature* 557, 202–206. doi: 10.1038/s41586-018-0091-5

ACKNOWLEDGMENTS

We are grateful for numerous discussions on this topic with R. Nakamura and O. W. Roberts, both from Space Research Institute, Graz.

- Pollock, C., Moore, T., Jacques, A., Burch, J., Gliese, U., Saito, Y., et al. (2016). Fast plasma investigation for magnetospheric multiscale. *Space Sci. Rev.* 199, 331–406. doi: 10.1007/s11214-016-0245-4
- Retino, A., Sundkvist, D., Vaivads, A., Mozer, F., Andre, M., and Owen, C. (2007). *In situ* evidence of magnetic reconnection in turbulent plasma. *Nat. Phys.* 3, 235–238. doi: 10.1038/nphys574
- Russell, C., Anderson, B., Baumjohann, W., Bromund, K., Dearborn, D., Fischer, D., et al. (2016). The magnetospheric multiscale magnetometers. *Space Sci. Rev.* 199, 189–256. doi: 10.1007/s11214-014-0057-3
- Schekochihin, A., Cowley, S., Dorland, W., Hammett, G., Howes, G., Quataert, E., et al. (2009). Astrophysical gyrokinetics: kinetic and fluid turbulent cascades in magnetized weakly collisional plasmas. *Astrophys. J. Suppl.* 182, 310–377. doi: 10.1088/0067-0049/182/1/310
- Schekochihin, A., Kawazura, Y., and Barnes, M. A. (2018). Constraints on ion versus electron heating by plasma turbulence at low beta. *J. Plasma Phys.* 85, 1–41. doi: 10.1017/S0022377819000345
- Servidio, S., Greco, A., Matthaeus, W., Osman, K., and Dmitruk, P. (2011). Statistical association of discontinuities and reconnection in magnetohydrodynamic turbulence. *J. Geophys. Res.* 116, 1–11. doi: 10.1029/2011JA016569
- Servidio, S., Matthaeus, W., Shay, M., Cassak, P., and Dmitruk, P. (2009). Magnetic reconnection in two-dimensional magnetohydrodynamic turbulence. *Phys. Rev. Lett.* 102, 115003–1–115003–4. doi: 10.1103/PhysRevLett.102.115003
- Shay, M., Haggerty, C., Phan, T., Drake, J., Cassak, P., Wu, P., et al. (2014). Electron heating during magnetic reconnection: a simulation scaling study. *Phys. Plasmas* 21, 122902–1–122902–11. doi: 10.1063/1.4904203
- Shay, M., Phan, T., Haggerty, C., Fujimoto, M., Drake, J., Malakit, K., and et al. (2016). Kinetic signatures of the region surrounding the x line in asymmetric (magnetopause) reconnection. *Geophys. Res. Lett.* 43, 4145–4154. doi: 10.1002/2016GL069034
- Stawarz, J., Eastwood, J., Phan, T., Gingell, I., Shay, M., Burch, J., et al. (2019). Properties of the turbulence associated with electron-only magnetic reconnection in earths magnetosheath. *Astrophys. J. Lett.* 877, 1–7. doi: 10.3847/2041-8213/ab21c8
- Torbert, R., Burch, J., Giles, B., Gershman, D., Pollock, C. J., Dorelli, J., Avanov, L., et al. (2016a). Estimates of terms in ohms law during an encounter with an electron diffusion region. *Geophys. Res. Lett.* 43, 5918–5925. doi: 10.1002/2016GL069553
- Torbert, R., Russell, C., Magnes, W., Ergun, R., Lindqvist, P., LeContel, O., et al. (2016b). The fields instrument suite on MMS: scientific objectives, measurements, and data products. *Space Sci. Rev.* 199, 105–135. doi: 10.1007/s11214-014-0109-8
- Tu, C., and Marsch, E. (1995). Mhd structures, waves and turbulence in the solar wind: observations and theories. *Space Sci. Rev.* 73, 1–210. doi: 10.1007/978-94-015-8541-5
- Vlahos, L., Anastasiadis, A., Papaioannou, A., Kouloumvakos, A., and Isliker, H. (2019). Sources of solar energetic particles. *Philos. Trans. R. Soc. A* 377, 1–26. doi: 10.1098/rsta.2018.0095
- Vörös, Z., Baumjohann, W., Nakamura, R., Runov, A., Volwerk, M., Asano, Y., et al. (2007). Spectral scaling in the turbulent earths plasma sheet revisited. *Nonlin. Processes Geophys.* 14, 535–541. doi: 10.5194/npg-14-535-2007
- Vörös, Z., Baumjohann, W., Nakamura, R., Volwerk, M., and Runov, A. (2006). Bursty bulk flow driven turbulence in the earths plasma sheet. *Space Sci. Rev.* 122, 301–311. doi: 10.1007/s11214-006-6987-7
- Vörös, Z., Yordanova, E., Echim, M., Consolini, G., and Narita, Y. (2016). Turbulence-generated proton-scale structures in the terrestrial magnetosheath. *Astrophys. J. Lett.* 819, 1–6. doi: 10.3847/2041-8205/819/1/L15
- Vörös, Z., Yordanova, E., Varsani, A., Genestreti, K., Khotyaintsev, Y., Li, W., et al. (2017). MMS observation of magnetic reconnection in the turbulent magnetosheath. *J. Geophys. Res. Space Phys.* 122, 11442–11467.
- Wan, M., Matthaeus, W. H., Roytershteyn, V., Karimabadi, H., Parashar, T., Wu, P., et al. (2015). Intermittent dissipation and heating in 3d kinetic plasma turbulence. *Phys. Rev. Lett.* 114, 1–4. doi: 10.1103/PhysRevLett.114.175002
- Wilder, F., Ergun, R., Burch, J., Ahmadi, N., Eriksson, S., Phan, T., et al. (2018). The role of the parallel electric field in electron-scale dissipation at reconnecting currents in the magnetosheath. *J. Geophys. Res.* 123, 6533–6547. doi: 10.1029/2018JA025529
- Yang, Y., Matthaeus, W., Parashar, T., Haggerty, C., Roytershteyn, V., Daughton, W., et al. (2017). Energy transfer, pressure tensor, and heating of kinetic plasma. *Phys. Plasmas* 24, 1–14. doi: 10.1063/1.490421
- Yordanova, E., Vörös, Z., Varsani, A., Graham, D., Norgren, C., Khotyainstev, Y., et al. (2016). Electron scale structures and magnetic reconnection signatures in the turbulent magnetosheath. *Geophys. Res. Lett.* 43, 5969–5978. doi: 10.1002/2016GL069191
- Zenitani, S., Hesse, M., Klimas, A., Black, C., and Kuznetsova, M. (2011). The inner structure of collisionless magnetic reconnection: the electron-frame dissipation measure and hall fields. *Phys. Plasmas* 18, 1–9. doi: 10.1063/1.3662430
- Zimbardo, G., Greco, A., Sorriso-Valvo, L., Perri, S., Vörös, Z., Aburjania, G., et al. (2010). Magnetic turbulence in the geospace environment. *Space Sci. Rev.* 156, 89–134. doi: 10.1007/s11214-010-9692-5

Conflict of Interest Statement: The authors declare that the research was conducted in the absence of any commercial or financial relationships that could be construed as a potential conflict of interest.

Copyright © 2019 Vörös, Yordanova, Khotyaintsev, Varsani and Narita. This is an open-access article distributed under the terms of the Creative Commons Attribution License (CC BY). The use, distribution or reproduction in other forums is permitted, provided the original author(s) and the copyright owner(s) are credited and that the original publication in this journal is cited, in accordance with accepted academic practice. No use, distribution or reproduction is permitted which does not comply with these terms.



Kinetic Plasma Turbulence: Recent Insights and Open Questions From 3D3V Simulations

Silvio Sergio Cerri^{1*}, Daniel Grošelj² and Luca Franci³

¹ Department of Astrophysical Sciences, Princeton University, Princeton, NJ, United States, ² Max-Planck-Institut für Plasmaphysik, Garching, Germany, ³ School of Physics and Astronomy, Queen Mary University of London, London, United Kingdom

OPEN ACCESS

Edited by:

Denise Perrone,
Agenzia Spaziale Italiana, Italy

Reviewed by:

Christian L. Vásconez,
National Polytechnic School, Ecuador
Stephen Peter Gary,
Space Science Institute, United States

*Correspondence:

Silvio Sergio Cerri
scerri@astro.princeton.edu

Specialty section:

This article was submitted to
Space Physics,
a section of the journal
Frontiers in Astronomy and Space
Sciences

Received: 26 June 2019

Accepted: 20 September 2019

Published: 11 October 2019

Citation:

Cerri SS, Grošelj D and Franci L (2019) Kinetic Plasma Turbulence: Recent Insights and Open Questions From 3D3V Simulations. *Front. Astron. Space Sci.* 6:64. doi: 10.3389/fspas.2019.00064

Turbulence and kinetic processes in magnetized space plasmas have been extensively investigated over the past decades via *in-situ* spacecraft measurements, theoretical models and numerical simulations. In particular, multi-point high-resolution measurements from the *Cluster* and *MMS* space missions brought to light an entire new world of processes, taking place at the plasma kinetic scales, and exposed new challenges for their theoretical interpretation. A long-lasting debate concerns the nature of ion and electron scale fluctuations in solar-wind turbulence and their dissipation via collisionless plasma mechanisms. Alongside observations, numerical simulations have always played a central role in providing a test ground for existing theories and models. In this Perspective, we discuss the advances achieved with our 3D3V (reduced and fully) kinetic simulations, as well as the main questions left open (or raised) by these studies. To this end, we combine data from our recent kinetic simulations of both freely decaying and continuously driven fluctuations to assess the similarities and/or differences in the properties of plasma turbulence in the sub-ion range. Finally, we discuss possible future directions in the field and highlight the need to combine different types of numerical and observational approaches to improve the understanding of turbulent space plasmas.

Keywords: magnetic fields, plasma turbulence, solar wind, kinetic plasma simulations, turbulence intermittency, plasma waves

1. INTRODUCTION

With the establishment of satellite space missions, the near-Earth environment and the solar wind have provided unique opportunities to explore the physics of weakly collisional, magnetized plasmas (e.g., Bruno and Carbone, 2013; Chen, 2016; Verscharen et al., 2019). In particular, increasingly accurate *in-situ* measurements of plasma fluctuations and particle distribution functions from *Cluster* and *MMS* have uncovered an entire new world of kinetic processes occurring in plasma turbulence (e.g., Alexandrova et al., 2009, 2012, 2013; Sahraoui et al., 2009, 2010; Chen et al., 2010, 2019; Greco et al., 2016; Narita et al., 2016; Chasapis et al., 2017; Chen and Boldyrev, 2017; Huang et al., 2017; Roberts et al., 2017; Servidio et al., 2017). These observations highlight a change in the turbulent cascade at plasma microscales, challenging the community for a consistent theory of kinetic-range turbulence. In fact, several collisionless plasma processes may be simultaneously at play and compete with each other in determining the nature of ion-scale and

electron-scale fluctuations (e.g., Stawicki et al., 2001; Galtier and Bhattacharjee, 2003; Howes et al., 2008a; Gary and Smith, 2009; Schekochihin et al., 2009; Boldyrev and Perez, 2012; He et al., 2012; Podesta, 2012; Boldyrev et al., 2013; Matthaeus et al., 2014; Passot and Sulem, 2015, 2019; Kunz et al., 2018; Passot et al., 2018) and, consequently, how free energy cascades in phase space (e.g., Schekochihin et al., 2008; Servidio et al., 2017; Adkins and Schekochihin, 2018; Cerri et al., 2018; Eyink, 2018; Pezzi et al., 2018; Kawazura et al., 2019). Many observations at ion and sub-ion scales, specifically, suggest that turbulent fluctuations exhibit properties mainly typical of kinetic Alfvén waves (KAWs) (Leamon et al., 1998; Sahraoui et al., 2009; Podesta and TenBarge, 2012; Salem et al., 2012; Chen et al., 2013; Kiyani et al., 2013; Chen, 2016; Lacombe et al., 2017). The emergence of KAW-like fluctuations in kinetic turbulence has been also supported by means of a large number of theoretical and numerical works (e.g., Hollweg, 1999; Stawicki et al., 2001; Gary and Nishimura, 2004; Howes et al., 2008a; Gary and Smith, 2009; Sahraoui et al., 2012; TenBarge et al., 2012; Vásconez et al., 2014, 2015; Franci et al., 2015; Cerri et al., 2016; Pucci et al., 2016; Zhao et al., 2016; Valentini et al., 2017; Grošelj et al., 2019). Some of these studies rely on the so-called spectral field ratios, which provide a measure of the wave-like polarization properties of the turbulent fluctuations, as compared to what linear theory predicts (see, e.g., Boldyrev et al., 2013) and section 3.

In the above context, direct numerical simulations play a key role by providing a controlled test ground for different theories, providing information not accessible to observations. Enormous efforts have been recently made to understand 3D kinetic turbulence via numerical experiments (e.g., Howes et al., 2008b; Gary et al., 2012; TenBarge and Howes, 2013; Vasquez et al., 2014; Servidio et al., 2015; Told et al., 2015; Wan et al., 2015, 2016; Bañón Navarro et al., 2016; Comișel et al., 2016; Cerri et al., 2017b, 2018; Hughes et al., 2017a,b; Kobayashi et al., 2017; Franci et al., 2018a,b; Grošelj et al., 2018, 2019; Arzamasskiy et al., 2019; Roytershteyn et al., 2019; Zhdankin et al., 2019). In this Perspective, we combine data from our recent 3D3V studies (Cerri et al., 2017b; Franci et al., 2018b; Grošelj et al., 2019) to investigate whether common turbulence features exist in all three independently performed simulations (section 2), thus indicating a certain “universality” of kinetic-scale turbulence. Moreover, we also highlight possible model-dependent differences between the 3D hybrid-kinetic and fully kinetic simulations. We mention that this approach follows the general idea of adopting different models (and/or implementations) to study turbulent heating and dissipation in collisionless plasmas that was initiated within the “Turbulent Dissipation Challenge” framework (Parashar et al., 2015). Here we extend similar comparative analysis of the spectral properties that have been previously performed in a reduced two-dimensional setup (see Cerri et al., 2017a; Franci et al., 2017; Grošelj et al., 2017) to the more realistic three-dimensional geometry (section 3), and we present a new analysis of our data based on local structure functions (section 4). Finally, we discuss possible implications for sub-ion-scale turbulence and future directions emerging from this study (section 5).

2. DATA SETS

In the following, we consider three recent kinetic simulations in a six-dimensional phase space (“3D3V”) using: (i) CAMELIA, a hybrid particle-in-cell (PIC) code with massless electrons (Franci et al., 2018a), (ii) HVM, an Eulerian hybrid-Vlasov code with finite electron-inertia effects (Valentini et al., 2007), and (iii) OSIRIS, a fully kinetic PIC code (Fonseca et al., 2002, 2013). Unless otherwise specified, parallel (\parallel) and perpendicular (\perp) directions are defined with respect to the global mean magnetic field $\mathbf{B}_0 = B_0 \mathbf{e}_z$. Franci et al. (2018b) employed the CAMELIA code to investigate freely decaying, Alfvénic fluctuations in a cubic box ($L_{\parallel} = L_{\perp} = 128d_i$ with 512^3 grid points and 2048 particles per cell (ppc)) for $\beta_i = \beta_e = 0.5$, where $\beta_s = 8\pi n_0 T_s / B_0^2$ is the species beta. Cerri et al. (2017b) instead adopted the HVM code to study freely decaying compressive fluctuations in an elongated box ($L_{\parallel} = 2L_{\perp} \simeq 63d_i$ with $384^2 \times 64$ grid points in real space, and 51^3 points in a velocity space bounded by $|v/v_{th,i}| \leq 5$) for $\beta_i = \beta_e = 1$ and with a reduced ion-electron mass ratio of $m_i/m_e = 100$ (viz. including d_e -effects in a generalized Ohm’s law). Spectral filters were applied at runtime, determining a cutoff in the turbulent spectrum at $k_{\perp} d_i > 20$ and at $k_z d_i > 2$. Finally, Grošelj et al. (2019) use the OSIRIS code to investigate continuously driven Alfvénic fluctuations in a $\beta_i \approx \beta_e \approx 0.5$ plasma with $m_i/m_e = 100$. An elongated box was used ($L_{\parallel} = 2.56L_{\perp} \simeq 48.3d_i$ with $928^2 \times 1920$ grid points and 150 ppc per species). An example of $\delta \tilde{B}_{\perp} = \delta B_{\perp} / \delta B_{\perp}^{(\text{rms})}$ in a two-dimensional cut perpendicular to \mathbf{B}_0 is given in **Figure 1A**, along with a schematic representation of these simulations in the $(k_{\perp}, k_{\parallel})$ plane (**Figure 1B**).

In the following, the analysis of freely decaying simulations (viz., CAMELIA and HVM) is performed at the peak of the turbulent activity (cf, e.g., Servidio et al., 2015), while for the continuously driven OSIRIS run we consider the turbulence at the end of the simulation when the kinetic range spectra appear converged. Following Franci et al. (2018b) and Grošelj et al. (2019), PIC data have been filtered before performing the analysis to remove spectral regions dominated by particle noise. The OSIRIS data have been filtered for $k_{\perp} d_i > 30$ or $k_z d_i > 12$ and downsampled to a grid $464^2 \times 640$. Note that OSIRIS simulations require to resolve the Debye scale, while the physical scales of interest are well represented at a lower resolution. A short-time average over $\Delta t \Omega_{ce} = 2$ (Ω_{ce} being the electron cyclotron frequency) was also performed to further reduce electron-scale noise (Grošelj et al., 2019). The CAMELIA data have been filtered for $k_{\perp} d_i > 10$ or $k_z d_i > 2$. We also considered alternative filtering approaches confirming that our results are not very sensitive to such particular choice.

3. SPECTRAL SLOPES AND NORMALIZED FIELD RATIOS

Here we review and compare the standard set of spectral properties in our independently performed 3D kinetic simulations, namely the slopes of the turbulence power spectra and the spectral field ratios. Early theoretical predictions

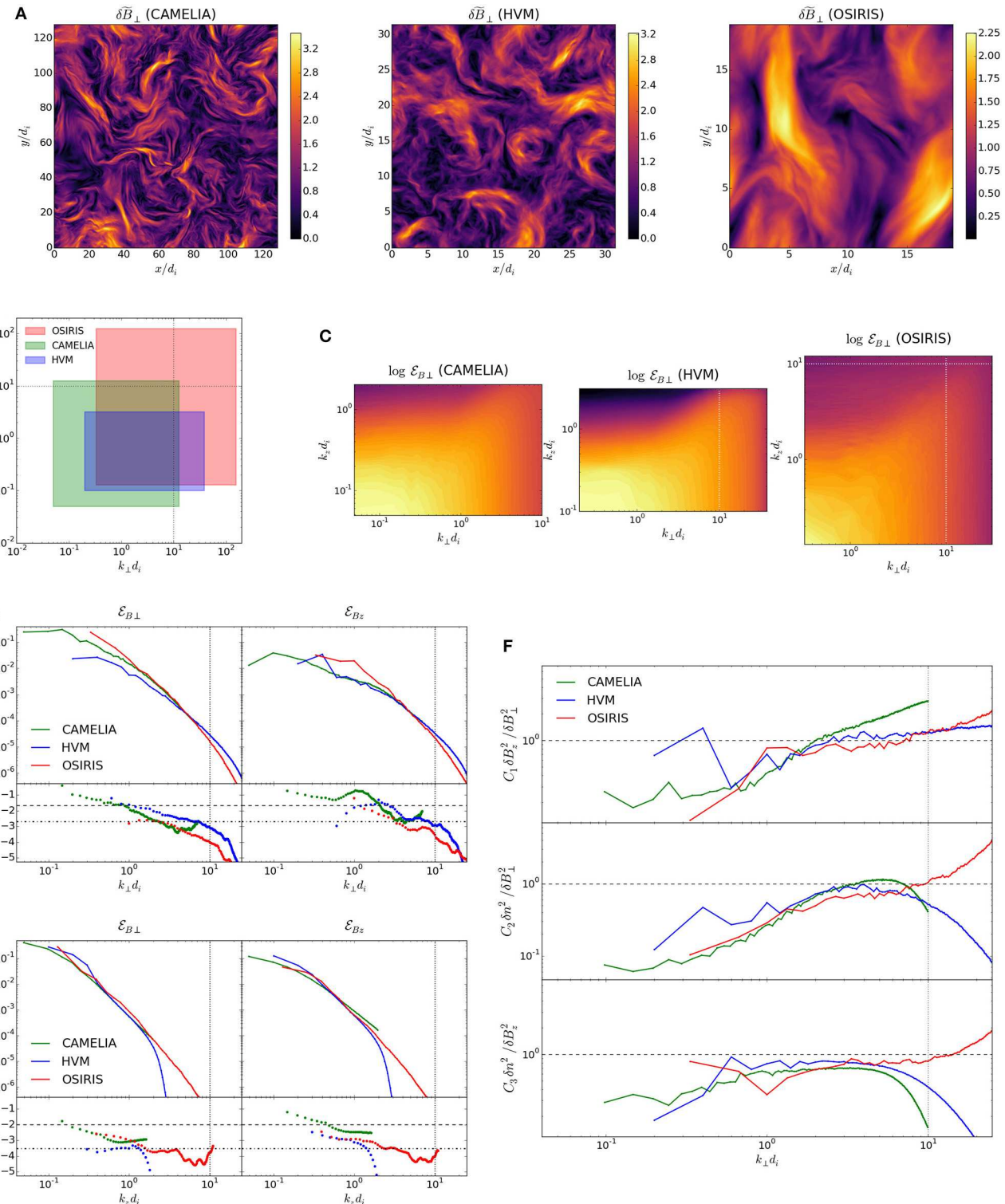


FIGURE 1 | (A) $\delta\bar{B}_\perp = \delta B_\perp / \delta B_\perp^{(\text{rms})}$ in a plane perpendicular to B_0 . **(B)** Nominal wavenumber-space representation of simulations. **(C)** δB_\perp spectrum in (k_\perp, k_z) space. White dotted lines mark $k d_e = 1$. **(D)** Top panels: reduced spectra vs. $k_\perp d_i$. Spectra have been shifted (see text). Bottom panels: local spectral exponents. Horizontal lines denote $-5/3$ (dashed) and $-8/3$ (dash-dotted) slopes. Vertical dotted line marks $k_\perp d_e = 1$. **(D)** Same as (E), but vs. $k_z d_i$. Here -2 (dashed) and $-7/2$ (dash-dotted) slopes are marked for reference. **(F)** Spectral ratios vs. k_\perp , normalized to the asymptotic KAW prediction (dashed horizontal lines; see text for details).

for sub-ion-range turbulence (e.g., Cho and Lazarian, 2004; Schekochihin et al., 2009) proposed a spectral scaling $\sim k_{\perp}^{-7/3}$ for the magnetic energy spectrum. However, solar wind observations typically exhibit much steeper magnetic spectra, namely $\sim k_{\perp}^{-2.8}$ (e.g., Alexandrova et al., 2009, 2013; Sahraoui et al., 2010; Chen, 2016; Kobayashi et al., 2017; Sorriso-Valvo et al., 2018). Similar spectral exponents were also reported in recent 3D kinetic simulations (Told et al., 2015; Cerri et al., 2017b, 2018; Franci et al., 2018a,b; Grošelj et al., 2018, 2019; Arzamasskiy et al., 2019). Recently, refined predictions were proposed to explain steeper spectra. Those include intermittency corrections (Boldyrev and Perez, 2012), dissipative effects (Howes et al., 2011; Passot and Sulem, 2015), and reconnection-mediated turbulence (Loureiro and Boldyrev, 2017; Mallet et al., 2017a). Further insight into the nature of kinetic-scale turbulence can be obtained from the spectral field ratios, which have been used to detect wave-like polarization properties in solar-wind turbulence and in kinetic simulations (e.g., Sahraoui et al., 2009; Salem et al., 2012; TenBarge et al., 2012; Chen et al., 2013; Kiyani et al., 2013; Cerri et al., 2017b; Franci et al., 2018b; Grošelj et al., 2018).

In **Figure 1C** the two-dimensional Fourier spectra, $\mathcal{E}(k_{\perp}, k_z)$, are shown. The wavenumber region (k_{\perp}, k_z) occupied by the turbulent fluctuations already highlights the anisotropic nature of the cascade, with energy preferentially flowing to high k_{\perp} . However, note that the 2D Fourier spectrum may exhibit a weaker anisotropy than the one typical of turbulent eddies, which are elongated along the *local* field direction (see, e.g., Cho and Vishniac, 2000). We perform a local analysis of anisotropy in section 4.1.

In **Figures 1D,E**, the reduced 1D spectra, $\mathcal{E}(k_{\perp})$ (upper panels), and their local slope (lower panels) are reported. To remove the effects of different energy injection conditions, the k_{\perp} -spectra have been normalized so that they overlap in the sub-ion range, at $k_{\perp}d_i \simeq 5$. According to the spectral anisotropy in **Figure 1C**, the k_z -spectra have been consequently matched at $k_zd_i \simeq 0.5$. For our choice of low-pass filter (see section 2), CAMELIA spectra artificially flatten beyond $k_{\perp}d_i \gtrsim 7$ due to PIC noise, and therefore we do not show CAMELIA data in this range in **Figure 1D**. Overall, the spectral slopes are consistent with each other, although the spectra obtained from the three simulations do not quite assume a universal shape. Close to the box scale, the spectral exponents are likely affected by the turbulence injection details. It is also possible that some of the sub-ion scale spectral exponents are not fully converged in terms of the box size (which was different for each simulation) and of the limited extent of sub-ion range itself. 3D3V simulations with a significantly larger sub-ion range are required to clarify this point. To some degree, differences at sub-ion scales could also be physical. In particular, the HVM simulation includes electron inertia effects in Ohm's law, while the OSIRIS results include the full electron kinetics, such as electron Landau damping and finite electron Larmor radius corrections. It is interesting to notice that OSIRIS spectra become steeper than the hybrid counterparts beyond $k_{\perp}d_i \gtrsim 3$, for our particular choice of the mass ratio ($m_i/m_e = 100$). This feature has been usually explained in terms of electron Landau damping (Grošelj et al., 2017; Chen et al., 2019), which is not included in the hybrid-kinetic model.

In **Figure 1F**, we report the comparison of spectral ratios, $C_1 \delta B_z^2 / \delta B_{\perp}^2$ (top), $C_2 \delta n^2 / \delta B_{\perp}^2$ (middle), and $C_3 \delta n^2 / \delta B_z^2$ (bottom). The ratios are normalized to the β -dependent kinetic Alfvén wave (KAW) eigenvalue from asymptotic linear theory ($\rho_i^{-1} \ll k_{\perp} \ll \rho_e^{-1}$ and $k_{\parallel} \ll k_{\perp}$), namely $C_1 = (2 + \beta)/\beta$, $C_2 = (2 + \beta)\beta/4$, and $C_3 = \beta^2/4$, where $\beta = \beta_i + \beta_e$ (see, e.g., Boldyrev et al., 2013, for details). In the normalized units, asymptotic KAW theory predicts a value of unity for all three ratios. This is essentially the result of KAWs developing a certain degree of magnetic compressibility at sub-ion scales, which sets the relation between δB_{\perp} and δB_{\parallel} , and requiring that compressive magnetic fluctuations are pressure balanced, which in turn provides a relation between δB_{\parallel} and δn (see, e.g., Schekochihin et al., 2009; Boldyrev et al., 2013). As found in previous studies (e.g., Salem et al., 2012; TenBarge et al., 2012; Chen et al., 2013; Cerri et al., 2017b; Franci et al., 2018b; Grošelj et al., 2018), the spectral field ratios are overall consistent with KAW-like turbulence at sub-ion scales. This is not completely surprising, as both in CAMELIA and OSIRIS simulations, Alfvénic fluctuations are injected. On the other hand, compressible magnetic fluctuations (i.e., including δB_{\parallel}) are injected in HVM run, and yet KAW-like fluctuations still develop. It was also proposed that KAWs may, quite generally, emerge as a result of Alfvén waves interacting with large-scale inhomogeneities (Pucci et al., 2016). Thus, the KAW-like spectral properties at sub-ion scales appear to be a relatively robust feature, independent of the details of the turbulent fluctuations injected at the MHD scales (cf. Cerri et al., 2017a). While the results are overall consistent, some differences are also seen, most notably in the high- k_{\perp} range ($k_{\perp}d_i \gtrsim 10$), which could be presumably attributed to various numerical artifacts. However, some deviations could also relate to differences between the hybrid-kinetic and fully kinetic model [for instance, some dispersion relation properties not being exactly the same (e.g., Told et al., 2016)].

So are the sub-ion-scale field polarizations indeed KAW-like? As discussed above, recent observations and kinetic simulations are consistent with such idea, although linear wave predictions are not necessarily satisfied precisely (e.g., Chen et al., 2013; Kiyani et al., 2013; Cerri et al., 2017b; Franci et al., 2018b). Chen et al. (2013) report an average value of 0.75 for the normalized ratio $C_2 \delta n^2 / \delta B_{\perp}^2$, whereas (asymptotic) KAW theory predicts a value of unity. That latter may be due to different reasons, among which we remark the following two: (i) sub-ion-range turbulence is not made of purely KAW-like fluctuations, and/or (ii) the asymptotic conditions that are used in the derivation of linear theory predictions are not met exactly because of the limited sub-ion range of scales and/or because of the inherently non-linear dynamics of turbulence. These two explanations are not mutually exclusive, of course. Indeed, sub-ion-scale turbulence can in principle include contributions from wave-like fluctuations of other nature. This may include fluctuations consistent with whistler (e.g., Gary and Smith, 2009), ion-cyclotron (e.g., Omidi et al., 2014; Zhao et al., 2018), or ion Bernstein waves (e.g., Podesta, 2012; Del Sarto et al., 2017; Grošelj et al., 2017), to name a few. On the other hand, the spectral ratios could also deviate from linear KAW predictions as a result of non-linear dynamics.

For example, Boldyrev et al. (2013) propose that, specifically the (normalized) $C_2 \delta n^2 / \delta B_{\perp}^2$ ratio may fall somewhat below the KAW prediction due to a (yet to be investigated) non-linear effect, analogous to the residual-energy phenomenon in MHD turbulence.

4. MULTI-POINT STRUCTURE FUNCTIONS

Beyond energy spectra, fluctuations across different scales may be investigated in more detail via structure functions, i.e., the moments of local field increments (e.g., Frisch, 1995; Biskamp, 2008). Two-point structure functions, $S_m^{(2)}$ (m being the order), are most common. However, these cannot quantitatively produce the correct scaling for fluctuations with power spectra steeper than $\sim k^{-3}$, assuming a clean power-law spectrum (Falcon et al., 2007; Cho and Lazarian, 2009). Therefore, structure functions using more than two points are generally required at kinetic scales. Essentially, higher-order increments yield a scale decomposition that is more effective in filtering out the large-scale fluctuations below $k \approx \pi/\ell$ in spectral space, where ℓ is the increment scale. We also mention that if the signal is a polynomial of degree $N - 2$, its corresponding 2nd-order, N -point structure function vanishes (Cho, 2019). This makes multi-point structure functions more suitable for the analysis of relatively smooth signals with steep spectra (Schneider et al., 2004). A detailed review of N -point increments, as well as their physical interpretation can be found in Cho (2019). Here, we consider for some field $f(\mathbf{x})$ the *conditional*, five-point structure functions:

$$S_m^{(5)}(\ell, \vartheta_{B_{\text{loc}}}) = \langle |\Delta f(\mathbf{x}, \ell)|^m | \ell, \vartheta_{B_{\text{loc}}} \rangle_x \quad (1)$$

where $\Delta f(\mathbf{x}, \ell) = [f(\mathbf{x}+2\ell) - 4f(\mathbf{x}+\ell) + 6f(\mathbf{x}) - 4f(\mathbf{x}-\ell) + f(\mathbf{x}-2\ell)]/\sqrt{35}$ is the (normalized) field increment, $\langle \dots \rangle_x$ is a space average, and $\vartheta_{B_{\text{loc}}}$ is the angle between the increment vector ℓ and the local mean magnetic field \mathbf{B}_{loc} . The term “conditional” implies that S_m are defined as conditional averages of $|\Delta f(\mathbf{x}, \ell)|^m$, using only those points in the statistical sample that fall within a given (narrow) range for ℓ and $\vartheta_{B_{\text{loc}}}$. We also considered three-point structure functions (see Figure 2A) and, for a limited number of cases, seven-point structure functions (not shown). Comparison between the three-point, five-point and seven-point structure functions shows not only qualitative similarities among the three cases, but an apparent quantitative convergence with increasing number of points. We chose to illustrate the results in Figure 2 in terms of five-point structure functions in order to provide better constraints for the theoretical predictions. Similar to two-point increments, where the local mean field is often defined as $\mathbf{B}_{\text{loc}}(\mathbf{x}, \ell) = [\mathbf{B}(\mathbf{x}) + \mathbf{B}(\mathbf{x}+\ell)]/2$ (e.g., Cho and Vishniac, 2000; Mallet et al., 2016), we obtain \mathbf{B}_{loc} by averaging over the points used for the increment. For five-point increments, a reasonable definition is $\mathbf{B}_{\text{loc}}(\mathbf{x}, \ell) = [\mathbf{B}(\mathbf{x}+2\ell) + 4\mathbf{B}(\mathbf{x}+\ell) + 6\mathbf{B}(\mathbf{x}) + 4\mathbf{B}(\mathbf{x}-\ell) + \mathbf{B}(\mathbf{x}-2\ell)]/16$. It is straightforward to check that such mean field definition filters out fluctuations around the scale of the increment $\sim \ell$, while preserving the contribution from scales larger than ℓ .

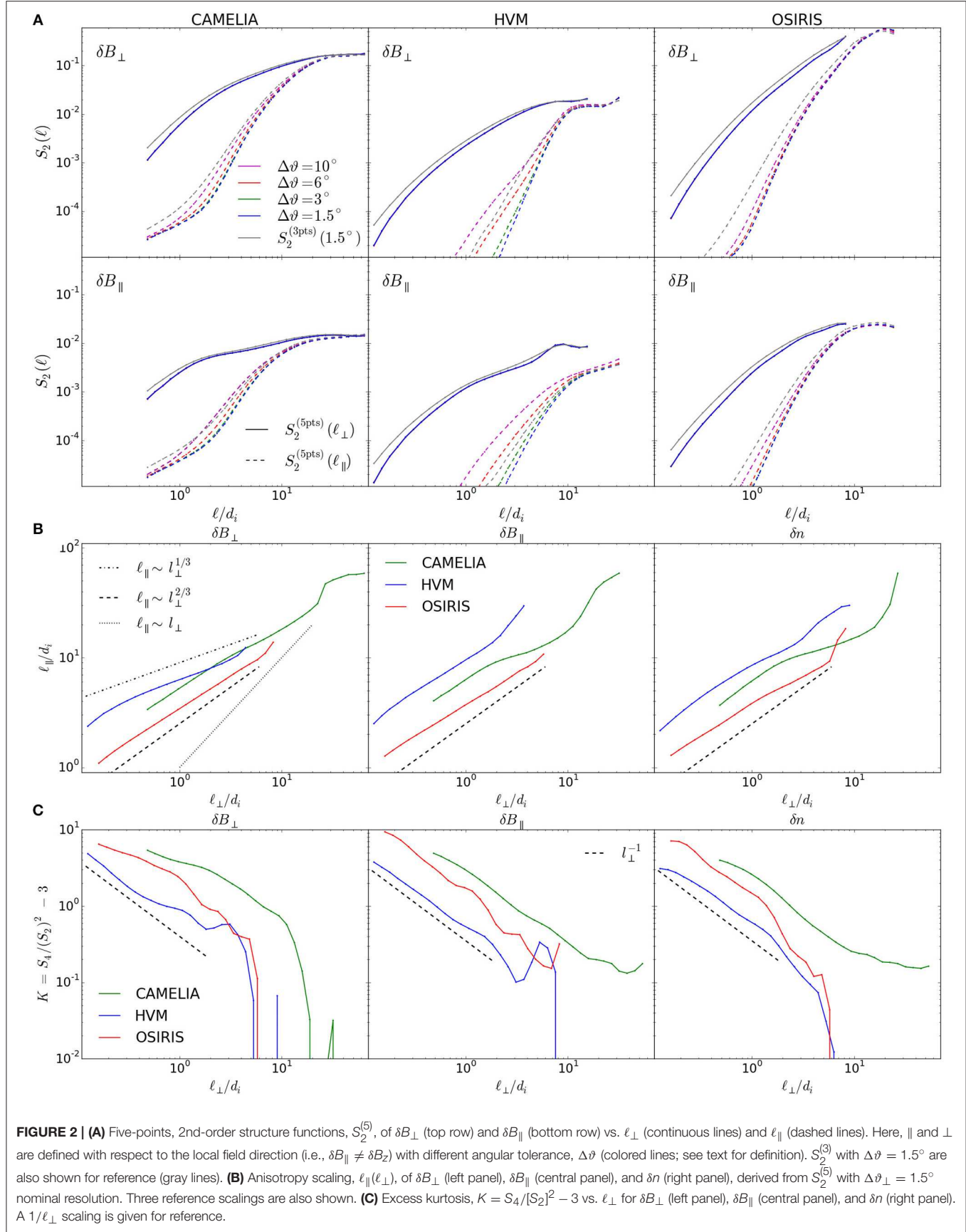
In what follows, we consider field-perpendicular, $S_m(\ell_{\perp}) \equiv S_m^{(5)}(\ell_{\perp}, 90^\circ - \Delta\vartheta \leq \vartheta_{B_{\text{loc}}} \leq 90^\circ)$, and field-parallel, $S_m(\ell_{\parallel}) \equiv S_m^{(5)}(\ell_{\parallel}, \vartheta_{B_{\text{loc}}} \leq \Delta\vartheta)$, five-point structure functions of the magnetic field and density fluctuations, where $\Delta\vartheta$ represents a finite angular tolerance used in practice to determine the *local* perpendicular and parallel directions. We reduce $\Delta\vartheta$ until the scalings appear converged. The field increments, from which we obtain the conditional structure functions, are evaluated at every grid point. In each grid point and at every scale, increments are sampled along random directions. The numbers of these random directions per grid point have been tested to provide a statistically significant (i.e., converged) sample. The sample that is used in the following is such that any structure function $S_m(\ell, \vartheta_{B_{\text{loc}}})$ counts at least 1.5×10^5 points per scale ℓ , in any given band for $\vartheta_{B_{\text{loc}}}$.

4.1. Spectral Anisotropy

A delicate point concerns the sub-ion-range spectral anisotropy, $k_{\parallel} \sim k_{\perp}^{\alpha}$ (cf., e.g., Schekochihin et al., 2009; Boldyrev and Perez, 2012; Cerri et al., 2018; Landi et al., 2019). As is known from MHD, electron-MHD (EMHD), and kinetic-reduced-MHD (KRMHD) turbulence (Cho and Vishniac, 2000; Cho and Lazarian, 2009; Meyrand et al., 2019), the true anisotropy is often revealed only when measured with respect to the *local*, scale-dependent mean magnetic-field direction. Somewhat contradicting estimates, obtained with different methods, for the sub-ion-scale anisotropy have been presented in recent works. Here, we revisit this issue using the above-mentioned implementation of five-point structure functions, consistently applied to all data.

In Figure 2A we show the perpendicular and parallel second-order structure function scalings, and in Figure 2B we show the inferred anisotropy, $\ell_{\parallel}(\ell_{\perp})$. The characteristic parallel length $\ell_{\parallel}(\ell_{\perp})$ at a given perpendicular scale ℓ_{\perp} is obtained by finding the value of ℓ_{\parallel} , at which the amplitudes of $S_2(\ell_{\parallel})$ and $S_2(\ell_{\perp})$ match. To illustrate the sensitivity to the local mean field direction, we show in Figure 2A the convergence with respect to the angular tolerance $\Delta\vartheta$. The parallel scalings appear converged at $\Delta\vartheta \simeq 3^\circ$ for CAMELIA data and at around $\Delta\vartheta \simeq 1.5^\circ$ for HVM, whereas the OSIRIS results are somewhat less sensitive to $\Delta\vartheta$ (converging already for $\Delta\vartheta \simeq 6^\circ$). This difference may occur because OSIRIS simulation exhibits the weakest anisotropy (in absolute values). Physically, $\Delta\vartheta$ should be approximately no larger than $\sim \ell_{\perp}/\ell_{\parallel}$ of the small-scale turbulent eddies. Thus, smaller $\Delta\vartheta$ are needed if a stronger anisotropy develops at the energy-containing scales.

All quantities seem to converge to a scaling close to $\ell_{\parallel} \sim \ell_{\perp}^{2/3}$ (although δB_{\perp} fluctuations in HVM exhibit a scaling closer to 1/3 over the range of scales across $\ell_{\perp} \sim d_i (= \rho_i)$). It is worth noticing, however, that this is not the end of the story, as the scaling is not quite 2/3 and additional effects such as B -field curvature may slightly change the anisotropy. Indeed, the field increments are taken along a straight line. If the local magnetic field lines are significantly curved over the extent of the increment stencil ($= 4\ell$ for five-point increments), the field increments will mix contributions from different field lines, in which case the anisotropy may be somewhat underestimated. It is worth mentioning that a scaling $\ell_{\parallel} \sim \ell_{\perp}^{2/3}$ was proposed in



Boldyrev and Perez (2012), based on a filling-factor correction for the fluctuation energy. Assuming the energy is concentrated in intermittent, two-dimensional structures as in Boldyrev and Perez (2012), the filling factor should scale as $k_{\perp}^{-1} \sim l_{\perp}$. The filling factor may be approximately estimated from the inverse scaling of the excess kurtosis (Matthaeus et al., 2015; see section 4.2). Our results shown in **Figure 2C** are indeed roughly consistent with an excess kurtosis scaling $\sim l_{\perp}^{-1}$, although this approximate scaling is overall better satisfied for δB_{\parallel} and δn than for δB_{\perp} . Finally, we mention that an alternative anisotropy estimate, based on a spectral band-pass filter (Cho and Lazarian, 2009), gives a somewhat stronger anisotropy than the five-point structure functions (not shown). On the other hand, qualitatively similar results are still obtained for all data. Thus, all simulations analyzed exhibit a similar sub-ion-scale anisotropy according to the particular diagnostics employed. Therefore, the differences that were previously reported in the literature could be mainly related to the different methods employed.

4.2. Intermittency: The “Saturation Problem”

Another relevant feature of kinetic plasma turbulence is the excess kurtosis of the fluctuations, $K(\ell_{\perp}) = S_4(\ell)/[S_2(\ell)]^2 - 3$. The increase of $K(\ell_{\perp})$ above zero is a measure of non-Gaussian statistics of the turbulent fluctuations (Frisch, 1995; Matthaeus et al., 2015). As seen in **Figure 2C**, the excess kurtosis gradually increases above the Gaussian value throughout the sub-ion scale range. Moreover, similar statistical trends are seen for δB_{\perp} , δB_{\parallel} , and δn [note that we take here the component of $\delta \mathbf{B}_{\perp}$ parallel to $\ell \times \mathbf{B}_{\text{loc}}$ to estimate the flatness of δB_{\perp} (see also Kiyani et al., 2013)]. In apparent contrast with our results, a number of observational studies of solar wind turbulence find non-Gaussian, yet nearly *scale-independent* turbulence statistics at sub-ion scales (Kiyani et al., 2009, 2013; Wu et al., 2013; Chen et al., 2014). Thus, it appears a process operates in the solar wind that saturates the turbulence statistics already near the transition to sub-ion scales ($\ell_{\perp} \lesssim d_i$). What could be the reason for this apparent contradiction? One clear difference is that the solar-wind fluctuations are already heavily non-Gaussian at MHD scales (Salem et al., 2009), whereas our 3D kinetic simulations do not quite share the same feature due to the limited simulation domain. We mention that even large-size 2D kinetic simulations (e.g., Wan et al., 2012; Franci et al., 2015; Leonardi et al., 2016) did not yet achieve $K(\ell_{\perp}) \gg 1$ in the MHD range ($\ell_{\perp} \gg d_i$). In this context, it may be worth pointing out that intermittency in MHD turbulence is commonly associated with the emergence of sheetlike structures (e.g., Chandran et al., 2015; Matthaeus et al., 2015; Mallet and Schekochihin, 2017), which may break apart via the tearing instability (causing the field lines to reconnect), once their perpendicular aspect ratio exceeds a critical threshold (Matthaeus and Lamkin, 1986; Boldyrev and Loureiro, 2017; Mallet et al., 2017b). For sub-ion-scale turbulence, the possible role of magnetic reconnection has been as well highlighted in a number of recent works (e.g., Franci et al., 2016, 2017; Cerri and Califano, 2017; Loureiro and Boldyrev, 2017; Mallet et al., 2017a; Papini et al., 2019). Moreover, a

recent observational study (Vech et al., 2018) argued that the spectral break at the tail of the MHD cascade may be controlled by reconnection. Therefore, the phenomenology of the cascade may critically depend on the morphology of the intermittent structures at the transition into the kinetic range (Mallet et al., 2017a). If the structures are indeed sufficiently sheetlike to be tearing unstable, collisionless reconnection might be one possible process that limits the growth of the sub-ion scale kurtosis (see also Biskamp et al., 1990; Chen et al., 2014). However, alternative possibilities such as collisionless damping of the fluctuations cannot be ruled out at this stage.

5. CONCLUDING REMARKS

So, what is the nature of sub-ion-scale fluctuations? From our independently performed 3D3V (hybrid and fully) kinetic simulations, a picture consistent with KAW turbulence phenomenology emerges. Moreover, our results imply a scale-dependent anisotropy, together with intermittent statistics of magnetic and density fluctuations at sub-ion scales. Thus, we conclude that within the range of parameters explored here, the statistical properties of ion-scale plasma turbulence (at $\beta \sim 1$) definitely show a certain degree of similarity, regardless of the precise details of the large-scale energy injection. On the other hand, slight differences can also be identified, some of which may be also model-dependent.

A number of key aspects will have to await the next-generation of 3D3V kinetic simulations. Ideally, future numerical experiments should aim to resolve both larger (MHD) scales, as well as a broader range between the ion and the electron scales by adopting significantly higher (if not realistic) mass ratios. These two aspects indeed appear to be both required in order to achieve (i) a possible saturation of the kurtosis at ion scales and (ii) a relevant sub-ion range of scales before electron-scale effects significantly come into play. Moreover, different aspects other than the spectral and statistical properties of the turbulent fluctuations will need to be considered in characterizing kinetic-range turbulence, as for instance, the dissipation mechanisms of turbulent fluctuations under different plasma conditions and the consequent energy partition among different species (e.g., Matthaeus et al., 2016; Parashar et al., 2018; Arzamasskiy et al., 2019; Kawazura et al., 2019; Zhdankin et al., 2019).

While certain progress was definitely achieved in recent years, many other plasma regimes and setups may need to be explored, and the process(es) underlying a possible universality of kinetic-range plasma turbulence (e.g., magnetic reconnection) need to be fully worked out. Moreover, a few relevant discrepancies between numerical simulations, theories and *in-situ* observations appear. These “anomalies” definitely call for an explanation by the space physics community. In this context, advances cannot be achieved without investing in next-generation *multi-spacecraft* missions. Multi-point *in situ* measurements of turbulent fluctuations from a large number of spacecrafts are indeed fundamental in order to disentangle the non-linear spatio-temporal character of plasma turbulence (see, e.g., Klein et al., 2019; Matthaeus et al., 2019;

TenBarge et al., 2019). This includes answering fundamental questions about, for instance, (i) the distribution of turbulent energy in space and time, (ii) the three-dimensional anisotropic structure of energy transfer across scales, (iii) the high-order statistics of the fluctuations, and (iv) the validity of Taylor's hypothesis over a broad range of time and spatial scales. Alongside observations, advances in computational capabilities are required to perform more realistic numerical simulations as discussed above, and compare these with spacecraft measurements. Finally, following the same spirit promoted by the "Turbulent Dissipation Challenge" (Parashar et al., 2015), we would like to end this Perspective by stressing that our community could benefit from comparisons such as the one performed here, involving various codes, models and diagnostics.

Note added: Arzamasskiy et al. (2019) recently reported a scale-independent anisotropy at ion scales (i.e., $\ell_{\parallel} \sim \ell_{\perp}$) based on a set of 3D driven hybrid-kinetic turbulence simulations. Using our structure function diagnostic applied to their data, we were able to qualitatively (and quantitatively) reproduce their result. A more detailed investigation along these lines is currently ongoing, but beyond the scope of this Perspective and will be presented elsewhere.

DATA AVAILABILITY STATEMENT

The data used in this study are available from the authors upon reasonable request.

AUTHOR CONTRIBUTIONS

SC, DG, and LF provided their HVM, OSIRIS, and CAMELIA simulation data, respectively. SC performed the spectral analysis, produced the figures, and wrote the paper, taking into account suggestions from DG and LF. DG implemented and performed the structure function analysis. All authors discussed the results.

REFERENCES

- Adkins, T. and Schekochihin, A. A. (2018). A solvable model of Vlasov-kinetic plasma turbulence in FourierHermite phase space. *J. Plasma Phys.* 84:905840107. doi: 10.1017/S0022377818000089
- Alexandrova, O., Chen, C. H. K., Sorriso-Valvo, L., Horbury, T. S., and Bale, S. D. (2013). Solar wind turbulence and the role of ion instabilities. *Space Sci. Rev.* 178, 101–139. doi: 10.1007/s11214-013-0004-8
- Alexandrova, O., Lacombe, C., Mangeney, A., Grappin, R., and Maksimovic, M. (2012). Solar wind turbulent spectrum at plasma kinetic scales. *Astrophys. J.* 760:121. doi: 10.1088/0004-637X/760/2/121
- Alexandrova, O., Saur, J., Lacombe, C., Mangeney, A., Mitchell, J., Schwartz, S. J., et al. (2009). Universality of solar-wind turbulent spectrum from MHD to electron scales. *Phys. Rev. Lett.* 103:165003. doi: 10.1103/PhysRevLett.103.165003
- Arzamasskiy, L., Kunz, M. W., Chandran, B. D. G., and Quataert, E. (2019). Hybrid-kinetic simulations of ion heating in Alfvénic turbulence. *Astrophys. J.* 879:53. doi: 10.3847/1538-4357/ab20cc
- Bañón Navarro, A., Teaca, B., Told, D., Groeselj, D., Crandall, P., and Jenko, F. (2016). Structure of plasma heating in gyrokinetic Alfvénic turbulence. *Phys. Rev. Lett.* 117:245101. doi: 10.1103/PhysRevLett.117.245101
- Biskamp, D. (2008). *Magnetohydrodynamic Turbulence*. Cambridge: Cambridge University Press.
- Biskamp, D., Welter, H., and Walter, M. (1990). Statistical properties of two-dimensional magnetohydrodynamic turbulence. *Phys. Fluids B* 2:3024.
- Boldyrev, S., Horaitez, K., Xia, Q., and Perez, J. C. (2013). Toward a theory of astrophysical plasma turbulence at subproton scales. *Astrophys. J.* 777:41. doi: 10.1088/0004-637X/777/1/41
- Boldyrev, S., and Loureiro, N. F. (2017). Magnetohydrodynamic turbulence mediated by reconnection. *Astrophys. J.* 844:125. doi: 10.3847/1538-4357/aa7d02
- Boldyrev, S., and Perez, J. C. (2012). Spectrum of kinetic-Alfvén turbulence. *Astrophys. J. Lett.* 758:L44. doi: 10.1088/2041-8205/758/2/L44
- Bruno, R., and Carbone, V. (2013). The solar wind as a turbulence laboratory. *Living Rev. Sol. Phys.* 10:2. doi: 10.12942/lrsp-2013-2
- Cerri, S. S., and Califano, F. (2017). Reconnection and small-scale fields in 2D-3V hybrid-kinetic driven turbulence simulations. *New J. Phys.* 19:025007. doi: 10.1088/1367-2630/aa5c4a
- Cerri, S. S., Califano, F., Jenko, F., Told, D., and Rincon, F. (2016). Subproton-scale cascades in solar wind turbulence: driven hybrid-kinetic simulations. *Astrophys. J. Lett.* 822:L12. doi: 10.3847/2041-8205/822/1/L12
- Cerri, S. S., Franci, L., Califano, F., Landi, S., and Hellinger, P. (2017a). Plasma turbulence at ion scales: a comparison between particle in cell

FUNDING

SC was supported by the National Aeronautics and Space Administration under Grant No. NNX16AK09G issued through the Heliophysics Supporting Research Program. LF was supported by the UK Science and Technology Facilities Council (STFC) grant ST/P000622/1.

ACKNOWLEDGMENTS

SC and DG acknowledge the generous hospitality of the Wolfgang Pauli Institute in Vienna, where the first discussions leading to this work took place. We acknowledge PRACE for awarding us access to Marconi at CINECA, Italy, where the calculations with the HVM code were performed under the grant No. 2017174107. The Cray XC40, Shaheen, at the King Abdullah University of Science and Technology (KAUST) in Thuwal, Saudi Arabia was utilized for the simulation performed with the OSIRIS code. LF acknowledges PRACE for awarding him access to Cartesius at SURFsara, the Netherlands, through the DECI-13 (Distributed European Computing Initiative) call (project HybTurb3D) where the HPIC simulation was performed, and INAF and CINECA for awarding him access to Marconi within the framework of the MoU New Frontiers in Astrophysics: HPC and New Generation Data Exploration (project INA17_C4A26), where new further analysis of the HPIC data has been performed. The authors would like to acknowledge the OSIRIS Consortium, consisting of UCLA and IST (Lisbon, Portugal) for the use of OSIRIS 3.0 and for providing access to the OSIRIS 3.0 framework. SC acknowledges Dr. C. Cavazzoni and Dr. M. Guarasi (CINECA, Italy) for their contributions to HVM code parallelization, performance and implementation on Marconi-KNL. The authors also acknowledge useful discussions with Alfred Mallet, Lev Arzamasskiy, Bill Dorland, Matt Kunz, Simone Landi, Emanuele Papini, Frank Jenko, and David Burgess.

- and Eulerian hybrid-kinetic approaches. *J. Plasma Phys.* 83:705830202. doi: 10.1017/S0022377817000265
- Cerri, S. S., Kunz, M. W., and Califano, F. (2018). Dual phase-space cascades in 3D hybrid-vlasov-maxwell turbulence. *Astrophys. J. Lett.* 856:L13. doi: 10.3847/2041-8213/aab557
- Cerri, S. S., Servidio, S., and Califano, F. (2017b). Kinetic cascade in solar-wind turbulence: 3D3V hybrid-kinetic simulations with electron inertia. *Astrophys. J. Lett.* 846:L18. doi: 10.3847/2041-8213/aa87b0
- Chandran, B. D. G., Schekochihin, A. A., and Mallet, A. (2015). Intermittency and alignment in strong RMHD turbulence. *Astrophys. J.* 807:39. doi: 10.1088/0004-637X/807/1/39
- Chasapis, A., Matthaeus, W. H., Parashar, T. N., Fuselier, S. A., Maruca, B. A., Phan, T. D., et al. (2017). High-resolution statistics of solar wind turbulence at kinetic scales using the magnetospheric multiscale mission. *Astrophys. J. Lett.* 844:L9. doi: 10.3847/2041-8213/aa7ddd
- Chen, C. H. K. (2016). Recent progress in astrophysical plasma turbulence from solar wind observations. *J. Plasma Phys.* 82:535820602. doi: 10.1017/S0022377816001124
- Chen, C. H. K., and Boldyrev, S. (2017). Nature of kinetic scale turbulence in the Earth's magnetosheath. *Astrophys. J.* 842:122. doi: 10.3847/1538-4357/aa74e0
- Chen, C. H. K., Boldyrev, S., Xia, Q., and Perez, J. C. (2013). Nature of subproton scale turbulence in the solar wind. *Phys. Rev. Lett.* 110:225002. doi: 10.1103/PhysRevLett.110.225002
- Chen, C. H. K., Horbury, T. S., Schekochihin, A. A., Wicks, R. T., Alexandrova, O., and Mitchell, J. (2010). Anisotropy of solar wind turbulence between ion and electron scales. *Phys. Rev. Lett.* 104:255002. doi: 10.1103/PhysRevLett.104.255002
- Chen, C. H. K., Klein, K. G., and Howes, G. G. (2019). Evidence for electron Landau damping in space plasma turbulence. *Nat Commun.* 10:740. doi: 10.1038/s41467-019-08435-3
- Chen, C. H. K., Sorriso-Valvo, L., Šafránková, J., and Němeček, Z. (2014). Intermittency of solar wind density fluctuations from ion to electron scales. *Astrophys. J. Lett.* 789:L8. doi: 10.1088/2041-8205/789/1/L8
- Cho, J. (2019). A technique for removing large-scale variations in regularly and irregularly spaced data. *Astrophys. J.* 874:75. doi: 10.3847/1538-4357/ab06f3
- Cho, J., and Lazarian, A. (2004). The anisotropy of electron magnetohydrodynamic turbulence. *Astrophys. J. Lett.* 615, L41–L44. doi: 10.1086/425215
- Cho, J., and Lazarian, A. (2009). Simulations of electron magnetohydrodynamic turbulence. *Astrophys. J.* 701, 236–252. doi: 10.1088/0004-637X/701/1/236
- Cho, J., and Vishniac, E. T. (2000). The anisotropy of magnetohydrodynamic Alfvénic turbulence. *Astrophys. J.* 539, 273–282. doi: 10.1086/309213
- Comişel, H., Naruyuki, Y., Narita, Y., and Motschmann, U. (2016). On the role of ion-scale whistler waves in space and astrophysical plasma turbulence. *Ann. Geophys.* 34, 975–984. doi: 10.5194/angeo-34-975-2016
- Del Sarto, D., Pegoraro, F., and Tenerani, A. (2017). ‘Magneto-elastic’ waves in an anisotropic magnetised plasma. *Plasma Phys. Control. Fusion* 59:045002. doi: 10.1088/1361-6587/aa56bd
- Eyink, G. L. (2018). Cascades and dissipative anomalies in nearly collisionless plasma turbulence. *Phys. Rev. X* 8:041020. doi: 10.1103/PhysRevX.8.041020
- Falcon, E., Fauve, S., and Laroche, C. (2007). Observation of intermittency in wave turbulence. *Phys. Rev. Lett.* 98:154501. doi: 10.1103/PhysRevLett.98.154501
- Fonseca, R. A., Silva, L. O., Tsung, F. S., Decyk, V. K., Lu, W., Ren, C., et al. (2002). OSIRIS: a three-dimensional, fully relativistic particle in cell Code for modeling plasma based accelerators. *Lecture Notes Comput. Sci.* 2331:342–351. doi: 10.1007/3-540-47789-636
- Fonseca, R. A., Vieira, J., Fiura, F., Davidson, A., Tsung, F. S., Mori, W. B., et al. (2013). Exploiting multi-scale parallelism for large scale numerical modelling of laser wakefield accelerators. *Plasma Phys. Control. Fusion* 55:124011. doi: 10.1088/0741-3335/55/12/124011
- Franci, L., Cerri, S. S., Califano, F., Landi, S., Papini, E., Verdini, A., et al. (2017). Magnetic reconnection as a driver for a sub-ion-scale cascade in plasma turbulence. *Astrophys. J. Lett.* 850:L16. doi: 10.3847/2041-8213/aa93fb
- Franci, L., Hellinger, P., Guarasi, M., Chen, C. H. K., Papini, E., Verdini, A., et al. (2018a). Three-dimensional simulations of solar wind turbulence with the hybrid code camelia. *J. Phys. Conf. Ser.* 1031:012002. doi: 10.1088/1742-6596/1031/1/012002
- Franci, L., Landi, S., Matteini, L., Verdini, A., and Hellinger, P. (2015). High-resolution hybrid simulations of kinetic plasma turbulence at proton scales. *Astrophys. J.* 812:21. doi: 10.1088/0004-637X/812/1/21
- Franci, L., Landi, S., Matteini, L., Verdini, A., and Hellinger, P. (2016). Plasma beta dependence of the ion-scale spectral break of solar Wind turbulence: high-resolution 2D hybrid simulations. *Astrophys. J.* 833:91. doi: 10.3847/1538-4357/833/1/9
- Franci, L., Landi, S., Verdini, A., Matteini, L., and Hellinger, P. (2018b). Solar wind turbulent cascade from MHD to sub-ion scales: large-size 3D hybrid particle-in-cell simulations. *Astrophys. J.* 853:26. doi: 10.3847/1538-4357/aaa3e8
- Frisch, U. (1995). *Turbulence. The Legacy of A. N. Kolmogorov.* Cambridge: Cambridge University Press.
- Galtier, S., and Bhattacharjee, A. (2003). Anisotropic weak whistler wave turbulence in electron magnetohydrodynamics. *Phys. Plasmas* 10, 3065–3076. doi: 10.1063/1.1584433
- Gary, S. P., Chang, O., and Wang, J. (2012). Forward cascade of whistler turbulence: three-dimensional particle-in-cell simulations. *Astrophys. J.* 755:142. doi: 10.1088/0004-637X/755/2/142
- Gary, S. P., and Nishimura, K. (2004). Kinetic Alfvén waves: linear theory and a particle-in-cell simulation. *J. Geophys. Res.* 109:A02109. doi: 10.1029/2003JA010239
- Gary, S. P., and Smith, C. W. (2009). Short-wavelength turbulence in the solar wind: linear theory of whistler and kinetic Alfvén fluctuations. *J. Geophys. Res.* 114:A12105. doi: 10.1029/2009JA014525
- Greco, A., Perri, S., Servidio, S., Yordanova, E., and Veltri, P. (2016). The complex structure of magnetic field discontinuities in the turbulent solar wind. *Astrophys. J.* 823:L39. doi: 10.3847/2041-8205/823/2/L39
- Grošelj, D., Cerri, S. S., Bañón Navarro, A., Willmott, C., Told, D., Loureiro, N. F., et al. (2017). Fully kinetic versus reduced-kinetic modeling of collisionless plasma turbulence. *Astrophys. J.* 847:28. doi: 10.3847/1538-4357/aa894d
- Grošelj, D., Chen, C. H. K., Mallet, A., Samtaney, R., Schneider, K., and Jenko, F. (2019). Kinetic turbulence in astrophysical plasmas: waves and/or structures? *Phys. Rev. X* 9:031037. doi: 10.1103/PhysRevX.9.031037
- Grošelj, D., Mallet, A., Loureiro, N. F., and Jenko, F. (2018). Fully kinetic simulation of 3D kinetic Alfvén Turbulence. *Phys. Rev. Lett.* 120:105101. doi: 10.1103/PhysRevLett.120.105101
- He, J., Tu, C., Marsch, E., and Yao, S. (2012). Do oblique Alfvén/Ion-cyclotron or fast-mode/whistler waves dominate the dissipation of solar wind turbulence near the proton inertial length? *Astrophys. J. Lett.* 745:L8. doi: 10.1088/2041-8205/745/1/L8
- Hollweg, J. V. (1999). Kinetic Alfvén wave revisited. *J. Geophys. Res.* 104, 14811–14820.
- Howes, G. G., Cowley, S. C., Dorland, W., Hammett, G. W., Quataert, E., and Schekochihin, A. A. (2008a). A model of turbulence in magnetized plasmas: implications for the dissipation range in the solar wind. *J. Geophys. Res.* 113:A05103. doi: 10.1029/2007JA012665
- Howes, G. G., Dorland, W., Cowley, S. C., Hammett, G. W., Quataert, E., Schekochihin, A. A., et al. (2008b). Kinetic simulations of magnetized turbulence in astrophysical plasmas. *Phys. Rev. Lett.* 100:065004. doi: 10.1103/PhysRevLett.100.065004
- Howes, G. G., Tenbarge, J. M., and Dorland, W. (2011). A weakened cascade model for turbulence in astrophysical plasmas. *Phys. Plasmas* 18, 102305–102305. doi: 10.1063/1.3646400
- Huang, S. Y., Hadid, L. Z., Sahraoui, F., Yuan, Z. G., and Deng, X. H. (2017). On the existence of the kolmogorov inertial range in the terrestrial magnetosheath turbulence. *Astrophys. J. Lett.* 836:L10. doi: 10.3847/2041-8213/836/1/L10
- Hughes, R. S., Gary, S. P., and Wang, J. (2017a). Particle-in-cell simulations of electron and ion dissipation by whistler turbulence: variations with electron β . *Astrophys. J.* 835:L15. doi: 10.3847/2041-8213/835/1/L15
- Hughes, R. S., Gary, S. P., Wang, J., and Parashar, T. N. (2017b). Kinetic Alfvén turbulence: electron and ion heating by particle-in-cell simulations. *Astrophys. J. Lett.* 847:L14. doi: 10.3847/2041-8213/aa8b13
- Kawazura, Y., Barnes, M., and Schekochihin, A. A. (2019). Thermal disequilibrium of ions and electrons by collisionless plasma turbulence. *Proc. Natl. Acad. Sci. U.S.A.* 116, 771–776. doi: 10.1073/pnas.1812491116
- Kiyani, K. H., Chapman, S. C., Khotyaintsev, Y. V., Dunlop, M. W., and Sahraoui, F. (2009). Global scale-invariant dissipation in collisionless plasma turbulence. *Phys. Rev. Lett.* 103:075006. doi: 10.1103/PhysRevLett.103.075006

- Kiyani, K. H., Chapman, S. C., Sahraoui, F., Hnat, B., Fauvarque, O., and Khotyaintsev, Y. V. (2013). Enhanced magnetic compressibility and isotropic scale invariance at sub-ion larmor scales in solar wind turbulence. *Astrophys. J.* 763:10. doi: 10.1088/0004-637X/763/1/10
- Klein, K. G., Alexandrova, O., Bookbinder, J., Caprioli, D., Case, A. W., Chandran, B. D. G., et al. (2019). [Plasma 2020 Decadal] multipoint measurements of the solar wind: a proposed advance for studying magnetized turbulence. *arXiv [Pre-print]. arXiv:1903.05740*.
- Kobayashi, S., Sahraoui, F., Passot, T., Laveder, D., Sulem, P. L., Huang, S. Y., et al. (2017). Three-dimensional simulations and spacecraft observations of sub-ion scale turbulence in the solar wind: influence of landau damping. *Astrophys. J.* 839:122. doi: 10.3847/1538-4357/aa67f2
- Kunz, M. W., Abel, I. G., Klein, K. G., and Schekochihin, A. A. (2018). Astrophysical gyrokinetics: turbulence in pressure-anisotropic plasmas at ion scales and beyond. *J. Plasma Phys.* 84:715840201. doi: 10.1017/S0022377818000296
- Lacombe, C., Alexandrova, O., and Matteini, L. (2017). Anisotropies of the magnetic field fluctuations at kinetic scales in the solar wind: cluster observations. *Astrophys. J.* 848:45. doi: 10.3847/1538-4357/aa8c06
- Landi, S., Franci, L., Papini, E., Verdini, A., Matteini, L., and Hellinger, P. (2019). Spectral anisotropies and intermittency of plasma turbulence at ion kinetic scales. *arXiv [Pre-print]. arXiv:1904.03903*.
- Leamon, R. J., Smith, C. W., Ness, N. F., Matthaeus, W. H., and Wong, H. K. (1998). Observational constraints on the dynamics of the interplanetary magnetic field dissipation range. *J. Geophys. Res.* 103, 4775–4788. doi: 10.1029/97JA03394
- Leonardis, E., Sorriso-Valvo, L., Valentini, F., Servidio, S., Carbone, F., and Veltri, P. (2016). Multifractal scaling and intermittency in hybrid Vlasov-Maxwell simulations of plasma turbulence. *Phys. Plasmas* 23:022307. doi: 10.1063/1.4942417
- Loureiro, N. L., and Boldyrev, S. (2017). Collisionless reconnection in magnetohydrodynamic and kinetic turbulence. *Astrophys. J.* 850:182.
- Mallet, A., and Schekochihin, A. A. (2017). A statistical model of three-dimensional anisotropy and intermittency in strong alfvénic turbulence. *Mon. Not. R. Astron. Soc.* 466:3918. doi: 10.1093/mnras/stw3251
- Mallet, A., Schekochihin, A. A., and Chandran, B. D. G. (2017a). Disruption of Alfvénic turbulence by magnetic reconnection in a collisionless plasma. *J. Plasma Phys.* 83:905830609. doi: 10.1017/S0022377817000812
- Mallet, A., Schekochihin, A. A., and Chandran, B. D. G. (2017b). Disruption of sheet-like structures in Alfvénic turbulence by magnetic reconnection. *Mon. Not. R. Astron. Soc.* 468, 4862–4871. doi: 10.1093/mnras/stx670
- Mallet, A., Schekochihin, A. A., Chandran, B. D. G., Chen, C. H. K., Horbury, T. S., Wicks, R. T., et al. (2016). Measures of three-dimensional anisotropy and intermittency in strong alfvénic turbulence. *Mon. Not. R. Astron. Soc.* 459:2130. doi: 10.1093/mnras/stw802
- Matthaeus, W. H., Bandyopadhyay, R., Brown, M. R., Borovsky, J., Carbone, V., Caprioli, D., et al. (2019). [Plasma 2020 Decadal] the essential role of multi-point measurements in turbulence investigations: the solar wind beyond single scale and beyond the Taylor Hypothesis. *arXiv [Pre-print]. arXiv:1903.06890*.
- Matthaeus, W. H., and Lamkin, S. L. (1986). Turbulent magnetic reconnection. *Phys. Fluids* 29, 2513–2534.
- Matthaeus, W. H., Oughton, S., Osman, K. T., Servidio, S., Wan, M., Gary, S. P., et al. (2014). Nonlinear and linear timescales near kinetic scales in solar wind turbulence. *Astrophys. J.* 790:155. doi: 10.1088/0004-637X/790/2/155
- Matthaeus, W. H., Parashar, T. N., Wan, M., and Wu, P. (2016). Turbulence and proton-electron heating in kinetic plasma. *Astrophys. J. Lett.* 827:L7. doi: 10.3847/2041-8205/827/1/L7
- Matthaeus, W. H., Wan, M., Servidio, S., Greco, A., Osman, K. T., Oughton, S., et al. (2015). Intermittency, nonlinear dynamics and dissipation in the solar wind and astrophysical plasmas. *Philos. Trans. Roy. Soc. Lond. Ser. A* 373:20140154. doi: 10.1098/rsta.2014.0154
- Meyrand, R., Kanekar, A., Dorland, W., and Schekochihin, A. A. (2019). Fluidization of collisionless plasma turbulence. *Proc. Natl. Acad. Sci. U.S.A.* 116, 1185–1194. doi: 10.1073/pnas.1813913116
- Narita, Y., Nakamura, R., Baumjohann, W., Glassmeier, K.-H., Motschmann, U., Giles, B., et al. (2016). On electron-scale whistler turbulence in the solar wind. *Astrophys. J. Lett.* 827:L8. doi: 10.3847/2041-8205/827/1/L8
- Omidi, N., Isenberg, P., Russell, C. T., Jian, L. K., and Wei, H. Y. (2014). Generation of ion cyclotron waves in the corona and solar wind. *J. Geophys. Res.* 119, 1442–1454. doi: 10.1002/2013JA019474
- Papini, E., Franci, L., Landi, S., Verdini, A., Matteini, L., and Hellinger, P. (2019). Can hall magnetohydrodynamics explain plasma turbulence at sub-ion scales? *Astrophys. J.* 870:52. doi: 10.3847/1538-4357/aaf003
- Parashar, T. N., Matthaeus, W. H., and Shay, M. A. (2018). Dependence of kinetic plasma turbulence on plasma β . *Astrophys. J. Lett.* 864:L21. doi: 10.3847/2041-8213/aadb8b
- Parashar, T. N., Salem, C., Wicks, R. T., Karimabadi, H., Gary, S. P., and Matthaeus, W. H. (2015). Turbulent dissipation challenge: a community-driven effort. *J. Plasma Phys.* 81:905810513. doi: 10.1017/S0022377815000860
- Passot, T., and Sulem, P. L. (2015). A model for the non-universal power law of the solar wind sub-ion-scale magnetic spectrum. *Astrophys. J. Lett.* 812:L37. doi: 10.1088/2041-8205/812/2/L37
- Passot, T., and Sulem, P. L. (2019). Imbalanced kinetic Alfvén wave turbulence: from weak turbulence theory to nonlinear diffusion models for the strong regime. *arXiv [Pre-print]. arXiv:1902.04295*.
- Passot, T., Sulem, P. L., and Tassi, E. (2018). Gyrofluid modeling and phenomenology of low- β_e Alfvén wave turbulence. *Phys. Plasmas* 25:042107. doi: 10.1063/1.5022528
- Pezzi, O., Servidio, S., Perrone, D., Valentini, F., Sorriso-Valvo, L., Greco, A., et al. (2018). Velocity-space cascade in magnetized plasmas: numerical simulations. *Phys. Plasmas*. 25:060704. doi: 10.1063/1.5027685
- Podesta, J. J. (2012). The need to consider ion Bernstein waves as a dissipation channel of solar wind turbulence. *J. Geophys. Res.* 117:A07101. doi: 10.1029/2012JA017770
- Podesta, J. J., and TenBarge, J. M. (2012). Scale dependence of the variance anisotropy near the proton gyroradius scale: additional evidence for kinetic Alfvén waves in the solar wind at 1 AU. *J. Geophys. Res.* 117:A10106. doi: 10.1029/2012JA017724
- Pucci, F., Vásconez, C. L., Pezzi, O., Servidio, S., Valentini, F., Matthaeus, W. H., et al. (2016). From Alfvén waves to kinetic Alfvén waves in an inhomogeneous equilibrium structure. *J. Geophys. Res.* 121, 1024–1045. doi: 10.1002/2015JA022216
- Roberts, O. W., Narita, Y., and Escoubet, C. P. (2017). Direct measurement of anisotropic and asymmetric wave vector spectrum in ion-scale solar wind turbulence. *Astrophys. J.* 851:L11. doi: 10.3847/2041-8213/aa9bf3
- Roytershteyn, V., Boldyrev, S., Delzanno, G. L., Chen, C. H. K., Grošelj, D., and Loureiro, N. F. (2019). Numerical study of inertial kinetic-alfvén turbulence. *Astrophys. J.* 870:103. doi: 10.3847/1538-4357/aaf288
- Sahraoui, F., Belmont, G., and Goldstein, M. L. (2012). New insight into short-wavelength solar wind fluctuations from vlasov theory. *Astrophys. J.* 748:100. doi: 10.1088/0004-637X/748/2/100
- Sahraoui, F., Goldstein, M. L., Belmont, G., Canu, P., and Rezeau, L. (2010). Three dimensional anisotropic k spectra of turbulence at subproton scales in the solar wind. *Phys. Rev. Lett.* 105:131101. doi: 10.1103/PhysRevLett.105.131101
- Sahraoui, F., Goldstein, M. L., Robert, P., and Khotyaintsev, Y. V. (2009). Evidence of a cascade and dissipation of solar-wind turbulence at the electron gyroscale. *Phys. Rev. Lett.* 102:231102. doi: 10.1103/PhysRevLett.102.231102
- Salem, C., Mangeney, A., Bale, S. D., and Veltri, P. (2009). Solar wind magnetohydrodynamics turbulence: anomalous scaling and role of intermittency. *Astrophys. J.* 702:537. doi: 10.1088/0004-637X/702/1/537
- Salem, C. S., Howes, G. G., Sundkvist, D., Bale, S. D., Chaston, C. C., Chen, C. H. K., et al. (2012). Identification of kinetic Alfvén wave turbulence in the solar wind. *Astrophys. J. Lett.* 745:L9. doi: 10.1088/2041-8205/745/1/L9
- Schekochihin, A. A., Cowley, S. C., Dorland, W., Hammert, G. W., Howes, G. G., Plunk, G. G., et al. (2008). Gyrokinetic turbulence: a nonlinear route to dissipation through phase space. *Plasma Phys. Control. Fusion* 50:124024. doi: 10.1088/0741-3335/50/12/124024
- Schekochihin, A. A., Cowley, S. C., Dorland, W., Hammert, G. W., Howes, G. G., Quataert, E., et al. (2009). Astrophysical gyrokinetics: kinetic and fluid turbulent cascades in magnetized weakly collisional plasmas. *Astrophys. J.* 182, 310–377. doi: 10.1088/0067-0049/182/1/310
- Schneider, K., Farge, M., and Kevlahan, N. (2004). “Spatial intermittency in two-dimensional turbulence: a wavelet approach,” in *Woods Hole Mathematics, Perspectives in Mathematics and Physics*, Vol 34, eds N.

- Tongring and R. C. Penner (Singapore: World Scientific), 302–328. doi: 10.1142/97898127013980007
- Servidio, S., Chasapis, A., Matthaeus, W. H., Perrone, D., Valentini, F., Parashar, T. N., et al. (2017). Magnetospheric multiscale observation of plasma velocity-space cascade: hermite representation and theory. *Phys. Rev. Lett.* 119:205101. doi: 10.1103/PhysRevLett.119.205101
- Servidio, S., Valentini, F., Perrone, D., Greco, A., Califano, F., Matthaeus, W. H., et al. (2015). A kinetic model of plasma turbulence. *J. Plasma Phys.* 81:325810107. doi: 10.1017/S0022377814000841
- Sorriso-Valvo, L., Carbone, F., Perri, S., Greco, A., Marino, R., and Bruno, R. (2018). On the statistical properties of turbulent energy transfer rate in the inner heliosphere. *Sol. Phys.* 293:10. doi: 10.1007/s11207-017-1229-6
- Stawicki, O., Gary, S. P., and Li, H. (2001). Solar wind magnetic fluctuation spectra: dispersion versus damping. *J. Geophys. Res.* 106, 8273–8282. doi: 10.1029/2000JA000446
- TenBarge, J. M., Alexandrova, O., Boldyrev, S., Califano, F., Cerri, S. S., Chen, C. H. K., et al. (2019). [Plasma 2020 Decadal] Disentangling the spatiotemporal structure of turbulence using multi-spacecraft data. *arXiv [Preprint]*. arXiv:1903.05710.
- TenBarge, J. M., and Howes, G. G. (2013). Current sheets and collisionless damping in kinetic plasma turbulence. *Astrophys. J. Lett.* 771:L27. doi: 10.1088/2041-8205/771/2/L27
- TenBarge, J. M., Podesta, J. J., Klein, K. G., and Howes, G. G. (2012). Interpreting magnetic variance anisotropy measurements in the solar wind. *Astrophys. J.* 753:107. doi: 10.1088/0004-637X/753/2/107
- Told, D., Cookmeyer, J., Müller, F., Astfalk, P., and Jenko, F. (2016). Comparative study of gyrokinetic, hybrid-kinetic and fully kinetic wave physics for space plasmas. *New J. Phys.* 18:065011. doi: 10.1088/1367-2630/18/6/065011
- Told, D., Jenko, F., TenBarge, J. M., Howes, G. G., and Hammett, G. W. (2015). Multiscale nature of the dissipation range in gyrokinetic simulations of alfvénic turbulence. *Phys. Rev. Lett.* 115:025003. doi: 10.1103/PhysRevLett.115.025003
- Valentini, F., Trávníček, P., Califano, F., Hellinger, P., and Mangeney, A. (2007). A hybrid-Vlasov model based on the current advance method for the simulation of collisionless magnetized plasma. *JCoPh* 225, 753–770. doi: 10.1016/j.jcp.2007.01.001
- Valentini, F., Vásconez, C. L., Pezzi, O., Servidio, S., Malara, F., and Pucci, F. (2017). Transition to kinetic turbulence at proton scales driven by large-amplitude kinetic Alfvén fluctuations. *Astron. Astrophys.* 599:A8. doi: 10.1051/0004-6361/201629240
- Vásconez, C. L., Pucci, F., Valentini, F., Servidio, S., Matthaeus, W. H., and Malara, F. (2015). Kinetic alfvén wave generation by large-scale phase mixing. *Astrophys. J.* 815:7. doi: 10.1088/0004-637X/815/1/7
- Vásconez, C. L., Valentini, F., Camporeale, E., and Veltri, P. (2014). Vlasov simulations of kinetic Alfvén waves at proton kinetic scales. *Phys. Plasmas* 21:112107. doi: 10.1063/1.4901583
- Vasquez, B. J., Markovskii, S. A., and Chandran, B. D. G. (2014). Three-dimensional hybrid simulation study of anisotropic turbulence in the proton kinetic regime. *Astrophys. J.* 788:178. doi: 10.1088/0004-637X/788/2/178
- Vech, D., Mallet, A., Klein, K. G., and Kasper, J. C. (2018). Magnetic reconnection may control the ion-scale spectral break of solar wind turbulence. *Astrophys. J. Lett.* 855:L27. doi: 10.3847/2041-8213/aab351
- Verscharen, D., Klein, K. G., and Maruca, B. A. (2019). The multi-scale nature of the solar wind. *arXiv [Pre-print]*. arXiv:1902.03448.
- Wan, M., Matthaeus, W. H., Karimabadi, H., Roytershteyn, V., Shay, M., Wu, P., et al. (2012). Intermittent dissipation at kinetic scales in collisionless plasma turbulence. *Phys. Rev. Lett.* 109:195001. doi: 10.1103/PhysRevLett.109.195001
- Wan, M., Matthaeus, W. H., Roytershteyn, V., Karimabadi, H., Parashar, T., Wu, P., et al. (2015). Intermittent dissipation and heating in 3D kinetic plasma turbulence. *Phys. Rev. Lett.* 114:175002. doi: 10.1103/PhysRevLett.114.175002
- Wan, M., Matthaeus, W. H., Roytershteyn, V., Parashar, T. N., Wu, P., and Karimabadi, H. (2016). Intermittency, coherent structures and dissipation in plasma turbulence. *Phys. Plasmas* 23:042307. doi: 10.1063/1.4945631
- Wu, P., Perri, S., Osman, K., Wan, M., Matthaeus, W. H., Shay, M. A., et al. (2013). Intermittent heating in solar wind and kinetic simulations. *Astrophys. J. Lett.* 763:L30. doi: 10.1088/2041-8205/763/2/L30
- Zhao, G. Q., Feng, H. Q., Wu, D. J., Liu, Q., Zhao, Y., Zhao, A., et al. (2018). Statistical study of low-frequency electromagnetic cyclotron waves in the solar wind at 1 AU. *J. Geophys. Res.* 123, 1715–1730. doi: 10.1002/2017JA024979
- Zhao, J. S., Voitenko, Y. M., Wu, D. J., and Yu, M. Y. (2016). Kinetic Alfvén turbulence below and above ion cyclotron frequency. *J. Geophys. Res.* 121, 5–18. doi: 10.1002/2015JA021959
- Zhdankin, V., Uzdensky, D. A., Werner, G. R., and Begelman, M. C. (2019). Electron and ion energization in relativistic plasma turbulence. *Phys. Rev. Lett.* 122:055101. doi: 10.1103/PhysRevLett.122.055101

Conflict of Interest: The authors declare that the research was conducted in the absence of any commercial or financial relationships that could be construed as a potential conflict of interest.

Copyright © 2019 Cerri, Grošelj and Franci. This is an open-access article distributed under the terms of the Creative Commons Attribution License (CC BY). The use, distribution or reproduction in other forums is permitted, provided the original author(s) and the copyright owner(s) are credited and that the original publication in this journal is cited, in accordance with accepted academic practice. No use, distribution or reproduction is permitted which does not comply with these terms.



Collisionless Magnetic Reconnection and Waves: Progress Review

Yuri V. Khotyaintsev^{1*}, Daniel B. Graham¹, Cecilia Norgren² and Andris Vaivads³

¹ Swedish Institute of Space Physics, Uppsala, Sweden, ² Department of Physics and Technology, University of Bergen, Bergen, Norway, ³ Department of Space and Plasma Physics, KTH Royal Institute of Technology, Stockholm, Sweden

OPEN ACCESS

Edited by:

Benoit Lavraud,
UMR5277 Institut de Recherche en
Astrophysique et Planétologie (IRAP),
France

Reviewed by:

Lei Dai,
National Space Science Center (CAS),
China
Huishan Fu,
Beihang University, China

*Correspondence:

Yuri V. Khotyaintsev
yuri@irfu.se

Specialty section:

This article was submitted to
Space Physics,
a section of the journal
*Frontiers in Astronomy and Space
Sciences*

Received: 03 September 2019

Accepted: 23 October 2019

Published: 15 November 2019

Citation:

Khotyaintsev YV, Graham DB,
Norgren C and Vaivads A (2019)
Collisionless Magnetic Reconnection
and Waves: Progress Review.
Front. Astron. Space Sci. 6:70.
doi: 10.3389/fspas.2019.00070

Magnetic reconnection is a fundamental process whereby microscopic plasma processes cause macroscopic changes in magnetic field topology, leading to explosive energy release. Waves and turbulence generated during the reconnection process can produce particle diffusion and anomalous resistivity, as well as heat the plasma and accelerate plasma particles, all of which can impact the reconnection process. We review progress on waves related to reconnection achieved using high resolution multi-point *in situ* observations over the last decade, since early Cluster and THEMIS observations and ending with recent Magnetospheric Multiscale results. In particular, we focus on the waves most frequently observed in relation to reconnection, ranging from low-frequency kinetic Alfvén waves (KAW), to intermediate frequency lower hybrid and whistler-mode waves, electrostatic broadband and solitary waves, as well as the high-frequency upper hybrid, Langmuir, and electron Bernstein waves. Significant progress has been made in understanding localization of the different wave modes in the context of the reconnection picture, better quantification of generation mechanisms and wave-particle interactions, including anomalous resistivity. Examples include: temperature anisotropy driven whistlers in the flux pileup region, anomalous effects due to lower-hybrid waves, upper hybrid wave generation within the electron diffusion region, wave-particle interaction of electrostatic solitary waves. While being clearly identified in observations, some of the wave processes remain challenging for reconnection simulations (electron Bernstein, upper hybrid, Langmuir, whistler), as the instabilities (streaming, loss-cone, shell) which drive these waves require high resolution of distribution functions in phase space, and realistic ratio of Debye to electron inertia scales. We discuss how reconnection configuration, i.e., symmetric vs. asymmetric, guide-field vs. antiparallel, affect wave occurrence, generation, effect on particles, and feedback on the overall reconnection process. Finally, we outline some of the major open questions, such as generation of electromagnetic radiation by reconnection sites and role of waves in triggering/onset of reconnection.

Keywords: magnetic reconnection, turbulence, waves, instabilities, kinetic plasma processes

1. INTRODUCTION

Magnetic reconnection releases energy stored in the magnetic field via reconfiguration of the field topology (Biskamp, 2000). Such reconfiguration requires breaking of the ideal plasma frozen-in behavior. Magnetic reconnection is a fundamental plasma process, which operates in various plasma environments, such as the solar corona and chromosphere, planetary magnetospheres, solar

wind, astrophysical plasmas, and well as in laboratory devices such as tokamaks (Yamada et al., 2010).

Waves and turbulence can be generated by the reconnection and provide feedback on the reconnection process, or preexisting waves and turbulence can affect the onset of reconnection. At the largest scales and lowest frequencies this corresponds to MHD turbulence (Lazarian et al., 2015). In collisionless plasmas kinetic processes become important, as they can lead to generation of waves over a wide range of scales and frequencies, in ion, hybrid, and electron ranges. Such waves and turbulence are present in all parts of the reconnection region, such as outflows (Osman et al., 2015), separatrix regions (Viberg et al., 2013), ion and electron diffusion region (Fu et al., 2017; Graham et al., 2017a). Reconnection leads to the generation of sharp gradients in both real and phase space. Waves and kinetic instabilities generally tend to relax such gradients leading to thermalization of the particle distribution, pitch-angle scattering, heating, and diffusion. Waves-particle interactions were also suggested as one of the ways to introduce dissipation into a collisionless system, via anomalous resistivity (Drake, 2003).

Kinetic wave processes in relation to reconnection can be studied in laboratory experiments (Ji et al., 2004; Fox et al., 2012). But only *in situ* space observations can provide the detailed information on both the electromagnetic fields and the particle distribution functions, so that both the generation and effect on particles can be studied. Recent Cluster (Escoubet et al., 2001), THEMIS (Angelopoulos, 2008) and Magnetospheric Multiscale (MMS) (Burch et al., 2016) missions provided unique data from near-Earth space. This allowed us to study plasma kinetic processes in a much more quantitative way than before. Here we review recent advances in the understanding the kinetic processes coupling collisionless magnetic reconnection and waves. We focus on the observational results over the last decade, since early Cluster observations (Vaivads et al., 2006; Fujimoto et al., 2011) and ending with recent MMS results.

2. WAVE TYPES

Below we review the different waves types starting from the wave near the electron plasma frequency, f_{pe} , followed by lower frequency waves.

2.1. Upper Hybrid, Langmuir, Electron Bernstein Waves

In this section we discuss the waves near the electron plasma frequency f_{pe} , namely, Langmuir, upper hybrid (UH) and electron Bernstein, or equivalently electron cyclotron (EC), waves. The waves are generated by deformations in the electron distribution function, such as electron beams, ring, shell, or loss-cone distributions. These waves can grow at fast rates due to their high frequencies compared the other temporal scales associated with magnetic reconnection, and can thus act very quickly on electrons to dissipate unstable electron distributions or accelerate electrons, compared with timescales over which reconnection evolves. Moreover, these waves have typically relatively low group velocities compared with the electron thermal speed,

and thus they are likely to be observed in or close to the source regions. This makes these wave perfect markers of the electron distribution function deformations, in particular of the fine electron boundaries resulting from ongoing magnetic reconnection. Such boundaries can be difficult to identify directly in particle data, due to insufficient temporal resolution of particle measurements compared to the fast time scales of wave growth. For example, these waves can be used to identify electron boundaries in the separatrix regions related to electron beams (Vaivads et al., 2004; Retinó et al., 2006) and loss-cone-like distributions created by the partial loss of hot magnetospheric electrons on reconnected field lines (Khotyaintsev et al., 2006; Graham et al., 2016c).

Spacecraft observations and numerical simulations have shown that fast electron beams are generated in the separatrix regions and that they are often unstable. For fast weak beams waves near the plasma frequency are favored, e.g., Langmuir, beam-mode, or UH waves. Both UH and Langmuir waves have been reported in magnetotail reconnection from Wind and Cluster observations. For example, Farrell et al. (2002) and Farrell et al. (2003) found UH generated in the separatrix region of magnetotail reconnection. Langmuir waves were also reported in the separatrix regions by Deng et al. (2004). Electron Bernstein waves have been reported at DFs by THEMIS (Zhou et al., 2009b). At Earth's magnetopause the plasma frequency line was found to be enhanced in the separatrices Vaivads et al. (2004), Retinó et al. (2006). Using a case study from MMS, Zhou et al. (2016) found Langmuir-like waves in the magnetospheric separatrix and electron Bernstein (EC) and beam-mode like waves in the magnetosheath separatrices. Beam-mode like waves have also been reported in the magnetospheric separatrices (Burch et al., 2018).

Multi-point observations by Cluster allowed detailed mapping of the HF waves in the reconnection diffusion region in the magnetotail. These observations showed that Langmuir-like waves were found in the outer separatrices, where fast electron beams were simultaneously observed (Viberg et al., 2013). In addition, electron Bernstein waves and ESWs (discussed in the next section) were observed in the separatrix regions. New reconstruction methods can allow us to study waves in a more complex magnetic topology than a two-dimensional X line (Fu et al., 2015; Liu et al., 2019; Torbert et al., 2019).

Figure 1 shows an example of Langmuir waves observed in the separatrix of magnetotail reconnection reported by Viberg et al. (2013). **Figure 1A** shows a spectrogram of E , in which ESWs, EC (electron Bernstein) waves, and Langmuir waves are observed. **Figure 1B** shows an example of Langmuir waves and the associated electron distribution. The waves have peak frequency at f_{pe} and a clear electron beam was observed. The Langmuir waves tended to be observed in the outer separatrices, where the fastest electron beams are observed (**Figure 1C**).

In weakly magnetized plasmas $f_{pe} \approx f_{uh}$, so Langmuir and UH waves have very similar frequencies. Both Langmuir and UH waves have polarization close to linear, but can be distinguished by the electric field direction with respect to the ambient magnetic field. Langmuir waves (and beam-mode waves) are characterized by $E_{\parallel} \gg E_{\perp}$, while UH waves are characterized

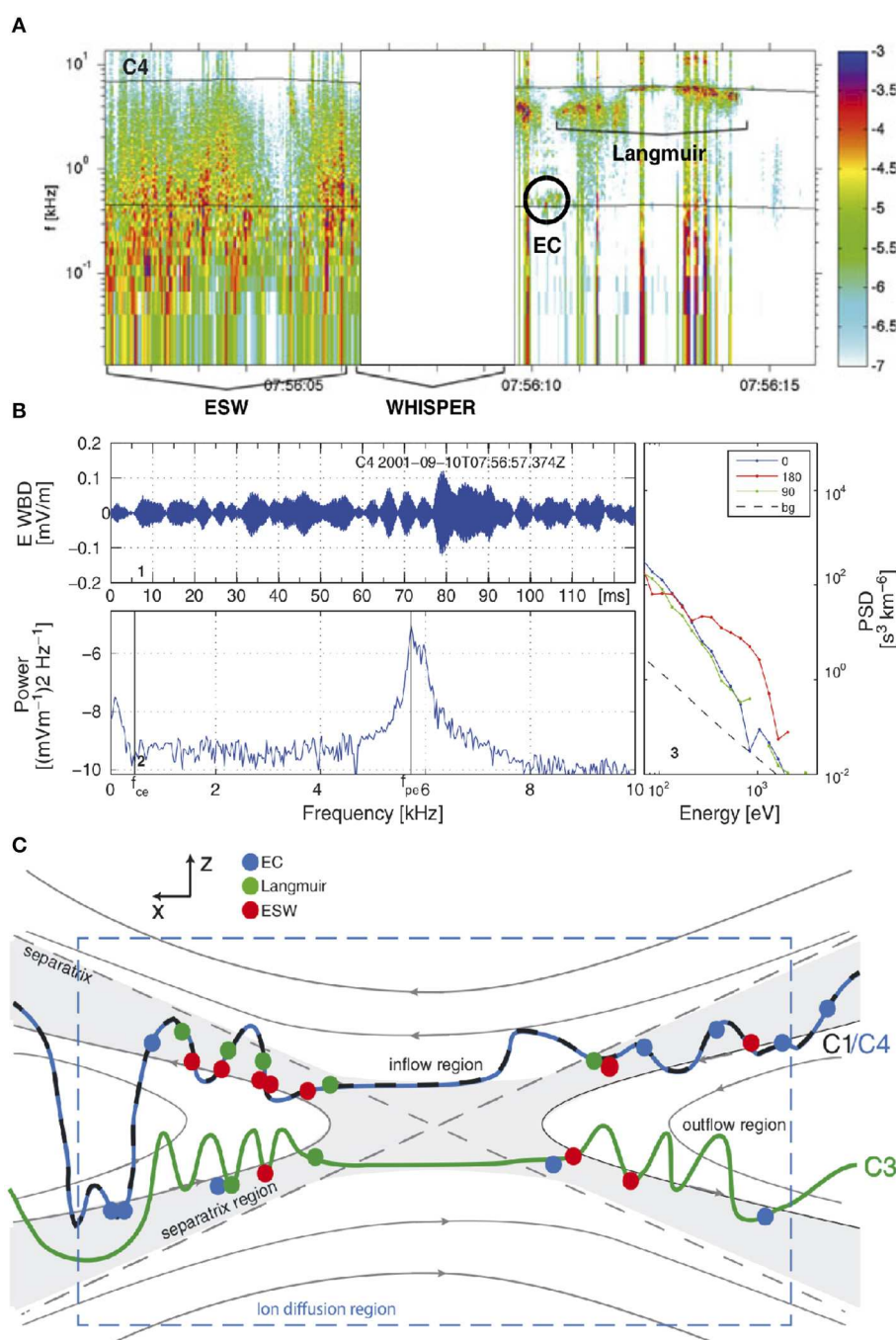


FIGURE 1 | Example of waves observed in the separatrix of magnetotail reconnection observed by Cluster from Viberg et al. (2013). **(A)** Electric field spectrogram showing ESWs, EC waves, and Langmuir waves. **(B)** Example of Langmuir waves: 1 Waveform of Langmuir waves, 2 Power spectrum, and 3 electron phase-space densities at pitch angles 0° (blue), 90° (green), and 180° (red). **(C)** A schematic showing the paths of the Cluster spacecraft across the reconnection region and locations of the observed ESWs, EC waves, and Langmuir waves.

by $E_\perp \gg E_\parallel$. Like UH waves, electron Bernstein waves (or EC waves) are characterized by $E_\perp \gg E_\parallel$, but have frequencies between harmonics of the electron cyclotron frequency. Thus, Langmuir and UH waves are straightforward to distinguish when

three-dimensional electric field data are available, as in the case of MMS.

Figure 2 shows an example of UH and electron Bernstein waves observed at Earth's magnetopause when reconnection

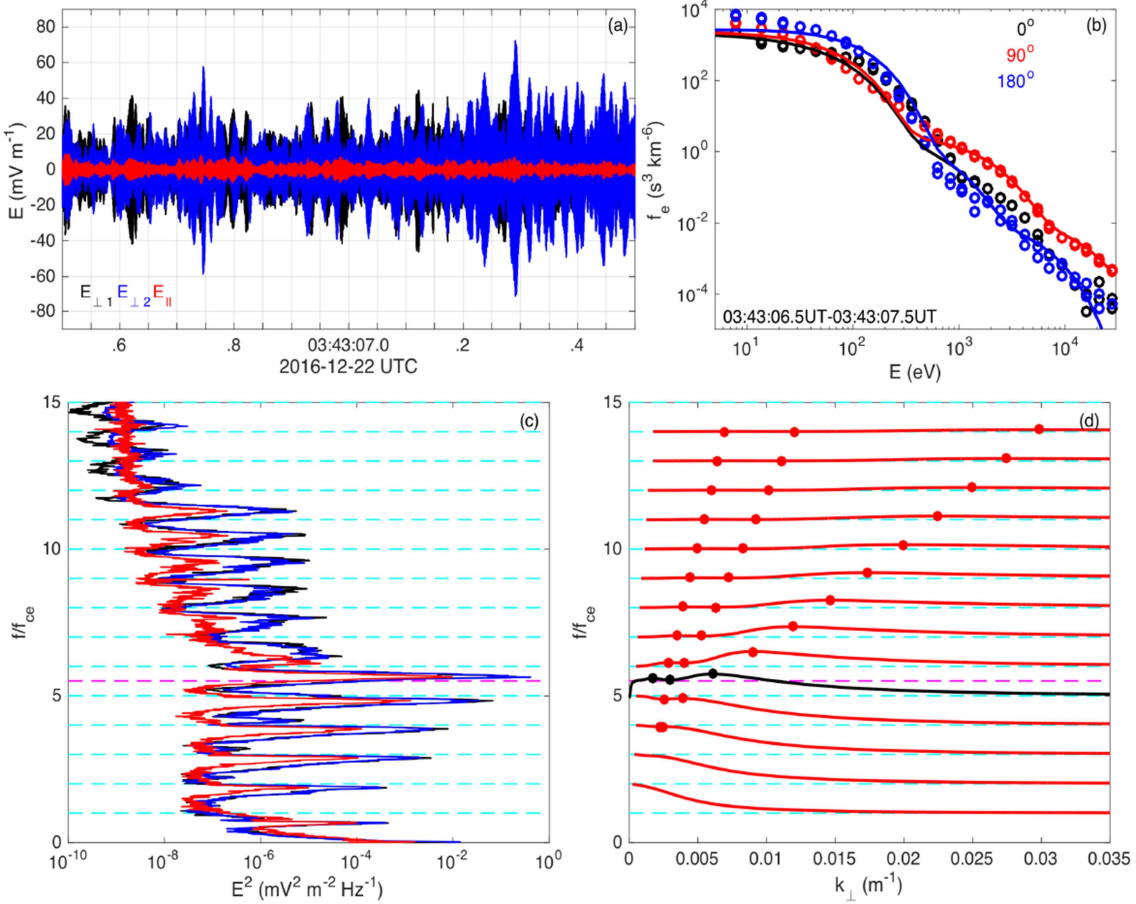
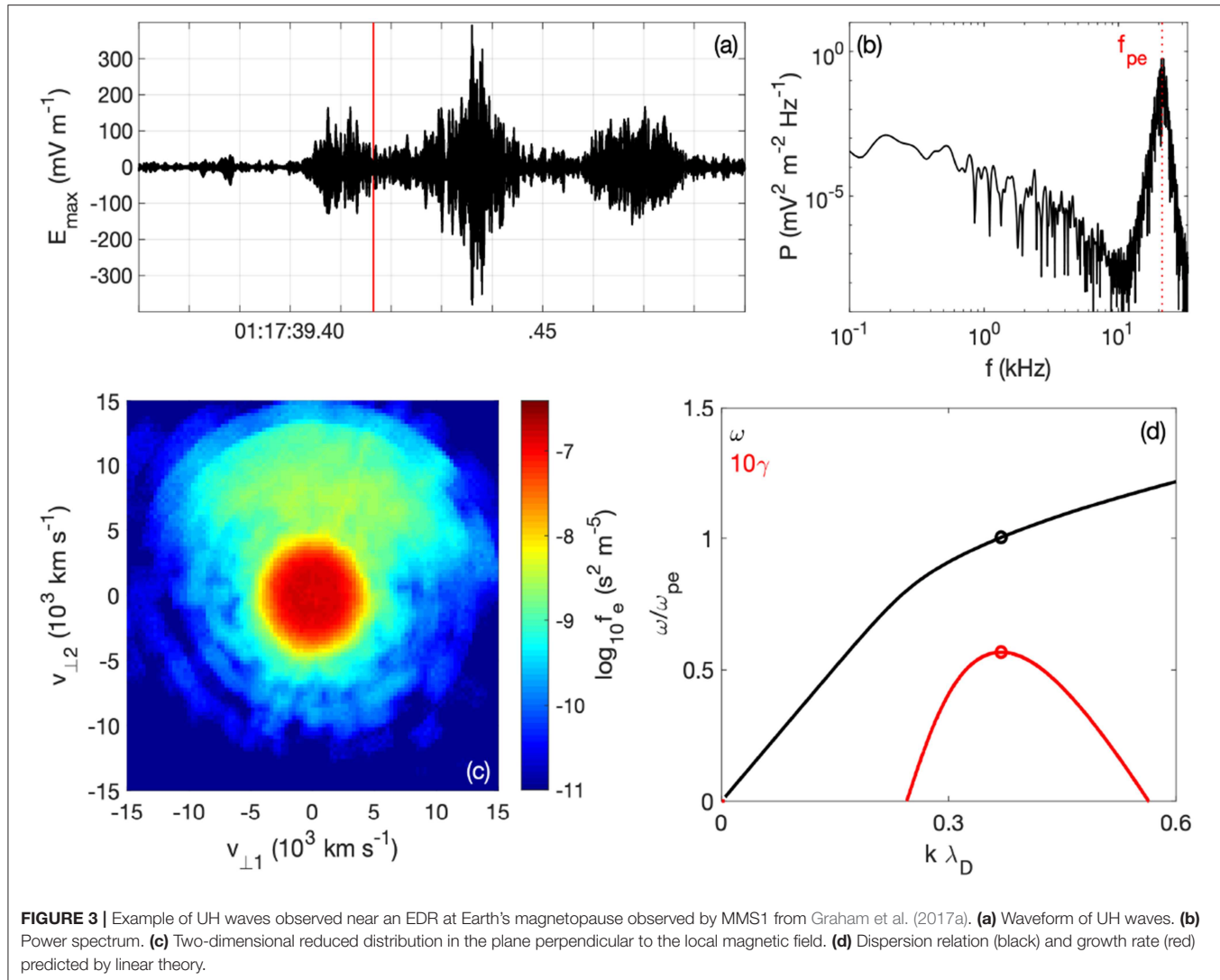


FIGURE 2 | Example of UH and electron Bernstein waves observed by MMS at the reconnecting magnetopause from Graham et al. (2018). **(a)** Waveform in field-aligned coordinates. **(b)** Observed electron distribution associated with the waves (circles) and fitted distribution (solid lines). The black, red, and blue colors indicate the phase-space densities at pitch angles $\theta = 0^\circ$, 90° , 180° , respectively. **(c,d)** Power spectra of the three electric field components. **(d)** Predicted dispersion relations of the UH waves (black), and electron Bernstein waves (red). The dots indicate points where the group velocity is zero. In **(c,d)** the cyan dashed lines indicate f_{ce} and the magenta dashed line indicates f_{uh} .

is ongoing. The waveform (**Figure 2a**) shows that $E_\perp \gg E_\parallel$, consistent with UH and Bernstein waves. The power spectrum (**Figure 2c**) shows a series of spectral peaks between harmonics of f_{ce} , with the largest power observed near f_{uh} consistent with UH waves. The other spectral peaks above and below f_{uh} are consistent with Bernstein waves. **Figure 2b** shows the associated electron distribution at pitch angles $\theta = 0^\circ$ (black), 90° (red), and 180° (blue), and a fit to the observed data. The distribution has a strong perpendicular temperature anisotropy at high energies, which is frequently observed in association with UH waves at the magnetopause (Graham et al., 2018). The dispersion relations of the UH and Bernstein waves are shown in **Figure 2d**. The peaks in the power spectra approximately correspond to the points of near-zero group velocity of the waves.

Plasma frequency waves near the electron diffusion region (EDR) have recently been investigated by the MMS spacecraft. Graham et al. (2017a) showed for the first time that UH-like waves occur near the EDR, where agyrotropic electron beams and

crescents develop, see **Figure 3**. **Figure 3a** shows the waveform of \mathbf{E} . The electric field is characterized by $E_\perp \gg E_\parallel$ and is approximately one-dimensional. The peak amplitude of the wave is ~ 400 mV m⁻¹, making the waves amongst the largest amplitude observed at the magnetopause. The power spectrum (**Figure 3b**) shows that waves have peak power close to $f_{pe} \approx f_{uh}$. So the waves are identified as UH waves. **Figure 3c** shows the electron velocity distribution function (VDF) observed at the same time as the waves. The VDF is characterized by a stationary core population and beam/crescent propagating perpendicular to the background magnetic field. This distribution exists in a spatial region of the local electron gyroradius size, and was found to be unstable to electron beam mode assuming the electrons are approximately unmagnetized (**Figure 3d**). The predicted wavelength of the unstable waves is well below the electron gyroradius size. Thus, the agyrotropic electron distributions (crescents) produced by reconnection within the EDR can be unstable to generation of UH waves, which in turn could modify the electron dynamics within the EDR.

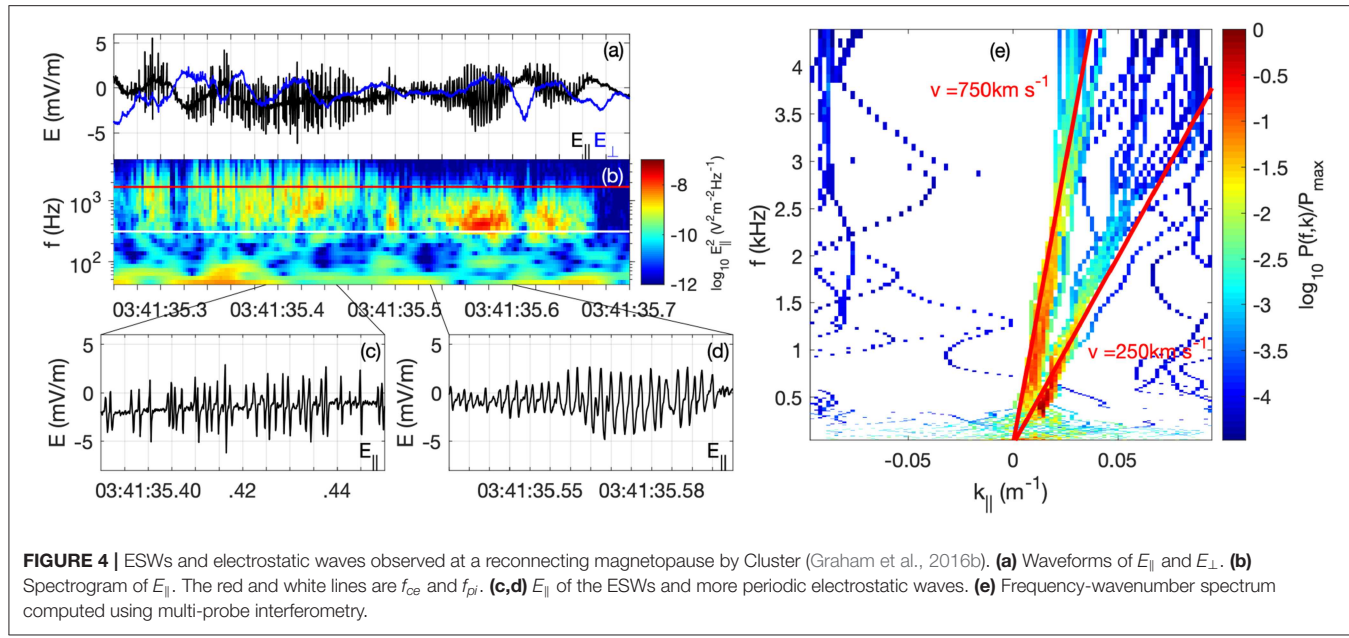


These results have been confirmed in subsequent studies. For example, Tang et al. (2019) found UH waves colocated with agyrotropic electron distributions at a narrow boundary at the magnetopause flank. Burch et al. (2019) found that the electron distributions associated with two EDRs in the magnetotail were unstable to large-amplitude Langmuir/beam-mode and UH waves. The observations showed that these wave reach large amplitudes ($\sim 100 \text{ mV m}^{-1}$), and nonlinear behavior in the form of electrostatic harmonics was observed (Dokgo et al., 2019). In each case a beam-plasma interaction was found to be the source of instability.

At present, there are very few simulations on plasma-frequency waves associated with magnetic reconnection, due to the difficulty in resolving at the same time Debye-scale high-frequency waves, low-density electron beams, and the overall reconnection structure. However, Fujimoto (2014) found beam-mode waves in the separatrices of symmetric reconnection. Recently, Dokgo et al. (2019) performed a local homogeneous simulation of UH waves generated by an agyrotropic electron

crescent. They found that electrostatic beam-mode-like waves were generated, consistent with observations. Additionally, they found that weak electromagnetic waves were generated at the fundamental and second harmonic frequencies due to nonlinear processes.

Langmuir and UH waves are important because they are a source of coherent freely propagating electromagnetic waves (O and X modes in a magnetized plasma) near the local plasma frequency and harmonics (in the radio frequency range). The generation of radio waves has primarily been studied in the solar wind and at planetary foreshocks [e.g., Melrose (2017), and references therein]. For example, type III radio bursts are associated with fast electron beams originating from the Sun, and are likely accelerated by magnetic reconnection. There are several mechanisms proposed for electromagnetic waves, including three-wave decay and coalescence, three-wave electromagnetic decay, linear mode conversion, and antenna mechanisms associated with nonlinear currents. The recent observations of Langmuir and UH waves associated with reconnection suggests



that radio waves may be generated in or near reconnection diffusion regions and the separatrices. The Langmuir and UH waves were observed at large-amplitudes, which suggests that nonlinear three-wave processes could occur. The waves observed in the separatrices and near the EDR, where density gradients are expected to occur, so linear mode conversion may be a viable source of radio emission. At present direct observations of electromagnetic waves generated at reconnection sites are currently lacking. Although studying radio emission source regions is challenging because the electrostatic waves at the plasma frequency and harmonics tend to dominate the electric field power, the observations provided by the four closely separated MMS spacecraft may provide a unique opportunity to study radio wave emission.

2.2. Broadband E_{\parallel} Waves

In this section we discuss broadband electrostatic waves (EWs) that propagate parallel to the ambient magnetic field. One subgroup of EWs are electrostatic solitary waves (ESWs), which are highly nonlinear solitary structures characterized by bipolar electric fields in the direction parallel to the ambient magnetic field. The bipolar electric field is associated with an electrostatic potential, and when this potential is positive, the ESWs are generally interpreted as propagating electron phase spaces holes (EHs) with inherently strong electron trapping. Following the initial work of Bernstein et al. (1957), a lot of attention has been spent on theoretical modeling of EHs. However, it was not until recently that MMS could make the first observations of the phase space depletion associated with ESWs (Mozer et al., 2018).

The frequencies of EWs and ESWs can extend from below the ion plasma frequency to the electron plasma frequency. Figure 4a shows an example of EW and ESW waveforms. Figure 4c shows a closeup of bipolar E_{\parallel} structures characteristic of ESWs, and Figure 4d shows a more periodic EW waveform.

The corresponding spectral representation of waves is shown in Figure 4b, the wave spectrum is broadband, covering the frequency range between f_{pi} and above f_{ce} .

Already early Cluster observations have connected the appearances of ESWs with electron streaming at reconnection separatrices both in the magnetotail (Cattell, 2005) and the dayside magnetopause (Retinó et al., 2006). In the magnetotail, during individual reconnection events, ESWs have been observed in all four separatrix regions (Viberg et al., 2013); the ESWs were primarily observed at the inner side of separatrix regions, the side that is closest to the current sheet center, see Figure 1C. At the dayside magnetopause, EWs and ESWs were observed both at the magnetospheric and magnetosheath sides of the reconnection exhaust (Graham et al., 2015, 2016b). EWs and ESWs have also been routinely observed at dipolarization fronts (Le Contel et al., 2017) and inside magnetic islands produced by magnetic reconnection (Khotyaintsev et al., 2010).

The length scales of EWs and ESWs are on the order of several Debye lengths, and therefore they can develop at the smallest scales relevant to reconnection, i.e., within the EDR. Using multi-probe interferometry between the Cluster electric field probes separated by ~ 100 m, Graham et al. (2016b) found an average peak-to-peak length of $9\lambda_D$ at the magnetopause, with EWs having slightly smaller length scales than ESWs. This was later confirmed for ESWs by MMS using multi-spacecraft interferometry (Steinvall et al., 2019b). Also using multi-probe interferometry on Polar (Franz et al., 2005) found somewhat smaller length scales when investigating small-amplitude ESWs in the plasma sheet boundary layer. However, due to the limitations of single spacecraft interferometry (maximum probe separation ~ 100 m limiting the maximum speed which can be resolved), their study excluded the larger velocity structures, which may impact the perceived average length scales. The waves' phase speeds range from ~ 0 up to $\gtrsim v_{Te}$ and increased

with increasing length scales (Franz et al., 2005; Graham et al., 2016b). The electric field amplitudes range from $< 1 \text{ mV/m}$ to a few hundreds mV/m in more rare cases (Graham et al., 2016b; Khotyaintsev et al., 2016), and are generally larger in the magnetotail than at the dayside magnetopause. Normalized to the electron temperature, the potential amplitude can span several orders of magnitude, from $e\phi/k_B T_e = 10^{-5}$ to above unity (Franz et al., 2005; Graham et al., 2016b; Norgren et al., 2019). At the magnetopause the potentials of EWs are in general lower than those of ESWs (Graham et al., 2016b). With MMS, four-spacecraft interferometry has become routinely applicable, resulting in unambiguous estimates of speeds and parallel length scales, and 3-D characterization of the wave structures (Holmes et al., 2018; Tong et al., 2018; Steinvall et al., 2019b).

Phase speeds of EWs and ESWs are highly dependent on their generation mechanism. For example, the Buneman instability which typically involves stationary ions and drifting electrons generates waves at low speeds, in general just above the ion thermal speed (Khotyaintsev et al., 2010; Norgren et al., 2015). Electron-electron streaming instabilities can generate waves at a large range of speeds, depending on the relative drift speed, temperature, and density of the electron populations (Omura et al., 1996). As such they have the potential to interact with a large part of the electron and ion populations and have generated considerable interest for their potential role in scattering and heating the plasma, and providing anomalous resistivity or drag.

Cluster showed that asymmetric reconnection was associated with EWs and ESWs propagating not only at different speeds, but also in different directions in close proximity to each other (Graham et al., 2015). The distinct wave speeds indicate the presence of complicated and/or evolving electron distributions, possibly related to complicated magnetic topologies and multiple source populations. **Figure 4** shows observed waveforms together with the time-frequency and wavenumber-frequency spectrograms of two wave packages propagating at distinct speeds. On the magnetospheric side of the reconnection current layer, ESWs have been observed to propagate away from the X line (Khotyaintsev et al., 2016; Mozer et al., 2016). Khotyaintsev et al. (2016) observed a strong electron jet, also directed away from the X line, which was closely associated with the observed waves. The authors concluded that the waves were generated by the Buneman instability, and likely aided in the thermalization of the jet (Khotyaintsev et al., 2016). Another study from the magnetopause showed that the interaction of cold magnetospheric electrons with warm magnetosheath electrons made possible through magnetic reconnection can generate EWs (Ergun et al., 2016).

In symmetric antiparallel reconnection, the strongest field-aligned electron flows are formed at the four separatrices, by electrons streaming toward the X line (Fujimoto, 2014; Egedal et al., 2015; Norgren et al., 2019). **Figure 5a** shows the localized parallel bipolar electric fields developed as a consequence of these accelerated electron flows in a numerical simulation of symmetric magnetic reconnection (Fujimoto, 2014). The accelerated population and subsequent wave-particle interaction can be seen in the electron phase space in **Figure 5b**. The inflowing electrons are accelerated above the thermal energies

toward the X line forming a beam, which gradually becomes more thermalized. The wave-particle interaction can be seen as modulations of the accelerated population. **Figure 5c** shows corresponding observations from a magnetic reconnection separatrix in the magnetotail made by MMS (Norgren et al., 2019). The colormap shows the 1-D reduced electron VDF, similar to **Figure 5b**. ESWs propagate toward the X line along the magnetic field with phase speeds v_{ph} (shown as dots) proportional to the beam speed. The bounding black lines show the range of speeds where the electrons can interact efficiently with the ESWs, defined as $v_{ph} \pm \sqrt{2e\phi/m_e}$, where ϕ is the maximum potential of the ESWs. This interaction range is large enough to encompass the beam and indicates that the wave-particle interaction is strong and can contribute to thermalizing the beam. Through a numerical simulation, Hesse et al. (2018) found that the heating generated by the electrostatic turbulence at the separatrices led to macroscopic quasi-viscosity that contributed to the overall energy balance.

In guide-field reconnection, the reconnection electric field has a component parallel to the magnetic field at the X line. This parallel electric field leads to enhanced field-aligned electron flows at two opposing of the four separatrices and merges them with the electron reconnection jet inside the EDR. At the same time the electron flows at the remaining two separatrices are suppressed. Numerical simulations showed that the intense field-aligned beams at the X line lead to electrostatic turbulence due to the relative drift between the ions and the electrons (Drake, 2003). The waves led to significant electron scattering and energization. However, while the anomalous drag associated with the waves was comparable in amplitude to the reconnection electric field, it was highly fluctuating and did not correlate spatially. Another numerical simulation predicted that the turbulence due to the electron jet in guide-field reconnection would evolve in two phases (Che et al., 2009). First, the Buneman instability would lead to the formation of electrostatic turbulence at low phase speeds and partially thermalize the beam. Eventually, the electron two-stream instability would take over, leading to higher phase speeds and continuing to thermalize the beam. This scenario was recently confirmed in an event study of guide-field reconnection at the dayside magnetopause by MMS (Khotyaintsev et al., 2019); it was shown that the electron reconnection jet was gradually thermalized due to the wave-particle interaction of broadband electrostatic turbulence.

While the thermalizing effect of ESWs on beams has been established, no quantitative estimates of anomalous resistivity, drag, cross field diffusion or momentum transfer due to ESWs have been made in association with magnetic reconnection. Vasko et al. (2017) derived diffusion coefficients based on ESWs observed in the inner magnetosphere, and found that the cross field diffusion due to the perpendicular electric fields was most efficient when the time scale of the ESWs as observed by the electrons were comparable to the local electron gyroperiod. As this should often be the case for ESWs observed in magnetic reconnection regions, it is likely that cross field diffusion is also efficient here. The parallel electron beams generated by reconnection are closely associated with velocity shears, and at the separatrices also with density and pressure gradients.

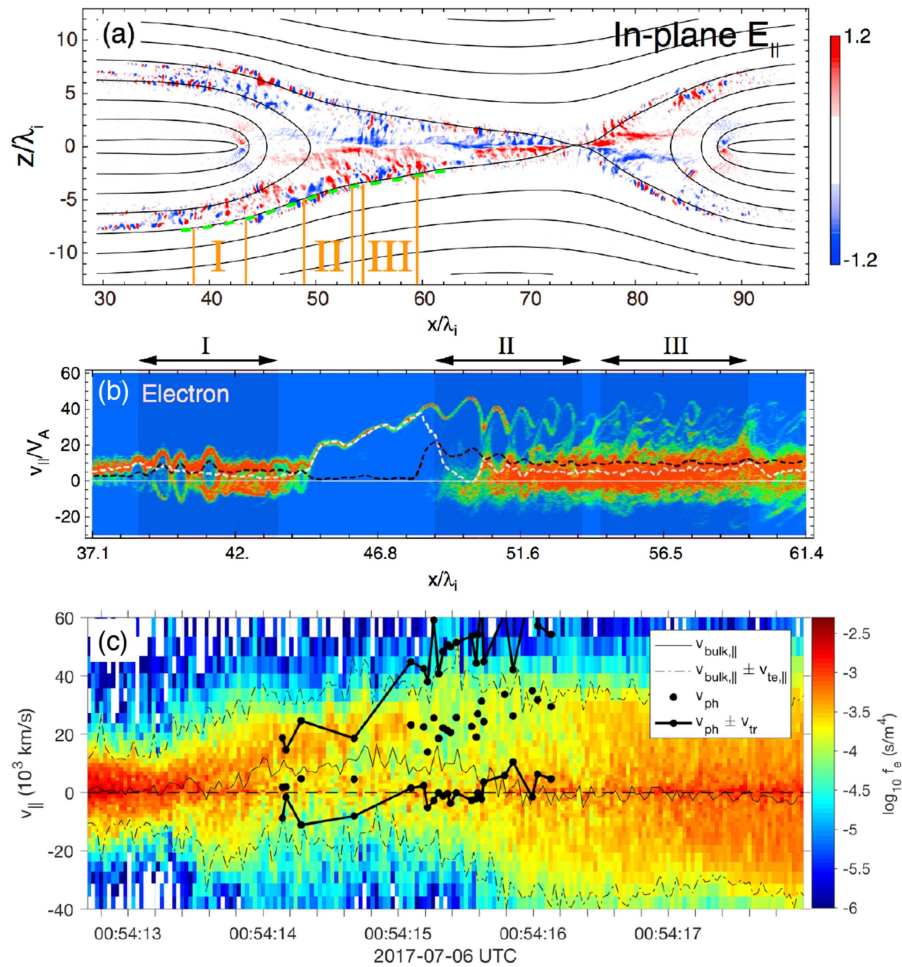


FIGURE 5 | Electron phase space holes observed at the separatrix regions of magnetic reconnection. The electrons are accelerated toward the X line through a potential drop. The streaming electrons lead to instabilities and electron trapping. **(a)** Parallel electric fields and **(b)** reduced electron phase space density along the green dashed line in panel a of a numerical simulation of symmetric magnetic reconnection. The white dashed line shows the bulk velocity while the black line shows the thermal speed. Adapted from Fujimoto (2014). **(c)** MMS observations from a separatrix region in the magnetotail. The colormap shows the reduced electron VDF in which we can see how the lobe electrons become accelerated. The black dots show the speeds of individual ESWs, while the bounding black lines show the range of velocities in which the ESWs and particle distribution can interact efficiently.

To quantify what effect these velocity shears and plasma gradients have on the wave instabilities, and how the wave-particle interaction affect the evolution of the plasma, wave quantities and gradients need to be measured simultaneously. This requires multi-scale separation of the spacecraft; separation on the order of electron kinetic scales to quantify the wave properties, and separation closer to ion kinetic scales to resolve plasma gradients. It is also necessary to compare the wave-particle interaction due to ESWs to that of the other wave modes commonly generated in the same regions, for example lower hybrid waves at the separatrices. In addition, to fully quantify the wave-particle interaction, even higher cadence velocity distribution function data than what are provided by MMS are required.

2.3. Whistlers

In the reconnection context, one of the most important properties of whistler waves is to provide fast and efficient pitch-angle scattering of electrons, which relaxes the temperature anisotropies and other non-thermal structures in the electron velocity distribution function (VDF). Whistlers can also transport energy in the form of Poynting flux, generally along the magnetic field. Whistlers have wavelength shorter than the ion inertial length, but much longer than the electron inertial lengths, so they are relevant for the scales larger than the typical EDR extent.

Whistlers are observed as fluctuations in E and B fields in the frequency range $\sim 0.1f_{ce} < f < 1f_{ce}$. The wave magnetic field polarization is right-handed and close to circular (Fu et al.,

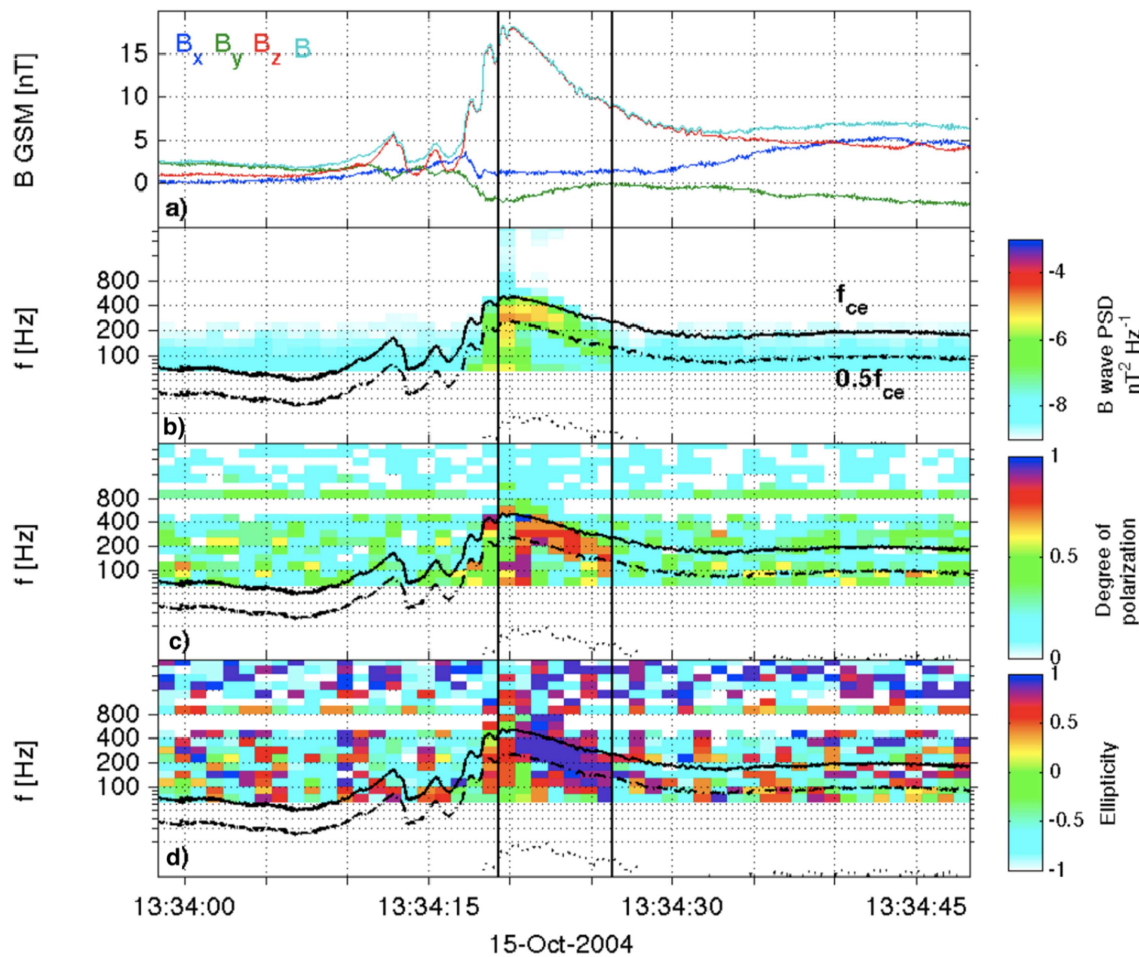


FIGURE 6 | Example of whistler waves observed in the flux pileup region (FPR) at the front of a reconnection jet. **(a)** Magnetic field with clear increase in B_z (FPR) characteristic for FPR (Sitnov et al., 2019). **(b–d)** Show power spectrum of magnetic fluctuations, degree of polarization and ellipticity all of which are enhanced in association with a whistler wave burst between 0.5 and 1 f_{ce} . Adapted from Viberg et al. (2014).

2019). Whistler magnetic fields typically have high degrees of polarization > 0.8 , high ellipticity $> +0.7$, and high planarity > 0.8 (Taubenschuss et al., 2014). **Figure 6** shows an example of whistlers with $\sim 0.5f_{ce} < f < 1f_{ce}$ observed in the flux pileup region (FPR) at the front of a reconnection jet (Viberg et al., 2014). The waves can be clearly identified by the high degree of polarization (panel c) and ellipticity close to 1 (right-handed).

For quasi field-aligned wave vectors, small angle between the wave vector \mathbf{k} and background \mathbf{B} , whistlers are electromagnetic, while for larger angles approaching the resonance cone, the waves become quasi electrostatic. This change in wave characteristic with wave normal angle is illustrated in **Figure 7B**, which shows the E_{long}/E ratio, where E_{long} in the longitudinal (along \mathbf{k}) component of the electric field.

In the context of reconnection whistlers were originally discussed in the frame of whistler mediated (Hall) reconnection (Mandt et al., 1994; Rogers et al., 2001), produced by the modified two-stream instability (MTSI) at ion kinetic scales within the reconnecting current sheet (Ji et al., 2004), or even as a means

of triggering the reconnection (Wei et al., 2007). Whistlers were reported at reconnection sites using GEOTAIL and early Cluster data (Deng and Matsumoto, 2001; Khotyaintsev et al., 2004; Stenberg et al., 2005), without a clear conclusion on their role or generation mechanism. Since then good progress has been achieved in understanding where exactly the whistlers appear in the reconnection picture. Detailed studies involving wave and electron data found that whistler generation can be attributed to unstable electron distributions, such as loss-cones, beams, and anisotropies, created by reconnection, see **Figure 7**.

Whistlers have been identified close to fronts of reconnection jets associated with regions of magnetic flux pileup (Le Contel et al., 2009; Khotyaintsev et al., 2011). This pileup occurs as the jet front region is squeezed in between the ambient plasma ahead of it and the jet itself. The pileup leads to betatron heating of electrons which creates a temperature anisotropy $T_{e\perp}/T_{e\parallel} > 1$, which becomes unstable to whistler generation. As a result, quasi field-aligned whistlers are generated by the cyclotron resonance. Whistlers introduce pitch-angle scattering at resonant energies

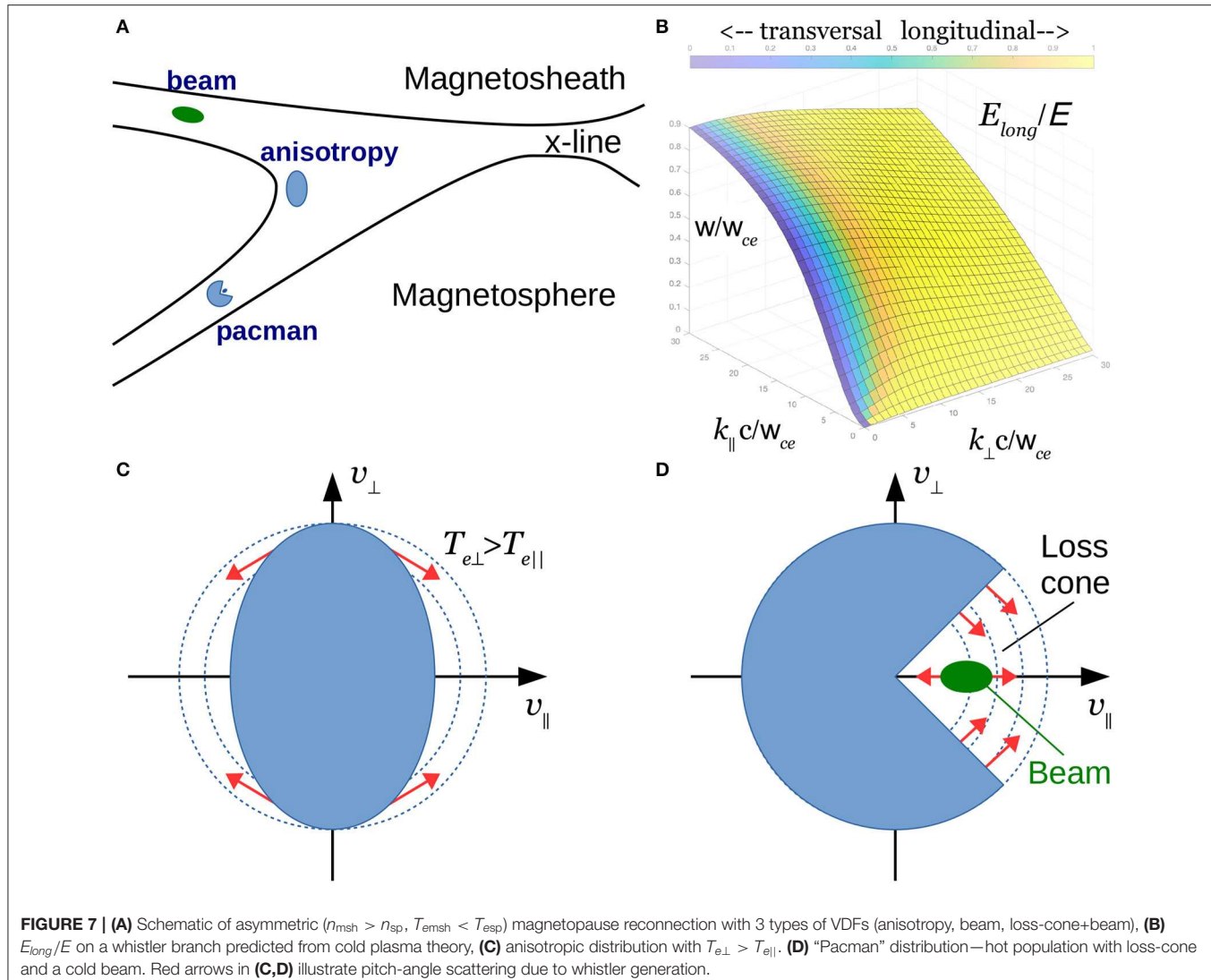


FIGURE 7 | (A) Schematic of asymmetric ($n_{msh} > n_{sp}$, $T_{emsh} < T_{esp}$) magnetopause reconnection with 3 types of VDFs (anisotropy, beam, loss-cone+beam), **(B)** E_{long}/E on a whistler branch predicted from cold plasma theory, **(C)** anisotropic distribution with $T_{e\perp} > T_{e\parallel}$. **(D)** “Pacman” distribution—hot population with loss-cone and a cold beam. Red arrows in **(C,D)** illustrate pitch-angle scattering due to whistler generation.

which leads to relaxation of the anisotropy (Khotyaintsev et al., 2011). Figure 7C illustrates such an anisotropic distribution; red arrows show the direction of pitch-angle scattering. At energies above the resonant the behavior is close adiabatic (Fu et al., 2011, 2013). Based on a statistical study of dipolarization fronts (DF, likely reconnection jet fronts) in the magnetotail whistlers were found in 30–60% of studied DF cases, and that generally whistlers are 7 times more likely to be observed near a DF than at any random location in the magnetotail (Viberg et al., 2014). Statistically the waves were found close to the center of the current sheet and in association with anisotropic electron distributions. This confirms the case study by Khotyaintsev et al. (2011), where the location of the whistler source at the center of the current sheet has been determined from multi-spacecraft observations of the wave Poynting flux. However, in more complex reconnection configurations, as in the case of plasmoid coalescence (secondary reconnection), the source of

pile-up driven whistlers can be located away from the center of the main current sheet (Fujimoto, 2017).

While the jet fronts are typically observed rather far (tens to hundreds of ion scales) from the X-line, the same FPR driven anisotropy can operate even within the diffusion region. A statistical survey of reconnection sites observed by Cluster have shown that the whistler waves are most often found in the pileup and separatrix regions (Huang et al., 2017). Using high resolution 2D PIC simulation, Fujimoto and Sydora (2008) have shown whistler generation in the downstream region of the electron outflow, where similar flux pileup is driven by the electron jet. The anisotropy is maximum in the center of the current sheet, and this is where the waves are generated and propagate away from the center in both directions and away from the X-line. Anisotropy driven whistlers in the vicinity of the EDR have been reported using THEMIS and MMS observations (Tang et al., 2013; Khotyaintsev et al., 2016). Cao et al. (2017) studied

wave generation in an EDR using a kinetic dispersion solver and observed electron distributions, and concluded that generation is due to the perpendicular temperature anisotropy of the slightly suprathermal (300 eV) electrons.

Another source of whistler generation related to reconnection is the loss-cone distributions created by reconnection in the separatrix regions for current sheets with very different electron temperatures on the two sides of the current sheet. A typical example of such a current sheet is the dayside magnetopause, with hot plasmashell population of one side, and significantly colder magnetosheath population on the other side. As reconnection proceeds, previously closed magnetospheric field lines become connected to the magnetosheath, which enables escape of hot plasmashell electrons with small pitch angles forming a loss-cone distribution at the magnetospheric side of the boundary. **Figure 7D** (but without the beam) shows an example of such a loss-cone distribution. Graham et al. (2016c) and Uchino et al. (2017) reported whistlers in the magnetospheric separatrix region at the dayside magnetopause. The wave generation was consistent with the loss-cone mechanism, and the observed waves propagated toward the X-line and had small wave normal angles (Graham et al., 2016b). Such waves should not be confused with similar quasi-field-aligned whistlers observed close to the separatrix but on closed field lines (Contel et al., 2016), which are generated at the magnetic equator or in high-latitude B-minima (Vaivads et al., 2007).

Also electron beams, which are characteristic of the separatrix regions, can generate whistlers. The generation in this case is by Landau resonance, and thus the waves have oblique wave normal angles (Fujimoto, 2014; Muñoz and Büchner, 2016). As mentioned above, such oblique waves are more electrostatic than the quasi-parallel waves. Such a generation mechanism has been suggested by observations based on the connection between whistlers and ESWs (Huang et al., 2016; Wilder et al., 2016; Zhou et al., 2018). Such waves have oblique wave normal angles of $\sim 45^\circ$, have large amplitude electric fields with polarization close to linear, i.e., E_\perp and E_{\parallel} of similar amplitude (Wilder et al., 2017; Khotyaintsev et al., 2019). Solving a kinetic dispersion solver using the observed electron distributions suggests whistler generation by electron beams is viable for both magnetotail and magnetopause conditions (Khotyaintsev et al., 2019; Ren et al., 2019).

In addition to direct generation by the beam, Goldman et al. (2014) suggested that whistlers can be generated by electron holes (ESWs) propagating along the separatrices via the Čerenkov mechanism. However, until now there were no observations supporting this picture. Recent MMS observations in the magnetotail show existence of EHs with associated right-hand polarized magnetic components consistent with whistlers (Steinvall et al., 2019a). The magnetic signature is rather localized to the EHs, i.e., no freely propagating whistler is observed as suggested by simulations (Goldman et al., 2014). However, this result can be specific to the studied plasma conditions, and other conditions need to be investigated.

Deeper into the separatrix regions on the magnetospheric side of the magnetopause the loss-cone can co-exist with a beam distribution, where the beam consists of the magnetosheath

electrons accelerated by reconnection, forming a “pacman” distribution, **Figure 7D**. Such distributions can be unstable to both quasi-parallel and oblique whistlers at the same time. This is supported by reported events where the quasi-parallel and oblique whistlers co-exist in the separatrix regions on the magnetospheric side of the magnetopause (Zhou et al., 2018; Khotyaintsev et al., 2019).

Figure 7A summarizes different types of VDFs leading to whistler generation in the vicinity of the X-line. While the pile-up and beam generation operate in any current sheet configurations, the loss-cone requires large electron temperature difference across the current sheet.

Following these recent observational advances, we now need to more quantitatively understand the role of whistler waves for reconnection. What is the efficiency of wave-particle interaction, scattering/pitch-angle diffusion rates? How much does the Poynting flux transported by whistlers away from the reconnection site contribute to overall energy dissipation? We need to better understand the overall interaction between EHs and whistlers. Also the loss-cone driven whistlers have not been simulated, and will require new high-resolution simulations. While for the beam driven whistler more detailed observations are needed to better understand and characterize them.

2.4. Lower Hybrid Waves

In magnetic reconnection, lower hybrid (LH) waves are one of the most extensively studied wave modes. LH waves are found near the LH frequency $f_{LH} \approx \sqrt{f_{ce}f_{ci}}$. In this frequency range the electrons remain approximately frozen in, while ions are approximately unmagnetized. LH waves were proposed as a source of anomalous resistivity, as well as electron and ion heating, and particle transport Davidson and Gladd (1975), Treumann et al. (1991), Cairns and McMillan (2005). The source of these waves is most often attributed to the lower hybrid drift instability (LHDI), which becomes unstable due to density gradients and the associated diamagnetic current. The closely related modified two-stream instability, as well as complex ion VDFs, are also sources of LH waves. Thus, the waves are expected to occur at plasma boundaries, including those associated with magnetic reconnection, where cross-field currents and gradients occur.

Theoretically, the wave properties have been studied extensively and are generally well understood. Both theory and simulations show that the fastest growing modes are quasi-electrostatic waves, which develop at the edges of current sheets where the density gradient is largest. Slower growing electromagnetic modes develop closer to the neutral point (Daughton, 2003). These electromagnetic modes can modify the structure of the current sheet, and are closely related to kink and sausage modes (e.g., Yoon et al., 2002).

Early spacecraft observations found large-amplitude electric field fluctuations at plasma boundaries, such as at Earth's magnetopause and plasma sheet boundary layer. The fluctuations were found to be close to the lower hybrid frequency (e.g., Cattell and Mozer, 1986; Bale et al., 2002).

Cluster and THEMIS observations have furthered our understanding of the wave properties, in particular the

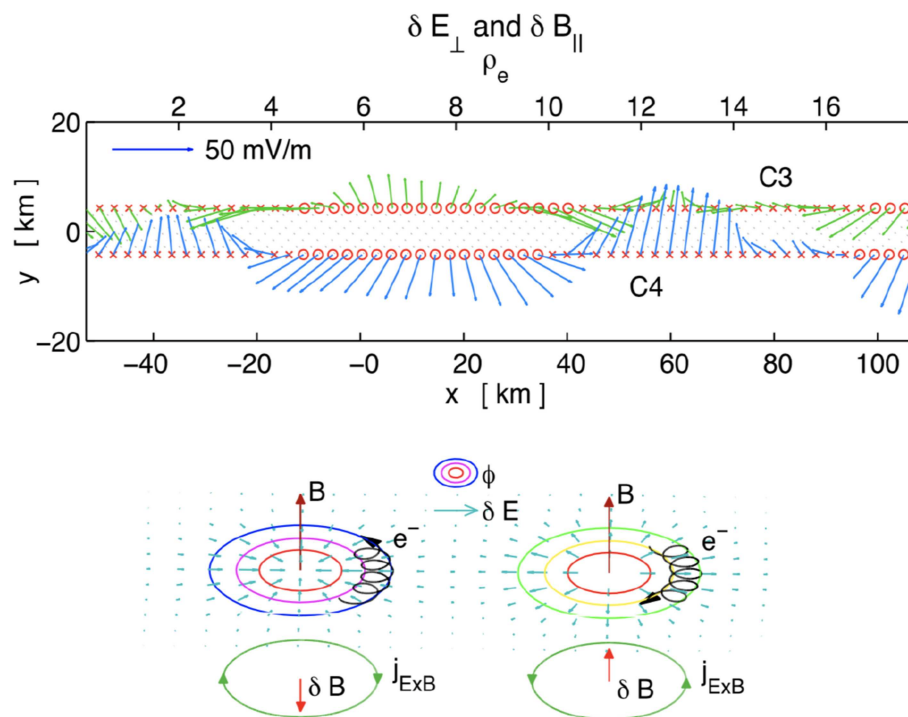


FIGURE 8 | Example of lower hybrid waves observed by two Cluster spacecraft (Norgren et al., 2012). The waves had significant transverse electric fields forming alternating converging and diverging structures associated with corresponding negative and positive potentials, respectively. The potential structures and electric fields are associated with vortex-like electron motion as illustrated in the schematic.

electromagnetic properties of the waves. For example, Zhou et al. (2009b) found quasi-electrostatic LH waves at the edge of a magnetotail current sheet and more electromagnetic waves near the center. Similar electromagnetic drift waves have been reported near the EDR of asymmetric reconnection by MMS (Ergun et al., 2017). Using Cluster, Norgren et al. (2012) were able to determine the phase speed and wavelength of the waves using observations from two closely separated spacecraft. The waves were found to have $k\rho_e \sim 0.5 - 1$, consistent with quasi-electrostatic LH waves. The magnetic field fluctuations associated with the waves were found to be due to the electron motion associated with the electrostatic potential of the waves. Figure 8 (top) shows the electric field vectors from two spacecraft and schematic of the electron motion associated with the wave potential. From these two spacecraft observations regions of diverging and converging fields were observed, corresponding to positive and negative electrostatic potentials, respectively. Magnetic field fluctuations δB_{\parallel} parallel and antiparallel to the background magnetic field were found to be correlated with diverging and converging electric fields. Figure 8 (bottom) shows the electron motion associated the electrostatic potentials of lower hybrid waves. The $E \times B$ motion of the electrons around the potential, and negligible ion motion, results in δB_{\parallel} , according to Ampere's law. The relationship between E_{\perp} and B_{\parallel} fluctuations can be used to estimate the phase velocity of the waves (Norgren et al., 2012).

Lower hybrid waves have often been observed at reconnection jet fronts/DFs (Zhou et al., 2009a; Khotyaintsev et al., 2011; Divin et al., 2015a; Greco et al., 2017; Pan et al., 2018). The cross-field current and density gradient associated with DFs provides the source of LH waves. The waves have properties similar to LH waves associated with reconnection, namely, they are quasi-electrostatic with $k\rho_e \sim 0.5$. Pan et al. (2018) showed that the LH waves resulted in a rippling structure of a DF, which is seen as perturbations in B and n . Three-dimensional simulations have confirmed that LH waves are generated at DFs (Divin et al., 2015b). Some simulations show that DFs become rippled due to the kinetic interchange/ballooning instability (Pritchett and Coroniti, 2010; Vapirev et al., 2018), which is closely related to LHDI and produced waves with similar properties.

The anomalous contributions to magnetic reconnection have been evaluated with Cluster and THEMIS (Vaivads, 2004; Silin et al., 2005; Mozer et al., 2011), in particular the anomalous drag $D = -\langle n_e \delta E \rangle / \langle n_e \rangle$ and the cross-field diffusion D_{\perp} , where $\langle \dots \rangle$ corresponds to spatial averaging. With these spacecraft only fields measurements are capable of resolving lower hybrid waves, so density perturbations were inferred using the spacecraft potential and electron velocity fluctuations were assumed to be moving at the convection velocity. These observations found that anomalous drag was small (Mozer et al., 2011), while cross-field diffusion can be significant (Vaivads, 2004).

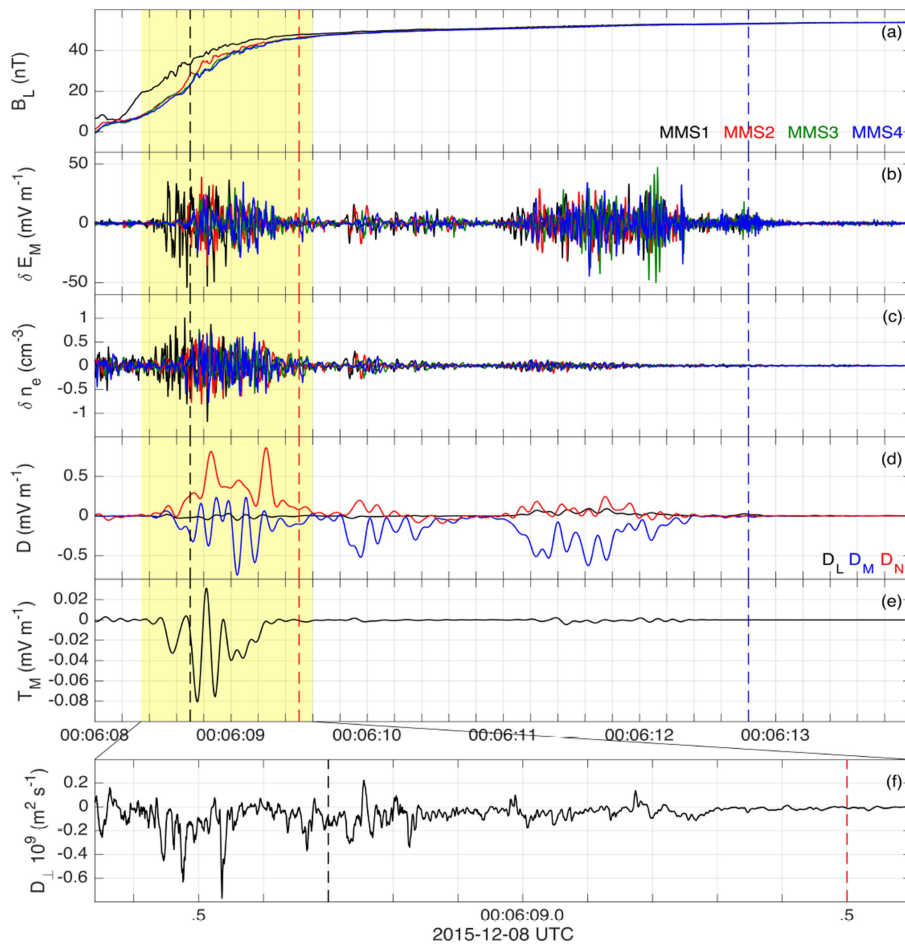


FIGURE 9 | Anomalous terms associated with the LH waves at a reconnecting magnetopause. Figure is reproduced from Graham et al. (2017b). **(a)** B_L obtained from the four MMS spacecraft. **(b)** δE_M associated with LH waves. **(c)** δn_e associated with LH waves inferred from the spacecraft potential. **(d,e)** Anomalous drag D and anomalous viscosity T_M in the M direction estimated over the four spacecraft. **(f)** Cross-field diffusion coefficient D_{\perp} associated with the diffusion region lower hybrid waves averaged over the four spacecraft. The black, red, and blue dashed lines mark the diffusion region, peak parallel electron heating, and ion edge, respectively (defined in Graham et al., 2017b).

Recently, lower hybrid waves have been frequently observed by MMS in the ion diffusion regions of magnetopause reconnection, where there is a large cross-field current and a density gradient (Graham et al., 2016a, 2017b; Khotyaintsev et al., 2016; Zhou et al., 2018). In each case the waves were found to be consistent with generation by LHDI and the estimated wavenumbers were $k\rho_e \sim 0.5$, corresponding to the quasi-electrostatic mode. The waves were found at or adjacent to regions of intense parallel electron heating, reaching anisotropies up to $T_{\parallel}/T_{\perp} \sim 5$ (Graham et al., 2017b). The wave properties were determined using the method in Norgren et al. (2012). In addition, Graham et al. (2017b) found a second group of LH waves in the magnetosospheric inflow region driven by the interaction between cold magnetospheric ions and magnetosheath ions undergoing finite gyroradius motion on the magnetospheric side of the current sheet. These waves were suggested to be a source of heating of the cold ion population.

The anomalous fields associated with LH waves was recently investigated by Graham et al. (2017b) using the MMS spacecraft. Using four closely separated spacecraft enables a more reliable estimate of the anomalous terms associated with the LH waves. **Figure 9** shows an example of LH waves observed at the reconnecting magnetopause and the estimated anomalous terms. **Figures 9a,b** show that the LH waves occur on the magnetosospheric side of the current sheet. **Figure 9c** shows the electron density fluctuations inferred from the spacecraft potential. The density fluctuations are correlated with the electric field fluctuations of the waves. The anomalous drag D estimated from the four spacecraft peaks at close to 1 mV m^{-1} , similar to previous estimates. **Figure 9e** shows $T_M = \langle \delta V_{eN} \delta B_L \rangle$, which approximates the anomalous viscosity computed in numerical simulations (Price et al., 2016, 2017; Le et al., 2017, 2018). This term was found to be much smaller than D . **Figure 9f** shows that the cross-field diffusion coefficient D_{\perp} reaches $-0.8 \times 10^9 \text{ m}^2 \text{ s}^{-1}$ and tends to be negative, corresponding to significant electron

diffusion from the magnetosheath side of the current sheet to the magnetospheric side. These results are in good agreement with the earlier results of Cluster and THEMIS, and suggest that the anomalous fields do not contribute significantly to reconnection. However, like the Cluster and THEMIS observations, density perturbations were inferred from the spacecraft potential and the electron velocity fluctuations were inferred by assuming they undergo $\mathbf{E} \times \mathbf{B}$ drift motion, rather than direct particle measurements. Further work is therefore required to determine the precise role of LH waves in reconnection.

The highest temporal resolution electron moments available on MMS are sufficiently high to resolve fluctuations at the lower hybrid frequency, enabling the wave properties to be studied in unprecedented detail. Recent observations by Graham et al. (2019) have confirmed that $\delta\mathbf{E} \approx -\delta\mathbf{V}_e \times \mathbf{B}$ for LH waves. In addition, large-amplitude $\delta\mathbf{V}_{e,\parallel}$ were observed, indicating a finite k_{\parallel} associated with the waves, which enables interaction with parallel propagating electrons via Landau resonance (Cairns and McMillan, 2005).

LH waves have been studied extensively with numerical simulations. However, only recently have three-dimensional simulations of magnetic reconnection been able investigate the role of LH waves. Recent simulations have investigated in detail the anomalous terms associated with LH waves generated by asymmetric reconnection (Price et al., 2016, 2017; Le et al., 2017, 2018). At present, the relative importance of the anomalous fields for ongoing reconnection is still debated. For example, Le et al. (2017) and Le et al. (2018) concluded that the anomalous terms were relatively unimportant, while Price et al. (2016) and Price et al. (2017) concluded that the anomalous terms were more important. Finally, Le et al. (2017) and Le et al. (2018) showed that parallel electron heating was enhanced in the magnetospheric inflow and separatrices when LH waves are present, compared with two-dimensional simulations, which suppress these waves. Lower hybrid waves can heat electron via Landau resonance if the waves have a finite parallel wave number (Cairns and McMillan, 2005). These intense regions of parallel heating have been observed by MMS (Graham et al., 2017b; Wang et al., 2017), although the relative importance of wave-particle interactions associated with LH waves vs. large-scale electric fields is still debated.

Further work is required to determine the role of anomalous contributions to reconnection, both with simulations and observations. Theoretical and numerical studies have shown that LH waves can heat electrons and ions. However, observational work is required to determine the role of lower hybrid waves in particle heating, and its relative importance to other processes associated with reconnection. Although observations have frequently been compared with theoretical predictions (typically in the local approximation), detailed comparisons of observations with simulations are generally lacking.

2.5. Ion Frequency Waves

At low frequencies below the lower hybrid frequency and particularly below the ion gyrofrequency, the ion dynamics start to dominate and ions are often the free energy source for those low frequency waves. Magnetic reconnection leads to

ion distributions that are far from thermal equilibrium, such as temperature anisotropy, and which are thus potential free energy source for waves. The low frequency waves can be important for energy conversion, energy transport and structuring of the reconnection process. Despite the potential importance of these waves, they have not been extensively studied experimentally or in numerical simulations. Here we will first focus on one of the most important wave types—Kinetic Alfvén waves (KAWS), and at the end of the section mention also other types of plasma waves.

KAWS are known to be important in forming of the diffusion region (Rogers et al., 2001; Dai, 2009, 2018), in transporting energy away from the reconnection site (Shay et al., 2011; Liang et al., 2016), setting up field aligned currents and eventually also interacting with the ionosphere (Duan et al., 2016). There is no well defined way to identify KAWS in data. However, KAWS are characterized by wave vectors being close to perpendicular to the ambient magnetic field, electric/magnetic field ratio close to or above the local Alfvén speed, low values of magnetic field compression. KAWS have a characteristic scale size transverse to the ambient magnetic field that is comparable to or smaller than ion kinetic scales, while parallel scale that can be very large. KAWS transport energy along the magnetic field primarily through the Poynting flux, they are efficient in ion heating both perpendicular and parallel to the ambient magnetic field, as well as electron heating parallel to the magnetic field. In addition, parallel ion beams can form due to their Landau damping (Liang et al., 2017).

There are several mechanisms proposed for the generation of KAWS. One is the diffusion region itself where the setup of the Hall structure of the diffusion region directly corresponds to KAWS propagating away from the diffusion region along the separatrix regions (Shay et al., 2011; Zhang et al., 2017; Huang et al., 2018). Other mechanisms that have been suggested are the firehose instability leading to the generation of KAWS (Jiansen et al., 2018; Wang et al., 2018), KAW generation due to intermittent reconnection (Cao et al., 2013), KAWS being part of the turbulence generated in reconnection outflows (Huang et al., 2012). There has been progress in the understanding the relationship between KAWS and magnetic reconnection, but there are still many open questions.

On the observational side, in recent decades there have been KAW studies using Cluster, MMS and THEMIS data. The high resolution of the MMS data have enabled a very detailed analysis of KAWS within a reconnection outflow jet (Zhang et al., 2017), including KAW's dispersion properties and the associated wave-particle interactions (Gershman et al., 2017). Several studies have shown that significant earthward Poynting flux is carried by KAWS in the plasma sheet boundary layer (Stawarz et al., 2017) and in fast earthward flows within the plasma sheet (Chaston et al., 2012; Duan et al., 2016). It is widely accepted now that the fast flows in plasma sheet and active plasma sheet boundary layer are both result of magnetic reconnection. **Figure 10** shows observations by THEMIS in fast earthward flows within plasma sheet where large energy fluxes in KAWS is observed. Observations show that ion energy flux dominates by more than a factor of ten the Poynting flux of KAWS indicating

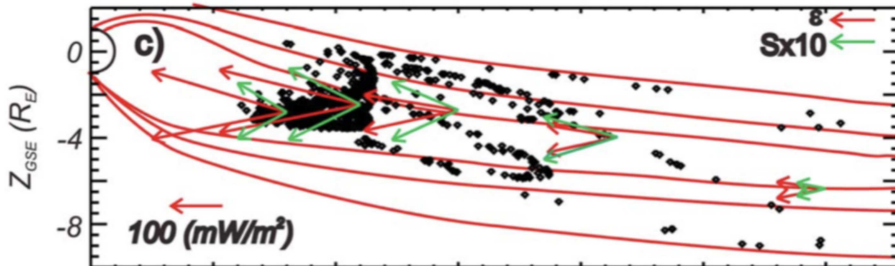


FIGURE 10 | Average values of earthward ion energy flux (red arrows) and Poynting flux (green arrows) in the Earth's magnetotail (Chaston et al., 2012).

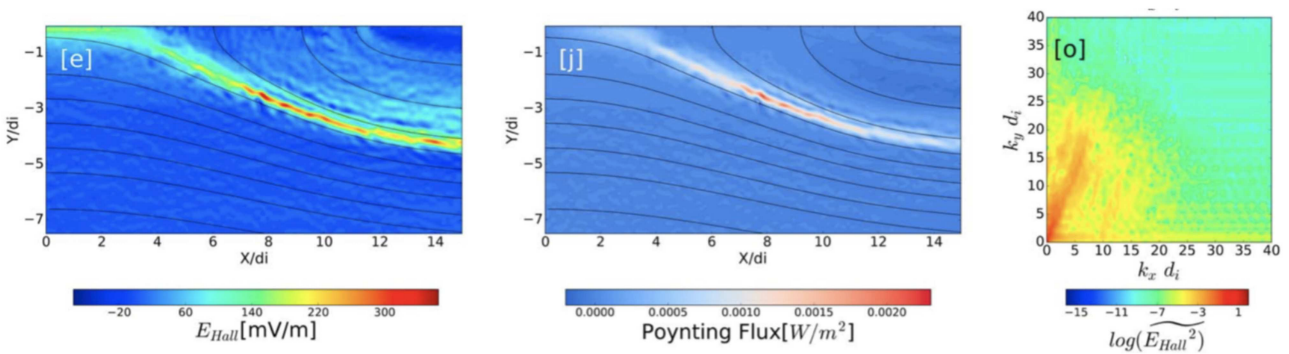


FIGURE 11 | Kinetic Alfvén wave observations in the separatrix region using 2D PIC simulations (Huang et al., 2018). **(Left)** Hall electric field corresponding to KAW generated in reconnection diffusion region. **(Middle)** Poynting flux in X-direction showing large Poynting flux carried by KAW along the separatrix region away from the reconnection site. **(Right)** wave-number spectrum that shows that large amplitude electric fields are almost field aligned structures with perpendicular scale comparable to the ion kinetic scales and thus being consistent with KAW properties.

that ion flows are a potential source of KAWs. In addition, the Poynting flux intensity increases at distances below $15 R_E$ indicating that particularly reconnection jet breaking can be a source of KAWs. It is the consensus of most studies that the Poynting flux carried by KAW is sufficient to drive auroral acceleration processes down in the ionosphere (Angelopoulos et al., 2002; Chaston et al., 2012). Vaivads et al. (2010) have shown that in the case of asymmetric reconnection, the separatrix region on the low-density side (where Alfvén speed is higher) of the current sheet can develop a KAW edge in addition to well known electron and ion edges (Lindstedt et al., 2009), and the KAW edge lies in between ion and electron edges.

The progress on the theory/simulation side in the last decade has focused in several directions. One has been further development of the work by Rogers et al. (2001) showing the importance of KAWs in the structure of the reconnection diffusion region (Shay et al., 2011; Dai et al., 2017; Huang et al., 2018), particularly associating the Hall structure of magnetic reconnection diffusion and separatrix regions to KAWs propagating away from the reconnection site, see **Figure 11**. Another has been looking into the propagation of KAW along the separatrix region and showing that their damping is consistent with Landau damping (Sharma Pyakurel et al., 2018). Finally,

there has been also work showing ion field-aligned acceleration due to KAWs (Liang et al., 2017).

There are several open questions related to KAW and reconnection where we can expect significant progress in the nearest years. One is understanding KAW propagation to ionosphere, particularly using conjunction studies among spacecraft such as Cluster and MMS. Another is understanding electron field-aligned acceleration due to KAW, particularly non-linear mechanisms such as double layer formation. Another important question is the role of KAWs in ion heating including mass resolved observations. We know from low altitude ionospheric observations that KAWs can be very important for ion heating but similar systematic observations in relation to magnetic reconnection are lacking. Finally, we expect significant improvement in our understanding of KAW generation mechanisms in the reconnection jet outflow and breaking regions.

There are other low-frequency wave modes that have been recently addressed in several studies. One is firehose instability that requires large parallel anisotropy either due to the ion parallel heating or field aligned beams. Such anisotropies are observed in the reconnection outflow regions, particularly close to the separatrix region (Hietala et al., 2015). The firehose

instability has been discussed also as a possible source of Pi2 pulsations that can occur in relation to the earthward reconnection jets (Wang et al., 2018). On the other hand, the statistical studies of fluctuations in reconnection jets have shown that, similar to the solar wind turbulence, the ion distribution functions show that their anisotropies are controlled by firehose, proton cyclotron and mirror instabilities (Vörös, 2011). More studies are needed, particularly kinetic scale studies using MMS data, to confirm the overall relationship between low-frequency modes and reconnection.

2.6. Discussion

Below we summarize our current understanding on how the wave occurrence and generation differ between the simplest symmetric antiparallel configuration of the reconnection site, and the ones with density and temperature asymmetries across the reconnecting layer, as well as with the presence of a guide field.

In symmetric antiparallel configurations the main agents driving waves are (1) electron dynamics in the EDR vicinity, (2) electron streaming in separatrix regions, (3) pileup of magnetic field, (4) cross-field currents at kinetic scales, and (5) ion dynamics in outflows.

- (1) Complex *electron dynamics* in the EDR vicinity results in agyrotropic electron VDFs, such as crescents and agyrotropic beams. These distributions can be unstable to generation of large amplitude UH and Langmuir/beam-mode waves. The driving instabilities can be understood as non-magnetized beam-plasma instabilities, as they develop at scales below the electron gyroradius in weakly magnetized plasmas. And they lead to relaxation of the beams.
- (2) *Electron streaming* in separatrix regions provides free energy for generation of Langmuir waves, EWs, ESWs, and oblique whistlers. The wave growth and subsequent nonlinear trapping of the streaming populations by large-amplitude waves leads to thermalization of the electron population, and generally couples the different streaming populations. For sufficiently slow wave speeds, the waves can couple the streaming electrons to ions (anomalous drag). Finite perpendicular extent of the waves and ESWs can also provide transfer of momentum across the velocity gradient (anomalous viscosity).
- (3) Magnetic flux *pileup* leads to anisotropic distributions with $T_{e\perp} > T_{e\parallel}$ via the betatron mechanism. Such anisotropic distributions drive parallel whistlers. The whistlers then scatter the electron in pitch-angle, reducing the anisotropy. The scattering introduces non-adiabatic behavior into an otherwise adiabatic (betatron) electron response to the pileup, which results in overall electron heating (magnetic pumping).
- (4) *Cross-field currents* at kinetic scales appear both in the ion diffusion region (Hall currents) as well as at the fronts of the reconnection jets where sharp gradients in density and the magnetic field exist. Such currents can drive LHDI, MTSI, and KAWs. LHDI is confined to the low- β side of the boundaries and its overall effect is to relax the driving gradient. This corresponds to cross-field diffusion of electrons. Despite the non-linear amplitudes typically observed at the magnetopause, LHDI does not provide substantial anomalous resistivity to support reconnection. LHDI can also lead to electron heating in the field-aligned direction. KAWs transport energy away from the reconnection region and heat ions (parallel and perpendicular to \mathbf{B}) and electrons (parallel to \mathbf{B}).
- (5) *Ion dynamics* in the reconnection outflow jets results in development of strongly anisotropic ion VFDs. Like in the solar wind, the anisotropy range is controlled by firehose, proton cyclotron and mirror instabilities. Development of these instabilities leads to generation of low-frequency wave modes in the outflow and gradual thermalization of the ion VDFs.
- (6) Large electron *temperature asymmetry* across the reconnection layer provides an additional driving agent, not present in symmetric reconnection. It can lead to unstable loss-cone distributions at the hotter side of the layer. Such loss-cones are created as the fast hot electrons escape to the other side of the layer once a field-line becomes reconnected. The unstable distributions can drive UH waves and field-aligned whistlers. The wave growth leads to pitch-angle scattering of resonant electrons, which fill the loss-cone. This reduces the ambipolar E_{\parallel} driven by the escape of the hot population and thus reduces acceleration by this E_{\parallel} of the colder component from the other side of the boundary.
- (7) In a configuration with a guide field, the electron *current at the X-line* is a parallel current, with electrons being largely magnetized. Such fast electron flows at the X-line can become unstable, for example to the Buneman instability. The instabilities lead to thermalization of the electron distribution in the parallel to \mathbf{B} direction, and thus to electron heating. The slow phase velocity of the Buneman instability allows it couple electrons to ions, and thus it can potentially introduce anomalous resistivity.

3. SUMMARY AND OUTLOOK

In summary, there is great progress in understanding the waves in the context of collisionless magnetic reconnection over the last two decades, owing to the new data provided by the Cluster, THEMIS, and MMS missions. Localization of the different wave modes in the reconnection picture has been established. Reconnection jet fronts have been identified as important regions of energy conversion and wave generation. This new knowledge of waves can be particularly useful to study reconnection sites in planetary systems, in particular at kinetic scales, as planetary missions typically have comparable wave instruments to Cluster and MMS, but not the particle instruments.

There is substantial progress in quantification of the wave generation mechanisms and wave-particle interactions. While observed in the *in-situ* data, several waves modes (EC, UH, Langmuir, loss-cone whistler) are still challenging for simulations—instabilities which require fine coverage in phase space at the relevant energies, or Debye scales. More high-resolution simulations are needed to fully incorporate kinetic wave process into the reconnection theory.

Anomalous resistivity has been evaluated from the data for some waves (LHD). To address the higher frequency waves new experimental data with faster electron measurements to resolve VDFs at the relevant time scale is needed.

There is little progress on understanding the electromagnetic radiation from reconnection sites using *in situ* observations, which is crucial for application to solar and astrophysical radio emissions. There is some indirect progress via better quantification of waves near the plasma frequency, but much more work is needed before one could use such *in situ* knowledge to better interpret radio emission from reconnection region at the Sun (Cairns et al., 2018).

Reconnection triggering/onset problem remains mostly theoretical, possibly because of difficulty of capturing the X-line formation in a dynamic unstable current sheet. Addressing this problem from an observational point of view can be done with a cross-scale multi-spacecraft configuration having a large number of points (more than 4), to simultaneously capture the large-scale

current sheet evolution and the EDR. Cross-scale configurations of the existing space missions and new dedicated missions are needed to understand the coupling between the different parts of the reconnection region, the corresponding energy conversion, and particle acceleration.

AUTHOR CONTRIBUTIONS

All authors participated in planning the paper and drafting the outline. Each of the authors had primary responsibility for at least one of the chapters, and secondary responsibility for several other chapters.

FUNDING

This work was supported by the Swedish National Space Agency, grant 128/17, and the Swedish Research Council, grant 2016-05507. Work at the University of Bergen was supported by the Research Council of Norway/CoE under contract 223252/F50.

ACKNOWLEDGMENTS

This work has been partially supported by International Space Science Institute (Bern).

REFERENCES

- Angelopoulos, V. (2008). The THEMIS mission. *Space Sci. Rev.* 141:5. doi: 10.1007/s11214-008-9336-1
- Angelopoulos, V., Chapman, J. A., Mozer, F. S., Scudder, J. D., Russell, C. T., Tsuruda, K., et al. (2002). Plasma sheet electromagnetic power generation and its dissipation along auroral field lines. *J. Geophys. Res. Space Phys.* 107, SMP 14–1–SMP 14–20. doi: 10.1029/2001JA900136
- Bale, S. D., Mozer, F. S., and Phan, T. (2002). Observation of lower hybrid drift instability in the diffusion region at a reconnecting magnetopause. *Geophys. Res. Lett.* 29, 33–1–33–4. doi: 10.1029/2002GL016113
- Bernstein, I. B., Greene, J. M., and Kruskal, M. D. (1957). Exact nonlinear plasma oscillations. *Phys. Rev.* 108, 546–550. doi: 10.1103/PhysRev.108.546
- Biskamp, D. (2000). *Magnetic Reconnection in Plasmas (Cambridge Monographs on Plasma Physics)*. Cambridge: Cambridge University Press.
- Burch, J. L., Dokgo, K., Hwang, K. J., Torbert, R. B., Graham, D. B., Webster, J. M., et al. (2019). High-frequency wave generation in magnetotail reconnection: linear dispersion analysis. *Geophys. Res. Lett.* 46, 4089–4097. doi: 10.1029/2019GL082471
- Burch, J. L., Moore, T. E., Torbert, R. B., and Giles, B. L. (2016). Magnetospheric multiscale overview and science objectives. *Space Sci. Rev.* 199, 5–21. doi: 10.1007/s11214-015-0164-9
- Burch, J. L., Webster, J. M., Genestreti, K. J., Torbert, R. B., Giles, B. L., Fuselier, S. A., et al. (2018). Wave phenomena and beam-plasma interactions at the magnetopause reconnection region. *J. Geophys. Res. Space Phys.* 123, 1118–1133. doi: 10.1002/2017JA024789
- Cairns, I. H., Lobzin, V. V., Donea, A., Tingay, S. J., McCauley, P. I., Oberoi, D., et al. (2018). Low altitude solar magnetic reconnection, type III solar radio bursts, and X-ray emissions. *Sci. Rep.* 8:1676. doi: 10.1038/s41598-018-19195-3
- Cairns, I. H., and McMillan, B. F. (2005). Electron acceleration by lower hybrid waves in magnetic reconnection regions. *Phys. Plasmas* 12:102110. doi: 10.1063/1.2080567
- Cao, D., Fu, H. S., Cao, J. B., Wang, T. Y., Graham, D. B., Chen, Z. Z., et al. (2017). MMS observations of whistler waves in electron diffusion region. *Geophys. Res. Lett.* 44, 3954–3962. doi: 10.1002/2017GL072703
- Cao, J. B., Wei, X. H., Duan, A. Y., Fu, H. S., Zhang, T. L., Reme, H., et al. (2013). Slow magnetosonic waves detected in reconnection diffusion region in the Earth's magnetotail. *J. Geophys. Res. Space Phys.* 118, 1659–1666. doi: 10.1002/jgra.50246
- Cattell, C. (2005). Cluster observations of electron holes in association with magnetotail reconnection and comparison to simulations. *J. Geophys. Res.* 110:A01211. doi: 10.1029/2004JA010519
- Cattell, C. A., and Mozer, F. S. (1986). Experimental determination of the dominant wave mode in the active near-Earth magnetotail. *Geophys. Res. Lett.* 13, 221–224. doi: 10.1029/GL013i003p00221
- Chaston, C. C., Bonnell, J. W., Clausen, L., and Angelopoulos, V. (2012). Correction to “Energy transport by kinetic-scale electromagnetic waves in fast plasma sheet flows”. *J. Geophys. Res. Space Phys.* 117:A09202. doi: 10.1029/2012JA018476
- Che, H., Drake, J. F., Swisdak, M., and Yoon, P. H. (2009). Nonlinear development of streaming instabilities in strongly magnetized plasma. *Phys. Rev. Lett.* 102:145004. doi: 10.1103/PhysRevLett.102.145004
- Contel, O. L., Retinò, A., Breuillard, H., Mirioni, L., Robert, P., Chasapis, A., et al. (2016). Whistler mode waves and Hall fields detected by MMS during a dayside magnetopause crossing. *Geophys. Res. Lett.* 43, 5943–5952. doi: 10.1002/2016GL068968
- Dai, L. (2009). Collisionless magnetic reconnection via Alfvén eigenmodes. *Phys. Rev. Lett.* 102:245003. doi: 10.1103/PhysRevLett.102.245003
- Dai, L. (2018). Structures of hall fields in asymmetric magnetic reconnection. *J. Geophys. Res. Space Phys.* 123, 7332–7341. doi: 10.1029/2018JA025251
- Dai, L., Wang, C., Zhang, Y., Lavraud, B., Burch, J., Pollock, C., et al. (2017). Kinetic Alfvén wave explanation of the Hall fields in magnetic reconnection. *Geophys. Res. Lett.* 44:2016GL071044. doi: 10.1002/2016GL071044

- Daughton, W. (2003). Electromagnetic properties of the lower-hybrid drift instability in a thin current sheet. *Phys. Plasmas* 10, 3103–3119. doi: 10.1063/1.1594724
- Davidson, R. C., and Gladd, N. T. (1975). Anomalous transport properties associated with the lower-hybrid-drift instability. *Phys. Fluids* 18, 1327–1335. doi: 10.1063/1.861021
- Deng, X. H., and Matsumoto, H. (2001). Rapid magnetic reconnection in the Earth's magnetosphere mediated by whistler waves. *Nature* 410, 557–560. doi: 10.1038/35069018
- Deng, X. H., Matsumoto, H., Kojima, H., Mukai, T., Anderson, R. R., Baumjohann, W., et al. (2004). Geotail encounter with reconnection diffusion region in the Earth's magnetotail: evidence of multiple X lines collisionless reconnection? *J. Geophys. Res. Space Phys.* 109:A05206. doi: 10.1029/2004JA010632
- Divin, A., Khotyaintsev, Y. V., Vaivads, A., and André, M. (2015a). Lower hybrid drift instability at a dipolarization front. *J. Geophys. Res. Space Phys.* 120, 1124–1132. doi: 10.1002/2014JA020528
- Divin, A., Khotyaintsev, Y. V., Vaivads, A., André, M., Markidis, S., and Lapenta, G. (2015b). Evolution of the lower hybrid drift instability at reconnection jet front. *J. Geophys. Res. Space Phys.* 120, 2675–2690. doi: 10.1002/2014JA020503
- Dokgo, K., Hwang, K.-J., Burch, J. L., Choi, E., Yoon, P. H., Sibeck, D. G., et al. (2019). High-frequency wave generation in magnetotail reconnection: nonlinear harmonics of upper hybrid waves. *Geophys. Res. Lett.* doi: 10.1029/2019GL083361
- Drake, J. F. (2003). Formation of electron holes and particle energization during magnetic reconnection. *Science* 299, 873–877. doi: 10.1126/science.1080333
- Duan, S. P., Dai, L., Wang, C., Liang, J., Lui, A. T. Y., Chen, L. J., et al. (2016). Evidence of kinetic Alfvén eigenmode in the near-Earth magnetotail during substorm expansion phase. *J. Geophys. Res. Space Phys.* 121, 4316–4330. doi: 10.1002/2016JA022431
- Egedal, J., Daughton, W., Le, A., and Borg, A. L. (2015). Double layer electric fields aiding the production of energetic flat-top distributions and superthermal electrons within magnetic reconnection exhausts. *Phys. Plasmas* 22:101208. doi: 10.1063/1.4933055
- Ergun, R. E., Chen, L.-J., Wilder, F. D., Ahmadi, N., Eriksson, S., Usanova, M. E., et al. (2017). Drift waves, intense parallel electric fields, and turbulence associated with asymmetric magnetic reconnection at the magnetopause. *Geophys. Res. Lett.* 44, 2978–2986. doi: 10.1002/2016GL072493
- Ergun, R. E., Holmes, J. C., Goodrich, K. A., Wilder, F. D., Stawarz, J. E., Eriksson, S., et al. (2016). Magnetospheric multiscale observations of large-amplitude, parallel, electrostatic waves associated with magnetic reconnection at the magnetopause: waves associated with reconnection. *Geophys. Res. Lett.* 43, 5626–5634. doi: 10.1002/2016GL068992
- Escoubet, C. P., Fehringer, M., and Goldstein, M. (2001). The cluster mission. *Ann. Geophys.* 19, 1197–1200. doi: 10.5194/angeo-19-1197-2001
- Farrell, W. M., Desch, M. D., Kaiser, M. L., and Goetz, K. (2002). The dominance of electron plasma waves near a reconnection X-line region. *Geophys. Res. Lett.* 29, 8–1–8–4. doi: 10.1029/2002GL014662
- Farrell, W. M., Desch, M. D., Ogilvie, K. W., Kaiser, M. L., and Goetz, K. (2003). The role of upper hybrid waves in magnetic reconnection. *Geophys. Res. Lett.* 30:2259. doi: 10.1029/2003GL017549
- Fox, W., Porkolab, M., Egedal, J., Katz, N., and Le, A. (2012). Observations of electron phase-space holes driven during magnetic reconnection in a laboratory plasma. *Phys. Plasmas* 19:032118. doi: 10.1063/1.3692224
- Franz, J. R., Kintner, P. M., Pickett, J. S., and Chen, L.-J. (2005). Properties of small-amplitude electron phase-space holes observed by Polar. *J. Geophys. Res. Space Phys.* 110:A09212. doi: 10.1029/2005JA011095
- Fu, H. S., Khotyaintsev, Y. V., André, M., and Vaivads, A. (2011). Fermi and betatron acceleration of suprathermal electrons behind dipolarization fronts. *Geophys. Res. Lett.* 38:L16104. doi: 10.1029/2011GL048528
- Fu, H. S., Khotyaintsev, Y. V., Vaivads, A., Retinò, A., and André, M. (2013). Energetic electron acceleration by unsteady magnetic reconnection. *Nat. Phys.* 9, 426–430. doi: 10.1038/nphys2664
- Fu, H. S., Peng, F. Z., Liu, C. M., Burch, J. L., Gershman, D. G., and Le Contel, O. (2019). Evidence of electron acceleration at a reconnecting magnetopause. *Geophys. Res. Lett.* 46, 5645–5652. doi: 10.1029/2019GL083032
- Fu, H. S., Vaivads, A., Khotyaintsev, Y. V., André, M., Cao, J. B., Olshevsky, V., et al. (2017). Intermittent energy dissipation by turbulent reconnection. *Geophys. Res. Lett.* 44, 37–43. doi: 10.1002/2016GL071787
- Fu, H. S., Vaivads, A., Khotyaintsev, Y. V., Olshevsky, V., André, M., Cao, J. B., et al. (2015). How to find magnetic nulls and reconstruct field topology with MMS data? *J. Geophys. Res. Space Phys.* 120, 3758–3782. doi: 10.1002/2015JA021082
- Fujimoto, K. (2014). Wave activities in separatrix regions of magnetic reconnection. *Geophys. Res. Lett.* 41, 2721–2728. doi: 10.1002/2014GL059893
- Fujimoto, K. (2017). Bursty emission of whistler waves in association with plasmoid collision. *Ann. Geophys.* 35, 885–892. doi: 10.5194/angeo-35-885-2017
- Fujimoto, K., and Sydora, R. D. (2008). Whistler waves associated with magnetic reconnection. *Geophys. Res. Lett.* 35:L19112. doi: 10.1029/2008GL035201
- Fujimoto, M., Shinohara, I., and Kojima, H. (2011). Reconnection and waves: a review with a perspective. *Space Sci. Rev.* 160, 123–143. doi: 10.1007/s11214-011-9807-7
- Gershman, D. J., F-Viñas, A., Dorelli, J. C., Boardsen, S. A., Avanov, L. A., Bellan, P. M., et al. (2017). Wave-particle energy exchange directly observed in a kinetic Alfvén-branch wave. *Nat. Commun.* 8:14719. doi: 10.1038/ncomms14719
- Goldman, M., Newman, D., Lapenta, G., Andersson, L., Gosling, J., Eriksson, S., et al. (2014). Čerenkov emission of quasiparallel whistlers by fast electron phase-space holes during magnetic reconnection. *Phys. Rev. Lett.* 112:145002. doi: 10.1103/PhysRevLett.112.145002
- Graham, D., Khotyaintsev, Y., Vaivads, A., Norgren, C., André, M., Webster, J., et al. (2017a). Instability of agyrotropic electron beams near the electron diffusion region. *Phys. Rev. Lett.* 119:025101. doi: 10.1103/PhysRevLett.119.025101
- Graham, D. B., Khotyaintsev, Y. V., Norgren, C., Vaivads, A., Andre, M., Drake, J. F., et al. (2019). Universality of lower hybrid waves at Earth's magnetopause. *JGR Space Phys.* doi: 10.1029/2019JA027155. [Epub ahead of print].
- Graham, D. B., Khotyaintsev, Y. V., Norgren, C., Vaivads, A., André, M., Lindqvist, P.-A., et al. (2016a). Electron currents and heating in the ion diffusion region of asymmetric reconnection. *Geophys. Res. Lett.* 43, 4691–4700. doi: 10.1002/2016GL068613
- Graham, D. B., Khotyaintsev, Y. V., Norgren, C., Vaivads, A., André, M., Toledo-Redondo, S., et al. (2017b). Lower hybrid waves in the ion diffusion and magnetosospheric inflow regions. *J. Geophys. Res. Space Phys.* 122, 517–533. doi: 10.1002/2016JA023572
- Graham, D. B., Khotyaintsev, Y. V., Vaivads, A., and André, M. (2015). Electrostatic solitary waves with distinct speeds associated with asymmetric reconnection. *Geophys. Res. Lett.* 42, 215–224. doi: 10.1002/2014GL062538
- Graham, D. B., Khotyaintsev, Y. V., Vaivads, A., and André, M. (2016b). Electrostatic solitary waves and electrostatic waves at the magnetopause. *J. Geophys. Res. Space Phys.* 121, 3069–3092. doi: 10.1002/2015JA021527
- Graham, D. B., Vaivads, A., Khotyaintsev, Y. V., and André, M. (2016c). Whistler emission in the separatrix regions of asymmetric magnetic reconnection. *J. Geophys. Res. Space Phys.* 121, 1934–1954. doi: 10.1002/2015JA021239
- Graham, D. B., Vaivads, A., Khotyaintsev, Y. V., André, M., Le Contel, O., Malaspina, D. M., et al. (2018). Large-amplitude high-frequency waves at earth's magnetopause. *J. Geophys. Res. Space Phys.* 123, 2630–2657. doi: 10.1002/2017JA025034
- Greco, A., Artemyev, A., Zimbardo, G., Angelopoulos, V., and Runov, A. (2017). Role of lower hybrid waves in ion heating at dipolarization fronts. *J. Geophys. Res. Space Phys.* 122, 5092–5104. doi: 10.1002/2017JA023926
- Hesse, M., Norgren, C., Tenfjord, P., Burch, J. L., Liu, Y.-H., Chen, L.-J., et al. (2018). On the role of separatrix instabilities in heating the reconnection outflow region. *Phys. Plasmas* 25:122902. doi: 10.1063/1.5054100
- Hietala, H., Drake, J. F., Phan, T. D., Eastwood, J. P., and McFadden, J. P. (2015). Ion temperature anisotropy across a magnetotail reconnection jet. *Geophys. Res. Lett.* 42, 7239–7247. doi: 10.1002/2015GL065168
- Holmes, J. C., Ergun, R. E., Newman, D. L., Ahmadi, N., Andersson, L., Contel, O. L., et al. (2018). Electron phase-space holes in three dimensions: multispacecraft observations by magnetospheric multiscale. *J. Geophys. Res. Space Phys.* 123, 9963–9978. doi: 10.1029/2018JA025750
- Huang, H., Yu, Y., Dai, L., and Wang, T. (2018). Kinetic alfvén waves excited in two-dimensional magnetic reconnection. *J. Geophys. Res. Space Phys.* 123, 6655–6669. doi: 10.1029/2017JA025071
- Huang, S. Y., Fu, H. S., Yuan, Z. G., Vaivads, A., Khotyaintsev, Y. V., Retino, A., et al. (2016). Two types of whistler waves in the hall reconnection region. *J. Geophys. Res. Space Phys.* 121, 6639–6646. doi: 10.1002/2016JA022650

- Huang, S. Y., Yuan, Z. G., Sahraoui, F., Fu, H. S., Pang, Y., Zhou, M., et al. (2017). Occurrence rate of whistler waves in the magnetotail reconnection region. *J. Geophys. Res. Space Phys.* 122, 7188–7196. doi: 10.1002/2016JA023670
- Huang, S. Y., Zhou, M., Sahraoui, F., Vaivads, A., Deng, X. H., André, M., et al. (2012). Observations of turbulence within reconnection jet in the presence of guide field. *Geophys. Res. Lett.* 39:L11104. doi: 10.1029/2012GL052210
- Ji, H., Terry, S., Yamada, M., Kulsrud, R., Kuritsyn, A., and Ren, Y. (2004). Electromagnetic fluctuations during fast reconnection in a laboratory plasma. *Phys. Rev. Lett.* 92:115001. doi: 10.1103/PhysRevLett.92.115001
- Jiansen, H., Xingyu, Z., Yajie, C., Chadi, S., Michael, S., Hui, L., et al. (2018). Plasma heating and alfvénic turbulence enhancement during two steps of energy conversion in magnetic reconnection exhaust region of solar wind. *Astrophys. J.* 856:148. doi: 10.3847/1538-4357/aab3cd
- Khotyaintsev, Y., Vaivads, A., Ogawa, Y., Popielawska, B., André, M., Buchert, S., et al. (2004). Cluster observations of high-frequency waves in the exterior cusp. *Ann. Geophys.* 22, 2403–2411. doi: 10.5194/angeo-22-2403-2004
- Khotyaintsev, Y. V., Cully, C. M., Vaivads, A., André, M., and Owen, C. J. (2011). Plasma jet braking: energy dissipation and nonadiabatic electrons. *Phys. Rev. Lett.* 106:165001. doi: 10.1103/PhysRevLett.106.165001
- Khotyaintsev, Y. V., Graham, D. B., Norgren, C., Eriksson, E., Li, W., Johlander, A., et al. (2016). Electron jet of asymmetric reconnection. *Geophys. Res. Lett.* 43, 5571–5580. doi: 10.1002/2016GL069064
- Khotyaintsev, Y. V., Graham, D. B., Steinvall, K., Alm, L., Vaivads, A., Johlander, A., et al. (2019). Electron heating by debye-scale turbulence in guide-field reconnection. *arXiv:* 1908.09724.
- Khotyaintsev, Y. V., Vaivads, A., André, M., Fujimoto, M., Retinò, A., and Owen, C. J. (2010). Observations of slow electron holes at a magnetic reconnection site. *Phys. Rev. Lett.* 105:165002. doi: 10.1103/PhysRevLett.105.165002
- Khotyaintsev, Y. V., Vaivads, A., Retinò, A., André, M., Owen, C. J., and Nilsson, H. (2006). Formation of inner structure of a reconnection separatrix region. *Phys. Rev. Lett.* 97:205003. doi: 10.1103/PhysRevLett.97.205003
- Lazarian, A., Eynink, G., Vishniac, E., and Kowal, G. (2015). Turbulent reconnection and its implications. *Philos. Trans. Ser. A Math. Phys. Eng. Sci.* 373:2041. doi: 10.1098/rsta.2014.0144
- Le Contel, O., Nakamura, R., Breuillard, H., Argall, M. R., Graham, D. B., Fischer, D., et al. (2017). Lower hybrid drift waves and electromagnetic electron space-phase holes associated with dipolarization fronts and field-aligned currents observed by the magnetospheric multiscale mission during a substorm. *J. Geophys. Res. Space Phys.* 122, 12236–12257. doi: 10.1002/2017JA024550
- Le Contel, O., Roux, A., Jacquay, C., Robert, P., Berthomier, M., Chust, T., et al. (2009). Quasi-parallel whistler mode waves observed by THEMIS during near-earth dipolarizations. *Ann. Geophys.* 27, 2259–2275. doi: 10.5194/angeo-27-2259-2009
- Le, A., Daughton, W., Chen, L.-J., and Egedal, J. (2017). Enhanced electron mixing and heating in 3-D asymmetric reconnection at the Earth's magnetopause. *Geophys. Res. Lett.* 44, 2096–2104. doi: 10.1002/2017GL072522
- Le, A., Daughton, W., Ohia, O., Chen, L.-J., Liu, Y.-H., Wang, S., et al. (2018). Drift turbulence, particle transport, and anomalous dissipation at the reconnecting magnetopause. *Phys. Plasmas* 25:062103. doi: 10.1063/1.5027086
- Liang, J., Lin, Y., Johnson, J. R., Wang, X., and Wang, Z.-X. (2016). Kinetic Alfvén waves in three-dimensional magnetic reconnection. *J. Geophys. Res. Space Phys.* 121, 6526–6548. doi: 10.1002/2016JA022505
- Liang, J., Lin, Y., Johnson, J. R., Wang, Z.-X., and Wang, X. (2017). Ion acceleration and heating by kinetic Alfvén waves associated with magnetic reconnection. *Phys. Plasmas* 24:102110. doi: 10.1063/1.4991978
- Lindstedt, T., Khotyaintsev, Y. V., Vaivads, A., André, M., Fear, R. C., Lavraud, B., et al. (2009). Separatrix regions of magnetic reconnection at the magnetopause. *Ann. Geophys.* 27, 4039–4056. doi: 10.5194/angeo-27-4039-2009
- Liu, Y. Y., Fu, H. S., Olshevsky, V., Pontin, D. I., Liu, C. M., Wang, Z., et al. (2019). SOTE: a nonlinear method for magnetic topology reconstruction in space plasmas. *Astrophys. J. Suppl. Ser.* 244:31. doi: 10.3847/1538-4365/ab391a
- Mandt, M. E., Denton, R. E., and Drake, J. F. (1994). Transition to whistler mediated magnetic reconnection. *Geophys. Res. Lett.* 21, 73–76. doi: 10.1029/93GL03382
- Melrose, D. B. (2017). Coherent emission mechanisms in astrophysical plasmas. *Rev. Mod. Plasma Phys.* 1. doi: 10.1007/s41614-017-0007-0
- Mozer, F., Agapitov, O., Artemev, A., Burch, J., Ergun, R., Giles, B., et al. (2016). Magnetospheric multiscale satellite observations of parallel electron acceleration in magnetic field reconnection by fermi reflection from time domain structures. *Phys. Rev. Lett.* 116:145101. doi: 10.1103/PhysRevLett.116.145101
- Mozer, F., Agapitov, O., Giles, B., and Vasko, I. (2018). Direct observation of electron distributions inside millisecond duration electron holes. *Phys. Rev. Lett.* 121:135102. doi: 10.1103/PhysRevLett.121.135102
- Mozer, F. S., Wilber, M., and Drake, J. F. (2011). Wave associated anomalous drag during magnetic field reconnection. *Phys. Plasmas* 18:102902. doi: 10.1063/1.3647508
- Muñoz, P. A. and Büchner, J. (2016). Non-Maxwellian electron distribution functions due to self-generated turbulence in collisionless guide-field reconnection. *Phys. Plasmas* 23:102103. doi: 10.1063/1.4963773
- Norgren, C., André, M., Graham, D. B., Khotyaintsev, Y. V., and Vaivads, A. (2015). Slow electron holes in multicomponent plasmas. *Geophys. Res. Lett.* 42, 7264–7272. doi: 10.1002/2015GL065390
- Norgren, C., Hesse, M., Tenfjord, P., Graham, D. B., Khotyaintsev, Y. V., Vaivads, A., et al. (2019). Electron acceleration and thermalization at magnetotail separatrices. *arXiv:* 1908.11138.
- Norgren, C., Vaivads, A., Khotyaintsev, Y. V., and André, M. (2012). Lower hybrid drift waves: space observations. *Phys. Rev. Lett.* 109:055001. doi: 10.1103/PhysRevLett.109.055001
- Omura, Y., Matsumoto, H., Miyake, T., and Kojima, H. (1996). Electron beam instabilities as generation mechanism of electrostatic solitary waves in the magnetotail. *J. Geophys. Res. Space Phys.* 101, 2685–2697. doi: 10.1029/95JA03145
- Osman, K. T., Kiyani, K. H., Matthaeus, W. H., Hnat, B., Chapman, S. C., and Khotyaintsev, Y. V. (2015). Multi-spacecraft measurement of turbulence within a magnetic reconnection jet. *Astrophys. J.* 815:L24. doi: 10.1088/2041-8205/815/2/L24
- Pan, D.-X., Khotyaintsev, Y. V., Graham, D. B., Vaivads, A., Zhou, X.-Z., André, M., et al. (2018). Rippled electron-scale structure of a dipolarization front. *Geophys. Res. Lett.* 45, 12116–12124. doi: 10.1029/2018GL080826
- Price, L., Swisdak, M., Drake, J. F., Burch, J. L., Cassak, P. A., and Ergun, R. E. (2017). Turbulence in three-dimensional simulations of magnetopause reconnection. *J. Geophys. Res. Space Phys.* 122, 11086–11099. doi: 10.1002/2017JA024227
- Price, L., Swisdak, M., Drake, J. F., Cassak, P. A., Dahlin, J. T., and Ergun, R. E. (2016). The effects of turbulence on three-dimensional magnetic reconnection at the magnetopause. *Geophys. Res. Lett.* 43, 6020–6027. doi: 10.1002/2016GL069578
- Pritchett, P. L., and Coroniti, F. V. (2010). A kinetic ballooning/interchange instability in the magnetotail. *J. Geophys. Res. Space Phys.* 115:A06301. doi: 10.1029/2009JA014752
- Ren, Y., Dai, L., Li, W., Tao, X., Wang, C., Tang, B., et al. (2019). Whistler waves driven by field-aligned streaming electrons in the near-Earth magnetotail reconnection. *Geophys. Res. Lett.* 46, 5045–5054. doi: 10.1029/2019GL083283
- Retinò, A., Vaivads, A., André, M., Sahraoui, F., Khotyaintsev, Y., Pickett, J. S., et al. (2006). Structure of the separatrix region close to a magnetic reconnection X-line: cluster observations. *Geophys. Res. Lett.* 33:L06101. doi: 10.1029/2005GL024650
- Rogers, B. N., Denton, R. E., Drake, J. F., and Shay, M. A. (2001). Role of dispersive waves in collisionless magnetic reconnection. *Phys. Rev. Lett.* 87:195004. doi: 10.1103/PhysRevLett.87.195004
- Sharma Pyakurel, P., Shay, M. A., Haggerty, C. C., Parashar, T. N., Drake, J. F., Cassak, P. A., et al. (2018). Super-Alfvénic propagation and damping of reconnection onset signatures. *J. Geophys. Res. Space Phys.* 123, 341–349. doi: 10.1002/2017JA024606
- Shay, M. A., Drake, J. F., Eastwood, J. P., and Phan, T. D. (2011). Super-Alfvénic propagation of substorm reconnection signatures and poynting flux. *Phys. Rev. Lett.* 107:065001. doi: 10.1103/PhysRevLett.107.065001
- Silin, I., Büchner, J., and Vaivads, A. (2005). Anomalous resistivity due to nonlinear lower-hybrid drift waves. *Phys. Plasmas* 12:062902. doi: 10.1063/1.1927096
- Sitnov, M., Birn, J., Ferdousi, B., Gordeev, E., Khotyaintsev, Y., Merkin, V., et al. (2019). Explosive magnetotail activity. *Space Sci. Rev.* 215:31. doi: 10.1007/s11214-019-0599-5

- Stawarz, J. E., Eastwood, J. P., Varsani, A., Ergun, R. E., Shay, M. A., Nakamura, R., et al. (2017). Magnetospheric multiscale analysis of intense field-aligned Poynting flux near the Earth's plasma sheet boundary. *Geophys. Res. Lett.* 44, 7106–7113. doi: 10.1002/2017GL073685
- Steinvall, K., Khotyaintsev, Y. V., Graham, D. B., Vaivads, A., Contel, O. L., and Russell, C. T. (2019a). Observations of electromagnetic electron holes and evidence of cherenkov whistler emission. *arXiv: 1908.11198*.
- Steinvall, K., Khotyaintsev, Y. V., Graham, D. B., Vaivads, A., Lindqvist, P.-A., Russell, C. T., et al. (2019b). Multispacecraft analysis of electron holes. *Geophys. Res. Lett.* 46, 55–63. doi: 10.1029/2018GL080757
- Stenberg, G., Oscarsson, T., André, M., Vaivads, A., Morooka, M., Cornilleau-Wehrlin, N., et al. (2005). Electron-scale sheets of whistlers close to the magnetopause. *Ann. Geophys.* 23, 3715–3725. doi: 10.5194/angeo-23-3715-2005
- Tang, B.-B., Li, W. Y., Graham, D. B., Rager, A. C., Wang, C., Khotyaintsev, Y. V., et al. (2019). Crescent-shaped electron distributions at the nonreconnecting magnetopause: magnetospheric multiscale observations. *Geophys. Res. Lett.* 46, 3024–3032. doi: 10.1029/2019GL082231
- Tang, X., Cattell, C., Dombeck, J., Dai, L., Wilson, L. B., Breneman, A., et al. (2013). THEMIS observations of the magnetopause electron diffusion region: large amplitude waves and heated electrons. *Geophys. Res. Lett.* 40, 2884–2890. doi: 10.1002/grl.50565
- Taubenschuss, U., Khotyaintsev, Y. V., Santolík, O., Vaivads, A., Cully, C. M., Contel, O. L., et al. (2014). Wave normal angles of whistler mode chorus rising and falling tones. *J. Geophys. Res. Space Phys.* 119, 9567–9578. doi: 10.1002/2014JA020575
- Tong, Y., Vasko, I., Mozer, F. S., Bale, S. D., Roth, I., Artemyev, A. V., et al. (2018). Simultaneous multispacecraft probing of electron phase space holes. *Geophys. Res. Lett.* 45, 11513–11519. doi: 10.1029/2018GL079044
- Torbert, R. B., Dors, I., Argall, M. R., Genestreti, K. J., Burch, J. L., Farrugia, C. J., et al. (2019). A new method of 3d magnetic field reconstruction. *arXiv: 1909.11255*.
- Treumann, R. A., LaBelle, J., and Pottelette, R. (1991). Plasma diffusion at the magnetopause: the case of lower hybrid drift waves. *J. Geophys. Res. Space Phys.* 96, 16009–16013. doi: 10.1029/91JA01671
- Uchino, H., Kurita, S., Harada, Y., Machida, S., and Angelopoulos, V. (2017). Waves in the innermost open boundary layer formed by dayside magnetopause reconnection. *J. Geophys. Res. Space Phys.* 122, 3291–3307. doi: 10.1002/2016JA023300
- Vaivads, A. (2004). Cluster observations of lower hybrid turbulence within thin layers at the magnetopause. *Geophys. Res. Lett.* 31:L03804. doi: 10.1029/2003GL018142
- Vaivads, A., Khotyaintsev, Y., André, M., Retinò, A., Buchert, S., Rogers, B., et al. (2004). Structure of the magnetic reconnection diffusion region from four-spacecraft observations. *Phys. Rev. Lett.* 93:105001. doi: 10.1103/PhysRevLett.93.105001
- Vaivads, A., Khotyaintsev, Y., André, M., and Treumann, R. (2006). "Plasma waves near reconnection sites," in *Geospace Electromagnetic Waves and Radiation*, Lecture Notes in Physics, eds J. W. LaBelle and R. A. Treumann (Berlin; Heidelberg: Springer), 251–269.
- Vaivads, A., Retinò, A., Khotyaintsev, Y. V., and André, M. (2010). The Alfvén edge in asymmetric reconnection. *Ann. Geophys.* 28, 1327–1331. doi: 10.5194/angeo-28-1327-2010
- Vaivads, A., Santolík, O., Stenberg, G., André, M., Owen, C. J., Canu, P., et al. (2007). Source of whistler emissions at the dayside magnetopause. *Geophys. Res. Lett.* 34:L09106. doi: 10.1029/2006GL029195
- Vapirev, A., Lapenta, G., Divin, A., Markidis, S., Henri, P., Goldman, M., et al. (2018). Formation of a transient front structure near reconnection point in 3-D PIC simulations. *J. Geophys. Res. Space Phys.* 118, 1435–1449. doi: 10.1002/jgra.50136
- Vasko, I. Y., Agapitov, O. V., Mozer, F. S., Artemyev, A. V., Krasnoselskikh, V. V., and Bonnell, J. W. (2017). Diffusive scattering of electrons by electron holes around injection fronts. *J. Geophys. Res. Space Phys.* 122, 3163–3182. doi: 10.1002/2016JA023337
- Viberg, H., Khotyaintsev, Y. V., Vaivads, A., André, M., Fu, H. S., and Cornilleau-Wehrlin, N. (2014). Whistler mode waves at magnetotail dipolarization fronts. *J. Geophys. Res. Space Phys.* 119, 2605–2611. doi: 10.1002/2014JA019892
- Viberg, H., Khotyaintsev, Y. V., Vaivads, A., André, M., and Pickett, J. S. (2013). Mapping HF waves in the reconnection diffusion region. *Geophys. Res. Lett.* 40, 1032–1037. doi: 10.1002/grl.50227
- Vörös, Z. (2011). Magnetic reconnection associated fluctuations in the deep magnetotail: ARTEMIS results. *Nonlin. Process. Geophys.* 18, 861–869. doi: 10.5194/npg-18-861-2011
- Wang, C.-P., Xing, X., Liu, Y.-H., and Runov, A. (2018). A case study of connection between ground magnetic field perturbations and tail current sheet bursty flows at $X = -60$ RE. *J. Geophys. Res. Space Phys.* 123, 1822–1833. doi: 10.1002/2017JA024972
- Wang, S., Chen, L.-J., Hesse, M., Wilson, L. B., Bessho, N., Gershman, D. J., et al. (2017). Parallel electron heating in the magnetospheric inflow region. *Geophys. Res. Lett.* 44, 4384–4392. doi: 10.1002/2017GL073404
- Wei, X. H., Cao, J. B., Zhou, G. C., Santolík, O., Rème, H., Dandouras, I., et al. (2007). Cluster observations of waves in the whistler frequency range associated with magnetic reconnection in the Earth's magnetotail. *J. Geophys. Res. Space Phys.* 112:A10225. doi: 10.1029/2006JA011771
- Wilder, F. D., Ergun, R. E., Goodrich, K. A., Goldman, M. V., Newman, D. L., Malaspina, D. M., et al. (2016). Observations of whistler mode waves with nonlinear parallel electric fields near the dayside magnetic reconnection separatrix by the Magnetospheric Multiscale mission. *Geophys. Res. Lett.* 43, 5909–5917. doi: 10.1002/2016GL069473
- Wilder, F. D., Ergun, R. E., Newman, D. L., Goodrich, K. A., Trattner, K. J., Goldman, M. V., et al. (2017). The nonlinear behavior of whistler waves at the reconnecting dayside magnetopause as observed by the Magnetospheric Multiscale mission: a case study. *J. Geophys. Res. Space Phys.* 122, 5487–5501. doi: 10.1002/2017JA024062
- Yamada, M., Kulsrud, R., and Ji, H. (2010). Magnetic reconnection. *Rev. Mod. Phys.* 82, 603–664. doi: 10.1103/RevModPhys.82.603
- Yoon, P. H., Lui, A. T. Y., and Sitnov, M. I. (2002). Generalized lower-hybrid drift instabilities in current-sheet equilibrium. *Phys. Plasmas* 9, 1526–1538. doi: 10.1063/1.1466822
- Zhang, Y. C., Lavraud, B., Dai, L., Wang, C., Marchaudon, A., Avanov, L., et al. (2017). Quantitative analysis of a Hall system in the exhaust of asymmetric magnetic reconnection. *J. Geophys. Res. Space Phys.* 122, 5277–5289. doi: 10.1002/2016JA023620
- Zhou, M., Ashour-Abdalla, M., Berchem, J., Walker, R. J., Liang, H., El-Alaoui, M., et al. (2016). Observation of high-frequency electrostatic waves in the vicinity of the reconnection ion diffusion region by the spacecraft of the Magnetospheric Multiscale (MMS) mission. *Geophys. Res. Lett.* 43, 4808–4815. doi: 10.1002/2016GL069010
- Zhou, M., Ashour-Abdalla, M., Deng, X., Schriver, D., El-Alaoui, M., and Pang, Y. (2009a). THEMIS observation of multiple dipolarization fronts and associated wave characteristics in the near-Earth magnetotail. *Geophys. Res. Lett.* 36:L20107. doi: 10.1029/2009GL040663
- Zhou, M., Berchem, J., Walker, R. J., El-Alaoui, M., Goldstein, M. L., Lapenta, G., et al. (2018). Magnetospheric multiscale observations of an ion diffusion region with large guide field at the magnetopause: current system, electron heating, and plasma waves. *J. Geophys. Res. Space Phys.* 123, 1834–1852. doi: 10.1002/2017JA024517
- Zhou, M., Deng, X. H., Li, S. Y., Pang, Y., Vaivads, A., Rème, H., et al. (2009b). Observation of waves near lower hybrid frequency in the reconnection region with thin current sheet. *J. Geophys. Res. Space Phys.* 114:A02216. doi: 10.1029/2008JA013427

Conflict of Interest: The authors declare that the research was conducted in the absence of any commercial or financial relationships that could be construed as a potential conflict of interest.

Copyright © 2019 Khotyaintsev, Graham, Norgren and Vaivads. This is an open-access article distributed under the terms of the Creative Commons Attribution License (CC BY). The use, distribution or reproduction in other forums is permitted, provided the original author(s) and the copyright owner(s) are credited and that the original publication in this journal is cited, in accordance with accepted academic practice. No use, distribution or reproduction is permitted which does not comply with these terms.



Anisotropy of the Spectral Index in Ion Scale Compressible Turbulence: MMS Observations in the Magnetosheath

Owen Wyn Roberts^{1*}, Yasuhito Narita¹, Rumi Nakamura¹, Zoltán Vörös¹ and Daniel Gershman²

¹ Space Research Institute, Austrian Academy of Sciences, Graz, Austria, ² NASA Goddard Space Flight Center, Greenbelt, MD, United States

OPEN ACCESS

Edited by:

Antonella Greco,
University of Calabria, Italy

Reviewed by:

Roberto Bruno,
Institute for Space Astrophysics and
Planetology (INAF), Italy

Hui Li,
National Space Science Center (CAS),
China

Jiansen He,
Peking University, China

*Correspondence:

Owen Wyn Roberts
owen.roberts@oeaw.ac.at

Specialty section:

This article was submitted to
Space Physics,
a section of the journal
Frontiers in Physics

Received: 31 May 2019

Accepted: 29 October 2019

Published: 20 November 2019

Citation:

Roberts OW, Narita Y, Nakamura R, Vörös Z and Gershman D (2019) Anisotropy of the Spectral Index in Ion Scale Compressible Turbulence: MMS Observations in the Magnetosheath. *Front. Phys.* 7:184.
doi: 10.3389/fphy.2019.00184

Turbulence in the Earth's magnetosheath at ion kinetic scales is investigated with the Magnetospheric MultiScale (MMS) spacecraft. The multi-point measurements allow the three dimensional power spectra in wave-vector space to be determined. Previously the three dimensional structure of fluctuations in the magnetic field and density (using spacecraft potential as a proxy) were possible with Cluster. However, using the excellent time resolution data set provided from both the Fluxgate Magnetometer (FGM) and the Fast Plasma Investigation (FPI) on MMS the spectra can be determined for a number of different parameters such as ion velocity, and ion temperatures parallel and perpendicular to the mean magnetic field directions. The spectra for different fluctuations show similar features to one another such as a strong power anisotropy with respect to the mean magnetic field direction, such that the energy decays faster in the direction parallel to the mean magnetic field than the perpendicular direction. A weak non-gyrotropy is also seen in the direction of the bulk velocity similar to what has been seen in magnetic field fluctuations with Cluster at ion kinetic scales in the solar wind. Velocity fluctuations are shown to be the most anisotropic. The density and temperature fluctuations exhibit similar anisotropies but are much weaker in comparison.

Keywords: magnetosheath, turbulence, plasma, dissipation, kinetic plasma

1. INTRODUCTION

Turbulence is a phenomenon characterized by disordered fluctuations in several of the fluid's parameters over a large range of time and length scales. For a neutral fluid this might include density, velocity, and temperature, however in a space plasma there are also fluctuations in electromagnetic fields due to a very high conductivity [1, 2]. Typically most of the research on the topic of *in situ* plasma turbulence have been performed using magnetic field data as the data are often operationally simpler to obtain with high time resolution. To obtain a more complete understanding of the turbulent fluctuations, measurements are required for parameters other than the electromagnetic fields. While density can be obtained from spacecraft potential (e.g., [3–5]), other plasma measurements such as velocity and temperature require a direct plasma measurement. Typically plasma instruments are mounted looking in one direction on a spinning spacecraft and use the spin to obtain data azimuthally. Thus, the time resolution is limited to the spacecraft spin, which is typically not fast enough to resolve ion kinetic scales.

In a plasma the presence of a magnetic field gives rise to a variety of different anisotropies [6–8], such as in the power $P_{\perp} \gg P_{\parallel}$ [9–12], wave-vectors $k_{\perp} \gg k_{\parallel}$ [5, 13–15], spectral indices $\alpha_{\perp} > \alpha_{\parallel}$ [9, 16–18] here parallel and perpendicular refer to the direction with respect to the mean magnetic field direction. In the solar wind, expansion effects also exist which can result in a second preferred direction [19, 20], this can result in a non-gyrotropic power distributions with different powers in different perpendicular directions which have been observed experimentally [13, 17, 20–23].

The majority of plasma turbulence studies have employed single spacecraft measurements, where spatial information is obtained by assuming Taylor's hypothesis [24], where the turbulent fluctuation is assumed to vary slowly with respect to the measurement time. By analyzing intervals with different orientations of the magnetic field with respect to the bulk flow direction, the three dimensional structure is inferred. Using this approach single spacecraft observations have revealed correlations between solar wind measurements in the directions perpendicular to the magnetic field are longer than in the parallel direction [25] giving a “Maltese Cross” pattern showing the dominance of perpendicular wave-vectors. Furthermore, when the data are classified as fast (typically above 500 km/s) the opposite is true [26] with parallel wave-vectors dominating. This same pattern has been observed in variables other than magnetic field by Smith et al. [27], where velocity, temperature, and density show similar correlations as the magnetic field. Recently Wang et al. [28], used the self correlation technique and revealed with intervals to reveal similar anisotropies to Dasso et al. [26] for intervals of length 1–2 days, but become more isotropic as the intervals become smaller i.e., when looking at smaller scales in the inertial range.

The power of magnetic fluctuations in the solar wind at large inertial scales [where a magnetohydrodynamic (MHD) description is valid] have been found to be generally smaller along the magnetic field direction with respect to the perpendicular direction and the spectrum in this direction is steeper with a spectral index of -2 [9, 29] compared with an index of $-5/3$ in the perpendicular direction. Structure function analysis has also been performed on magnetic field data revealing anisotropic power that also evolves toward smaller scales [22], and that fluctuations in the magnitude of the magnetic field (a proxy for the compressible fluctuations) are more anisotropic than the trace fluctuations in the fast solar wind.

At smaller scales often plasma data are usually not available as the instruments lack the necessary time resolution. This limitation allows the study of plasma fluctuations only in the low frequency inertial range where a fluid description is still valid. At higher spacecraft frame frequencies (denoted by subscript sc) above around $f_{sc} \gtrsim 1$ Hz the fluctuations become comparable to proton gyration frequencies. Above these frequencies the protons cannot follow the magnetic field any longer and become demagnetized, while electrons remain magnetized and can still follow the magnetic field due to their smaller gyroradius. This region is often marked by a break in the power spectral density and a steepening of the spectrum [5, 30–35]. The location of the break has been measured to be fairly independent of plasma β

[33, 34] and varies with heliocentric distance [32]. Both of these observations can be explained by the break corresponding to the scale of the ion cyclotron resonance. Additionally the location of the break has been observed by single spacecraft observations to be independent of the angle between the magnetic field and the bulk velocity [35]. This was interpreted by Duan et al. [35] due to the ion diffusion region (where ions decouple from electrons) being approximately isotropic in wave-vector space. The scales smaller than the spectral break is often termed the dissipation/dispersion range, or the ion kinetic range, and a fluid description is no longer valid.

In some conditions Taylor's hypothesis may break down, should turbulent fluctuations become very dispersive, when bulk speeds are low, or different modes appear at once in the plasma [36–38]. The magnetosheath is an especially interesting plasma as it typically has a higher magnetic field strength, a lower bulk velocity, and has a much larger compressibility than the solar wind. The lower speed and larger fluctuation amplitudes make the breakdown of Taylor's hypothesis in this region more likely when juxtaposed with the super Alfvénic solar wind. To overcome the limitations imposed by Taylor's hypothesis two other approaches to understand the structure of turbulence are possible which are through either multi-point measurements, or from direct numerical simulation.

Different numerical simulation schemes have been used to investigate the structure of turbulence, however recently an expanding box MHD approach can also include expansion effects present in the solar wind allowing the large scale three dimensional structure to be simulated [19, 39]. The other approach is to use multi-point measurements, which are possible with Cluster and MMS. These techniques rely on differences or correlations between spacecraft pairs e.g., multi spacecraft structure functions/cross correlations [40–42] where gyrotropy is assumed. These techniques have also revealed anisotropic power and spectral indices parallel and perpendicular to the mean field direction. Another approach is to use multi-point signal resonator technique [13] which assumes a plane wave geometry of the fluctuations and make use of the phase delay between measurement points [5, 13, 43] but does not make an assumption of gyrotropy. However, these studies performed with Cluster have mostly been performed using magnetic field data, or spacecraft potential [5, 18]. This study will expand on the previous work done by Cluster in the inertial and kinetic ranges, and use the Magnetospheric MultiScale mission [44] and its exceptionally high time resolution plasma data from the Fast Plasma Investigation [45] (FPI) instrument to characterize the structure of turbulent fluctuations in the transition from fluid to kinetic scales in the Earth's magnetosheath.

2. DATA/METHODOLOGY

We use data from the MMS spacecraft [44] during an interval of burst mode which occurred on the 7th of September 2015 13:59:50.000–14:04:57.200UT early in the mission where the spacecraft have separations of the order of 140 km before the spacecraft achieved their close separations for their primary goal

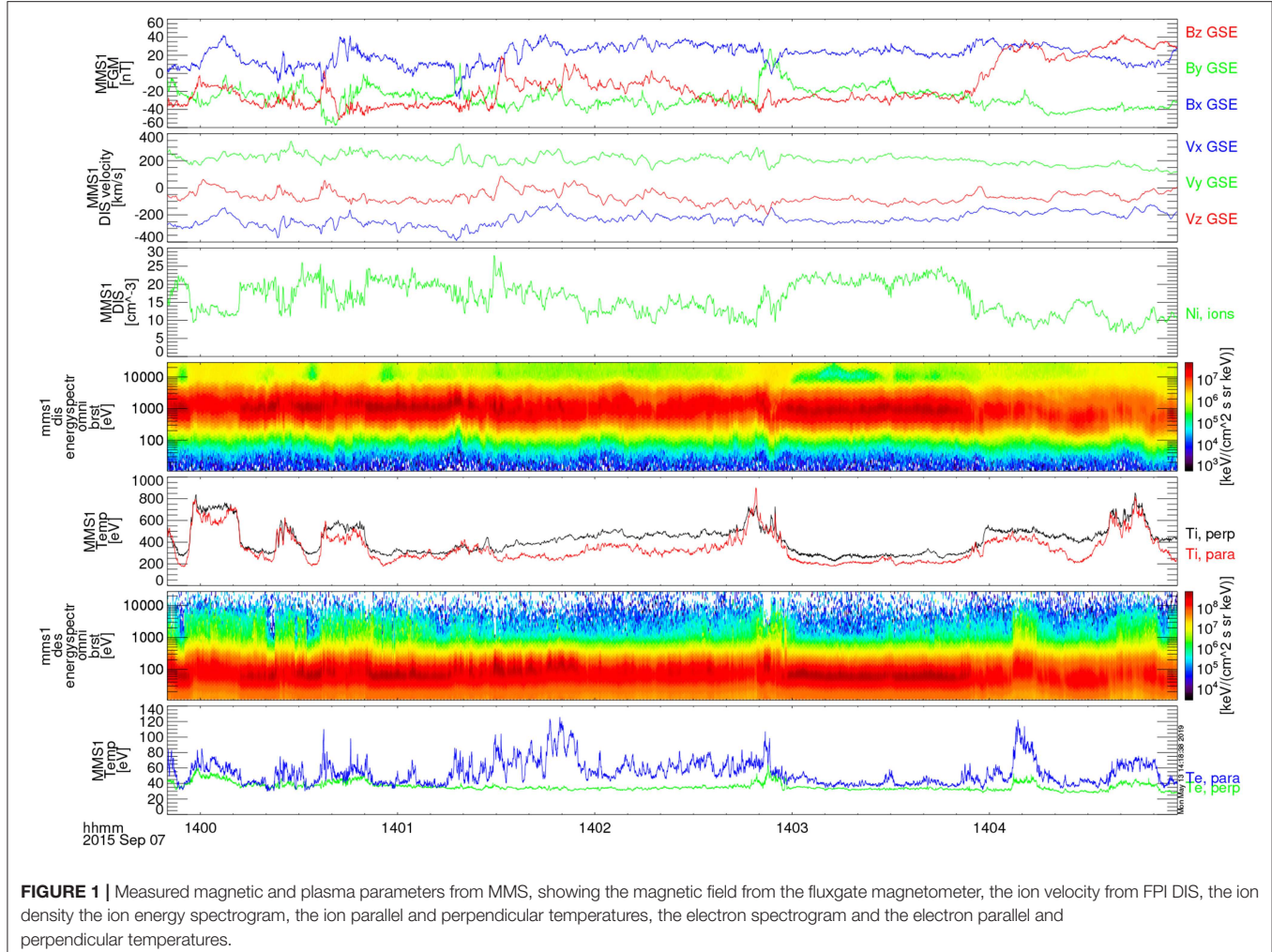


FIGURE 1 | Measured magnetic and plasma parameters from MMS, showing the magnetic field from the fluxgate magnetometer, the ion velocity from FPI DIS, the ion density the ion energy spectrogram, the ion parallel and perpendicular temperatures, the electron spectrogram and the electron parallel and perpendicular temperatures.

of studying magnetic reconnection. This is ideal for investigating the scales near proton gyration/inertial scales. The spacecraft were in the dusk side flank of the magnetosheath downstream of the quasi-perpendicular shock. A summary of the interval is shown in **Figure 1** which shows the magnetic field, ion velocity, ion density and ion and electron temperatures and mean parameters of the interval are given in **Table 1**.

The multi-point signal resonator technique [13] (MSR) will be used to analyze the different measurements given in **Figure 1**. Whereas, previously this technique (or its predecessor k-filtering/wave telescope) has been applied to electromagnetic [46], magnetic fields [14], and to density derived from spacecraft potential [5]. In this study we will investigate magnetic, velocity, temperature, and density fluctuations. For direct comparisons to the plasma data the magnetic field data will be resampled to the ion measurement time tags. The MSR technique relies on weak time stationarity, and spatial homogeneity of the signal. The signal seems fairly homogeneous in terms of the mean value throughout the interval, however after 14:03:30 the fluctuations seem a little less Alfvénic. This however makes up only a minority of the overall signal and is unlikely to have a large effect on

TABLE 1 | Showing the mean and standard deviation of several plasma parameters during the interval.

B [nT]	45.8 ± 6.2
V_i [km/s]	322 ± 51
V_e [km/s]	302 ± 88
n_i [cm^{-3}]	16.1 ± 4.4
β_i	1.2 ± 0.5
β_e	0.1 ± 0.07
$T_{i\perp}$ [eV]	424.2 ± 125.4
$T_{i\parallel}$ [eV]	344.0 ± 130.7
$T_{e\perp}$ [eV]	36.0 ± 5.1
$T_{e\parallel}$ [eV]	53.9 ± 15.7

the results based on testing with slightly different intervals than shown here. It should also be noted that a fine balance needs to be struck between the need sufficient data points for ensemble averaging and the weak stationarity of the signal. Especially when intervals such as this one where the MMS separations are large enough to study the ion kinetic range are extremely rare. As an

additional test we applied the same analysis to the full resolution magnetic field (where more data points are available than the ion data) of the shorter interval up to 14:03:30 and the method yielded similar results for the magnetic field. Thus, we can be confident that the analysis is justified for this interval.

The MSR technique also supposes that the signal can be described mathematically as a superposition of plane waves with random phases in the spirit of Fourier analysis, and a small component of incoherent noise. Essentially the technique uses the time series sampled at each spacecraft and the signal can be filtered for a frequency ω_{sc} using a Fourier transform, and for wave-vector \mathbf{k} using the multiple measurement points. Thus, only power related to a plane wave with frequency ω_{sc} and wave-vector \mathbf{k} is transmitted through the filter, thus by investigating a number of wave-vectors a distribution of power in wave-vector space can be estimated at a given frequency $P(\omega_{sc}, \mathbf{k})$. It is important to note that this does not require that the different plane waves that the signal can be decomposed into correspond to any particular linear wave solutions of the Vlasov equation.

In the case of using magnetic or velocity data, three components at each spacecraft can be used as an input giving a total of 12 time series, however for magnetic field data the filter can be further refined by enforcing the solution to conform to the divergence free condition for magnetic field which is termed a constraining matrix [47]. The application of the method to density is detailed in Roberts et al. [5], where there are only four time series input and similarly to the velocity case no constraining condition can be imposed. The unique capabilities of MMS allow it to be used on velocity, temperature fluctuations as well as a direct measurement of the density. In this study we will use the DC magnetic field from the fluxgate magnetometers (FGM) [48] which have a sampling rate of 128 Hz in burst mode and the ion plasma measurements from the Fast Plasma Investigation's Dual Ion Spectrometers [45] (FPI-DIS) which has a rate of 6.6Hz. As previously mentioned the magnetic field data is resampled to the ion time tags.

The method is subject to some limitations; the smallest scale that can be investigated is limited by the mean inter-spacecraft distance $k_{\max} = \pi/\langle d \rangle$ which is the primary driver for the choice of interval. The value k_{\max} defines a cube in wave-vector space that extends from $-k_{\max}$ to $+k_{\max}$, such that the length of one of the sides of the cube is $2\pi/\langle d \rangle$. The k_{\max} length scale is related to a timescale for an advected structure giving an upper frequency bound of $f_{\max} = V_i/2\langle d \rangle$. Where we take the bulk speed to be the ion bulk speed. Conversely the large scale limit is set to $k_{\max}/25$ when the error of determining a wave-vector becomes larger than 10% for a simulated plane wave [5, 49]. The technique also assumes weak stationarity and that the fluctuations can be described as a superposition of plane waves and incoherent noise. The method has been tested for a signal made of intermittent bursts of activity [50], where it is shown that coherence in the signal does not affect the ability to resolve incoherent features. Furthermore, spatially repeating coherent structures (with a Poisson distributed size and spacing) can be recovered, and resemble wave-packets that have a random phase. Additionally a test was performed using both the MSR method and multi-spacecraft timing, which are based on different

assumptions yielded similar results for an interval where several different intermittent coherent structures were identified [51].

In this work we will analyze the results from the MSR method in two different ways; Firstly $P(\mathbf{k})$ will be obtained by integrating $P(\omega_{sc}, \mathbf{k})$ with respect to the plasma frame frequency to investigate the anisotropies in the power distribution. This integration is performed between the limits $f_{\min} = 0.06, f_{\max} = 1$ Hz which come from the spacecraft mean separation ~ 140 km and the bulk flow speed. This will give a measurement in the power in wave-vector space, where we will for each measurement quantify the possible anisotropies and agyrotropies present. Secondly, we will also reduce the three dimensional spectra to spectra along one direction to investigate how the spectral index in the dissipation/dispersion range varies with the angle from the magnetic field.

3. RESULTS

3.1. One Dimensional Spectra

We begin this section by investigating the typical one dimensional analysis usually performed by investigating the Fourier spectra of the various different plasma parameters. Different Fourier spectra are shown in **Figure 2**, for magnetic field, ion velocity density and parallel and perpendicular ion thermal speeds. The frequencies corresponding to the proton gyroradius and inertial lengths $f_{\rho_i} = V_i/2\pi\rho_i = 0.80$ Hz, $f_{di} = V_i/2\pi d_i = 0.87$ Hz are indicated in orange assuming a mean bulk flow indicated in **Table 1**. The velocity and magnetic spectra are fitted with two power laws, the density and perpendicular thermal speed spectra are fitted with three power laws while the parallel thermal speed is fitted with one power law. The error on the spectral indices is obtained from the residuals of linear least squares fitting for log power against log wave-number. The break frequency is found by fitting the two power laws from opposite sides of the spectral break and then finding the intersection of the two lines. This procedure is done twice for the density/perpendicular thermal speed spectra as there are two break locations. **Figures 2A,B** show the spectra of the magnetic field (in Alfvén units) resampled to the ion velocity time tags and the ion velocity respectively. At large scales a spectral index close to $-5/3$ is obtained for the magnetic field with the velocity spectra being noticeably shallower, closer to $-3/2$ as is often observed in the solar wind and in the magnetosheath [52–54]. The inertial range is not always seen in the magnetosheath especially in the outer magnetosheath as the interaction of the solar wind with the Earth's bow shock destroys the correlations in the inertial range and results in a $1/f$ spectrum which transitions straight to the ion kinetic range without having time for an inertial range to develop.

In this case the observations are taken in the inner magnetosheath such that a well-developed inertial range is seen and is followed by a break and then a steepening with the ion velocity being steeper than the magnetic field [55, 56]. The magnetic field fluctuations dominate the velocity fluctuations in this case which may be due to the development of 2D structures such as the Alfvén vortex at inertial scales [51, 57–60] or current sheet or flux rope like structures [61–63].

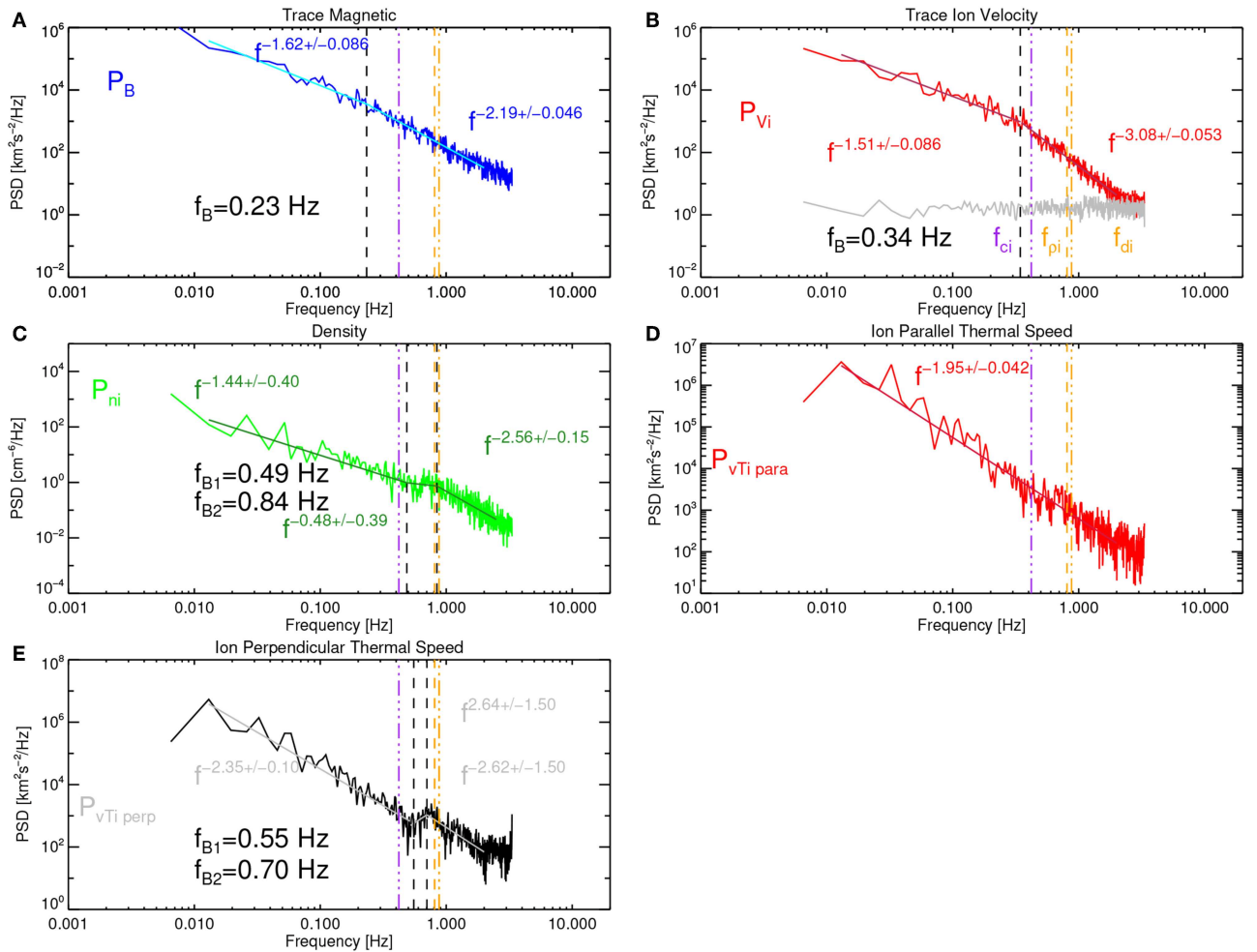


FIGURE 2 | Power spectral densities of measured quantities. **(A)** shows the trace magnetic field **(B)** shows the trace ion velocity (red) and the estimated noise floor in gray **(C)** shows the density **(D,E)** show the parallel and perpendicular temperatures.

At a spacecraft frame frequency near $\sim 0.2 - 0.4$ Hz there is a spectral break which is far from both the Taylor shifted inertial and Larmor scales. In the solar wind for extreme values of β the break location (e.g., [64]) has been shown to agree better with the larger of the two scales, although for typical values of β in the solar wind there is not much effect [34]. Alternatively the break in the solar wind shows good agreement for a variety of heliocentric distances with the scale expected for cyclotron resonance [65] $f_c = V_i/2\pi(\rho_i + d_i) = f_{\rho i}f_{di}/(f_{\rho i}f_{di}) = 0.42$ Hz which we denote in **Figure 2** as a purple vertical line. For the case presented it seems that the measured break point is more closely related to that expected for cyclotron resonance. Interestingly, for the density spectrum the first break agrees well with the f_c and the second break agrees well with the other break scales. A small bump is seen in this range for the perpendicular thermal speed, while no clear break can be found in the parallel thermal speed and only a single power law is fitted. The bump in the perpendicular thermal speed spectra could be due to cyclotron resonance (e.g., [33, 66, 67]) which could act at this range of scales and the wave-particle interaction

would be expected to heat protons in the perpendicular direction. However, no signature is seen in the trace magnetic spectra but a flattening is seen in the density spectra, which could suggest that a small scale compressible process is active. The time series in **Figure 1** show that there is an anti-correlation between density and temperature suggesting that the compressible fluctuations exhibit pressure balance. One possibility is that slow waves could be responsible (e.g., [68, 69]). Compressible slow waves are heavily damped in a plasma such as the magnetosheath due to the very high ion to electron temperature ratio. However, they are damped proportionally to k_{\parallel} thus could exist as pressure balanced structures $k_{\parallel} = 0$ or highly oblique kinetic slow waves $k_{\perp} \gg k_{\parallel}$. There is some evidence from numerical simulations of the magnetosheath behind the quasi parallel shock that suggests that slow waves can exist in these conditions [69].

At kinetic scales the dominance of the magnetic spectra could be due to kinetic Alfvén wave like fluctuations [56, 70], rather than kinetic slow waves. This suggests that should slow waves be responsible for the bump in the perpendicular temperature and the density they are not dominant at smaller scales. The gray trace

show the estimation of the FPI velocity noise floor [55], showing that noise becomes significant near $f_{sc} = 1.5$ Hz in the ion data.

Figure 2C shows spectra of the ion density, contrary to the magnetic field and velocity spectra a single clear break is not identified. Rather there exists a transition region which begins near the expectation for cyclotron resonance where the spectra flatten before it steepens near the inertial/Larmor scales. The transition in the density scale has been often observed in the solar wind and has been modeled as being due to the presence of compressible slow waves at large scales and kinetic Alfvén waves at small scales [71, 72]. The location where these two phenomena exist is dependant on the plasma beta with a smaller beta giving a larger transition region. However, it is not clear whether this is applicable for the magnetosheath, as other phenomena such as mirror modes are much more common in the magnetosheath and contribute significantly to the compressible power at inertial scales.

The nature of the thermal speed spectra of plasma turbulence is the subject of recent debate [73]. With high time resolution measurements of the solar wind only available from the Faraday Cup on Spektr-R. These spectra showed similarities to the spectra of the velocity fluctuations [74, 75] although it is argued by Gogoberidze et al. [73] that effects due to anisotropic temperatures and the measurement from the Faraday cup are misleading. In their work they argue that the proton thermal velocity should have a shape more similar to the compressible fluctuations, or the trace magnetic fluctuations. The thermal speed spectra are shown in **Figures 2D,E**. The perpendicular thermal speed spectra somewhat resembles the compressible fluctuations and in the same region as a flattening is seen in the density spectrum a small bump is seen at the same range.

While we have presented the Fourier power spectra of several different parameters here the key limitation is that these are along a single path of the spacecraft through the plasma (Taylor's hypothesis). But power distributions and spectral indices are anisotropic and it is possible that spectra of different parameters could resemble the spectra taken along a certain direction. We will now use the multi-spacecraft capabilities of MMS to explore the different spectra in three dimensions.

3.2. Three Dimensional Spectra

In this section we move on to multi-spacecraft analysis of the fluctuations using the MSR technique. Turbulence spectra show the power is concentrated at low frequencies (and wave-numbers). However to get a full distribution of the power in wave-vector space it is insufficient to only consider the low frequency Fourier modes as their power corresponds to power at small wavenumbers. Therefore, an integration is needed in frequency to contribute the powers at higher wave-numbers. Thus, after obtaining a four dimensional power $P(\omega_{sc}, \mathbf{k})$ at each spacecraft frequency we integrate between spacecraft frame frequencies of 0.06–1Hz to obtain the power distribution in wave-vector space $P(\mathbf{k})$. One of the advantages of this technique is that Taylor's hypothesis is not invoked, so there are no concerns about the validity of Taylor's hypothesis when integrating higher frequencies. **Figure 3** shows the three dimensional power distributions obtained through the application of the MSR

technique to various different measured parameters. These distributions have been integrated over the third direction to give a two dimensional representation of the vector quantities, the magnetic field (a), the velocity (b). Meanwhile **Figure 4** shows the scalar quantities density (a) and parallel and perpendicular ion temperatures (b,c). The co-ordinate system is the mean field aligned system with the $\mathbf{e}_{\parallel} = \mathbf{B}_0/|\mathbf{B}_0|$, $\mathbf{e}_{\perp 1} = \mathbf{e}_{\parallel} \times \mathbf{V}_i/|\mathbf{V}_i|$, and $\mathbf{e}_{\perp 2} = \mathbf{e}_{\parallel} \times \mathbf{e}_{\perp 1}$ such that the bulk flow is primarily in the $-\mathbf{e}_{\perp 2}$ direction.

All spectra show similar shapes to one another but there are slight differences. To quantify the relative levels of anisotropy and agyrotropy in the power distributions of different powers we use eigenvalues of the stress tensor where the i,j elements of the tensor are defined in Equation (1).

$$A_{ij} = \frac{1}{n} \int (k_i - \langle k_i \rangle)(k_j - \langle k_j \rangle) P(\mathbf{k}) d^3 \mathbf{k} \quad (1)$$

Where the angled brackets denote the centre of the power distribution. This metric has often been used to quantify the geometrical properties of numerically simulated velocity distribution functions (e.g., [76]). The eigenvectors of this stress tensor give three orthogonal components $[\mathbf{e}_1, \mathbf{e}_2, \mathbf{e}_3]$ which are aligned with the major axis and two perpendicular axes where the corresponding eigenvalues satisfy $\lambda_1 > \lambda_2 > \lambda_3$. The eigenvalues can be used to define an anisotropy index λ_1/λ_3 and a non-gyrotropy index λ_1/λ_2 .

For a sphere all eigenvalues would be equal and for a gyrotopic cigar like shape which is elongated along one axis the two smaller eigenvalues would be equal. The results in **Table 2** demonstrate that not only that magnetic fluctuations are anisotropic but all parameters investigated are anisotropic and show similar distributions. We note that the power distributions of the vector fields are more irregular than those of scalar quantities, this may be due to the number of components put into the MSR method i.e., 12 vs. 4.

The most anisotropic component is the velocity. This perhaps reflects the differences in the one dimensional spectra as proton kinetic effects become important and the velocity spectrum steepens significantly compared to the magnetic spectra [56]. Meanwhile the spectra of other parameters are much less steep than the ion velocity. The scalar components are less anisotropic than the both magnetic and velocity fields which is different to cases in the solar wind where the compressible component can be more anisotropic [22, 56]. In the fast solar wind at inertial scales this has been interpreted to be due to slow waves which are damped proportionally to k_{\parallel} , thus only the fluctuations with the most perpendicular wave-vectors can survive, while the incompressible component contains Alfvén waves which do not have such a sensitivity to the propagation angle. However, in the magnetosheath the compressible component is unlikely to be due to kinetic slow waves as they are more severely damped due to the plasma conditions i.e., high ion to electron temperature ratio (e.g., [77]). The dominance of the magnetic field spectra over the velocity spectra suggests that for this interval slow waves are not dominant at kinetic scales, but could explain the bump in

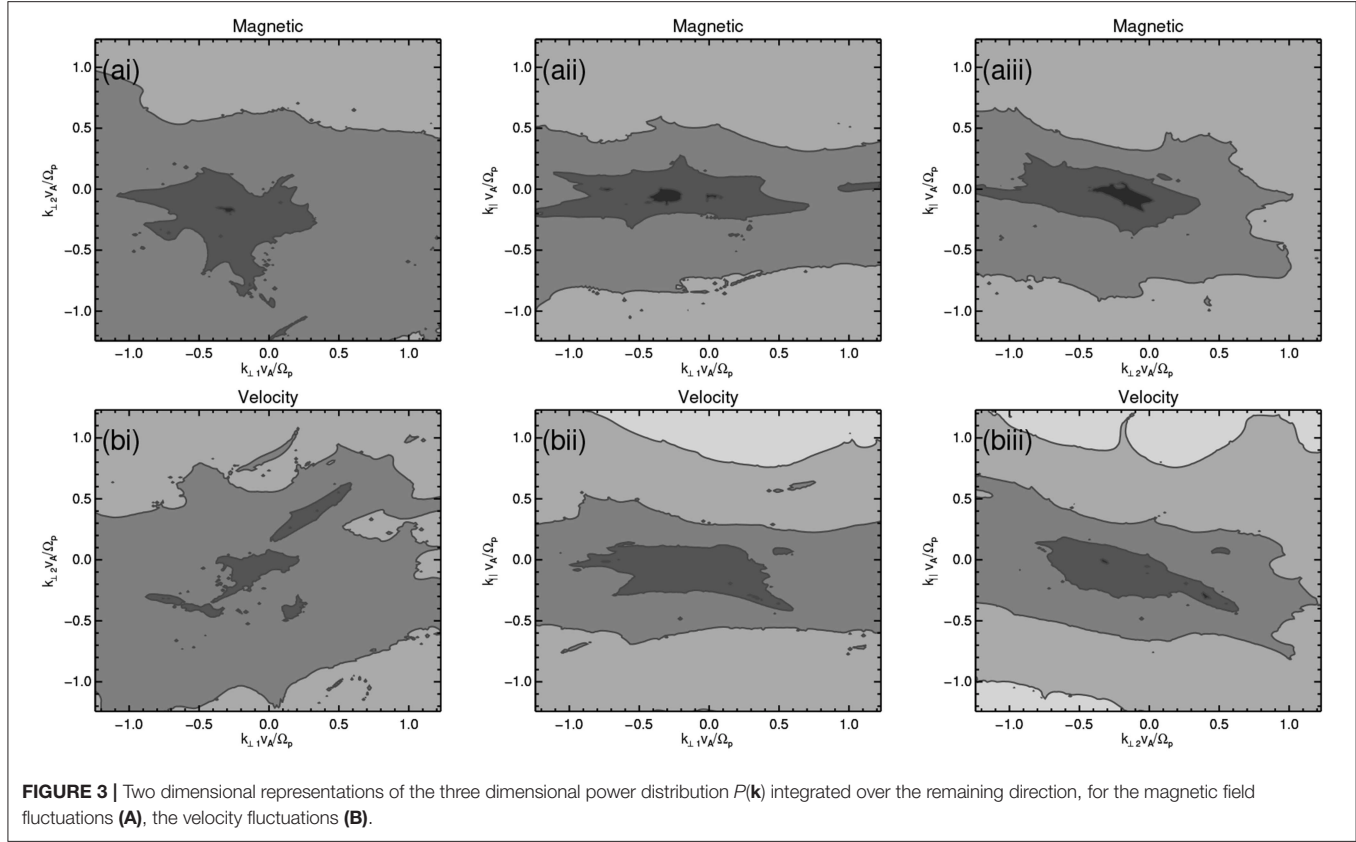


FIGURE 3 | Two dimensional representations of the three dimensional power distribution $P(\mathbf{k})$ integrated over the remaining direction, for the magnetic field fluctuations (A), the velocity fluctuations (B).

the perpendicular temperature and the flattening in the density spectra. This could be due to damping before they can cascade to the kinetic range. However, simulations do suggest that slow waves can exist in this environment at kinetic scales (e.g., [69]). One possibility is that pressure balanced structures could exist at kinetic scales as they are undamped. This interpretation has a weakness, as the compressible three dimensional spectra are less anisotropic than the magnetic and velocity components whereas pressure balanced structures are expected to be highly anisotropic. We suggest that something else must contribute to the compressibility, perhaps structures such as mirror modes which are quasi aligned with the magnetic field giving a smaller anisotropy than the magnetic components.

The similarity in the shapes of the distributions echoes previous work at large scales by Smith et al. [27], where similar shapes in the correlation lengths were found when using magnetic, velocity, density, and temperature. There are also suggestions here of non-gyrotropy which seems to be larger when the anisotropy is larger. The reason for this is not fully understood, some hypotheses include sampling effects due to the velocity direction [78], a remnant of a large scale effect due to the bow shock, or a preferred cascade direction. A comparison with a simulation with a known distribution of power in wave-vector space should be performed to confirm or refute the sampling effect described by Turner et al. [78]. To be able to fully understand the causes of this anisotropy more intervals should be analyzed in the magnetosheath an the

solar wind and comparisons made with numerical simulations which incorporate other effects which can cause second preferred directions to appear. There is also a weak asymmetry with respect to the \mathbf{e}_\parallel direction showing more power $k_\parallel < 0$.

3.3. Anisotropy of Spectral Index

To further investigate the anisotropy we reduce the full distributions to a one dimensional spectrum. We focus only on the spectral index of the dissipation scale as inertial scales have too few points in wave-vector space for an accurate determination of the spectral index due to the interspacecraft distances being too small. The distributions are converted to cylindrical coordinates and the perpendicular direction is defined as the integration over the azimuthal direction, the distribution is then folded to give a spectrum in (k_\parallel, k_\perp) . Finally this is reduced to a one dimensional spectrum by taking a 1D cut through the distribution.

One dimensional spectra in directions parallel and perpendicular to the mean magnetic fields in Figures 5, 6, and in the flow direction in Figure 7. Further details of the normalization of both the MSR spectra and the conversion and normalization of the spectra in Figure 2 are given in the Appendix. It is important to note that an incorrect normalization was displayed in Roberts et al. [17] where the spectrum was divided by k rather than Δk and the total power was missing. Figure 5 shows the one dimensional cut along the parallel direction, for the five different quantities in this study. The scales

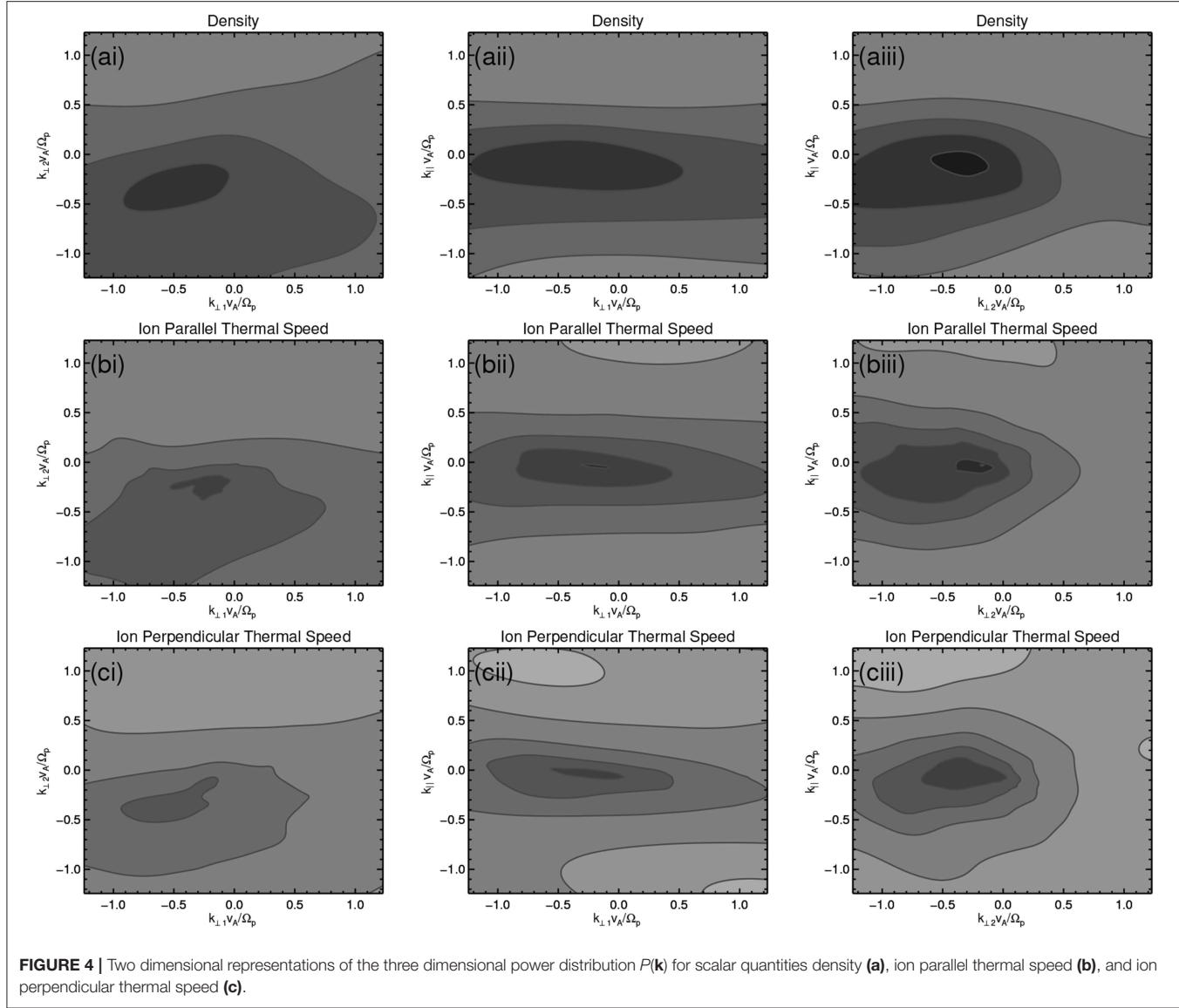


FIGURE 4 | Two dimensional representations of the three dimensional power distribution $P(\mathbf{k})$ for scalar quantities **(a)**, ion parallel thermal speed **(b)**, and ion perpendicular thermal speed **(c)**.

TABLE 2 | Results of the anisotropy and non-gyrotropy analysis for the different three dimensional spectra surveyed.

Quantity	λ_1/λ_3	λ_1/λ_2	θ_{\max}
B	4.48	1.45	93
V_i	4.66	2.06	89
n_i	2.23	1.28	101
$V_{ti\parallel}$	2.18	1.28	95
$V_{ti\perp}$	2.41	1.56	80

The anisotropy is quantified as the largest eigenvalue over the smallest value. The non-gyrotropy is quantified as the maximum over the intermediate eigenvalue. The orientation of the power distribution with respect to the mean magnetic field direction is calculated using the largest eigenvector and expressed in degrees $\theta_{\max} = \cos^{-1} \mathbf{e}_1 \cdot \mathbf{e}_{\parallel}$.

corresponding to the Larmor radius and inertial length are shown in orange and the scale corresponding to the cyclotron frequency is shown in purple similarly to Figure 2. Figure 5

shows an interesting feature that there is an enhancement in the parallel power and in the perpendicular thermal speed. This could be an indication of ion cyclotron waves, which cannot be seen in the time series as the streamwise wave-vector is far from parallel. This signature is also at the low wave-number end which may be less accurate [49]. Confirmation could be made by investigating another interval with larger separations so that the scales can be studied with more accuracy. Future work should seek to perform comparisons with time intervals where the magnetic field is along the velocity direction where the signature would be able to be seen in the spacecraft frame Fourier spectra. There are several results in the fast solar wind that show signatures of ion cyclotron waves for intervals with radial fields. However, it is not clear whether cyclotron waves are present but can only be seen for times when the magnetic field is pointing radially [10, 79].

Figure 6 shows the same plots but for the perpendicular direction, while Figure 7 shows the reduced one dimensional

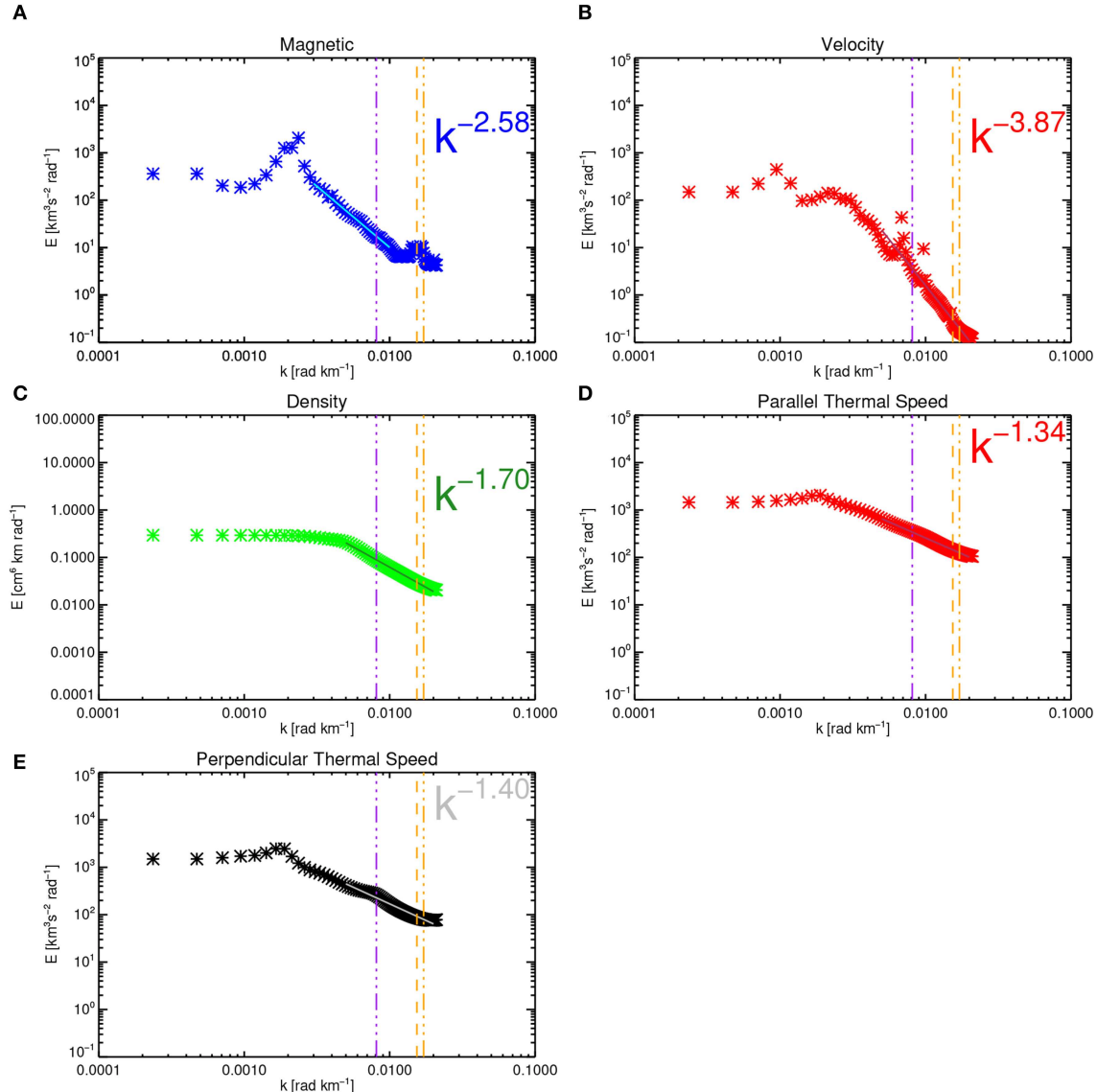


FIGURE 5 | Reduced one dimensional spectral densities, for **(A)** magnetic field **(B)** velocity, **(C)** density, **(D)** ion parallel thermal speed, and **(E)** ion perpendicular thermal speed. The orange vertical lines denote the ion inertial and Larmor radius while the purple vertical lines denote the length corresponding to the cyclotron frequency. The solid lines denote power law fits to the data and the obtained spectral index is indicated on the plot.

spectrum for an angle of 50° which is approximately along the bulk velocity direction. This is plotted with the spacecraft frame spectral density (corresponding to the PSD in Figure 2) with the wave-number determined by assuming Taylor's hypothesis $k = 2\pi f/V_i$. Both vector spectra show reasonable agreement with the best agreement with the velocity. The results here are different to Figure 2E in [17] as in that paper the comparison with the flow direction spectra was made by averaging in the Cartesian coordinates for comparing the two perpendicular components rather than a one dimensional cut. Therefore, it is likely that the power there did not match as well due to the stronger agyrotropy which was averaged over. Additionally here a 1D cut is used through the spectra. At

smaller scales the spectra differ possibly due to the Taylor's hypothesis losing validity for compressible components or due to spatial aliased power contributing at smaller scales. Spatial aliasing might be more prevalent for the scalar quantities when compared to the spectra of the time series as there are fewer inputs into the method. Aliasing is also suppressed by the constraining condition of the magnetic field. This explains why the power from the MSR method is much higher for the scalar quantities at small scales. To have a definitive conclusion about the application of the method to scalar components and to understand the agyrotropy comparisons of the method with numerically simulated data will be performed in the future.

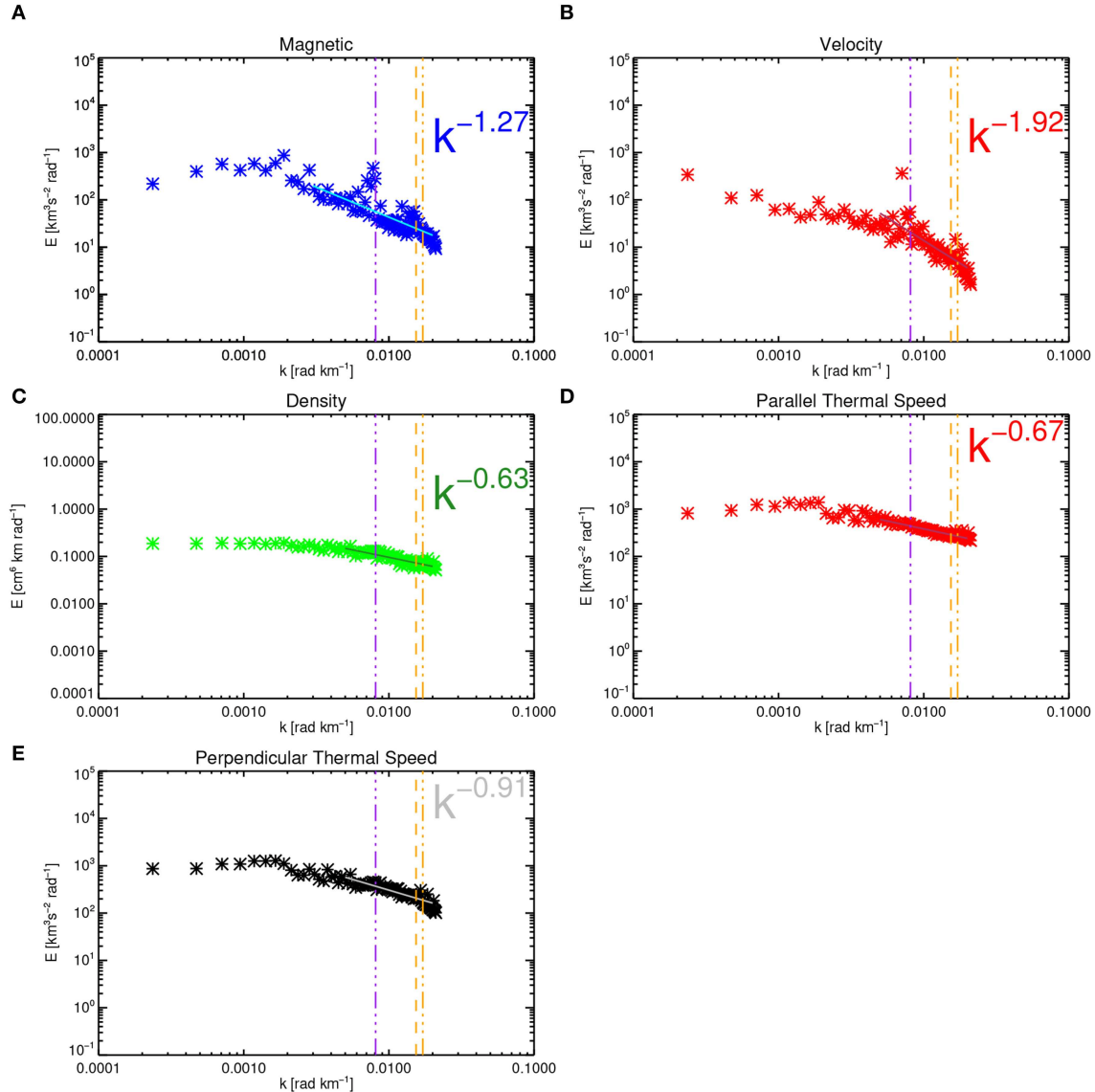


FIGURE 6 | The same as **Figure 5** but for the perpendicular direction.

The results from **Figures 5–7** are summarized succinctly in **Figure 8**, where the spectral indices are plotted as a function of angle from the magnetic field. The spectra are fitted at several angles from the mean magnetic field direction (diamonds) and are compared to the value for the one dimensional spectra (circles) in **Figure 2**. The two vector spectra agree well with the spectral indices measured in frequency space apart from the density and perpendicular thermal speed most likely due to the nature of the spectra having a transition region/bump, or due to the lack of a constraining condition/fewer time series inputs as mentioned previously. The comparison between the spectral indices in frequency space and wave-number is difficult to make in some cases. This is because the spectral break location varies between each parameter as observed in **Figure 2**. However,

the wave-vector range available is controlled by the spacecraft separations which remains the same. Therefore, in some cases there may be more Fourier modes present in the inertial range (or kinetic range) for different parameters due to the different location of the break. This is seen in the density spectrum and the perpendicular thermal speed spectra where we indicate the spectral indices of both the inertial and kinetic ranges in **Figure 8**. This is essentially a limitation having multiple spacecraft at only a single length scale. Future multi-spacecraft plasma turbulence missions should be designed to sample multiple length scales simultaneously.

All spectra show a steepening of the spectra toward directions close to the mean magnetic field direction. Here we define the mean magnetic field to be the mean over the entire interval.

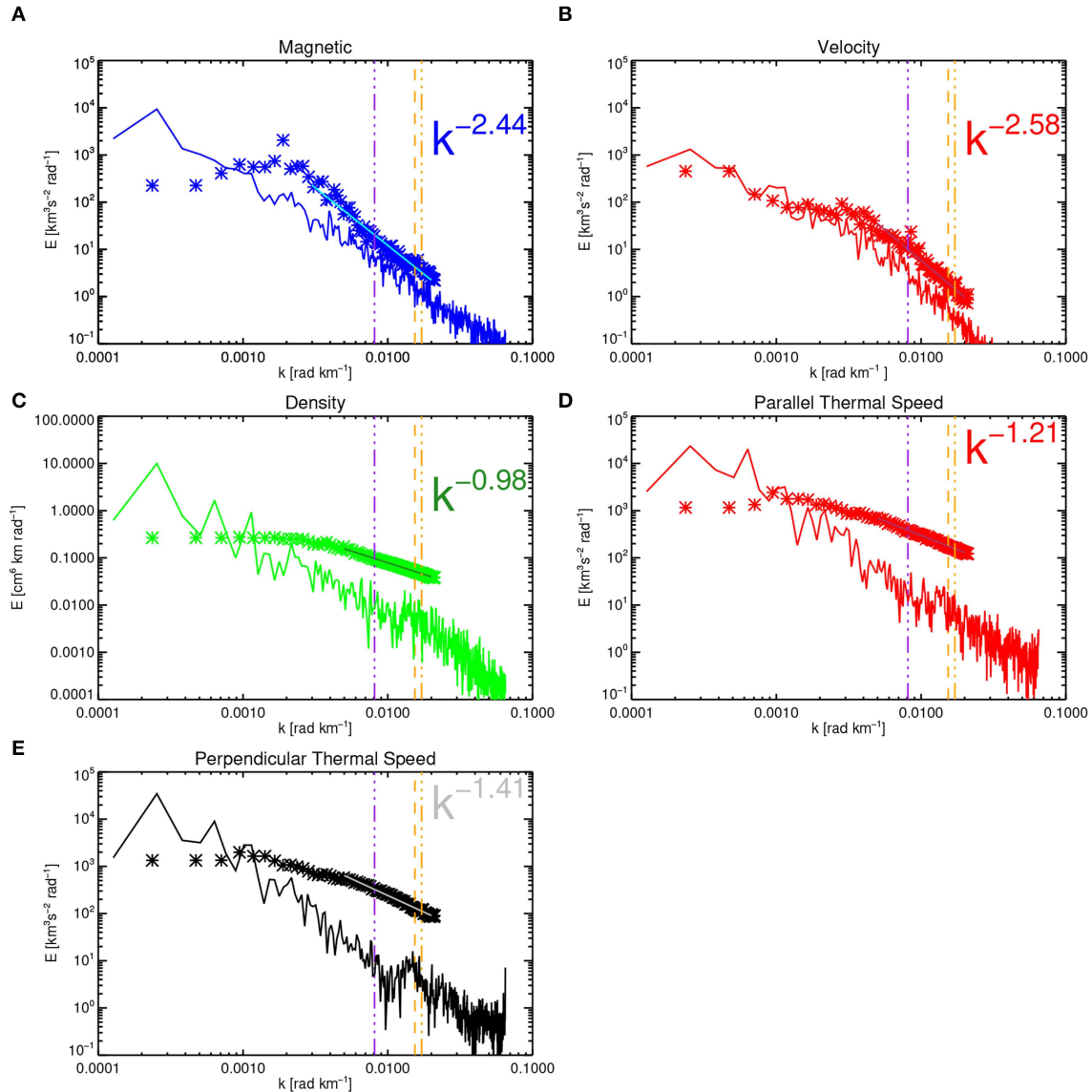


FIGURE 7 | The same as Figures 5, 6 but for the flow direction. The points denote the values obtained from the multi spacecraft method while the solid lines denote the spacecraft frame spectra with the wave-numbers calculated from assuming Taylor's hypothesis. The spectral fits to the points also shown by the power law fits and the spectral index is indicated on the panels.

A tendency toward a steepening in the parallel direction has been observed at larger scales [9] by varying investigating different orientations of the magnetic field and also with multi-spacecraft analysis at dissipation scales [42]. One of the predictions of a critically balanced cascade [80] is a spectral index relation for the magnetic field such that a Kolmogorov $-5/3$ spectrum in the perpendicular direction corresponds to a spectral index of -2 in the parallel direction in the inertial range. Extensions of this theory which assume a cascade of critically balanced kinetic Alfvén waves predict a parallel scaling of -5 and a perpendicular scaling of $-7/3$ [72, 81, 82]. Although the perpendicular scaling of the magnetic field is close to the $-7/3$ the parallel spectral index is far from -5 , suggesting that this description is incomplete.

The presence of intermittency [83] or Landau damping [84] could modify the predictions of spectral indices to $-8/3$ in the perpendicular direction. Following the scaling relation $k_{\parallel} \propto k_{\perp}^{2/3}$ this would correspond to a scaling of $-7/2$ in the parallel direction [83] which are more consistent with the observations reported here. Alternatively, the nature of the anisotropy in the spectral indices could be explained by a non-elliptic geometry of the power distribution without the need for critical balance [85].

An interesting feature shown here is that the density spectrum and the temperature spectra show similar evolution of the spectral index from ~ -2.0 to ~ -1.5 . The similarity of the density and the thermal speeds is consistent with the interpretations of Gogoberidze et al. [73], although this

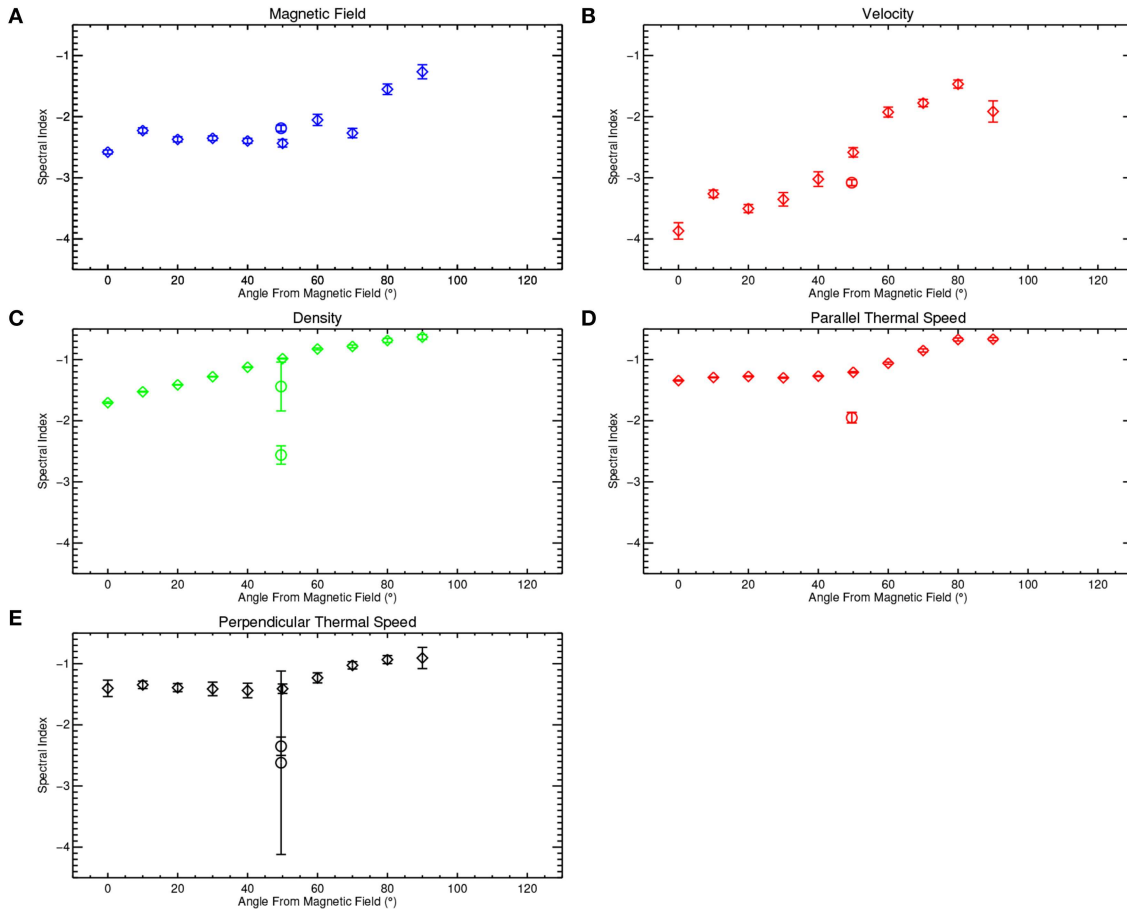


FIGURE 8 | Anisotropy of spectral indices, showing magnetic field **(A)**, ion velocity **(B)**, density **(C)**, ion parallel thermal speed **(D)**, ion perpendicular thermal speed. The diamonds show the points obtained from the integrations of the results in **Figures 3, 4** and the circles show the points corresponding to the one dimensional frequency spectra in **Figure 2**. The two circular points in **(C,E)** denote the inertial range index and the kinetic range spectral index values. The error bars denote the error from the residuals of linear least squares fitting for log power against log wave-number.

comparison is not completely clear when investigating only the one dimensional PSD as a function of frequency shown in **Figure 2**. The extreme steepness in the velocity spectrum could be due to the ions becoming demagnetized and no longer participating in the cascade or it could be interpreted in terms of the Alfvén ratio which decreases rapidly and can be interpreted as a signature of a kinetic Alfvén wave [56, 70, 86].

3.4. Summary

In this study we have extended the MSR analysis technique to turbulent fields and scalars other than the magnetic field in the magnetosheath. The fields surveyed show both, power anisotropy, and anisotropy of spectral index. The anisotropy is the strongest in the velocity fluctuations which exhibits a steep power law at ion scales. The electron velocity (not shown) shows a much flatter spectra in the ion dissipation range of $f^{-0.8}$ compared with the ion velocity spectra ($f^{-3.08}$) indicating the ions are no longer magnetized whereas the electrons remain magnetized indicating differences in the ion and electron velocities and that the Hall effect is present. However,

the electron dynamics is outside of the scope of this work but will be investigated in the future, with a smaller choice of inter-spacecraft distance. The compressible component of the turbulence appears to be less anisotropic for the magnetosheath. This is in contrast to some observations in the solar wind [22]. This suggests that the compressibility is different to that in the solar wind and likely to be due to compressible structures that are quasi aligned with the magnetic field direction.

The anisotropy of spectral index is investigated, finding that the spectra are steeper in the direction parallel to the mean magnetic field direction for all parameters measured. The vector fields show the largest variations, while the scalars show smaller variations. When compared to the 1D frequency spectra the spectral indices are similar except in the case of density which is most likely due to the small difference in the inertial range scaling and the transition range which comes between the inertial and dissipation ranges.

The thermal speed spectra and the density spectra show similar evolution of the spectral indices from parallel orientations to perpendicular ones suggesting that the prediction of

Gogoberidze et al. [73] is correct. Finally the similarity of the density spectra with the thermal speed spectra may hint that particle heating and the energy cascade rate has a strong link to the compressibility of the plasma (e.g., [87, 88]). There is also evidence that compressible slow waves and their interactions with Alfvén waves are simultaneously observed with heating signatures in proton velocity distribution functions [68]. These studies all highlight the importance of compressibility in understanding turbulent heating in a plasma.

There is also a hint of non-gyrotropy, although its origins and significance remain unclear. For this interval the anisotropy and non-gyrotropy appear to increase with one another, however more observations will be required to draw any conclusions from this case study. In the future the effect of the plasma beta, and the type of plasma should be investigated (i.e., fast/slow solar wind inner/outer magnetosheath etc.) which can all affect the level of anisotropy (e.g., [18, 89]). These measurements are only possible due to the unique capabilities of MMS combining both multiple sampling points and high time resolution plasma measurements.

Here we investigate the ion dynamics, and will extend this work to electron dynamics when the stationarity of the fluctuations in the electron velocity is justified for the analysis. The structure of the fluctuations at ion scales are similar to one another irrespective of the parameters. Finally we have

demonstrated that fully three dimensional observations of plasma parameters in the Earth's magnetosheath are possible with MMS, however one of the key limitations here is the ability to only study a single scale at once. Ideally all the relevant scales of the turbulence should be sampled simultaneously, this requirement should be a driver for the design of future spacecraft missions.

DATA AVAILABILITY STATEMENT

The datasets analyzed for this study can be found in the MMS science data archive <https://lasp.colorado.edu/mms/sdc/public/>.

AUTHOR CONTRIBUTIONS

OR analyzed the data and drafted the manuscript. YN, ZV, and RN contributed to the interpretation of the analysis and general improvements in the manuscript. DG contributed to the interpretation of the FPI data and general improvements in the manuscript.

FUNDING

RN was supported by Austrian FWF projects I2016-N20. ZV was supported by the Austrian FWF projects P28764-N27.

REFERENCES

- Bruno R, Carbone V. The solar wind as a turbulence laboratory. *Living Rev Solar Phys.* (2013) **10**:2. doi: 10.12942/lrsp-2013-2
- Kiyani KH, Osman KT, Chapman SC. Dissipation and heating in solar wind turbulence: from the macro to the micro and back again. *Philos Trans R Soc Math Phys Eng Sci.* (2015) **373**:2014015. doi: 10.1098/rsta.2014.0155
- Kellogg P, Horbury T. Rapid density fluctuations in the solar wind. *Ann Geophys.* (2005) **23**:3765–73. doi: 10.5194/angeo-23-3765-2005
- Yao S, He JS, Marsch E, Tu CY, Pedersen A, Rème H, et al. Multi-scale anti-correlation between electron density and magnetic field strength in the solar wind. *Astrophys J.* (2011) **728**:146. doi: 10.1088/0004-637X/728/2/146
- Roberts OW, Narita Y, Li X, Escoubet CP, Laakso H. Multipoint analysis of compressive fluctuations in the fast and slow solar wind. *J Geophys Res Space Phys.* (2017) **122**:6940–63. doi: 10.1002/2016JA023552
- Horbury TS, Wicks RT, Chen CHK. Anisotropy in space plasma turbulence: solar wind observations. *Space Sci Rev.* (2012) **172**:325–42. doi: 10.1007/s11214-011-9821-9
- Oughton S, Matthaeus W, Wan M, Osman KT. Anisotropy in solar wind plasma turbulence. *Philos Trans R Soc A Math Phys Eng Sci.* (2015) **373**:20140152. doi: 10.1098/rsta.2014.0152
- Narita Y. Space–time structure and wavevector anisotropy in space plasma turbulence. *Living Rev Solar Phys.* (2018) **15**:2. doi: 10.1007/s41116-017-0010-0
- Horbury T, Foreman M, Oughton S. Anisotropic scaling of magnetohydrodynamic turbulence. *Phys. Rev. Lett.* (2008) **101**:1–4. doi: 10.1103/PhysRevLett.101.175005
- Podesta JJ, Gary S. Magnetic helicity spectrum of solar wind fluctuations as a function of the angle with respect to the local mean magnetic field. *Astrophys J.* (2011) **734**:15. doi: 10.1088/0004-637X/734/1/15
- He J, Tu C, Marsch E, Bourouaine S, Pei Z. Radial evolution of the wavevector anisotropy of solar wind turbulence between 0.3 and 1 AU. *Astrophys J.* (2013) **773**:72. doi: 10.1088/0004-637x/773/1/72
- Yan L, He J, Zhang L, Tu C, Marsch E, Chen CHK, et al. Spectral anisotropy of elssässer variables in two-dimensional wave-vector space as observed in the fast solar wind turbulence. *Astrophys J.* (2016) **816**:L24. doi: 10.3847/2041-8205/816/2/L24
- Narita Y, Glassmeier KH, Motschmann U. High-resolution wave number spectrum using multi-point measurements in space—the Multi-point Signal Resonator (MSR) technique. *Ann Geophys.* (2011) **29**:351–60. doi: 10.5194/angeo-29-351-2011
- Roberts OW, Li X, Li B. Kinetic plasma turbulence in the fast solar wind measured by cluster. *Astrophys J.* (2013) **769**:58. doi: 10.1088/0004-637X/769/1/58
- Roberts OW, Li X, Jeska L. A statistical study of the solar wind turbulence at ion kinetic scales using the K -filtering technique and cluster data. *Astrophys J.* (2015) **802**:1–13. doi: 10.1088/0004-637X/802/1/2
- Wicks RT, Horbury TS, Chen CHK, Schekochihin A. Anisotropy of imbalanced Alfvénic turbulence in fast solar wind. *Phys Rev Lett.* (2011) **106**:1–4. doi: 10.1103/PhysRevLett.106.045001
- Roberts OW, Narita Y, Escoubet CP. Direct measurement of anisotropic and asymmetric wave vector spectrum in ion-scale solar wind turbulence. *Astrophys J.* (2017) **851**:L11. doi: 10.3847/2041-8213/aa9bf3
- Roberts OW, Narita Y, Escoubet CP. Three-dimensional density and compressible magnetic structure in solar wind turbulence. *Ann Geophys.* (2018) **36**:527–39. doi: 10.5194/angeo-36-527-2018
- Dong Y, Verdini A, Grappin R. Evolution of turbulence in the expanding solar wind, a numerical study. *Astrophys J.* (2014) **793**:118. doi: 10.1088/0004-637X/793/2/118
- Vech D, Chen CHK. Testing the effects of expansion on solar wind turbulence. *Astrophys J.* (2016) **832**:L16. doi: 10.3847/2041-8205/832/1/L16
- Saur J, Bieber JW. Geometry of low-frequency solar wind magnetic turbulence: evidence for radially aligned Alfvénic fluctuations. *J Geophys Res.* (1999) **104**:9975.
- Chen C, Mallet A, Schekochihin A, Horbury T, Wicks RT, Bale S. Three-dimensional structure of solar wind turbulence. *Astrophys J.* (2012) **758**:1–5. doi: 10.1088/0004-637X/758/2/120
- Narita Y, Comişel H, Motschmann U. Spatial structure of ion-scale plasma turbulence. *Front Phys.* (2014) **2**:13. doi: 10.3389/fphy.2014.00013

24. Taylor GI. The spectrum of turbulence. *Proc R Soc A Math Phys Eng Sci.* (1938) **164**:476–90.
25. Matthaeus W, Goldstein M, Roberts DA. Evidence for the presence of quasi-two-dimensional nearly incompressible fluctuations in the solar wind. *J Geophys Res.* (1990) **95**:20673.
26. Dasso S, Milano L, Matthaeus W, Smith C. Anisotropy in fast and slow solar wind fluctuations. *Astrophys J.* (2005) **635**:181–4. doi: 10.1086/499559
27. Smith CW, Vasquez BJ, Stempkowski MR. Analysis of multi-dimensional correlation functions in the solar wind. *AIP Confer Proc.* (2013) **271**:271–4. doi: 10.1063/1.4811040
28. Wang X, Tu C, He J. 2D isotropic feature of solar wind turbulence as shown by self-correlation level contours at hour timescales. *Astrophys J.* (2019) **871**:93. doi: 10.3847/1538-4357/aa64f
29. Forman MA, Wicks RT, Horbury T. Detailed fit of “Critical Balance” theory to solar wind turbulence measurements. *Astrophys J.* (2011) **733**:76. doi: 10.1088/0004-637X/733/2/76
30. Smith CW, Hamilton K, Vasquez BJ, Leamon RJ. Dependence of the dissipation range spectrum of interplanetary magnetic fluctuations on the rate of energy cascade. *Astrophys J.* (2006) **645**:L85–8. doi: 10.1086/506151
31. Alexandrova O, Lacombe C, Mangeney A, Grappin R, Maksimovic M. Solar wind turbulent spectrum at plasma kinetic scales. *Astrophys J.* (2012) **760**:121. doi: 10.1088/0004-637X/760/2/121
32. Bruno R, Trenchi L, Telloni D. Spectral slope variation at proton scales from fast to slow solar wind. *Astrophys J.* (2014) **793**:L15. doi: 10.1088/2041-8205/793/1/L15
33. Woodham LD, Wicks RT, Verscharen D, Owen CJ. The role of proton cyclotron resonance as a dissipation mechanism in solar wind turbulence: a statistical study at ion-kinetic scales. *Astrophys J.* (2018) **856**:49. doi: 10.3847/1538-4357/aa03d
34. Wang X, Tu CY, He JS, Wang LH. Ion-scale spectral break in the normal plasma beta range in the solar wind turbulence. *J Geophys Res Space Phys.* (2018) **123**:68–75. doi: 10.1002/2017JA024813
35. Duan D, He J, Pei Z, Huang S, Wu H, Verscharen D, et al. Angular independence of break position for magnetic power spectral density in solar wind turbulence. *Astrophys J.* (2018) **865**:89. doi: 10.3847/1538-4357/aad9aa
36. Howes GG, Klein KG, TenBarge JM. Validity of the taylor hypothesis for linear kinetic waves in the weakly collisional solar wind. *Astrophys J.* (2014) **789**:106. doi: 10.1088/0004-637X/789/2/106
37. Klein KG, Howes GG, TenBarge JM. The violation of the taylor hypothesis in measurements of solar wind turbulence. *Astrophys J.* (2014) **790**:L20. doi: 10.1088/2041-8205/790/2/L20
38. Narita Y. Error estimate of Taylor’s frozen-in flow hypothesis in the spectral domain. *Ann Geophys.* (2017) **35**:325–31. doi: 10.5194/angeo-35-325-2017
39. Verdini, Grappin R, Verdini A, Grappin R. Imprints of expansion on the local anisotropy of solar wind turbulence. *Astrophys J.* (2015) **808**:L34. doi: 10.1088/2041-8205/808/2/L34
40. Osman K, Horbury T. Quantitative estimates of the slab and 2-D power in solar wind turbulence using multispacecraft data. *J Geophys Res.* (2009) **114**:1–8. doi: 10.1029/2008JA014036
41. Osman K, Horbury T. Multi-spacecraft measurement of anisotropic power levels and scaling in solar wind turbulence. *Ann Geophys Atmos.* (2009) **2008**:3019–25. doi: 10.5194/angeo-27-3019-2009
42. Chen CHK, Horbury TS, Schekochihin AA, Wicks RT, Alexandrova O, Mitchell J. Anisotropy of solar wind turbulence between ion and electron scales. *Phys Rev Lett.* (2010) **104**:1–4. doi: 10.1103/PhysRevLett.104.255002
43. Narita Y, Gary S, Saito S, Glassmeier KH, Motschmann U. Dispersion relation analysis of solar wind turbulence. *Geophys Res Lett.* (2011) **38**:2–5. doi: 10.1029/2010GL046588
44. Burch JL, Moore TE, Torbert RB, Giles BL. Magnetospheric multiscale overview and science objectives. *Space Sci Rev.* (2016) **199**:5–21. doi: 10.1007/s11214-015-0164-9
45. Pollock C, Moore T, Jacques A, Burch J, Giese U, Saito Y, et al. Fast plasma investigation for magnetospheric multiscale. *Space Sci Rev.* (2016) **199**:331–406. doi: 10.1007/s11214-016-0245-4
46. Tjulin A, Pincon J, Sahraoui F, André M, Cornilleau-Wehrlin N. The k-filtering technique applied to wave electric and magnetic field measurements from the Cluster satellites. *J Geophys Res.* (2005) **110**:1–17. doi: 10.1029/2005JA011125
47. Motschmann U, Woodward TI, Glassmeier KH, Southwood DJ, Pincon J. Wave length and direction filtering by magnetic measurements at satellite arrays : generalized minimum variance analysis. *J Geophys Res.* (1996) **101**:4961–5.
48. Russell CT, Anderson BJ, Baumjohann W, Bromund KR, Dearborn D, Fischer D, et al. The magnetospheric multiscale magnetometers. *Space Sci Rev.* (2016) **199**:189–256. doi: 10.1007/s11214-014-0057-3
49. Sahraoui F, Belmont G, Goldstein M, Rezeau L. Limitations of multispacecraft data techniques in measuring wave number spectra of space plasma turbulence. *J Geophys Res.* (2010) **115**:1–10. doi: 10.1029/2009JA014724
50. Roberts O, Li X, Jeska L. Validation of the k-filtering technique for a signal composed of random phase plane waves and non-random coherent structures. *Geosci Inform Data Syst.* (2014) **3**:247–54. doi: 10.5194/gi-3-247-2014
51. Perrone D, Alexandrova O, Roberts OW, Lion S, Lacombe C, Walsh A, et al. Coherent structures at ion scales in fast solar wind: cluster observations. *Astrophys J.* (2017) **849**:49. doi: 10.3847/1538-4357/aa9022
52. Podesta JJ, Roberts DA, Goldstein ML. Power spectrum of small-scale turbulent velocity fluctuations in the solar wind. *J Geophys Res.* (2006) **111**:A10109. doi: 10.1029/2006JA011834
53. Matteini L, Alexandrova O, Chen CHK, Lacombe C. Electric and magnetic spectra from MHD to electron scales in the magnetosheath. *Mon Notices R Astron Soc.* (2017) **466**:945–51. doi: 10.1093/mnras/stw3163
54. Bandyopadhyay R, Chasapis A, Chhiber R, Parashar TN, Maruca BA, Matthaeus WH, et al. Solar wind turbulence studies using MMS fast plasma investigation data. *Astrophys J.* (2018) **866**:81. doi: 10.3847/1538-4357/aade93
55. Gershman DJ, Viñas AF, Dorelli JC, Goldstein ML, Shuster J, Avanov LA, et al. Energy partitioning constraints at kinetic scales in low- β turbulence. *Phys Plasmas.* (2018) **25**:022303. doi: 10.1063/1.5009158
56. Roberts OW, Toledo-Redondo S, Perrone D, Zhao J, Narita Y, Gershman D, et al. Ion-scale kinetic Alfvén turbulence: MMS measurements of the Alfvén ratio in the magnetosheath. *Geophys Res Lett.* (2018) **45**:7974–84. doi: 10.1029/2018GL078498
57. Alexandrova O, Mangeney A, Maksimovic M, Cornilleau-Wehrlin N, Bosqued JM, André M. Alfvén vortex filaments observed in magnetosheath downstream of a quasi-perpendicular bow shock. *J Geophys Res.* (2006) **111**:A12208. doi: 10.1029/2006JA011934
58. Alexandrova O. Solar wind vs. magnetosheath turbulence and Alfvén vortices. *Nonlinear Process Geophys.* (2008) **15**:95–108. doi: 10.5194/npg-15-95-2008
59. Perrone D, Alexandrova O, Mangeney A, Maksimovic M, Lacombe C, Rakoto V, et al. Compressive coherent structures at ion scales in the slow solar wind. *Astrophys J.* (2016) **826**:196. doi: 10.3847/0004-637X/826/2/196
60. Roberts OW, Li X, Alexandrova O, Li B. Observation of an MHD Alfvén vortex in the slow solar wind. *J Geophys Res Space Phys.* (2016) **121**:3870–81. doi: 10.1002/2015JA022248
61. Karimabadi H, Roytershteyn V, Vu HX, Omelchenko YA, Scudder J, Daughton W, et al. The link between shocks, turbulence, and magnetic reconnection in collisionless plasmas. *Phys Plasmas.* (2014) **21**:062308. doi: 10.1063/1.4882875
62. Vörös Z, Yordanova E, Echim MM, Consolini G, Narita Y. Turbulence-generated proton-scale structures in the terrestrial magnetosheath. *Astrophys J Lett.* (2016) **819**:L15. doi: 10.3847/2041-8205/819/1/L15
63. Chasapis A, Yang Y, Matthaeus WH, Parashar TN, Haggerty CC, Burch JL, et al. Energy conversion and collisionless plasma dissipation channels in the turbulent magnetosheath observed by the magnetospheric multiscale mission. *Astrophys J.* (2018) **862**:32. doi: 10.3847/1538-4357/aac775
64. Chen CHK, Leung L, Boldyrev S, Maruca BA, Bale S. Ion-scale spectral break of solar wind turbulence at high and low beta. *Geophys Res Lett.* (2014) **41**:8081–8. doi: 10.1002/2014GL062009
65. Bruno R, Trenchi L. Radial dependence of the frequency break between fluid and kinetic scales in the solar wind fluctuations. *Astrophys J Lett.* (2014) **787**:1–5. doi: 10.1088/2041-8205/787/2/L24
66. Wicks RT, Alexander RL, Stevens M, Wilson LB III, Moya PS, Viñas A, et al. A proton-cyclotron wave storm generated by unstable proton distribution functions in the solar wind. *Astrophys J.* (2016) **819**:6. doi: 10.3847/0004-637X/819/1/6
67. Lion S, Alexandrova O, Zaslavsky A. Coherent events and spectral shape at ion kinetic scales in the fast solar wind turbulence. *Astrophys J.* (2016) **824**:1–13. doi: 10.3847/0004-637X/824/1/47

68. He J, Tu C, Marsch E, Chen CHK, Wang L, Pei Z, et al. Proton heating in solar wind compressible turbulence with collisions between counter-propagating waves. *Astrophys J.* (2015) **813**:L30. doi: 10.1088/2041-8205/813/2/L30
69. Hao Y, Lu Q, Gao X, Wang H, Wu D, Wang S. Two-dimensional hybrid simulations of filamentary structures and kinetic slow Waves Downstream of a Quasi-parallel Shock. *Astrophys J.* (2018) **861**:57. doi: 10.3847/1538-4357/aacb2c
70. Zhao JS, Voitenko Y, Yu MY, Lu JY, Wu DJ. Properties of short-wavelength oblique Alfvén and slow waves. *Astrophys J.* (2014) **793**:107. doi: 10.1088/0004-637X/793/2/107
71. Chandran BDG, Quataert E, Howes GG, Xia Q, Pongkitwanichakul P. Constraining low-frequency Alfvénic turbulence in the solar wind using density-fluctuation measurements. *Astrophys J.* (2009) **707**:1668–75. doi: 10.1088/0004-637X/707/2/1668
72. Schekochihin A, Cowley SC, Dorland W, Hammett GW, Howes G, Quataert E, et al. Astrophysical gyrokinetics: kinetic and fluid turbulent cascades in magnetized weakly collisional plasmas. *Astrophys J Suppl Ser.* (2009) **182**:310–77. doi: 10.1088/0067-0049/182/1/310
73. Gogoberidze G, Voitenko YM, Machabeli G. Temperature spectra in the solar wind turbulence. *Mon Notices R Astron Soc.* (2018) **480**:1864–9. doi: 10.1093/mnras/sty1914
74. Safrankova J, Nemeczk Z, Prech L, Zastenker G. Ion kinetic scale in the solar wind observed. *Phys Rev Lett.* (2013) **110**:025004. doi: 10.1103/PhysRevLett.110.025004
75. Šafránková J, Nemeczk Z, Nemec F, Prech L, Chen CHK, Zastenker GN. Power spectral density of fluctuations of bulk and thermal speeds in the solar wind. *Astrophys J.* (2016) **825**:121. doi: 10.3847/0004-637X/825/2/121
76. Servidio S, Valentini F, Perrone D, Greco A, Califano F, Matthaeus WH, et al. A kinetic model of plasma turbulence. *J Plasma Phys.* (2014) **81**:325810107. doi: 10.1017/S0022377814000841
77. Peter Gary S. *Theory of Space Plasma Microinstabilities*. Cambridge, UK: Cambridge University Press (1993). p. 193.
78. Turner AJ, Gogoberidze G, Chapman S, Hnat B, Müller WC. Nonaxisymmetric anisotropy of solar wind turbulence. *Phys Rev Lett.* (2011) **107**:095002. doi: 10.1103/PhysRevLett.107.095002
79. He J, Tu C, Marsch E, Yao S, HuiTian. Possible evidence of alfvén-cyclotron waves in the angle distribution of magnetic helicity of solar wind turbulence. *Astrophys J.* (2011) **731**:85. doi: 10.1088/0004-637X/731/2/85
80. Goldreich P, Sridhar S. Toward a theory of interstellar turbulence. 2: Strong alfvénic turbulence. *Astrophys J.* (1995) **438**:763–75.
81. Cho J, Lazarian A. The anisotropy of electron magnetohydrodynamic turbulence. *Astrophys J.* (2004) **615**:41–4. doi: 10.1086/425215
82. Chen CHK, Wicks RT, Horbury TS, Schekochihin A. Interpreting power anisotropy measurements in plasma turbulence. *Astrophys J.* (2010) **711**:L79–83. doi: 10.1088/2041-8205/711/2/L79
83. Boldyrev S, Perez JC. Spectrum of kinetic-Alfvén turbulence. *Astrophys J.* (2012) **758**:L44. doi: 10.1088/2041-8205/758/2/L44
84. Howes GG, Cowley SC, Dorland W, Hammett GW, Quataert E, Schekochihin AA. A model of turbulence in magnetized plasmas: implications for the dissipation range in the solar wind. *J Geophys Res Space Phys.* (2008) **113**:1–24. doi: 10.1029/2007JA012665
85. Narita Y. Non-elliptic wavevector anisotropy for magnetohydrodynamic turbulence. *Ann Geophys.* (2015) **33**:1413–9. doi: 10.5194/angeo-33-1413-2015
86. Gary SP. Low-frequency waves on a high-beta collisionless plasma: polarization, compressibility and helicity. *J Plasma Phys.* (1986) **35**:431–47.
87. Hadid LZ, Sahraoui F, Galtier S, Huang SY. Compressible magnetohydrodynamic turbulence in the Earth's magnetosheath: estimation of the energy cascade rate using *in situ* spacecraft data. *Phys Rev Lett.* (2018) **120**:055102. doi: 10.1103/PhysRevLett.120.055102
88. Bandyopadhyay R, Chasapis A, Chhiber R, Parashar TN, Matthaeus WH, Shay MA, et al. Incompressible energy transfer in the Earth's magnetosheath: magnetospheric multiscale observations. *Astrophys J.* (2018) **866**:106. doi: 10.3847/1538-4357/aade04
89. Comișel H, Narita Y, Motschmann U. Wavevector anisotropy of plasma turbulence at ion kinetic scales: solar wind observations and hybrid simulations. *Nonlinear Process Geophys.* (2014) **21**:1075–83. doi: 10.5194/npg-21-1075-2014

Conflict of Interest: The authors declare that the research was conducted in the absence of any commercial or financial relationships that could be construed as a potential conflict of interest.

Copyright © 2019 Roberts, Narita, Nakamura, Vörös and Gershman. This is an open-access article distributed under the terms of the Creative Commons Attribution License (CC BY). The use, distribution or reproduction in other forums is permitted, provided the original author(s) and the copyright owner(s) are credited and that the original publication in this journal is cited, in accordance with accepted academic practice. No use, distribution or reproduction is permitted which does not comply with these terms.

APPENDIX

Normalization

The result from the MSR technique is a power spectrum as a function of spacecraft frame frequency ω_{sc} and wavevector \mathbf{k} . For this example velocity units will be used:

$$P_{MSR}(\omega_{sc}, \mathbf{k}) \quad [(\text{km/s})^2 (\text{s rad})] \quad (\text{A1})$$

To estimate the spectrum $P_{MSR}(\mathbf{k})$ an integration needs to be performed over ω_{sc} ,

$$P_{MSR}(\mathbf{k}) = \int P_{MSR}(\omega_{sc}, \mathbf{k}) d\omega_{sc} \quad [(\text{km/s})^2] \quad (\text{A2})$$

The power spectrum can be expressed in cylindrical coordinates:

$$P_{MSR}(\mathbf{k}) = P_{MSR}(k_{\parallel}, k_{\perp}, \phi) \quad (\text{A3})$$

To convert to a one dimensional spectrum the spectrum is averaged azimuthally:

$$P_{MSR}(k_{\parallel}, k_{\perp}) = \frac{1}{2\pi} \int_0^{2\pi} P_{MSR}(k_{\parallel}, k_{\perp}, \phi) d\phi \quad [(\text{km/s})^2] \quad (\text{A4})$$

This is then folded along the line $k_{\parallel} = 0$ (summed together and divided by 2) so there are only positive such that there are only positive components of k_{\parallel} .

A dimension conversion to spectral density in the wavevector domain;

$$P'_{MSR}(k_{\parallel}, k_{\perp}) = \frac{1}{\Delta k} P_{MSR}(k_{\parallel}, k_{\perp}) \quad [\text{km}^3/(\text{s}^2 \text{ rad})] \quad (\text{A5})$$

where the prime denotes the change of units. A one dimensional cut of the spectrum is taken such that:

$$P'_{MSR \text{ 1D}}(k_{\parallel}) = P'_{MSR}(k_{\parallel}, k_{\perp \text{ min}}) \quad (\text{A6})$$

Finally normalization to the fluctuation variance which assumes ergodicity of the signals reads:

$$E_{MSR \text{ 1D}}(k_{\parallel}) = \frac{\sigma^2}{P_{MSR \text{ Total}}(k_{\parallel})} P'_{MSR \text{ 1D}}(k_{\parallel}) \quad [\text{km}^3/(\text{s}^2 \text{ rad})] \quad (\text{A7})$$

where σ^2 is the variance measured in the time domain:

$$\sigma^2 = \frac{1}{T} \int |\delta \mathbf{V}_A|^2 dt \quad [(\text{km/s})^2] \quad (\text{A8})$$

The spectrum in Equation (A7) normalized to the variance over the total power:

$$P_{MSR \text{ Total}}(k_{\parallel}) = \sum_{k_{\parallel}} P_{MSR \text{ 1D}}(k_{\parallel}) \quad [(\text{km/s})^2] \quad (\text{A9})$$

Similarly to normalize the spectrum in the spacecraft frame time domain,

$$P_{TS}(f) \quad [(\text{km/s})^2 \text{ s}] \quad (\text{A10})$$

we convert the units by Taylor's hypothesis.

$$P_{TS}(k_s) = \int P_{TS}(f) \delta(2\pi f - k_s V_i) df \quad [(\text{km/s})^2] \quad (\text{A11})$$

Where k_s is the streamwise wave-number. The dimensions are then converted into the spectral density in the wave-number domain,

$$P'_{TS}(k_s) = \frac{\Delta f}{\Delta k} P_{TS}(k_s) \quad [\text{km}^3/(\text{s}^2 \text{ rad})] \quad (\text{A12})$$

This is normalized in the same way as for the MSR spectrum for the purpose of comparison:

$$E_{TS \text{ norm}}(k_s) = \frac{\sigma^2}{\sum_{k_s} P'_{TS}(k_s)} P'_{TS}(k_s) \quad [\text{km}^3/(\text{s}^2 \text{ rad})] \quad (\text{A13})$$



Discovery of an Electron Gyroradius Scale Current Layer: Its Relevance to Magnetic Fusion Energy, Earth's Magnetosphere, and Sunspots

OPEN ACCESS

Edited by:

Benoit Lavraud,

UMR5277 Institut de Recherche en Astrophysique et Planétologie (IRAP), France

Reviewed by:

Amy Catherine Rager,

The Catholic University of America, United States

Shan Wang,

University of Maryland, College Park, United States

*Correspondence:

Jaeyoung Park

jyparknm@gmail.com

†Present address:

Jaeyoung Park,

TAE Technologies, Foothill Ranch, CA, United States

Specialty section:

This article was submitted to

Plasma Physics,

a section of the journal

Frontiers in Astronomy and Space Sciences

Received: 14 October 2019

Accepted: 21 November 2019

Published: 13 December 2019

Citation:

Park J, Lapenta G, Gonzalez-Herrero D and Krall NA (2019) Discovery of an Electron Gyroradius Scale Current Layer: Its Relevance to Magnetic Fusion Energy, Earth's Magnetosphere, and Sunspots.

Front. Astron. Space Sci. 6:74.
doi: 10.3389/fspas.2019.00074

Jaeyoung Park^{1*†}, Giovanni Lapenta², Diego Gonzalez-Herrero² and Nicholas A. Krall¹

¹ Energy Matter Conversion Corporation, San Diego, CA, United States, ² Department of Mathematics, KU Leuven, University of Leuven, Leuven, Belgium

In the Earth's magnetosphere, sunspots and magnetic cusp fusion devices, the boundary between the plasma and the magnetic field is marked by a diamagnetic current layer with a rapid change in plasma pressure and magnetic field strength. First principles numerical simulations were conducted to investigate this boundary layer with a spatial resolution beyond electron gyroradius while incorporating a global equilibrium structure. The boundary layer thickness is discovered to be on the order of electron gyroradius scale due to a self-consistent electric field suppressing ion gyromotion at the boundary. Formed at the scale of the electron gyroradius, the electric field plays a critical role in determining equilibrium structure and plasma transport. The discovery highlights the necessity to incorporate electron gyroradius scale physics in studies aimed at advancing our understanding of fusion devices, the magnetosphere and sunspots.

Keywords: plasma diamagnetism, magnetic cusps, electron gyroradius scale current layer, plasma particle simulation, boundary layer phenomena

INTRODUCTION

In many plasma systems, the plasma is surrounded by magnetic fields leading to a fascinating array of natural and manmade phenomena. Plasma jet formation from accretion disks, Earth's magnetosphere, sunspots, and magnetic fusion devices are examples of plasma interaction with magnetic fields. At the boundary between the plasma and the magnetic field, if there is a change in plasma pressure or magnetic field strength, gyromotions of electrons and ions generate current, known as diamagnetic current, separating the plasma, and magnetic field (Krall and Trivelpiece, 1973). Among examples of plasma diamagnetic effects are the magnetopause in the Earth's magnetosphere, sharp boundary layers in magnetic cusp fusion devices, and the dark patches of sunspots (Hale, 1908; Chapman and Ferraro, 1930; Berkowitz et al., 1958; Braginskii and Kadomtsev, 1959; Sonnerup and Cahill, 1967; Spalding, 1971; Borrero and Ichimoto, 2011). In these systems, a diamagnetic current layer marks the boundary across which plasma penetration or loss to the magnetic field region is greatly reduced. The diamagnetic effect in these systems has been studied extensively, leading to the development of magnetohydrodynamics (MHD), the standard model for many solar, astrophysics and fusion plasmas over the past 50 years (Alfvén, 1942; Cowling, 1957).

However, an *ab initio* solution of plasma diamagnetic effects had remained elusive with some of the most fundamental questions yet to be answered (Alfvén, 1963). For example, there has been no definitive answer to the thickness of the diamagnetic current layer. Also unknown are the respective contributions of ions and electrons to the plasma diamagnetic current since there is significant difference in their gyroradii, a factor of 43 in the case of hydrogen ions at the same temperature as electrons. The lack of understanding remains because we are still trying to understand plasma dynamics at the scale of the electron gyroradius, the fundamental, yet smallest, length scale of plasma diamagnetism. While there have been many theoretical and numerical studies to investigate the boundary layer structure, these studies have been limited due to geometrical complexities and technical challenges and have been unable to resolve electron gyroradius scale physics while incorporating the global equilibrium structure (Dungey, 1961; Grad, 1961; Haines, 1977; Berchem, 1990; Bessho et al., 2016). At the same time, a number of observations indicate the importance of electron scale phenomena at the boundary such as formation of electron scale ion flow in laboratory magnetic cusp experiments (Hershkowitz et al., 1975). The recently launched Magnetospheric Multiscale (MMS) mission, designed to make electron scale plasma measurements, has started to generate observational data in the magnetopause demonstrating the importance of electron dynamics in magnetic reconnection and turbulence (Burch et al., 2016; Goodrich et al., 2016; Phan et al., 2018; Rager et al., 2018).

To explore the diamagnetic current layer on the electron gyroradius scale, we utilized a first-principles particle-in-cell (PIC) code, called the Energy Conserving semi-implicit model (ECsim), using its cylindrical coordinate implementation (Lapenta, 2012, 2017; Gonzalez-Herrero et al., 2019). The Ecsim simulates a collisionless plasma by solving Newton's equation for particle motion and Maxwell's equations for electric and magnetic fields, while conserving system energy. The simulations were conducted for a cylindrically symmetric magnetic cusp system known as the "Picket Fence" that was proposed as a magnetic confinement system for fusion energy, as shown in **Figure 1** (Tuck, 1958). In this configuration the magnetic field is expelled to a boundary layer close to the magnets while the plasma filled region is primarily devoid of any magnetic field: a most classical example of plasma diamagnetism. This magnetic field configuration is topologically reminiscent of the dayside Earth magnetosphere where the convex curvature of the Earth's dipole magnetic field faces the solar wind (Spalding, 1971; Berchem, 1990; Russell and Kivelson, 1995; Kallenrode, 2004). In this transition region, called the magnetosheath, the plasma has much higher density and lower magnetic field than the magnetospheric side closer to Earth. Another example of strong diamagnetism in astrophysics is that of sunspots (Kallenrode, 2004) where a region of low density and high magnetic field appears as a dark spot on the photosphere and is surrounded by a higher density and lower magnetic field environment. In all these examples the curvature of the magnetic field is directed in the same way as the density gradient: the high density is on the convex side of the curved magnetic field lines: the magnetic field lines wrap around the lower density higher magnetic field

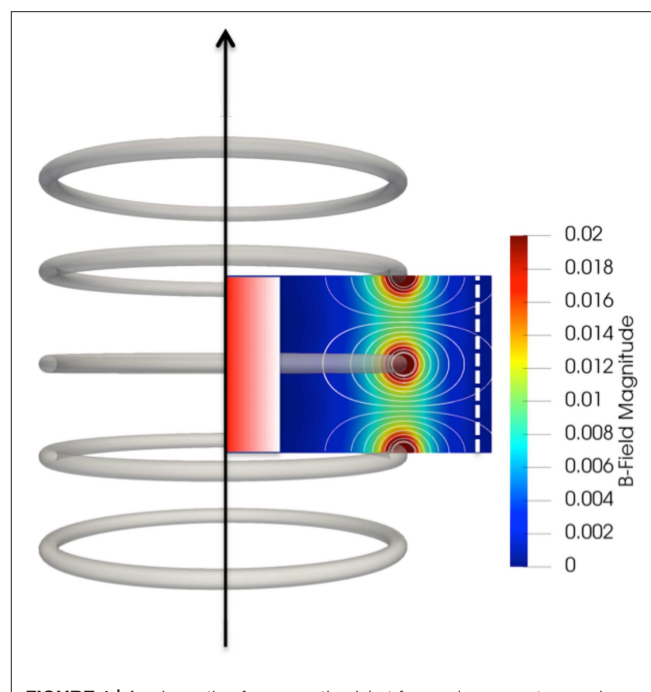


FIGURE 1 | A schematic of a magnetic picket fence plasma system and simulation domain. The schematic shows the contours of magnetic field magnitude and magnetic field lines from the coils without the presence of plasma. The plasma injection region in the central part of the picket fence is shown in graded red and the loss boundary is shown at the right side of the simulation domain as a dotted line.

region. Under these conditions the plasma is stable to interchange modes, a motive why the magnetosphere and sunspots are stable features and why the magnetic cusp concept is attractive as a magnetic fusion confinement device.

METHOD

In the present work, PIC simulations were used to investigate this boundary layer as a function of plasma pressure and ion mass with a spatial resolution beyond electron gyroradius while incorporating the global equilibrium structure. The exploration led to the discovery of a localized electric field at the electron gyroradius scale that transforms our understanding of plasma diamagnetic effects. Further details of the Ecsim code and simulation method are given in the **Supplementary Material**.

Figure 1 shows a schematic of a magnetic picket fence system used in the simulation. It consists of series of circular coils arranged along the vertical axis with opposite coil current direction between adjacent coils. These coils produce zero magnetic field near the central region near the axis and form a magnetic field wall near the coils. The magnetic picket fence was proposed by Tuck in 1954 as a magnetic confinement system to produce thermonuclear fusion reactions (Tuck, 1958). The picket fence is one of the magnetic confinement systems called "magnetic cusps," that are known to be stable against many of plasma instabilities (Berkowitz et al., 1958; Krall and Trivelpiece,

1973). In this report, the magnetic picket fence system was chosen for the following reasons.

1. Perfect magnetic field shielding by plasma diamagnetism has been experimentally observed in various magnetic cusp systems designed for fusion energy research (Spalding, 1971; Kitsunezaki et al., 1974; Haines, 1977; Pechacek et al., 1980). As such, the magnetic cusp system is well-suited to investigate diamagnetic effects of plasma. In addition, the magnetic field configuration of the picket fence is topologically identical to the dayside Earth magnetosphere with the convex curvature of the Earth's magnetic field facing the solar wind as well as the magnetic fields of sunspots (Spalding, 1971; Berchem, 1990; Kallenrode, 2004).
2. Due to their favorable magnetic field curvature, magnetic cusp systems have been shown to be stable against most, if not all, of macroscopic plasma instabilities in theory. This is because plasma must do work compressing the magnetic field if it expands at the boundary since the magnetic field is curved into the plasma on every surface. The lack of plasma instabilities in magnetic cusp systems has also been reported in many past experiments. This allows the simulation of underlying equilibrium to reach steady-state or at least quasi-steady state in a couple of plasma transit times, as determined by the slower species, i.e., ions.
3. A magnetic picket fence can be simulated with the periodic boundary condition in the axial direction. Most proposed fusion reactor configurations based on magnetic cusp system utilize many pairs of magnetic coils to provide sufficient reactor volume and needed confinement (Dolan, 1994). In the case of a magnetic picket fence utilizing many pairs of coils along the axial direction, the periodic boundary condition is a good approximation in the central region of the picket fence as shown in **Figure 1**. In the present study, a set of 27 coils are used in the simulation to provide the external magnetic field that is nearly periodic along the symmetric axis with 3 coils in the middle are inside the simulation domain as shown in **Figure 1**. In addition, the plasma refueling can be achieved by injection from the both ends to achieve steady-state operation, corresponding to volumetric plasma injection near the axis used as in the simulation.

For the study reported, we utilize a fully kinetic description of the equilibrium between plasma and magnetic field, where both electrons and ions are followed as particles interacting via electric and magnetic fields generated by the particles themselves as well as by the coils. The approached followed is the electromagnetic particle in cell (PIC) method. The full set of Maxwell's equations is discretized on a grid where particle moments are collected via first order basis spline interpolation to calculate the sources for Maxwell's equations. In the present paper, we utilized the Energy Conserving semi-implicit method (ECsim) in its cylindrical implementation called Ecsim-CYL (Lapenta, 2012, 2017; Gonzalez-Herrero et al., 2019) based on azimuthal symmetry of magnetic picket fence system. The Ecsim-CYL solves the field equations in two-dimensional (2D) cylindrical coordinates using a finite volume method. For the particles,

it solves all three components of velocity vectors, while only keeping radial and axial coordinates of particle positions. The numerical algorithm of Ecsim-CYL has been tested previously for accuracy and convergence (Gonzalez-Herrero et al., 2019).

We utilized the Ecsim-CYL code to investigate the plasma diamagnetic effects for the following reasons. The Ecsim-CYL conserves the system energy precisely down to machine precision even when the grid and time resolution severely under-resolve the electron plasma frequency or the electron Debye length. This energy conservation allows the simulation to operate without any artificial smoothing. While the field or the particle moment smoothing helps with noise and numerical stability, the use of smoothing leads to the violation of energy conservation and may disrupt the diamagnetic boundary layer leading to an artificially greater layer thickness caused by numerical effects rather than physical effects. Though, in principle, it is possible to avoid the under sampling of electron plasma frequency or Debye length, the numerical cost can be very high, about a factor of 100 or more for the plasma parameter spaces as shown in **Table 1**. This is because the Debye length is about a factor of 10 smaller than the electron gyroradius. This additional computational cost needs to be multiplied by each dimension, leading to a factor of 100 increase in 2D cylindrical geometry. On the other hand, the implicit PIC codes, such as Ecsim, have successfully demonstrated the ability to resolve critical electric field generation regarding charge separation between electrons and ions even when they are under sampling the Debye length (Gonzalez-Herrero et al., 2019). Considering that each run in **Table 2** already requires 10,000–150,000 CPU hours to generate an equilibrium solution, the use of the energy conserving algorithm of Ecsim was critical to resolve electron gyroradius scale physics in the boundary layer with built-in energy conservation. It is noted that the system energy is conserved to machine precision at all resolutions reported.

The results from the Ecsim code are presented using normalized code units (NCU) that are non-dimensional. The use of NCU allows the simulation results to be converted to various physical systems over a wide range of parameters. As such, we provide two physical examples where the results from the single simulation are converted to plasma parameters relevant to magnetic fusion devices and the Earth's magnetopause as shown in **Table 1**. In Ecsim, time is normalized to the ion plasma frequency, ω_{pi} , determined by the reference plasma density n_0 , as $\omega_{pi} = (n_0/m_i)^{0.5}$, where ω_{pi} is the ion plasma frequency and m_i is the ion mass in NCU. Electron plasma frequency is defined similarly, as $\omega_{pe} = (n_0/m_e)^{0.5}$, where ω_{pe} is the electron plasma frequency and m_e is the ion mass in NCU. Velocities are normalized to the speed of light that is set at 1. Distances are normalized to the ion inertial length, as $d_i = c/\omega_{pi}$. Separately, the charge of electrons and ions is set at 1 and the permittivity and permeability of free space, and Boltzmann coefficient are also set at 1 in NCU. Details of the unit conversion between the NCU and the physical system are provided in the **Supplementary Materials**.

Each simulation begins with plasma injection of electrons and ions from the center of the picket fence to achieve the preset

TABLE 1 | Summary of simulation parameters and results.

Variables	Run 1	Run 8	Magnetic fusion	Unit	Magneto-pause	Unit
Domain size	45 × 30	45 × 30	14.7 × 9.8	cm	148 × 99	km
Grid size	0.083	0.25	0.082	cm	0.82	km
Coil diameter	60	60	19.8	cm	197.6	km
Coli spacing	15	15	4.9	cm	49.4	km
Time step	0.125	0.25	2.75E-12	s	3.23E-05	s
Electron mass	1.56E-02	0.0156	9.1E-31	kg	9.1E-31	kg
Ion mass	1	28.69	1.67E-27	kg	1.67E-27	kg
Electron thermal speed	7.35E-02	7.35E-02	2.20E+09	cm/s	3.75E+08	cm/s
Ion thermal speed	9.19E-03	1.71E-03	5.14E+07	cm/s	8.76E+06	cm/s
Electron & Ion kinetic energy	8.44E-05	8.44E-05	2.77E+03	eV	80	eV
Mean value at the boundary along line 1						
Current layer thickness	0.6	0.9	0.297	cm	2.96	km
B-field	4.1E-03	4.0E-03	1325	Gauss	22.52	nT
Plasma density	0.12	0.120	2.0E+13	/cc	20.0	/cc
Electron gyroradius	0.28	0.29	0.094	cm	0.95	km
Ion gyroradius	2.24	12.30	4.05	cm	40.5	km
Debye length	0.027	0.027	8.74E-03	cm	0.015	km
Ion inertial length	2.89	15.46	5.10	cm	51.0	km
Electron transit time	8.16E+02	8.16E+02	8.97E-09	s	5.27E-02	s
Ion transit time	6.53E+03	3.50E+04	3.84E-07	s	2.26E+00	s

This table compares the various simulation parameters and results from Run 1 and Run 8 using normalized code unit (NCU) and simulation parameters and results of Run 8 converted for two plasma regimes relevant for a magnetic fusion system and the Earth's magnetopause.

TABLE 2 | Summary of simulation runs with key parameters.

Run ID	Case	Vol. avg. pressure	Ion mass (in me)	Grid size	Time step	Number of particles
1	Baseline	5.2E-05	64	g4: 540 × 360	0.25	172 M
2	Pr-0.12	1.2E-06	64	g2: 180 × 120	0.25	11 M
3	Pr-0.77	7.7E-06	64	g2: 180 × 120	0.25	11 M
4	Pr-5.2	5.2E-05	64	g2: 180 × 120	0.25	11 M
5	Pr-7.3	7.3E-05	64	g2: 180 × 120	0.25	18 M
6	Mass-1	5.2E-05	1	g2: 180 × 120	0.25	11 M
7	Mass-16	5.3E-05	16	g2: 180 × 120	0.25	11 M
8	Mass-1836	5.0E-05	1836	g2: 180 × 120	0.25	12 M
9	g0	5.2E-05	64	g0: 45 × 30	0.25	0.67 M
10	g1	5.2E-05	64	g1: 90 × 60	0.25	2.7 M
11	g2	5.2E-05	64	g2: 180 × 120	0.25	11 M
12	g3	5.2E-05	64	g3: 360 × 240	0.25	76 M
13	N80	5.2E-05	64	g2: 180 × 120	0.25	0.73 M
14	N320	5.2E-05	64	g2: 180 × 120	0.25	2.9 M
15	N1280	5.2E-05	64	g2: 180 × 120	0.25	11 M
16	N5120	5.2E-05	64	g2: 180 × 120	0.25	47 M
17	dt-0.125	5.2E-05	64	g2: 180 × 120	0.125	11 M
18	dr-0.5	5.2E-05	64	g2: 180 × 120	0.5	11 M
19	Mass-4	5.2E-05	4	g2: 180 × 120	0.25	11 M
20	Mass-256	5.0E-05	256	g2: 180 × 120	0.25	11 M

Results from Run 1 through 12 are discussed in the main text and the results from Run 13–20 are discussed in the **Supplementary Materials**.

plasma pressure and ends when the equilibrium reaches quasi-steady state as shown in **Figure 2**. The red graded region in **Figure 1** shows the area of volumetric plasma injection. In NCU with the length scale normalized to ion inertial length, the size of the simulation domain is 45 in radius and 30 in height or axial length, as shown in **Figure 3d**, while the injection region is 9 in radius and 30 in height. Coils in the picket fence have a diameter of 60 and the spacing between two adjacent coils is 15. During initialization, ions and electrons are injected with the same temperature with an electron thermal velocity of 7.35×10^{-2} times the speed of light in NCU. The ion thermal velocity, on the other hand, is adjusted as a function of ion mass to maintain the same temperature for both species. A typical time step is $0.25/w_{pi}$, during which a thermal electron travels $1.84 \times 10^{-2}/d_i$ and a thermal ion travels $2.3 \times 10^{-3}/d_i$ in NCU. Once injected, the plasma expands and fills the picket fence system while interacting with the externally applied magnetic field. During expansion, the plasma expels a magnetic field from the plasma and forms a boundary. The temporal duration of the injection phase is $8,000/w_{pi}$, corresponding to 10 times the electron transit time or 1.2 times the ion transit time for the ion mass of $m_i = 64 m_e$. The transit time is defined as the time for thermal ions and electrons to move across one coil diameter. The injection is conducted incrementally for 160 times during the initialization phase with an equal amount of plasma injections leading to gradual increases in the total kinetic energy of the plasma in the picket fence and plasma diamagnetic effects as shown in the top row of **Figure 2**. Incremental injection is used to build up plasma pressure in the picket fence gradually without generating shocks or significant plasma flow, to investigate the quiescent equilibrium between the static plasma pressure and magnetic field pressure.

Once the preset plasma pressure is reached in the picket fence, the initialization phase is complete and the system is relaxed toward a steady-state, as shown in **Figure 2**. During the steady-state phase, plasma is maintained by incremental injection in the same central region of the picket fence to replenish the loss of plasma from the picket fence to the loss boundary at the right end of the simulation domain. The loss boundary is simulated as an absorbing wall for particles and electromagnetic waves, shown as a dotted line in **Figure 1**. It is located at $r = 42$, away from the coils at $r = 30$ to prevent the presence of the wall from affecting plasma equilibrium inside the picket fence. Nominally, the injection rate to sustain the plasma during the steady-state phase is ~ 18 times lower than the injection rate during the initialization phase. For example, a charge injection rate of ~ 3 per $22.5/w_{pi}$ is utilized to maintain a constant total charge of 1.89×10^4 in the picket fence system for Run 1 in **Table 2** during the steady-state. This injection rate corresponds to a particle confinement time of $1.1 \times 10^5/w_{pi}$, equivalent to ~ 135 electron transit time or ~ 17 ion transit time. While the injection rates for ions and electrons are allowed to vary from each other while replenishing their respective charge loss, the plasma loss quickly satisfies the ambipolar condition with equal loss of electrons and ions from the picket fence to the absorbing wall as shown in the bottom row of **Figure 2**. On the other hand, plasma injection during the steady-state phase requires

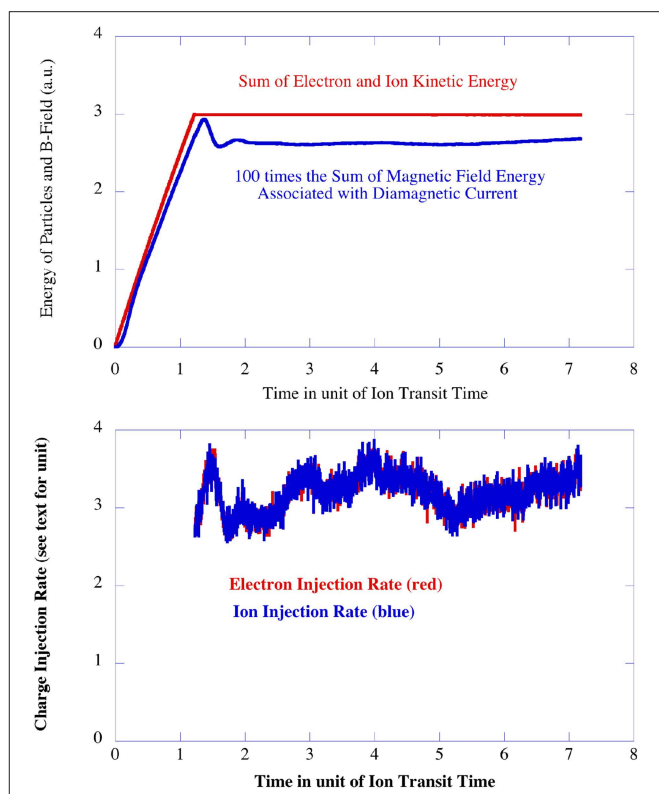


FIGURE 2 | A temporal setup showing the initialization phase and the steady-state phase in the simulation using a unit of ion transit time across the coil diameter of the picket fence. The top row shows the sum of particle kinetic energy in the simulation domain and the sum of magnetic field energy associated with diamagnetic current by the plasma multiplied by 100. The bottom row shows temporal variation of plasma injection rates for electrons and ions to sustain the constant total charge and total particle kinetic energy in the system. The results are from Run 4.

more kinetic energy per injected particles compared to plasma injection during the initialization phase by a factor of 2.5–3. This is equivalent to the energy confinement time of the system being 2.5–3 times shorter than the particle confinement time. A shorter energy confinement time is typical in most plasma systems as higher energy particles leave the systems faster than lower energy particles.

Nominally, the simulation is conducted for a minimum of 2.2 times the ion transit times after the initialization phase to ensure steady-state. By then, all equilibrium properties such as plasma density, current density, plasma pressure, plasma flow and magnetic field are nearly constant in space and time. As shown in M1 and M2 (Movies in **Supplementary Materials**), the location and the width of the boundary layer are constant with less than one to two pixels variation. The M1 is from Run 8 in **Table 2** that covers 7 ion transit times from beginning to an end and the M2 is from Run 1 in **Table 2** that covers to 3.5 ion transit time from the beginning to an end. Note that the sudden changes in radial ion mass flow, shown in the movies, are related to transition from the initialization phase to the steady-state phase, which involves change in plasma injection rate by a factor of ~ 18 .

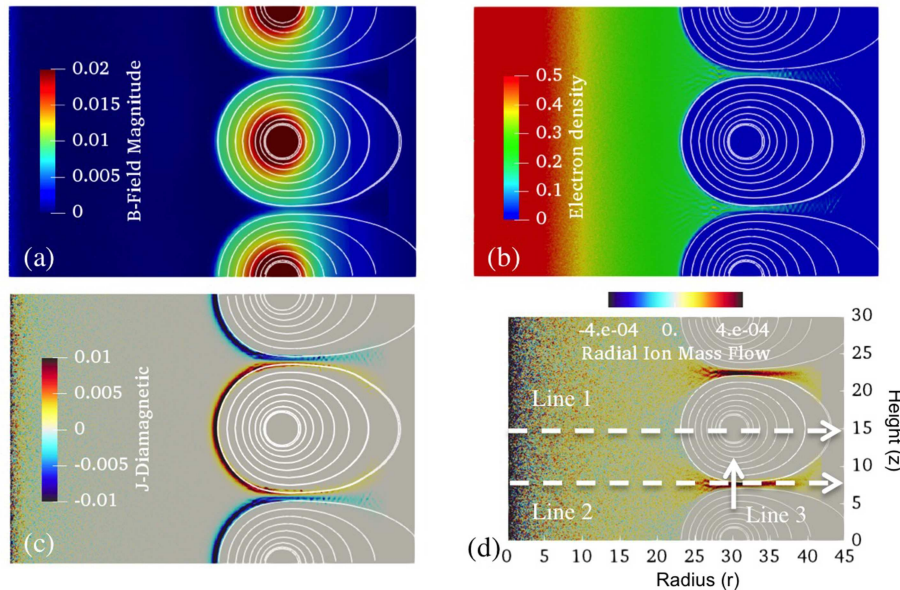


FIGURE 3 | Steady-state equilibrium profiles. Equilibrium profiles show contours of **(a)** magnitude of B-field, **(b)** electron density, **(c)** diamagnetic current density, and **(d)** radial ion mass flow with magnetic field lines from Run 1 in **Table 2**. Three lines of interest are defined in **(d)** for further analysis with Line 1 ($r = 0\text{--}45$ at $z = 15$), Line 2 ($r = 0\text{--}45$ at $z = 7.5$), and Line 3 ($r = 30$, $z = 4\text{--}11$).

For the present study, we have conducted systematic studies of equilibrium between the plasma and magnetic field as a function of plasma pressure and ion mass for a constant electron mass. In addition, several additional tests were conducted to ensure the numerical convergence with variation in grid size, time step, and number of simulation particles. **Table 2** summarizes the key parameters used in the simulations.

In summary, plasma dynamics in the magnetic picket fence system has been simulated using a fully kinetic PIC code to investigate diamagnetic effects. The simulations utilize the cylindrical symmetry in the angular direction and the periodic boundary condition in axial direction while preserving a dipole nature of the magnetic field in the simulation. A steady-state equilibrium is produced by injection of the plasma in the central part of the picket fence and the plasma loss boundary that absorbs ions and electrons that leak out of the picket fence system, as shown in **Figure 1**. It is noted that fully a kinetic PIC simulation of the diamagnetic current layer requires significant High Performance Computing (HPC) resources even in the simple geometrical setup of an axisymmetric magnetic picket fence system. Typical runs employ between 300 and 1,200 CPUs and require between 10,000 and 150,000 CPU hours to simulate the steady-state equilibrium while resolving electron gyroradius with satisfactory numerical convergence.

RESULTS

Steady-State Equilibrium

Figure 3 shows the steady-state equilibrium profile of a magnetic picket fence with a sharp boundary between plasma and magnetic field from Run 1 in **Table 2**. From right to left, the magnetic

field exhibits rapid decay across the boundary, leading to a field-free plasma region in the picket fence, as shown in **Figure 3a**. From left to right, the electron density profile exhibits similarly rapid decay across the boundary, leading to a plasma-free magnetic field region near the magnetic coils, as shown in **Figure 3b**. Across the boundary, layers of highly localized current are formed from plasma gyromotion separating plasma and magnetic field, as shown in **Figure 3c**. In addition, collimated ion flows are formed in the funnel-shaped cusp region, resulting in plasma leakage via the gap between the opposing sign of current layers, as shown in **Figure 3d**. For further analysis, three lines of interest are defined in **Figure 3d** to describe the boundary between plasma and magnetic field, as described in the Method section. While exhibiting distinctively different equilibrium properties along Lines 1, 2, and 3, the different regions of equilibrium are interconnected by plasma motion and magnetic field, highlighting the necessity of incorporating the global equilibrium structure when investigating boundary layers.

Figure 4 shows steady-state equilibrium profiles as a function of volume averaged plasma pressure for Runs 2, 3, 4, and 5 in **Table 2** to investigate the change in equilibrium from plasma pressure change. The top row shows magnitude of magnetic field contours with magnetic field lines drawn to highlight the change in boundary location. The second row shows plasma diamagnetic current density (note that the direction of diamagnetic current is in and out of the plane), with the third row showing electron density and the fourth row showing ion mass flow in a radial direction. Along Line 1 as defined in **Figure 3d**, the boundary between plasma and magnetic field exhibits similar behavior for all four values of pressure. The increase in plasma pressure is balanced by the compression of the

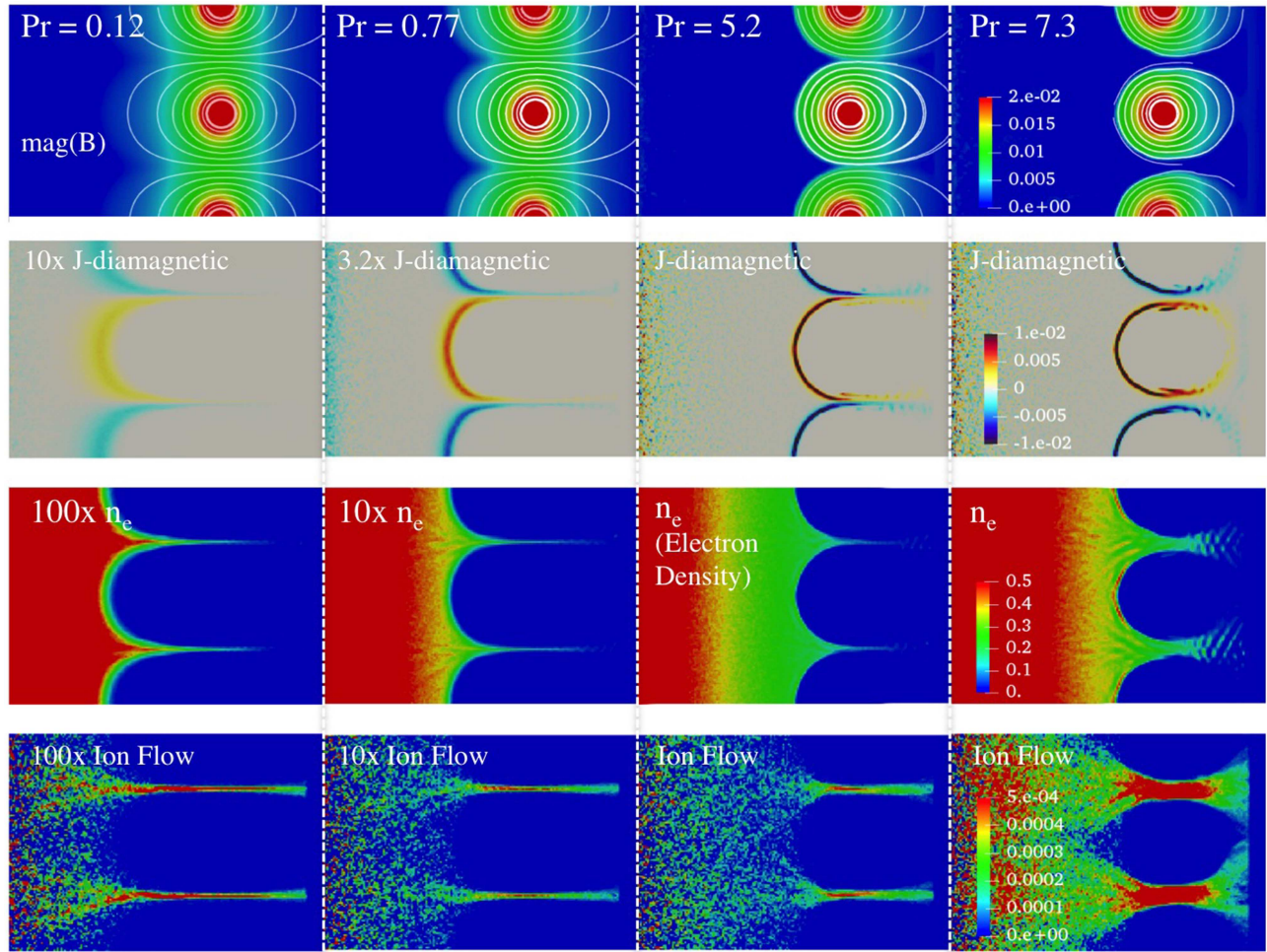


FIGURE 4 | Steady-state equilibrium profiles as a function of plasma pressure. Equilibrium profiles show magnetic field magnitude (top row), diamagnetic current density (second row), electron density (third row), and radial ion mass flow as a function of plasma pressure (fourth row) in the picket fence for four different volume averaged pressure values of 1.2×10^{-6} (First column from the left), 7.7×10^{-6} (second column), 5.2×10^{-5} (third column) and 7.3×10^{-5} (fourth column) from Runs 2, 3, 4, and 5 in **Table 2**. The current, density and flow profiles from the pressures of 7.7×10^{-6} and 5.2×10^{-5} are multiplied by different factors as noted in plots to utilize the same color scales shown on the fourth column.

magnetic field. The boundary, marked by localized current layers moves toward the higher magnetic field region near the coils and the thickness of the current layer decreases. In comparison, there are significant differences in equilibrium along Lines 2 and 3. For pressures of 1.2×10^{-6} , 7.7×10^{-6} , and 5.2×10^{-5} in NCU, the plasma is still bounded by the magnetic wall of the picket fence. At these pressures, diamagnetic current layers converge toward narrow gaps in the cusp region coinciding with collimated ion flow. When the pressure is increased to 7.3×10^{-5} in NCU, the magnetic wall fails along Line 2. While the current layers still converge toward each other, the gap between them is no longer narrow, with significantly wider density profile along Line 3 and increased radially outward ion flow.

Several features of the steady-state equilibrium in a magnetic picket fence in **Figures 3, 4** can be explained in a gross way with the standard MHD model. Equation (1) shows

the Momentum transport equation of the standard MHD model (Krall and Trivelpiece, 1973).

$$\rho \left(\frac{\partial V}{\partial t} + V \cdot \nabla V \right) = \frac{J \times B}{c} - \nabla p \quad (1)$$

where ρ is the mass density of plasma, V is the plasma flow velocity, J is the current density, B is the magnetic field strength, c is the speed of light and p is the plasma pressure. In a steady-state equilibrium, the first term on the left-hand side (*lhs*) becomes zero, leading to the relationship known as the pressure balance equation among plasma flow, current, magnetic field, and plasma pressure.

Along Line 1, the pressure balance between the plasma and magnetic field forms the boundary with diamagnetic current layers to match the change in magnetic field without plasma flow. With increasing plasma pressure, the boundary moves

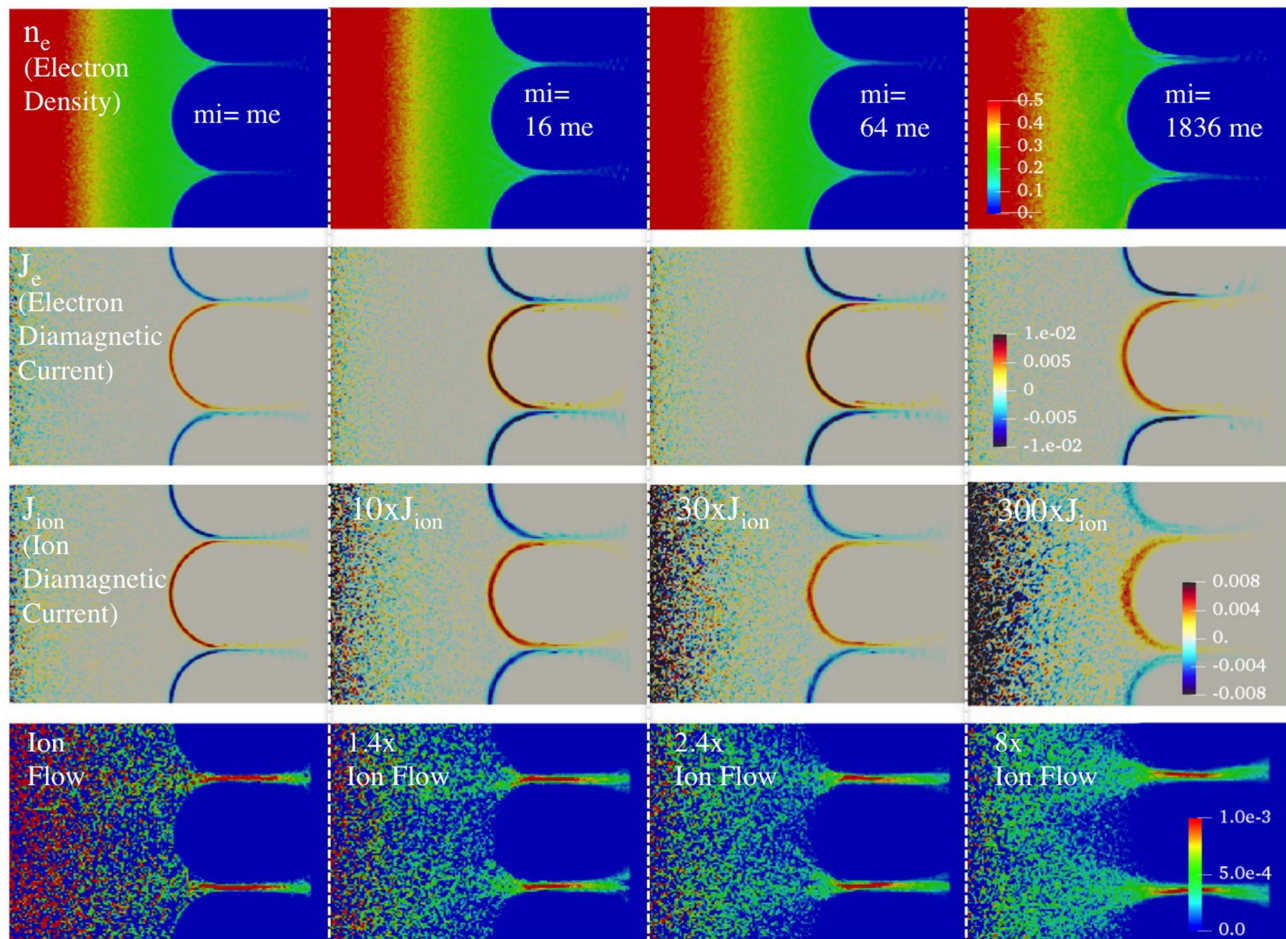


FIGURE 5 | Steady-state equilibrium as a function of ion mass. Equilibrium profiles show electron density (top row), electron diamagnetic current density (second row), ion diamagnetic current density (third row) and radial ion mass flow (fourth row) for 4 different ion masses of $m_i = m_e$ (first column from the left, from Run 6), $m_i = 16 m_e$ (second column, from Run 7), $m_i = 64 m_e$ (third column, from Run 4) and $m_i = 1,836 m_e$ (fourth column, from Run 8). To fit in the same color scales shown on the fourth column, the ion diamagnetic current density and ion flow are multiplied by different factors as noted in plots to utilize the same color scales shown on the fourth column.

to the higher B-field region as the plasma works against the magnetic field that is compressible. Since the boundary layer thickness depends on the gyromotion of the plasma, the layer thickness decreases with increasing plasma pressure as previously discussed. In comparison, the pressure gradient along Line 2 generates radially outward plasma flow from the central part of magnetic picket fence toward magnetic cusp openings between two adjacent coils as shown in **Figures 3, 4**. Past the magnetic cusp openings, the plasma flow then decreases as the magnetic flux expands and the plasma density decreases. Along Line 3, the magnetic field decreases in the plasma region with increasing plasma pressure due to the diamagnetic effects. If the plasma pressure becomes sufficiently high, the magnetic field inside the narrow gap becomes zero as the diamagnetic current provides complete shielding of the magnetic field by plasma. A further increase in the plasma pressure moves the boundary toward the coils similar to the boundary movement along Line 1, opening up the gap and leading to rapid leakage of plasma. Based on the similarity of magnetic field topology, the boundary layers along

Line 1 and Line 3 correspond to the magnetopause and sunspot boundary, while collimated plasma flow along Line 2 corresponds to plasma loss to Earth's polar cusp region.

Equilibrium as a Function of Ion Mass

Figure 5 shows plasma profiles in steady-state equilibrium for four different ion masses of $m_i = m_e$, $16 m_e$, $1,836 m_e$ from Runs 6, 7, 8, and $m_i = 64 m_e$ from Run 4 in **Table 1**. This study investigates the different roles of electrons and ions in determining equilibrium and boundary layer structure using a mass ratio between electrons and ions as a functional variable. The electron mass is kept constant and the ion mass is varied with the same temperature between electrons and ions. This results in an increase of ion gyroradius with respect to electron gyroradius. For example, the ion gyroradius for $m_i = 1,836 m_e$ is 43 times larger than the ion gyroradius for $m_i = m_e$. The top row of **Figure 5** shows electron density profiles. The second row shows electron diamagnetic current density, and the third row shows

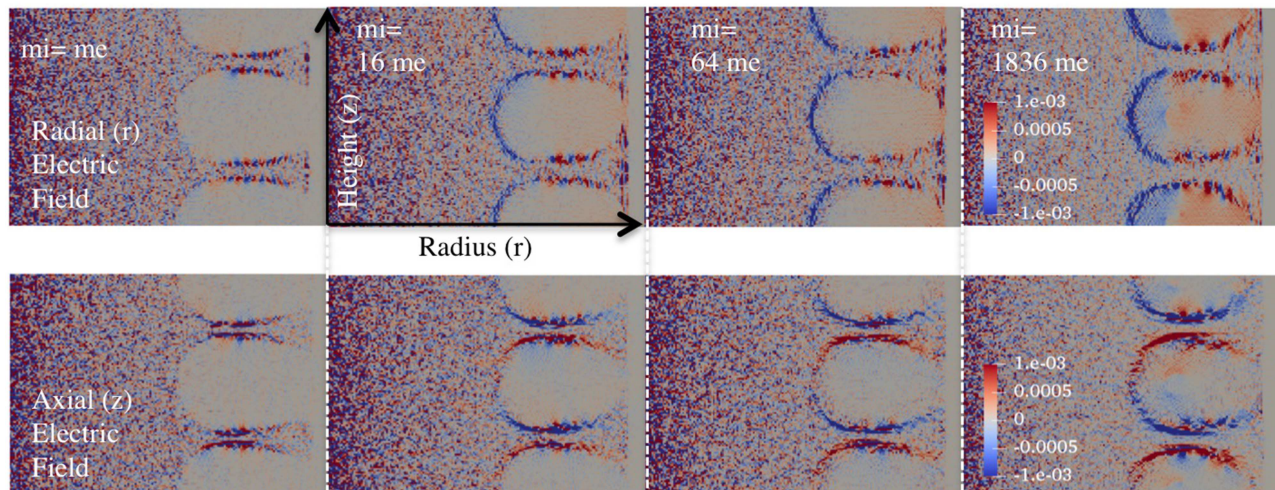


FIGURE 6 | Steady-state equilibrium profiles of electric field as a function of ion mass. Equilibrium profiles show electric field in the radial direction (**Top row**) and axial direction (**Bottom row**) for the same ion masses from Runs 4, 6, 7, and 8 as in **Figure 5**.

ion diamagnetic current density. The radial ion flows are shown in the fourth row.

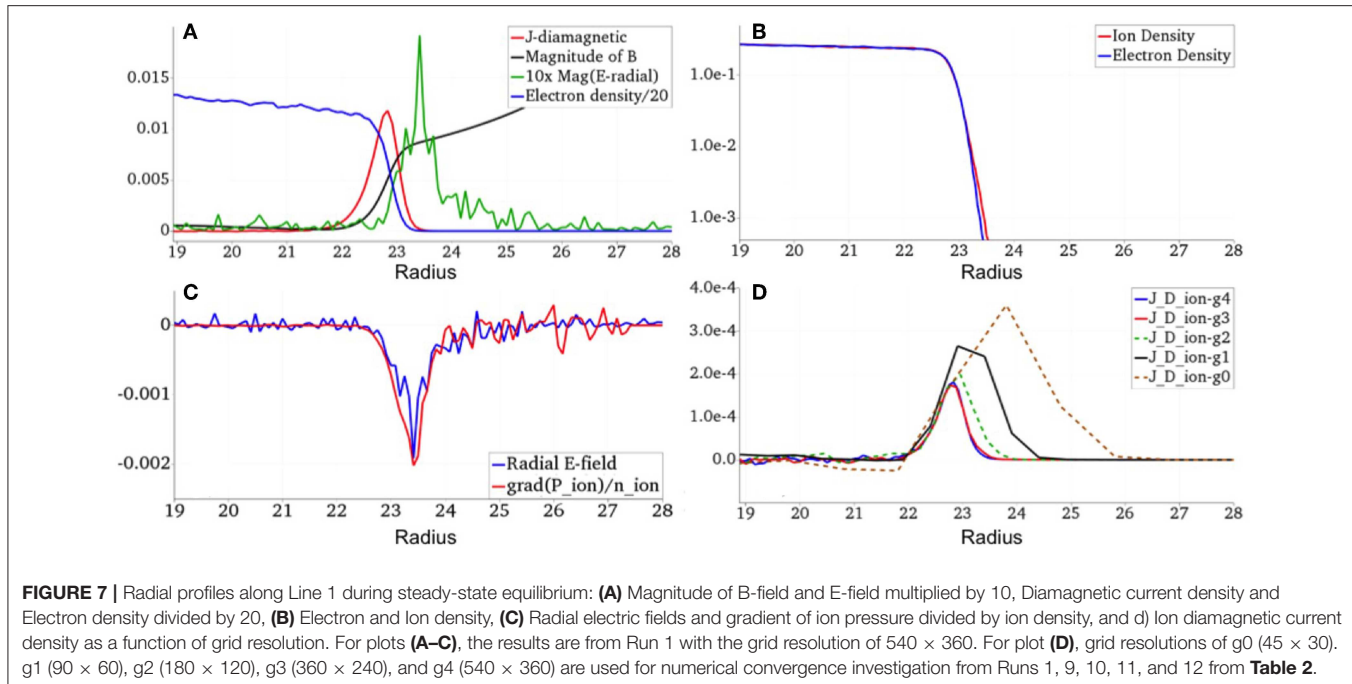
The main finding illustrated in **Figure 5** is that the equilibrium profiles between the plasma and magnetic field remain nearly identical in their shape when the ion mass and ion gyroradius are varied by a factor of 1,836 and a factor of 43, respectively. For example, the electron diamagnetic current layer occurs at the same location in space with only minor variation in its thickness. In terms of magnitude, electron density and electron diamagnetic current exhibit minimal change with ion mass variation. It is noted that the ion density is not plotted since the ion density is nearly equal to the electron density with the difference between the two is at least 2–3 orders of magnitude smaller than the electron density in the entire domain for all cases. In contrast, there are significant decreases in ion diamagnetic current by a factor of 100 or more between $m_i = m_e$ and $m_i = 1,836 m_e$, while the ion outward flow in the gap region between the adjacent coils decreases by 8 times along Line 3 (see **Figure 3**). These results were unexpected and prompted further investigation.

Figure 6 shows equilibrium profiles of radial electric field (top row) and axial electric field (bottom row) which can shed light on the unexpected finding from **Figure 5** for the same set of runs. Along Line 1, there is little electric field in the case of $m_i = m_e$, consistent with the equal gyroradius of electrons and ions. In comparison, a localized electric field is formed and intensifies at the boundary with increase in ion mass to $m_i = 16$, 64, and 1,836 m_e . The direction of the electric field is radially inward, thus in the direction of pushing ions from the boundary to the plasma region. With ions being pushed radially inward at the boundary, the electric field limits ion excursion into the magnetic field region, which in turn reduces the thickness of the boundary layer. The electric field also disrupts ion gyro-motion at the boundary leading to decreased ion contribution to the plasma diamagnetic current. In addition, the electric field intensity increases with ion mass in order to balance the larger

ion gyroradius for heavier ions. While Line 1 is used to describe the role of the localized electric field, the presence of the electric field is seen on the entire surface of the boundary. By comparing the radial and axial electric field, it is shown that the direction of the electric field is normal to the magnetic field line and inward to the plasma region. As this localized electric field at the boundary could explain the results from **Figure 5**, critical questions are the origin of the electric field and how to quantify its intensity.

ANALYSIS AND DISCUSSION

To investigate the origin of the localized electric field, equilibrium profiles along Line 1 are examined in detail in **Figure 7** for key plasma parameters in Equation (1). In order to suppress numerical noise related to the use of discrete particles in the PIC simulation, the plot utilizes averaging of 20 steady-state plasma profiles, as discussed in the Method section. **Figures 7A–C** show equilibrium profiles from Run 1 and **Figure 7D** shows ion diamagnetic current profiles as a function of grid resolution from Runs 1, 9, 10, 11, and 12 in **Table 2**. As shown in **Figure 7A**, the boundary layer exhibits rapid change in plasma density, magnetic field and the diamagnetic current when the thickness of the current layer is ~ 0.6 as measured by full-width-half-maximum (FWHM). In addition, the radial profile reveals the occurrence of an electric field and its location with respect to the current layer. **Figure 7B** shows the electron and ion density profile in a semi-log plot, exhibiting exponential decay of both ion, and electron density across the boundary layer. **Figure 7C** compares the radial electric field and the gradient of ion pressure divided by ion density showing that the electric field develops at the boundary as the ion pressure decreases. While detailed simulation parameters and results are summarized in **Table 1**, some relevant values are given here for Run 1. In NCU, the simulation utilizes an electron thermal velocity of



7.35×10^{-2} times the speed of light with an electron mass of $1/64$ and an ion thermal velocity of 9.2×10^{-3} times the speed of light with an ion mass of 1, with the speed of light and charge of electrons and ions normalized to 1. As shown in Figure 7A, a mean value of magnetic field magnitude is 4.1×10^{-3} in the current layer. This leads to the thermal electron gyroradius of 0.28 and the ion gyroradius of 2.24 since the gyroradius is given as the thermal velocity multiplied by the particle mass and the inverse of magnetic field in NCU. Therefore, the current layer thickness of 0.6 corresponds to approximately twice the electron gyroradius and a quarter the ion gyroradius.

During the analysis to quantify the electric field intensity, we have also discovered the importance of spatial resolution for PIC simulation, as shown in Figure 7D. Here we conducted a series of convergence tests with respect to the grid resolution from g_0 (45×30) to g_1 (90×60), g_2 (180×120), g_3 (360×240), and g_4 (540×360) corresponding to the grid size varying from 3.6, 1.8, 0.9, 0.45, and 0.30 times the electron gyroradius at the boundary. Figure 7D shows ion diamagnetic current density as a function of grid resolution. The simulation reaches a converged solution for g_3 and g_4 , while g_2 results seem to be reasonably close to the converged solution with respect to ion diamagnetic current density. On the other hand, without sufficient grid resolution, such as in the g_0 and the g_1 cases, numerical inadequacy leads to over-estimation of ion diamagnetic current density and its layer thickness in the boundary layer.

The results shown in Figures 7A–C are unexpected and outside the standard MHD model, whose solution of the current layer does not include the electric field. Instead, we compare the results with the equation known as generalized Ohm's law, including the Hall term and a scalar pressure, which relates the

current to the electric field, as shown in Equation (2) (Biskamp, 2000).

$$E = -\frac{V_i \times B}{c} + \frac{1}{ne} \times \frac{J \times B}{c} - \frac{\nabla p_e}{ne} \quad (2)$$

where E is the electric field, V_i is the velocity of ions, n is the plasma density, e is the electron charge and p_e is the pressure of electrons. It should be remarked that the simulations do not use this approximation. Equation (2) is used only to interpret the results. Within this scope, we can then simplify the pressure tensor with a scalar pressure and ignore the electron inertial terms. Furthermore, time varying terms are ignored in Equation (2) as we are interested in steady-state equilibrium. To focus on the most important terms, it is instructive to consider the consequences of assuming the limit where the electron inertia terms, the plasma resistivity term and other higher order terms such as off-diagonal pressure tensor terms are ignored as well as the difference between the electron density and the ion density. First, we note that the first term on the right-hand side (*rhs*) can be ignored at the boundary along Line 1 since there is no plasma mass flow as shown in Figure 1. We can then utilize Equation (1) to replace the $J \times B$ term, the second term on the *rhs* with the total pressure gradient reducing Equation (2) into a simple relation between the electric field and the ion pressure at the boundary.

$$E = \nabla p_i/ne \text{ or, } E = kT_i \nabla n_i/ne \quad (3)$$

where p_i is the pressure of ions, k is the Boltzmann coefficient, T_i is the ion temperature and n_i is the ion density.

This relationship between the electric field and the ion density gradient where the ion density gradient scale length is on

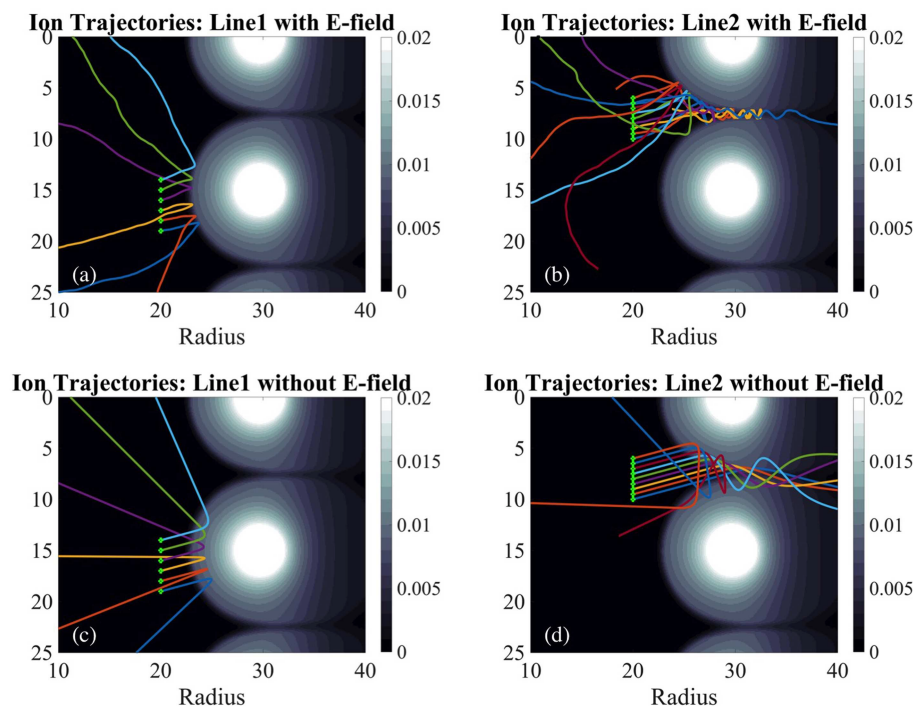


FIGURE 8 | Ion trajectories in the steady-state equilibrium with and without an electric field from Run 1. Panels **(a,b)** show ion trajectories with the self-consistent electric field and magnetic field from the simulation. Panels **(c,d)** show ion trajectories calculated with only the magnetic field to highlight the role of the electric field at the boundary in determining the thickness of the boundary layer and the plasma flow collimation.

the order of electron gyro-radius is the key discovery of the present study. Since the electric field intensity is proportional to the ion density gradient, it highlights the importance of fully resolving length scale down to the electron gyroradius in determining ion dynamics at the boundary. An approximate solution of this relationship can be expressed as $n_i \sim n_0 \exp(-eE_0(r-r_b)/kT_i)$, where n_0 is the ion density at the boundary location at $r = r_b$ and E_0 is mean electric field value in the boundary layer. The observed exponential decay of ion density shown in **Figure 7B** agrees with this solution. Finally, **Figure 7C** shows an agreement between the radial electric field and the gradient of ion pressure divided by the ion density, as shown in Equation (3).

To further understand the role of the electric field, **Figure 8** compares single particle ion trajectories in the equilibrium from Run 1 with and without the electric field along Lines 1 and 2 with green dots representing origins of their trajectories. All ions begin their motion with the same velocity vector angled at 15 degrees between radial velocity and axial velocity, and their kinetic energy equal to twice the kinetic energy of plasma injection during the initialization phase. As shown in **Figures 8a,b**, ion motions exhibit sharp reflection at the boundary due to the presence of the electric field. In comparison, ions would penetrate significantly deeper across the boundary layer if the electric field is ignored, as shown in **Figures 8c,d**. Along Line 1, the sharp reflection of ions at the boundary is consistent with the exponential ion density decay, with the characteristic decay length comparable to

electron gyroradius. The electric field also contributes to the ion flow collimation along Lines 2 and 3, with a width of ion flow significantly less than ion gyroradius, while suppressing plasma leakage, as shown in **Figure 8b**. Without the electric field at the boundary, the width of the ion flow would be significantly wider, as shown in **Figure 8d**. As such, this localized electric field may play a significant role in suppressing the plasma loss in magnetic cusp systems. Previously, the plasma loss rate of magnetic cusp device was conjectured to be proportional to the width of the cusp opening (Berkowitz et al., 1958; Grad, 1961; Spalding, 1971; Kitsunezaki et al., 1974; Hershkowitz et al., 1975; Haines, 1977; Pechacek et al., 1980). Since the minimum width of the cusp opening across Line 3 is twice the thickness of boundary layer along Line 1, the reduced plasma loss across the cusp opening due to the electric field is also consistent with the electron gyro-radius scale boundary layer.

The results from **Figure 8** show that the main role of the electric field at the boundary is to limit ion excursion at the boundary, which in turn limit charge separation between electrons and ions, as shown in **Figure 7B**. As the ion excursion is suppressed at the boundary, the ion density decreases rapidly at the boundary. This leads to the decrease of ion diamagnetic current with the ion diamagnetic current layer thickness comparable to the electron diamagnetic current layer thickness, as shown in **Figure 3**. At the same time, the gradient of ion density or ion pressure term becomes significant, which gives a rise to the electric field at the boundary as shown in

Figure 7C and Equation (3). Therefore, this electric field can be described as the self-consistent field since it occurs to prevent additional charge separation beyond the generation of the electric field leading to the electron gyroradius scale boundary layer. It is noted that the results from **Figure 8** provides a clear explanation for the previously unresolved rapid formation of collimated ion flow observed since the ion collimation is caused by the self-consistent electric field rather than ion gyromotion (Hershkowitz et al., 1975). It is noted that spatially localized electric fields and their role in limiting ion motion has been investigated in the boundary of tokamak magnetic confinement devices (Itoh and Itoh, 1988; Shoucri et al., 2004). In these works, the spatial scale of boundary layer and electric fields was found to be ion gyro-radius rather than electron gyro-radius as the deviation of electron motion from the magnetic flux surface was ignored. While the presence of a strong guiding magnetic field and the concave curvature of magnetic field lines at the boundary may play significant roles in determining the length scale of boundary layer and localized electric fields, it may be worthwhile to extend the previous works to the electron gyro-radius scale by allowing the decoupling of electron motion from the magnetic surface.

Our central result is that diamagnetic effects of plasma can produce electron-scale boundary layers across which current, density and magnetic field exhibit sharp transition on electron gyroradius scale length. This discovery comes at a fortuitous moment when the recently launched Magnetospheric Multiscale (MMS) mission has the capability to capture electron scale plasma dynamics both as a function of time from the high cadence of its instrumentation and space because of the short distance between its four spacecraft. It should therefore be possible in principle to observe our predicted structures. For example, Burch et al. reported an observation of electron scale current layers in the electron diffusion region of magnetic reconnection sites during magnetopause crossings by MMS spacecraft and identified the critical role of electron dynamics and localized electric fields in triggering magnetic reconnection (Burch et al., 2016). Localized electric fields have been reported also from previous missions such as Cluster (Wygant et al., 2005) and observed in simulation studies of the separation of scale of electrons and ions in reconnection (Zenitani et al., 2013) where the orbit of ions and electrons and the role of the pressure term is similar to the one reported here (Wang et al., 2016). Electron scale current layers have also been observed in the magnetosheath as part of the turbulent cascade with the observation of the electron jets in the absence of ion reconnection signature. (Phan et al., 2018). In addition, small scale magnetic holes produced by diamagnetic effects have been observed where the magnetic hole exhibits electric and magnetic field boundary structures on the order of ~ 30 km compared to the ion gyroradius of 100–1,000 km (Goodrich et al., 2016). Finally, the electron scale diamagnetic current layer has also been observed with the current produced predominantly by the divergence of pressure tensor near a magnetic reconnection region (Rager et al., 2018). While exact mechanisms producing such electron scale current layers and field structure requires further investigations, the electron scale diamagnetic current layer discovered in our

simulation could be a possible source of these electron scale plasma structures.

SUMMARY AND CONCLUSION

The fully kinetic first principles simulation resolving electron gyroradius scale length reported here led to the discovery of a localized and self-consistent electric field that plays a critical role in the boundary layer marked by a diamagnetic current between the plasma and surrounding magnetic fields. This electric field arises from the ion density or pressure gradient at the boundary and its main role is to limit charge separation between electrons and ions. By suppressing ion excursion across the boundary, the electric field leads the current layer thickness to the length scale of the electron gyroradius, the smallest and most fundamental length scale in the magnetic properties of plasma, instead of the much larger ion gyroradius. The electric field also affects plasma transport across the boundary by collimating plasma flow in the cusp region flow and reducing plasma leakage.

The localized electric field highlights the necessity to incorporate electron gyroradius scale physics in future studies aimed at advancing our understanding of fusion device performance, the magnetosphere and sunspots. In the case of magnetic cusp fusion devices, the findings from the present study encourage the resumption of research into magnetic cusp devices as potential thermonuclear fusion energy reactors. Magnetic cusp systems, in addition to their proven plasma stability and engineering simplicity, are one of the few magnetic fusion devices that allow direct injection of a charged particle beam into the central region (Krall et al., 1995; Park et al., 2015). The use of an electron beam may allow control of the electric field at the boundary toward the further improvement of plasma confinement in conjunction with flow collimation (Dolan, 1994). A numerical capability to accurately calculate the electric field offers the tantalizing potential to improve the performance of magnetic cusp devices toward net fusion energy generation. While the present work is focused on systems where the diamagnetic current layer separates a field-free plasma and a plasma-free magnetic field, the localized electric field may also play a role in plasma equilibrium and confinement at the boundaries of other fusion devices, such as the tokamak, stellarator, magnetic mirror, and Field Reversed Configuration (FRC). This is because the diamagnetic current and steep pressure gradient occur in the boundary layers of these devices where a localized electric field in the electron gyro-radius scale may play an important role in determining plasma transport. However, it is noted that unlike magnetic picket fence, these fusion systems are inherently three-dimensional systems and will require significantly higher computational resource to investigate electron gyro-radius scale physics. In the case of the Earth's magnetosphere, incorporating an electron gyroradius scale boundary layer in the quintessential equilibrium between the solar wind plasma and the Earth's magnetic field will provide new insights into magnetic reconnection and plasma turbulence. This is because

the gradient scales of the current layer and plasma pressure play a critical role in the reconnection rate and turbulence spectrum in magnetic reconnection and plasma turbulence. Extending experimental and theoretical tools toward electron gyroradius scale phenomena will help to take full advantage of the recently launched MMS mission.

DATA AVAILABILITY STATEMENT

All datasets generated for this study are included in the article/[Supplementary Material](#).

AUTHOR CONTRIBUTIONS

JP contributed to the conceptualization of the problem, conducted simulations and analysis, and prepared the manuscript. GL contributed to the development of the simulation code, conducted the analysis, and edited the manuscript. DG-H contributed to the development of the simulation code and provided the support for conducting simulations. NK contributed to the conceptualization of the problem and supported the analysis.

REFERENCES

- Alfvén, H. (1942). Existence of electromagnetic-hydrodynamic waves. *Nature* 150, 405–406.
- Alfvén, H. (1963). Hydromagnetics of the magnetosphere. *Space Sci. Rev.* 2, 862–870.
- Berchem, J. (1990). Hideo Okuda, a two-dimensional particle simulation of the magnetopause current layer. *J. Geophys. Res.* 95, 8133–8147.
- Berkowitz, J., Friedrichs, K. O., Goertzel, H., Grad, H., Killeen, J., and Rubin, E. (1958). “Cusped geometries,” in *Proceedings of the 2nd United Nations International Conference on Peaceful Uses of Atomic Energy*, Vol. 31, 171–197 (Geneva: United Nations)
- Bessho, N., Chen, L. J., and Hesse, M. (2016). Electron distribution functions in the diffusion region of asymmetric magnetic reconnection. *Geophys. Res. Lett.* 43, 1828–1836.
- Biskamp, D. (2000). *Magnetic Reconnection in Plasmas*. Cambridge: Cambridge University Press.
- Borrero, J. M., and Ichimoto, K. (2011). Magnetic structure of sunspots. *Living Rev. Sol. Phys.* 8, 4–98. doi: 10.12942/lrsp-2011-4
- Braginskii, S. I., and Kadomtsev, B. B. (1959). *Plasma Physics and the Problem of Controlled Thermonuclear Reactions*, Vol. 3. New York, NY: Pergamon Press.
- Burch, J. L., Torbert, R. B., Phan, T. D., Chen, L. J., Moore, T. E., Ergun, R. E., et al. (2016). Electron-scale measurements of magnetic reconnection in space. *Science* 352:aaf2939. doi: 10.1126/science.aaf2939
- Chapman, S., and Ferraro, V. C. A. (1930). A new theory of magnetic storms. *Nature* 126, 129–130.
- Cowling, T. G. (1957). *Magnetohydrodynamics*. New York, NY: Interscience.
- Dolan, T. J. (1994). Magnetic electrostatic plasma confinement. *Plasma Phys. Control. Fusion* 36, 1539–1593.
- Dungey, J. W. (1961). The steady state of the Chapman-Ferraro problem in two dimensions. *J. Geophys. Res.* 66, 1043–1047.
- Gonzalez-Herrero, D., Micera, A., Boella, E., Park, J., and Lapenta, G. (2019). ECsim-CYL: energy conserving semi-implicit particle in cell simulation in axially symmetric cylindrical coordinates. *Comput. Phys. Commun.* 236, 153–163. doi: 10.1016/j.cpc.2018.10.026
- Goodrich, K. A., Ergun, R. E., Wilder, R., Burch, J., Torbert, R., Khotyaintsev, Y., et al. (2016). MMS Multipoint electric field observations of small-scale magnetic holes. *Geophys. Res. Lett.* 43, 5953–5959. doi: 10.1002/2016GL069157
- Grad, H. (1961). Boundary layer between a plasma and a magnetic field. *Phys. Fluids* 4, 1366–1375.
- Haines, M. G. (1977). Plasma containment in cusp-shaped magnetic fields. *Nucl. Fusion* 17, 811–858.
- Hale, G. E. (1908). On the probable existence of a magnetic field in sun-spots. *Astrophys. J.* 28, 315–343.
- Hershkowitz, N., Leung, K. N., and Romesser, T. (1975). Plasma leakage through a low- β line cusp. *Phys. Rev. Lett.* 35, 277–280.
- Itoh, S.-I., and Itoh, K. (1988). Model of L to H-mode transition in Tokamak. *Phys. Rev. Lett.* 60, 2276–2279.
- Kallenrode, M.-B. (2004). *Space Physics: An Introduction to Plasmas and Particles in the Heliosphere and Magnetospheres*. New York, NY: Springer.
- Kitsunezaki, A., Tanimoto, M., and Sekiguchi, T. (1974). Cusp confinement of high beta plasmas produced by a laser pulse from a freely-falling deuterium ice pellet. *Phys. Fluids* 17, 1895–1902.
- Krall, N. A., Coleman, M., Maffei, K. C., Lovberg, J. A., Jacobsen, R. A., and Bussard, R. W. (1995). Forming and maintaining a potential well in a quasispherical magnetic trap. *Phys. Plasmas* 2, 146–160.
- Krall, N. A., and Trivelpiece, A. W. (1973). *Principles of Plasma Physics*. New York, NY: McGraw-Hill.
- Lapenta, G. (2012). Particle simulations of space weather. *J. Comput. Phys.* 231, 795–821. doi: 10.1016/j.jcp.2011.03.035
- Lapenta, G. (2017). Exactly energy conserving semi-implicit particle in cell formulation. *J. Comput. Phys.* 334, 349–366. doi: 10.1016/j.jcp.2017.01.002
- Park, J., Krall, N. A., Sieck, P. E., Offermann, D. T., Skillicorn, M., Sanchez, A., et al. (2015). High-energy electron confinement in a magnetic cusp configuration. *Phys. Rev. X* 5:021024.
- Park, J., Lapenta, G., Gonzalez-Herrero, D., and Krall, N. A. (2019). Discovery of an electron gyroradius scale current layer: its relevance to magnetic fusion energy earth magnetosphere and sunspots. *arXiv [Preprint]*. arXiv:1901.08041.
- Pechacek, R. E., Greig, J. R., Koopman, D. W., and DeSilva, A. W. (1980). Measurement of the plasma width in a ring cusp. *Phys. Rev. Lett.* 45, 256–259.
- Phan, T. D., Eastwood, J. P., Shay, M. A., Drake, J. F., Sonnerup, B. U. Ö, Fujimoto, M., et al. (2018). Electron magnetic reconnection without ion coupling in earth’s turbulent magnetosheath. *Nature* 557, 202–206. doi: 10.1038/s41586-018-0091-5
- Rager, A. C., Dorelli, J. C., Gershman, D. J., Uritsky, V., Avanov, L. A., Torbert, R. B., et al. (2018). Electron crescent distributions as a manifestation of

ACKNOWLEDGMENTS

The authors would like to thank Prof. John F. Santarius at Univ. Wisconsin, Madison and Prof. Yong Seok Hwang at Seoul National Univ. of Korea for their helpful discussion on plasma diamagnetic effects and Dr. Alan Roberts at Energy Matter Conversion Corporation and Mr. John Draper at Khon Kaen Univ. of Thailand for their assistance in editing of the manuscript. The initial funding for this work came from the internal corporate research and development funds of Energy Matter Conversion Corporation. This research used computational resources provided by NASA NAS and NCCS High Performance Computing, by Flemish Supercomputing Center (VSC), and by PRACE Tier-0 allocations. This manuscript has been released as a Pre-Print at arXiv (Park et al., 2019).

SUPPLEMENTARY MATERIAL

The Supplementary Material for this article can be found online at: <https://www.frontiersin.org/articles/10.3389/fspas.2019.00074/full#supplementary-material>

- diamagnetic drift in an electron-scale current sheet: magnetospheric multiscale observations using new 7.5 ms fast plasma investigation moments. *Geophys. Res. Lett.* 45, 578–584. doi: 10.1002/2017GL076260
- Russell, C. T., and Kivelson, M. G. (eds.). (1995). *Introduction to Space Physics*. Cambridge: University Press.
- Shoucri, M., Gerhauser, H., and Finken, K. H. (2004). Study of the generation of a charge separation and electric field at a plasma edge using Eulerian Vlasov codes in cylindrical geometry. *Comput. Phys. Commun.* 164, 138–149. doi: 10.1016/j.cpc.2004.06.022
- Sonnerup, B. U. Ö., and Cahill, L. J. Jr. (1967). Magnetopause structure and attitude from explorer 12 observations. *J. Geophys. Res.* 72, 171–183.
- Spalding, I. (1971). “Cusp containment,” in *Advances in Plasma Physics*, Vol. 4, eds A. Simon and W. B. Thomson (New York, NY: Interscience), 79–123.
- Tuck, J. L. (1958). “Review of controlled thermonuclear research at Los Alamos for mid 1958,” in *Proceedings of the 2nd United Nations International Conference on Peaceful Uses of Atomic Energy*, Vol. 32, 3–25 (Geneva: United Nations).
- Wang, S., Chen, L.-J., Hesse, M., Bessho, N., Gershman, D. J., Dorelli, J., et al. (2016). Two-scale ion meandering caused by the polarization electric field during asymmetric reconnection. *Geophys. Res. Lett.* 43, 7831–7839. doi: 10.1002/2016GL069842
- Wygant, J. R., Lysak, R., Songal, Y., Dombeck, J., McFadden, J., Mozer, F., et al. (2005). Cluster observations of an intense normal component of the electric field at a thin reconnecting current sheet in the tail and its role in the shock-like acceleration of the ion fluid into the separatrix region. *J. Geophys. Res. Space Phys.* 110:A09206. doi: 10.1029/2004JA010708
- Zenitani, S., Shinohara, I., Nagai, T., and Wada, T. (2013). Kinetic aspects of the ion current layer in a reconnection outflow exhaust. *Phys. Plasmas* 20:092120. doi: 10.1063/1.4821963

Conflict of Interest: The authors declare that the research was conducted in the absence of any commercial or financial relationships that could be construed as a potential conflict of interest.

Copyright © 2019 Park, Lapenta, Gonzalez-Herrero and Krall. This is an open-access article distributed under the terms of the Creative Commons Attribution License (CC BY). The use, distribution or reproduction in other forums is permitted, provided the original author(s) and the copyright owner(s) are credited and that the original publication in this journal is cited, in accordance with accepted academic practice. No use, distribution or reproduction is permitted which does not comply with these terms.



Cluster and MMS Simultaneous Observations of Magnetosheath High Speed Jets and Their Impact on the Magnetopause

C. Philippe Escoubet^{1*}, **K.-J. Hwang**², **S. Toledo-Redondo**^{3,4}, **L. Turc**⁵, **S. E. Haaland**^{6,7}, **N. Aunai**⁸, **J. Dargent**⁹, **Jonathan P. Eastwood**¹⁰, **R. C. Fear**¹¹, **H. Fu**¹², **K. J. Genestreti**¹³, **Daniel B. Graham**¹⁴, **Yu V. Khotyaintsev**¹⁴, **G. Lapenta**¹⁵, **Benoit Lavraud**³, **C. Norgren**⁶, **D. G. Sibeck**¹⁶, **A. Varsani**¹⁷, **J. Berchem**¹⁸, **A. P. Dimmock**¹⁴, **G. Paschmann**¹⁹, **M. Dunlop**^{12,20}, **Y. V. Bogdanova**²⁰, **Owen Roberts**²¹, **H. Laakso**²², **Arnaud Masson**²², **M. G. G. T. Taylor**¹, **P. Kajdič**²³, **C. Carr**¹⁰, **I. Dandouras**³, **A. Fazakerley**¹⁷, **R. Nakamura**²¹, **Jim L. Burch**², **B. L. Giles**¹⁶, **C. Pollock**²⁴, **C. T. Russell**²⁵ and **R. B. Torbert**¹³

OPEN ACCESS

Edited by:

Luca Sorriso-Valvo,

Escuela Politécnica Nacional, Ecuador

Reviewed by:

Zdenek Nemecék,
Charles University, Czechia

Nickolay Ivchenko,

Royal Institute of Technology, Sweden

*Correspondence:

C. Philippe Escoubet
philippe.escoubet@esa.int

Specialty section:

This article was submitted to
Space Physics,
a section of the journal
*Frontiers in Astronomy and Space
Sciences*

Received: 31 August 2019

Accepted: 20 December 2019

Published: 31 January 2020

Citation:

Escoubet CP, Hwang K-J, Toledo-Redondo S, Turc L, Haaland SE, Aunai N, Dargent J, Eastwood JP, Fear RC, Fu H, Genestreti KJ, Graham DB, Khotyaintsev YV, Lapenta G, Lavraud B, Norgren C, Sibeck DG, Varsani A, Berchem J, Dimmock AP, Paschmann G, Dunlop M, Bogdanova YV, Roberts O, Laakso H, Masson A, Taylor MGGT, Kajdič P, Carr C, Dandouras I, Fazakerley A, Nakamura R, Burch JL, Giles BL, Pollock C, Russell CT and Torbert RB (2020) Cluster and MMS Simultaneous Observations of Magnetosheath High Speed Jets and Their Impact on the Magnetopause. *Front. Astron. Space Sci.* 6:78. doi: 10.3389/fspas.2019.00078

¹ ESA, European Space Research and Technology Centre, Noordwijk, Netherlands, ² Southwest Research Institute, San Antonio, TX, United States, ³ IRAP, CNRS, UPS, CNES, Université de Toulouse, Toulouse, France, ⁴ Department of Electromagnetism and Electronics, University of Murcia, Murcia, Spain, ⁵ Department of Physics, Helsinki University of Technology, Helsinki, Finland, ⁶ University of Bergen, Bergen, Norway, ⁷ Max Planck Institute for Solar System Research, Göttingen, Germany, ⁸ UMR7648 Laboratoire de physique des plasmas (LPP), Palaiseau, France, ⁹ University of Pisa and National Interuniversity Consortium for the Physical Sciences of Matter (CNISM), Pisa, Italy, ¹⁰ Blackett Laboratory, Imperial College London, London, United Kingdom, ¹¹ School of Physics & Astronomy, University of Southampton, Southampton, United Kingdom, ¹² Space Science Institute, School of Astronautics, Beihang University, Beijing, China, ¹³ Space Science Center, University of New Hampshire, Durham, NC, United States, ¹⁴ Institute for Space Physics (Uppsala), Uppsala, Sweden, ¹⁵ Department of Mathematics, Center for Mathematical Plasma Astrophysics, KU Leuven, Leuven, Belgium, ¹⁶ Goddard Space Flight Center, National Aeronautics and Space Administration, Greenbelt, MD, United States, ¹⁷ Mullard Space Science Laboratory, Faculty of Mathematical and Physical Sciences, University College London, Dorking, United Kingdom, ¹⁸ Department of Physics and Astronomy, University of California, Los Angeles, Los Angeles, CA, United States, ¹⁹ Max Planck Institute for Extraterrestrial Physics, Garching, Germany, ²⁰ Rutherford Appleton Laboratory Space, Science and Technology Facilities Council, UK Research and Innovation, Didcot, United Kingdom, ²¹ IWF, Space Research Institute (OAW), Graz, Austria, ²² European Space Astronomy Centre, Madrid, Spain, ²³ Instituto de Geofísica, Universidad Nacional Autónoma de México, Cuernavaca, Mexico, ²⁴ Denali Scientific, Healy, AK, United States, ²⁵ Department of Earth, Planetary and Space Science, University of California, Los Angeles, Los Angeles, CA, United States

When the supersonic solar wind encounters the Earth's magnetosphere a shock, called bow shock, is formed and the plasma is decelerated and thermalized in the magnetosheath downstream from the shock. Sometimes, however, due to discontinuities in the solar wind, bow shock ripples or ionized dust clouds carried by the solar wind, high speed jets (HSJs) are observed in the magnetosheath. These HSJs have typically a V_x component larger than 200 km s^{-1} and their dynamic pressure can be a few times the solar wind dynamic pressure. They are typically observed downstream from the quasi-parallel bow shock and have a typical size around one Earth radius (R_E) in X_{GSE} . We use a conjunction of Cluster and MMS, crossing simultaneously the magnetopause, to study the characteristics of these HSJs and their impact on the magnetopause. Over 1 h 15 min interval in the magnetosheath, Cluster observed 21 HSJs. During the same period, MMS observed 12 HSJs and entered the magnetosphere several times. A jet was observed simultaneously by both MMS and Cluster and it is very likely that they were two distinct HSJs. This shows that HSJs are not localized into small regions but could span a region larger than $10 R_E$, especially when the quasi-parallel shock is covering the entire dayside magnetosphere under radial IMF. During this period, two

and six magnetopause crossings were observed, respectively, on Cluster and MMS with a significant angle between the observation and the expected normal deduced from models. The angles observed range between from 11° up to 114° . One inbound magnetopause crossing observed by Cluster (magnetopause moving out at 142 km s^{-1}) was observed simultaneous to an outbound magnetopause crossing observed by MMS (magnetopause moving in at -83 km s^{-1}), showing that the magnetopause can have multiple local indentation places, most likely independent from each other. Under the continuous impacts of HSJs, the magnetopause is deformed significantly and can even move in opposite directions at different places. It can therefore not be considered as a smooth surface anymore but more as surface full of local indentations. Four dust impacts were observed on MMS, although not at the time when HSJs are observed, showing that dust clouds would have been present during the observations. No dust cloud in the form of Interplanetary Field Enhancements was however observed in the solar wind which may exclude large clouds of dust as a cause of HSJs. Radial IMF and Alfvén Mach number above 10 would fulfill the criteria for the creation of bow shock ripples and the subsequent crossing of HSJs in the magnetosheath.

Keywords: magnetosheath, magnetopause, high-speed jet, multi-scale, turbulence

INTRODUCTION

The coupling between the solar wind and the Earth's magnetosphere is one of the most studied phenomena since the first spacecraft measurements of the magnetopause at the beginning of the 1960s (Cahill and Amazeen, 1963). A few years before these observations, two competing models were proposed for the solar wind-magnetosphere coupling. The first one, and nowadays most popular, was the magnetic reconnection between the interplanetary magnetic field (IMF) and the Earth magnetic field (Dungey, 1961). Reconnection on the frontside of the magnetosphere for southward IMF produces a large-scale motion of magnetic field lines from the dayside to the nightside and the reconnection in the magnetotail returns field lines back to the dayside. Many magnetospheric observations, such as cross-polar cap potential and ionospheric convection, latitude of the polar cusp, injections in the polar cusp, magnetopause reconnection jets and ion and electron diffusion regions, flux transfer events, and many others have been linked to the southward orientation of the IMF and made the reconnection process very popular. The second process was the viscous interaction of the solar wind with the magnetosphere (Axford and Hines, 1961). This viscous interaction was mainly based on three different processes: (1) Kelvin-Helmholtz instabilities (Miura, 1984) on the flanks of the magnetosphere transferring up to 2% of magnetosheath kinetic energy flux to the magnetosphere, (2) impulsive penetration of plasmoids (Lemaire and Roth, 1978; Heikkila, 1982) which could penetrate the magnetopause due to their excess of momentum density, and (3) diffuse entry of magnetosheath plasma through the magnetosphere via micro-instabilities generated by wave-particle interactions. Although viscous interaction is not much studied nowadays, as compared to reconnection, the three above processes have continued to be further studied, simulated, and compared to data, especially with the advent of multi-spacecraft

missions in the past 20 years. Viscous processes and kinetic scale mechanisms do not have to be mutually exclusive and may operate together via cross-scale coupling (Moore et al., 2016). For a review of all entry processes taking place in the magnetosphere see Wing et al. (2014).

Magnetosheath jets were first observed by Nemecěk et al. (1998) with INTERBALL-1 and MAGION-4 spacecraft. These observations reported ion flux enhancements, combining plasma density and plasma velocity. It was therefore not clear if these were density enhancements or velocity enhancements or a combination of both. Since no such enhancements were seen in the solar wind, the mechanism suggested was IMF discontinuities interacting with the bow shock and producing these flux enhancements in the magnetosheath. A few years later, Savin et al. (2004) reported magnetosheath speed jets using INTERBALL-1. Although, these jets were observed near the magnetopause the authors attributed them to magnetosheath phenomena. A few years later, using Cluster observations, Savin et al. (2008) showed that ion kinetic energy enhancements, well above solar wind kinetic energy, were observed just downstream of the bow shock, making them unlikely to be related to magnetopause processes. Furthermore, magnetosheath turbulence was observed associated with these high energy jets.

Using THEMIS string-of-pearls configuration at the beginning of the mission, Shue et al. (2009) reported a strong anti-sunward flow of -280 km s^{-1} which was followed by a sunward flow in the magnetosheath. The indentation of the magnetopause, about $1 R_E$ deep and $2 R_E$ wide was also observed. This was explained by the compression and subsequent rebound of the magnetosheath fast flow. The cause of this flow was related to the constant radial IMF (B_x dominant). Hietala et al. (2009), using the four Cluster spacecraft, proposed that bow shock ripples would be the source of the supermagnetosonic jets in the magnetosheath. These ripples were formed when the IMF was radial and the solar wind Mach number above 10. A few years

later, using a 3 h crossing of Cluster through the magnetosheath, Amata et al. (2011) reported eight high kinetic energy density jets throughout the magnetosheath. Although two jets were observed near the magnetopause, they did not satisfy the Walén test for signature of reconnection and were identified as magnetosheath jets. Furthermore, the magnetopause normal formed an angle of 97° with respect to the quiet time magnetopause normal and were explained as magnetosheath jets producing an indentation of the magnetopause.

In addition to jets, density enhancements have also been observed in the magnetosheath. Karlsson et al. (2012), using Cluster spacecraft potential observations, identified 56 density enhancements, in the magnetosheath. Their size could be very large, up to 10 R_E perpendicular to the background magnetic field, and 3–4 times larger along the magnetic field. Some of these density enhancements show a speed at least 10% above the background speed. Archer et al. (2012) investigated pressure pulses having 3–10 times the pressure of the magnetosheath background, due to both density and velocity enhancements. Their size was smaller, around 1 R_E parallel to the flow and 0.2–0.5 R_E in the perpendicular direction. No pressure pulses were observed simultaneously in the solar wind and most of the magnetosheath pressure pulses were observed behind the quasi-parallel bow shock. According to Archer et al. (2012), these pressure pulses would be produced by IMF discontinuities changing the shock geometry from quasi-parallel to quasi-perpendicular or vice versa.

Hietala and Plaschke (2013) used a simple shock ripple model when the IMF was aligned with the Sun-Earth line. Using 502 high speed jets (HSJs) observed with THEMIS together with OMNI data, they found that 97% could be produced by bow shock ripples. Ripples would have an amplitude to wave length ratio of 0.1 R_E /1 R_E and be present about 12% of the time. Plaschke et al. (2013) using an extensive database of 2,859 THEMIS HSJs showed that variations in solar wind parameters have very little influence on HSJ occurrence. On the other hand, they showed that HSJs are more often associated with slightly higher than average solar wind velocity, slightly enhanced magnetosonic Mach numbers and slightly lower than average solar wind densities. HSJs are found more often close to the bow shock and associated with the quasi-parallel bow shock. Finally, their temporal scale was around a few 10s of seconds, giving a spatial scale along the flow of 1 R_E , and their recurrence time was a few minutes. On the other hand (Gunell et al., 2014), found that HSJs could also be larger. From 64 HSJs over 13 magnetosheath crossings of Cluster, the size obtained along the flow ranged between 0.5 and 20 R_E with an average at 4.9 R_E . Using two Cluster spacecraft, Gunell et al. (2014) estimated their perpendicular upper limit diameter at 7.2 R_E . However, they indicated that it may have been overestimated. Using the THEMIS data set, Plaschke et al. (2016) estimated the size perpendicular to the flow of HSJs using multi-point measurements. The probability that an HSJ was observed by at least two spacecraft was computed and the characteristic perpendicular size 1.34 R_E was obtained. The dimension of HSJs along the flow was half this size, around 0.7 R_E . Plaschke et al. (2016) found that HSJs are observed about 3 times per hour under

all conditions and 9 times per hour under low cone angle (the angle between the Sun-Earth line and the IMF).

Archer and Horbury (2013) analyzed 4 months of THEMIS data and identified magnetosheath dynamic pressure enhancements when the pressure was larger than the solar wind dynamic pressure. They found that the probability to see pressure enhancements was 6 times higher behind the quasi-parallel bow shock (3% of the time) than behind the quasi-perpendicular bow shock (0.5%). The increase of solar wind speed was found to increase the probability of occurrence, especially behind the quasi-perpendicular bow shock. Contrary to previous observations and in agreement with Plaschke et al. (2013), solar wind discontinuities did not seem to play a great role in their generation. Plaschke et al. (2017) investigated the fine scale structures within HSJs observed by MMS after an IMF change of cone angle from 60° down to 20°. They found that small current sheets usually move with the jet, although a few of them move at different speed. The magnetic field in front of the jet is changed to a direction aligned with the jet direction. The strongest HSJ showed a dynamic pressure of 11.3 nPa as compared to 1.3 nPa of solar wind dynamic pressure. Although HSJs are ion scale structures, they have an impact on electrons; Liu et al. (2019) observed heating of electrons in the turbulent magnetosheath and could model it by varying the size of the HSJ. A review of HSJs has recently been published by Plaschke et al. (2018), addressing their characteristics, possible generation mechanisms and consequences on the magnetosphere and ionosphere.

Another phenomenon may also be involved in the generation of magnetosheath HSJs. In the early 80s, nano dust clouds have been observed in the solar wind (Russell et al., 1983) in the form of cusp-like increase of magnetic field also called Interplanetary Field Enhancements (IFEs). It was recently suggested that these clouds could also be related to plasma jets in the magnetosheath (e.g. Lai and Russell, 2018). Although IFEs are large objects lasting at least 10 min and occurring a few times a year, smaller clouds or nanoparticles may produce HSJs. Nanoparticles were first detected with electric field antenna as potential pulses lasting a fraction or a few milliseconds (e. g. Meyer-Vernet et al., 2009; Kellogg et al., 2016; Malaspina and Wilson, 2016; Vaverka et al., 2017, 2018). These nanoparticles were observed more often, between 10 and 20 impact/day (Kellogg et al., 2016), than IFEs. These impact rates are lower than HSJs observations of 3–9 per hour (Plaschke et al., 2016).

In this paper we will investigate the extent of HSJs and whether their properties vary across the magnetosheath. HSJs impact on the magnetopause is also investigated. For this investigation, we use an event when both Cluster and MMS are in the magnetosheath at the same time with a large separation distance (about 10 R_E). We use the two constellations of four spacecraft each, Cluster at a few 1,000s km separation and MMS at a few 10s of km, to obtain information on HSJs extent and magnetopause deformations. Sections Instrumentation and Orbits and Solar Wind Data present the orbits and solar wind data. Section Cluster and MMS Observations is devoted to the Cluster and MMS global observations and sections Magnetosheath HSJs and HSJs Impact on the Magnetopause focused on the

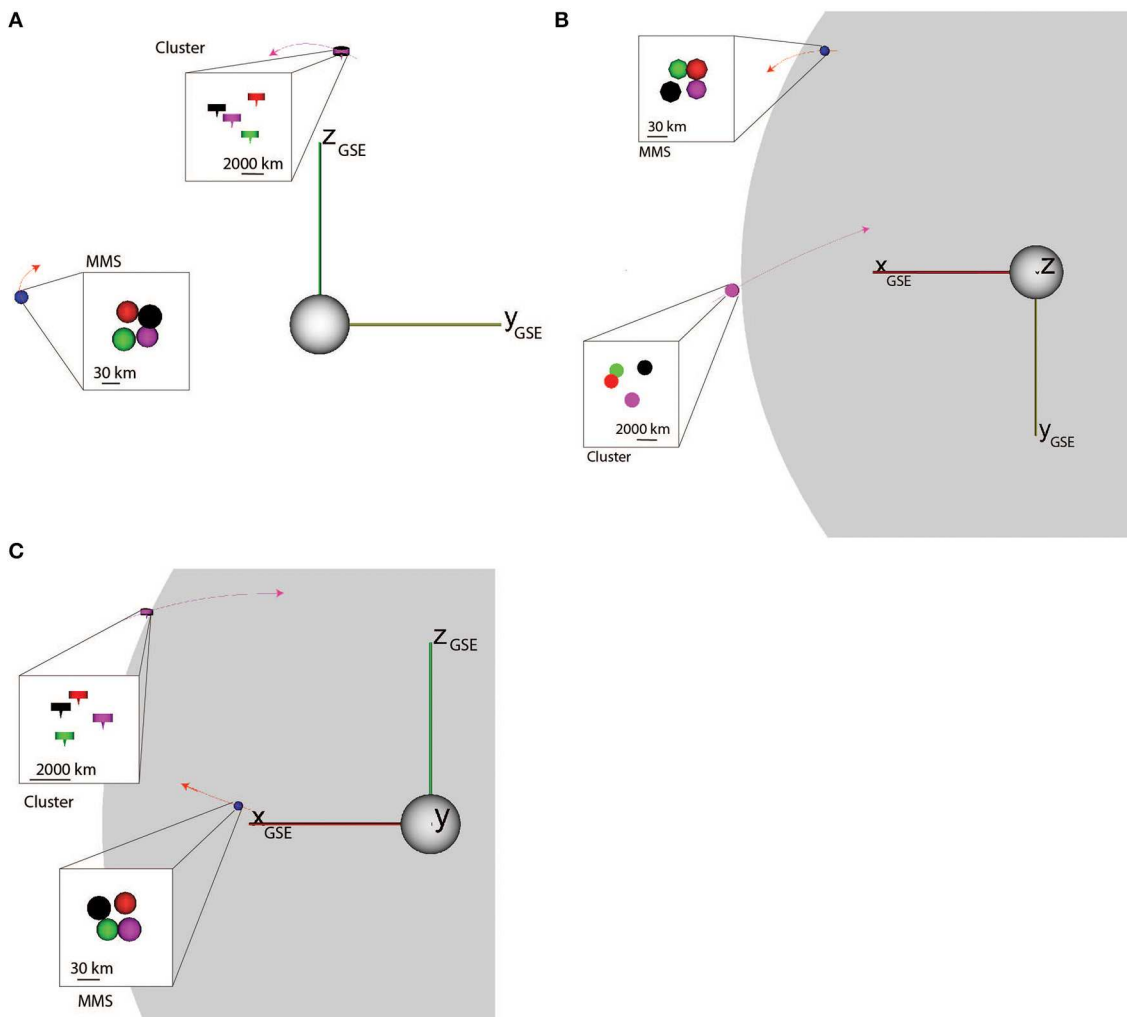


FIGURE 1 | Cluster and MMS position on 7 February 2017 at 00:40 UT in YZGSE (**A**), XYGSE (**B**), and XZGSE (**C**). The spacecraft configuration and size of the tetrahedron is shown in the small insets. Cluster and MMS are shown in classical colors: number 1 in black, 2 in red, 3 in green, and 4 in magenta. The shape of the Cluster spacecraft is represented as a flat cylinder with an arrow along the spin axis. The MMS spacecraft are shown as spheres. The magnetopause is shown in gray and the Cluster and MMS orbits in thin purple and red line, respectively.

magnetosheath HSJs and their impact on the magnetopause, respectively. Finally, we discuss the results in section Nanodust Investigation.

INSTRUMENTATION AND ORBITS

The Cluster mission comprises of four identical spacecraft that were launched in July and August 2000 in a polar orbit of $4 \times 19 R_E$ (Escoubet et al., 2001). The four spacecraft orbits are optimized to form a tetrahedron usually around the apogee, in the plasma sheet or in the magnetopause/exterior cusp. In the event used in this study a tetrahedron of 3,700 km was formed around the magnetopause. The Cluster data used are from the CIS ion spectrometer (Rème et al., 2001), PEACE electron detector (Johnstone et al., 1997), and the FGM magnetometer

(Balogh et al., 2001). Data were obtained from the Cluster science archive (Laakso et al., 2010).

The MMS mission is made of four identical spacecraft that were launched in March 2015 in an equatorial orbit of $1.2 \times 12 R_E$, which was then raised to $1.2 \times 25 R_E$ in spring 2017 (Burch et al., 2016). We use data just before the apogee raise in February 2017. MMS data used are the fast plasma investigation (FPI) (Pollock et al., 2016), from the fluxgate magnetometer (Russell et al., 2016) and from the axial and spin-plane double probe electric field instruments (Ergun et al., 2016; Lindqvist et al., 2016; Torbert et al., 2016). Data were obtained from the MMS science data center (Baker et al., 2016).

The Cluster and MMS GSE positions on 7 February 2017 at 00:40 UT are shown in Figure 1. Cluster spacecraft were well above the equator around the Sun-Earth line at $X_{GSE} = [9.9, 0.3, 7.1] R_E$ while MMS spacecraft were slightly above the

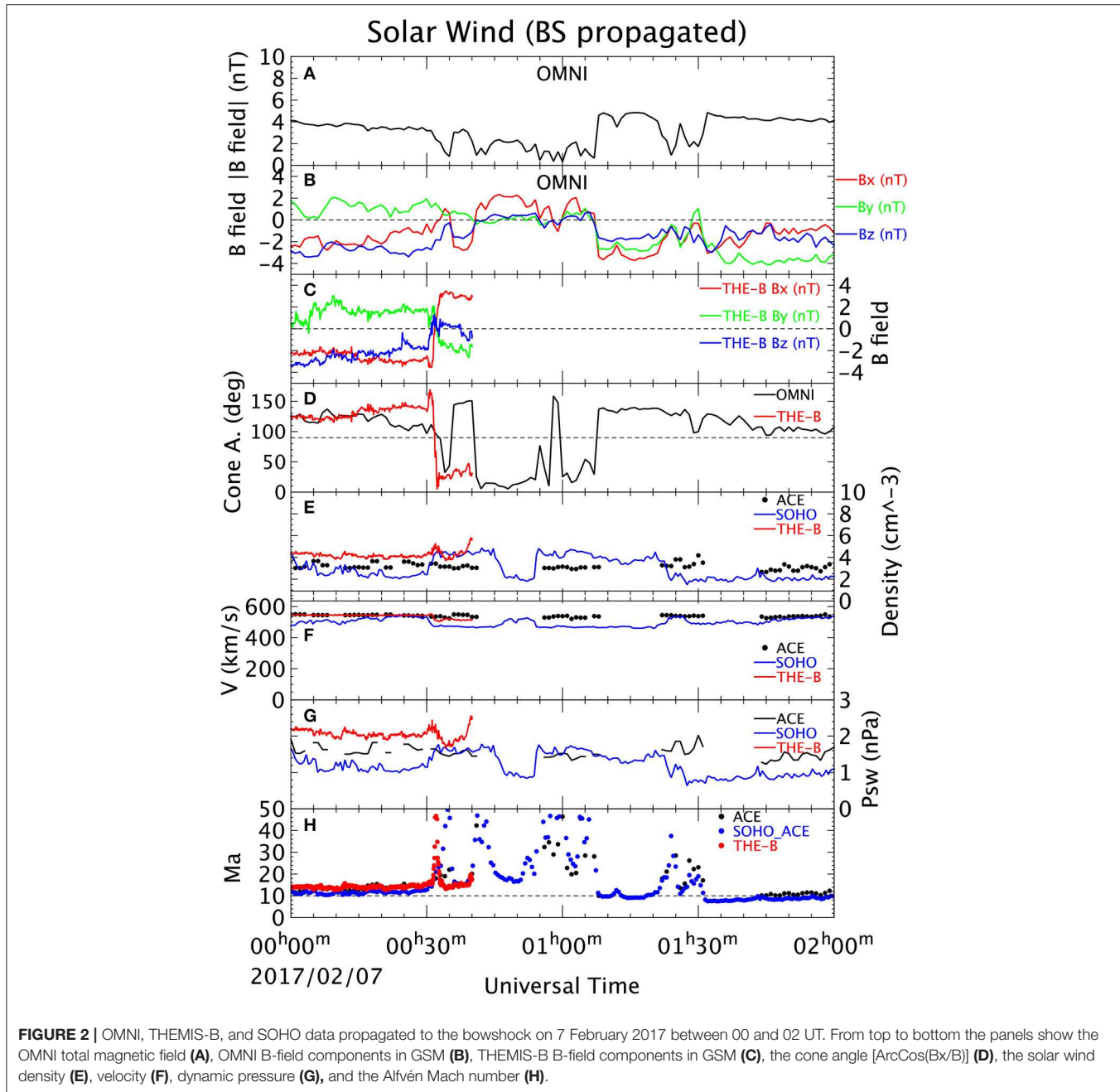


FIGURE 2 | OMNI, THEMIS-B, and SOHO data propagated to the bowshock on 7 February 2017 between 00 and 02 UT. From top to bottom the panels show the OMNI total magnetic field (**A**), OMNI B-field components in GSM (**B**), THEMIS-B B-field components in GSM (**C**), the cone angle [ArcCos(Bx/B)] (**D**), the solar wind density (**E**), velocity (**F**), dynamic pressure (**G**), and the Alfvén Mach number (**H**).

equator on the dawn side at $XYZ_{\text{GSE}} = [7.7, -8.0, 0.7] R_E$. The tetrahedron size formed by the Cluster spacecraft was around 3,700 km and the one formed by MMS was around 55 km. The Cluster spacecraft separation was therefore about 70 times larger than the MMS separation. The distance between Cluster and MMS was around $10.6 R_E$.

SOLAR WIND DATA

The solar wind data were obtained from the ACE spacecraft and propagated to the bow shock and are available from the

OMNI high resolution database (King and Papitashvili, 2005). Figure 2 shows the magnetic field (Figures 2A–D), the solar wind density (Figure 2E), the solar wind speed (Figure 2F), the solar wind dynamic pressure (Figure 2G), and the Alfvén Mach number (Figure 2H). The IMF (Figure 2A) was around 4 nT at the beginning and at the end of the 2h interval. In between 00:35 UT and 01:07 UT it decreased to values below 2 nT and as low as 0.38 nT at 01:00 UT. The IMF-Bz component (Figure 2B) was negative around -2 nT at the beginning of the interval up to 00:40 UT, then was around 0 nT up to 01:07 UT and again negative around -1.5 nT after that time. The IMF-By component

was positive around 1 nT at the beginning of the interval, then around 0 nT between 00:35 UT and 01:07 UT and then negative after that time around -3 nT. The IMF-B_x component was negative around -2 nT at the beginning and at the end of the interval and positive in the middle, between 00:40 UT and 01:07 UT. Note that between 00:40 UT and 01:07 UT, the IMF was almost purely radial with a dominant IMF-B_x component. The cone angle (**Figure 2D** black line) showed large values in the range $100\text{--}130^\circ$ up to 00:35 UT, then decreased to below 40° for a few minutes and then increased to above 150° for 5 min. After 00:41 UT, it decreased below 30° up to around 01:07 UT, except during a few minutes at 00:57 UT. After 01:07 UT, the cone angle was stable around 130° for 20 min and then slowly decreased down to 90° . The cone angle was therefore small (B_x dominant) between 00:33 UT and 01:07 UT. To check the propagation time of OMNI data we added THEMIS-B magnetic data on **Figure 2C** and the THEMIS-B cone angle in **Figure 2D** (red line). THEMIS B was in the solar wind close to the bow shock on the dusk side ($\text{XYZ}_{\text{GSE}} = [-35, 48, -4.9] \text{ R}_E$) and downstream of the terminator. We have shifted the data by -9 min to take into account the propagation to the bow shock. THEMIS-B data agree well with OMNI data from 00:00 to 00:30 UT, then it observed the change to low cone angle around 00:32 UT which is about 8 min before OMNI data. THEMIS-B started to observe reflected ions and waves after 00:40 UT and we did not include data afterwards. This shows that OMNI data can have some inaccuracy in time and changes in solar wind can be out by a few minutes or a few 10s of minutes when reaching the bow shock as shown by Case and Wild (2012).

Although showing three gaps of around 10 min, the plasma solar wind data showed rather constant values throughout the 2 h interval with a density around 3 cm^{-3} (**Figure 2D**), a speed around 540 km s^{-1} (**Figure 2E**), producing a solar wind dynamic pressure around 1.6 nT (**Figure 2F**). The solar wind speed is therefore faster and the density lower than average solar wind values. SOHO data with a time shift of 37 min. and THEMIS-B are also shown on **Figures 2E–H**. There are some differences between these spacecraft, mainly in density, which may come from the different instruments or calibrations used on these spacecraft. Their different position in the solar wind could also explain these differences. Radial IMF, high solar wind speed and low solar wind density are usually associated with magnetosheath HSJs (Plaschke et al., 2013).

CLUSTER AND MMS OBSERVATIONS

Figure 3 gives an overview of the event observed by Cluster 4 (C4), Cluster 1 (C1), and MMS1 ion and magnetic field data. The figure covers the same interval as in **Figure 2**, from 00:00 UT to 02:00 UT on 2017/02/07. The magnetosheath intervals are marked with a black bar at the bottom of the spectrograms on C4 and MMS1 (**Figures 3a,g**). Cluster was in the magnetosheath (high flux of ions from 100 eV to a few keVs) from the beginning of the interval up to around 01:07 UT when C4 crossed the magnetopause and entered the magnetosphere (substantial flux of high-energy ions above 10 keV). After about 10 min it went

back into the magnetosheath for about 12 min and after 01:28 entered again in the magnetosphere for the rest of the interval. At 00:25 UT there was a change of mode of the ion instrument on C4 which explains the apparent change of flux in **Figure 3a** but the spacecraft stayed the whole time in the magnetosheath. The magnetic field measured by C4 and MMS1 (**Figures 3c,i**) was small and turbulent in the magnetosheath and large and slowly varying in the magnetosphere. C1 ion data (**Figure 3d**) are limited to a 1-h interval but the data are in the highest time resolution (4 s) between 00:08 UT and 01:10 UT. MMS1 was almost all the time in the magnetosheath except during a few intervals between 00:40 UT and 01:06 UT and around 01:35 UT.

The plasma speeds (**Figures 3b,e,h**) were larger with large plasma jets in the magnetosheath (V_x component dominant) and small in the magnetosphere. These jets are characterized by a strong V_x components (red line) lasting a few minutes and reaching a speed down to -350 km s^{-1} . On Cluster, they start from 00:04 UT on C4 up to the entry in the magnetosphere at 01:30 UT. On MMS the period where jets are visible starts later at around 00:25 UT. The other difference is that V_y is around 0 and V_z is positive on Cluster while V_y is negative and V_z is around 0 on MMS. This is most likely due to their different position with respect to the subsolar point, Cluster at mid-latitude in the northern hemisphere and MMS on the dawn flank. **Table 1** lists the time and spacecraft observing the HSJs as well as their main properties such as the maximum speed, ion density, pressure, duration, and size.

MAGNETOSHEATH HSJS

We will now focus on the HSJ observed around 00:31 UT which is seen around the same time on Cluster and MMS. **Figure 4** shows C1 and MMS1 ion and magnetic field data between 00:25 UT and 00:35 UT on 2017/02/07. The Cluster ion (4 s temporal resolution) and magnetic field (5 vector/s) data are more variable than the ones measured by MMS1, although the temporal resolution is around the same for ions (around 4 s) and higher (16 vector/s) for the magnetic field on MMS1.

We define the boundaries of the HSJs with the threshold when the ion dynamic pressure (nmV_x^2) is half of the solar wind dynamic pressure (P_{sw}). Plaschke et al. (2013) defined the HSJs with $0.25 P_{\text{sw}}$ but in our case the factor 0.25 was found too low to isolate the HSJs, especially on MMS1. The boundaries of the HSJs are at 00:31:16 UT and 00:31:49 UT (dashed lines) in C1 data and 00:30:44 UT and 00:31:33 UT in MMS1 data. The HSJ is therefore starting 36 s earlier on MMS1 than on C1 and it is finishing 9 s earlier on MMS1. There is therefore an overlap in time of about of 24 s. The jet lasts longer in MMS1 (60 s) than in C1 (33 s) data and its peak in pressure is larger at MMS1 (5.3 nPa) than at C1 (3.5 nPa). These maxima of pressure are significantly larger than the pressure in the solar wind, which was around 2.0 nPa around that time.

Since there is a significant overlap in time, around 24 s, between the MMS1 and C1 HSJs, we could ask the question: is the HSJ seen on Cluster and MMS the same HSJ or are these two

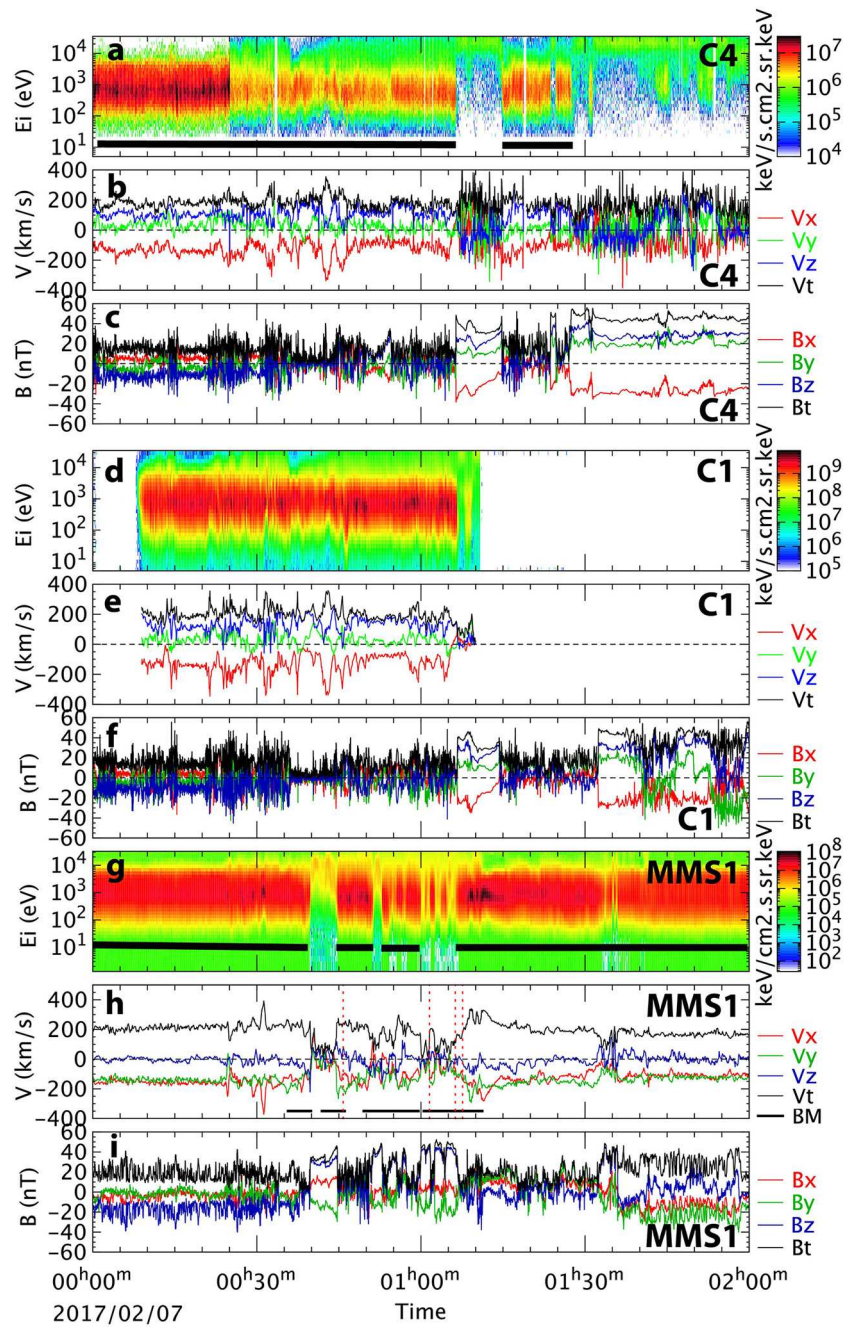


FIGURE 3 | Cluster 4 (C4), Cluster 1 (C1) and MMS1 ion and magnetic field data on 7 February 2017 between 00 and 02 UT. Top three panels show the ion energy spectrogram (a), the velocity (b) and the magnetic field (c) from C4. Following panels are the same for C1 (d–f) and MMS1 (g–i). Magnetosheath intervals are indicated by thick black lines at the bottom of the spectrograms (a,g). MMS1 burst mode intervals are marked by thin black lines on the MMS1 velocity panel (h). Dust impact are marked as thin dotted red dashed lines on the MMS1 velocity panel (h).

different HSJs? To address this question we estimate the size of these HSJs. We integrated the flow inside the HSJs using Equation (7) in Plaschke et al. (2016) and obtained $D_{\parallel}/C_1 = 1.2 R_E$ and $D_{\parallel}/MMS1 = 2.6 R_E$. The jet size observed by MMS1 is around 120% larger than the one observed by Cluster. If we assume a ratio between D_{\parallel} and D_{\perp} of ~ 0.5 , based on Plaschke et al.

(2016) jet multi-point statistical analysis, we obtain $D_{\perp C_1} = 2.4 R_E$ and $D_{\perp MMS1} = 5.2 R_E$. This assumption may not be valid for these HSJs since the HSJs studied in Plaschke et al. (2016) were smaller on average. The values estimated are, however, similar to the perpendicular size found by Gunell et al. (2014) based on a two-spacecraft analysis.

TABLE 1 | High speed jets characteristics.

SAT	Time (UT) (P _{Vx} max)	V max (X,Y,Z) (km s ⁻¹) in GSE	Ni (cm ⁻³)	P _{Vx} max (nPa)	Dt (sec)	D (R _E)	D _⊥ (R _E) (deduced from D)
C1	00:10:36	(-150,40,167)	27	1.04	13	0.30	0.60
C1	00:14:22	(-318,-68,27)	14	2.39	13	0.53	1.06
C1	00:15:18	(-262,86,21)	28	3.20	13	0.45	0.90
C1	00:20:56	(-227,33,54)	26	2.27	13	0.45	0.90
C1	00:21:26	(-364,80,5)	21	4.57	13	0.66	1.32
C1	00:23:51	(-264,85,-44)	32	3.70	21	0.86	1.72
C1	00:24:29	(-304,43,11)	30	4.56	26	0.98	1.96
MMS1	00:24:40	(-252,21,-2)	21	2.25	14	0.50	1
C1	00:25:25	(-280,123,70)	30	3.86	31	1.29	2.58
C1	00:25:50	(-203,92,153)	30	2.10	13	0.47	0.94
C1	00:27:03	(-219,22,165)	18	1.44	13	0.48	0.96
MMS1	00:29:19	(-257,-117,-28)	25	2.80	50	1.98	2.96
MMS1	00:31:16	(-373,-128,3)	23	5.33	49	2.58	5.16
C1	00:31:41	(-344,-8,83)	18	3.46	26	1.23	2.46
C1	00:32:28	(-307,62,-47)	24	3.73	9	0.38	0.76
MMS1	00:33:08	(-197,-121,8)	18	1.16	22	0.66	1.36
C1	00:35:53	(-214,-16,50)	34	2.63	21	0.45	0.90
MMS1	00:38:14	(-210,-124,-53)	22	1.64	22	0.83	1.66
C1	00:42:39	(-350,45,68)	21	4.37	84	4.30	8.6
C1	00:45:39	(-314,119,33)	21	3.45	31	1.21	2.42
MMS1	00:46:52	(-173,-193,-46)	32	1.62	22	0.87	1.74
C1	00:47:00	(-210,3,124)	29	2.12	21	0.78	1.56
C1	00:48:30	(-198,-17,124)	31	2.01	9	0.31	0.62
MMS1	00:49:11	(-196, to 125,-30)	25	1.58	54	1.95	3.90
C1	00:49:38	(-153,43,188)	37	1.45	13	0.48	0.96
MMS1	00:50:10	(-212,-80,-51)	37	2.78	36	1.23	2.46
MMS1	00:56:01	(-190,-195,-48)	17	1.03	14	0.60	1.20
C1	00:59:28	(-261,45,120)	21	3.80	78	3.99	7.98
C1	01:04:44	(-233,-71,99)	38	3.40	74	2.80	5.60
MMS1	01:09:22	(-193,-253,-108)	32	2.01	63	3.00	6.00
MMS1	01:11:05	(-273,-177,-30)	43	5.38	216	9.75	19.5
C4	01:15:33	(-221,-54, 43)	27	2.17	66	1.60	3.20
MMS1	01:23:10	(-169,-136,-16)	21	0.99	14	0.46	0.92

The spacecraft and the time when P_{Vx} is maximum is given as well as V_{max}, Ni, P_{Vx}, duration Dt, size parallel to flow D_{||} and size perpendicular to flow D_⊥ at the same time.

Figure 5 shows the position of Cluster and MMS and the HSJ detected at 00:31 UT, based on their estimated perpendicular size. Given the size of HSJs, the separation between Cluster and MMS seems too large to have detected the same jet and most likely each constellation detected a different jet. In addition, the jet direction is slightly different: it is pointing toward north on Cluster with V_{xyz} = (-344,-8,83) km s⁻¹ at 00:31:41 UT and toward dawn on MMS with V_{xyz} = (-373,-128,3) km s⁻¹ at 00:31:16 UT.

We will now analyze all HSJs observed during the 1.5 h interval by Cluster and MMS (see **Table 1**). During the first 24 min, only Cluster observed HSJs. MMS was in the magnetosheath at that time but only observed typical and fairly constant magnetosheath flows V_{xyz} (GSE) = (-150,-150,0) km s⁻¹ (see **Figure 3**). After 00:24:40 UT, HSJs are seen on both Cluster and MMS.

Figure 6 shows the maximum in V_x (**Figure 6A**), as well as V_y (**Figure 6B**), V_z (**Figure 6C**) and the magnitude V_t (**Figure 6D**) when V_x was maximum inside each HSJ. Cluster HSJs are shown in red asterisks and MMS ones in blue. Before 00:50 UT, the HSJs were faster, reaching values of V_x up to -380 km s⁻¹. After that time, the maximum reached was -280 km s⁻¹.

V_y flows (**Figure 6B**) show a split between Cluster and MMS HSJs. The ones observed by Cluster have a positive V_y (median of 43 ± 57 km s⁻¹) and the ones seen by MMS exhibit negative V_y values (median of -125 ± 68 km s⁻¹). The variance between HSJs is quite large and there is some overlap between the one sigma interval on V_y measured by Cluster and MMS. Apart from the HSJ measured by MMS1 at 00:25 UT, the MMS and Cluster HSJs can be separated into two groups of different V_y. V_z is positive at Cluster (median of 68 ± 67 km s⁻¹) and in general

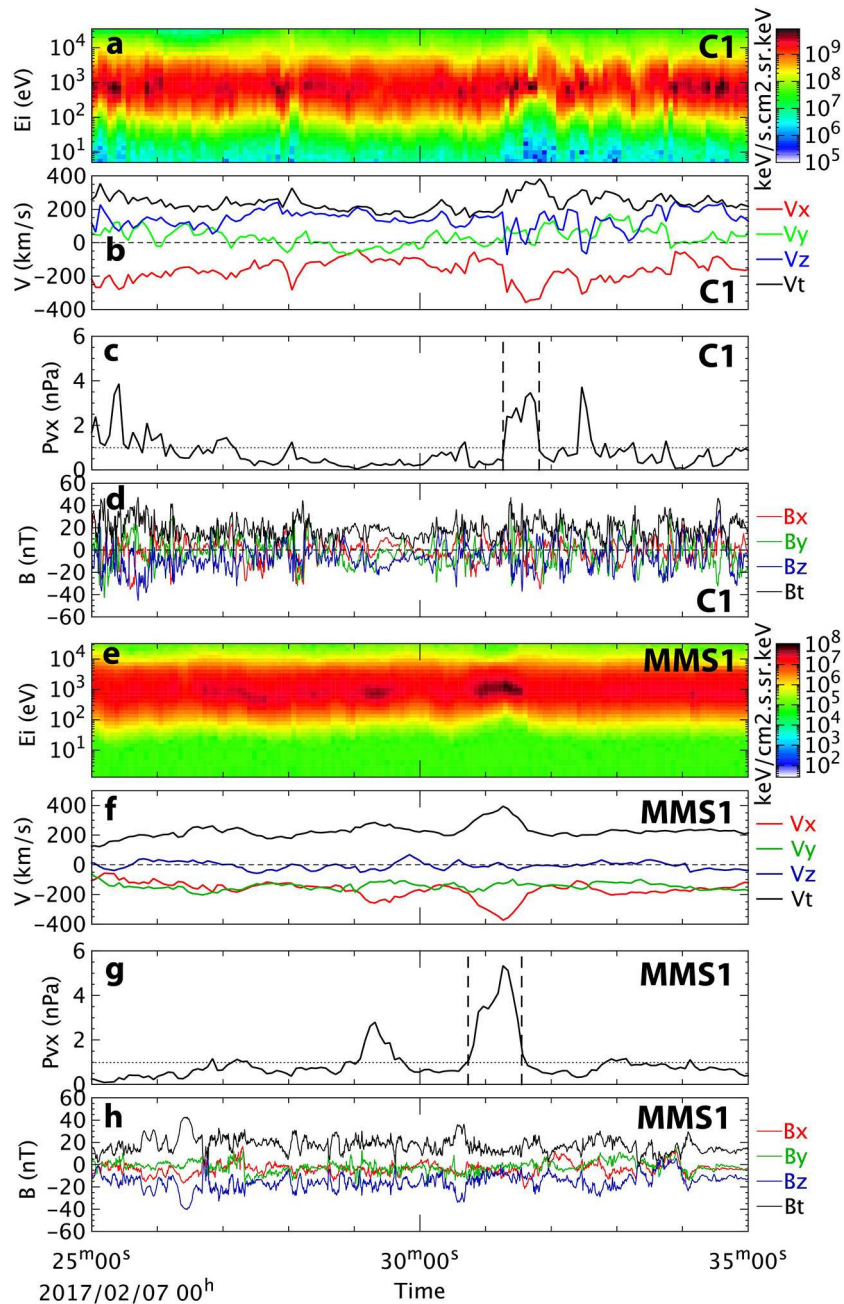
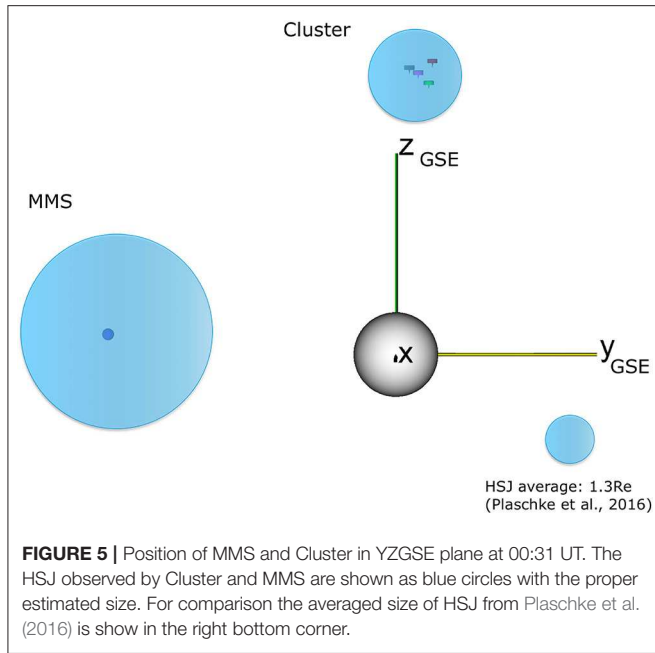


FIGURE 4 | C1 and MMS1 ion and magnetic field data between 00:25 UT and 00:35 UT. Top four panels show the ion spectrograms (a), ion velocity (b), ion dynamic pressure using V_x component to identify HSJ (c) and magnetic field (d). Four bottom panel show the same parameters for MMS1 (e–h). Dotted horizontal line on the pressure plots (c,g) marks half of the solar wind dynamic pressure, around 0.99 nPa at 00:30:30 UT. Dashed vertical lines (c,g) identify the boundaries of the HSJs observed on C1 and MMS1.

negative at MMS (median of $-30 \pm 32 \text{ km s}^{-1}$) except between 00:20 and 00:35 UT. Finally, V_t does not show much difference between Cluster (median of $276 \pm 47 \text{ km s}^{-1}$) and MMS (median of $263 \pm 53 \text{ km s}^{-1}$), oscillating between 200 and 400 km s^{-1} . The HSJs have therefore a strong component in $-Y$ direction at MMS location where its position in $-Y$ was large (**Figure 1A**) and in $+Z$ direction at Cluster location where its position in $+Z$ was large.

This may be due to their possible origin at the bow shock or to their propagation through the magnetosheath.

The dynamic pressure (P_{Vx}) values, calculated using the maximum V_x inside each HSJs, are plotted as a function of time in **Figure 7A**. P_{Vx} varies from 1 up to 5.4 nPa throughout the intervals with no clear changes before and after 00:45 UT. P_{Vx} seems larger on Cluster (median of $2.6 \pm 1.1 \text{ nPa}$) than on MMS



(median of 2.0 ± 1.5 nPa), however its variance is too large to draw any conclusion. When we compute the full dynamic pressure (nmV^2) we found that it is roughly the same at Cluster (3.7 ± 0.9 nPa) and at MMS (3.3 ± 1.9 nPa). Figure 7B shows that the duration of HSJs seems shorter Cluster (median of 21 ± 26 s) than at MMS (median of 36 ± 56 s), however, the variance is again too large to draw a conclusion.

The size of the HSJs along the flow are given in Figure 7C. D_{\parallel} shows an increase with time: starting low, below $2 R_E$ before 00:28 UT, and increasing up to almost $10 R_E$ at 01:11 UT. The estimate of the size of HSJs perpendicular to the flow (D_{\perp}) is done by assuming a ratio between D_{\parallel} and D_{\perp} of ~ 0.5 , based on Plaschke et al. (2016) jet statistical analysis. HSJs seems larger at MMS (median D_{\parallel} : $1.2 \pm 2.6 R_E$ and D_{\perp} : $2.4 \pm 5.2 R_E$) than Cluster (median D_{\parallel} : $0.7 \pm 1.6 R_E$ and D_{\perp} : $1.4 \pm 3.1 R_E$). However, the variance is again too large to draw a definite conclusion. If we compute the median value of all HSJs seen by both Cluster and MMS, we obtain $D_{\parallel} = 0.8 \pm 2.0 R_E$ and $D_{\perp} = 1.6 \pm 4.0 R_E$, which is similar to Plaschke et al. (2016) statistical size of $D_{\parallel} = 0.7 R_E$ and $D_{\perp} = 1.3 R_E$. Most of HSJs D_{\perp} (32 out of 33) are smaller than the separation between Cluster and MMS (around $10.6 R_E$). Except one, however, that may be large enough to be observed by both constellations, assuming the factor 2 between D_{\parallel} and D_{\perp} also applies for large HSJs.

The two largest events are observed by Cluster at 00:42 UT and by MMS at 01:11 UT. Their size parallel to the flow is, respectively, 4.3 and $9.75 R_E$. The distances of Cluster and MMS from the shock model of 2.2 and $3.6 R_E$ are smaller than these sizes. If we assume that HSJs are formed at the shock, this would mean that the HSJ duration is larger than the time it takes for them to cross the magnetosheath, in other words they would reach the magnetopause while still being connected to the bow shock. Another explanation could be that the large HSJs are formed by multiple HSJs merging together

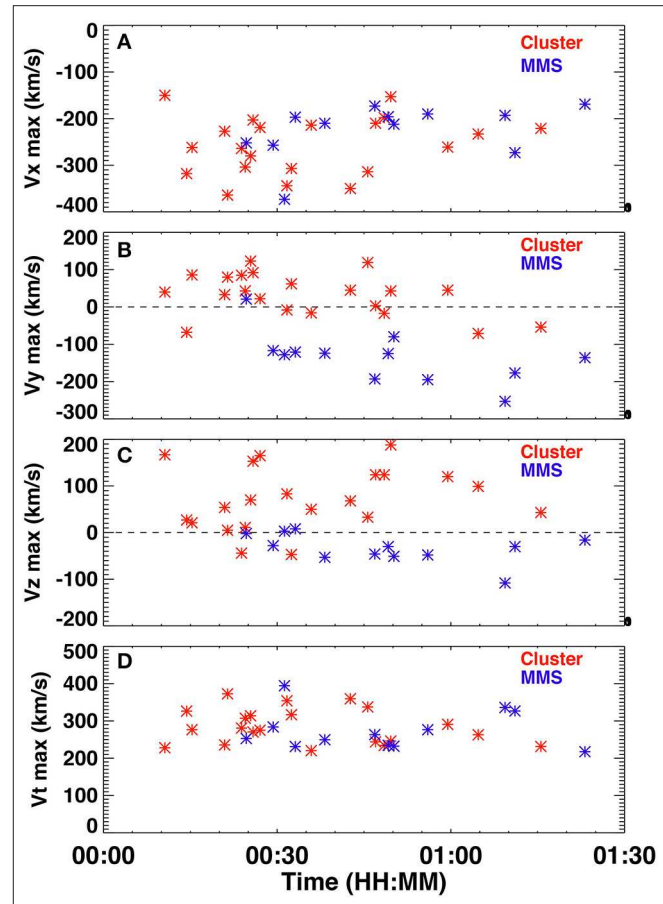


FIGURE 6 | HSJs velocity components V_x (A), V_y (B), V_z (C), and total velocity V_t (D). HSJs observed by Cluster are marked with red asterisks and the ones observed by MMS are shown with blue asterisks.

as they propagate through the magnetosheath. The large HSJ observed on MMS at 01:11:05 has a clear double peak in pressure (Figure 9G) at 01:10:15 UT and 01:11:05 UT and may be formed by two HSJs. We will look into more details at these two largest events and their impact on the magnetopause in the next section.

HSJS IMPACT ON THE MAGNETOPAUSE

The first large HSJ was observed by Cluster at 00:42 UT. Given its estimated perpendicular size of $8.6 R_E$, it could not have been observed by MMS which was around $10.6 R_E$ away from Cluster. MMS had entered the magnetosphere a few minutes earlier at 00:39:44 UT and entered again the magnetosheath at 00:44:45 UT. Figure 8 shows 10 min of C1 and MMS1 data (same format as Figure 4) around this HSJ. The maximum flow observed by C1 in V_x was -350 km s^{-1} and the maximum of P_{Vx} was 4.37 nPa . The two magnetopause crossings can be clearly seen on MMS1 data (Figures 8E–H) with the sharp change of energy in the ions going from sheath like plasma with energy around 1 keV to magnetospheric plasma with energy around 10

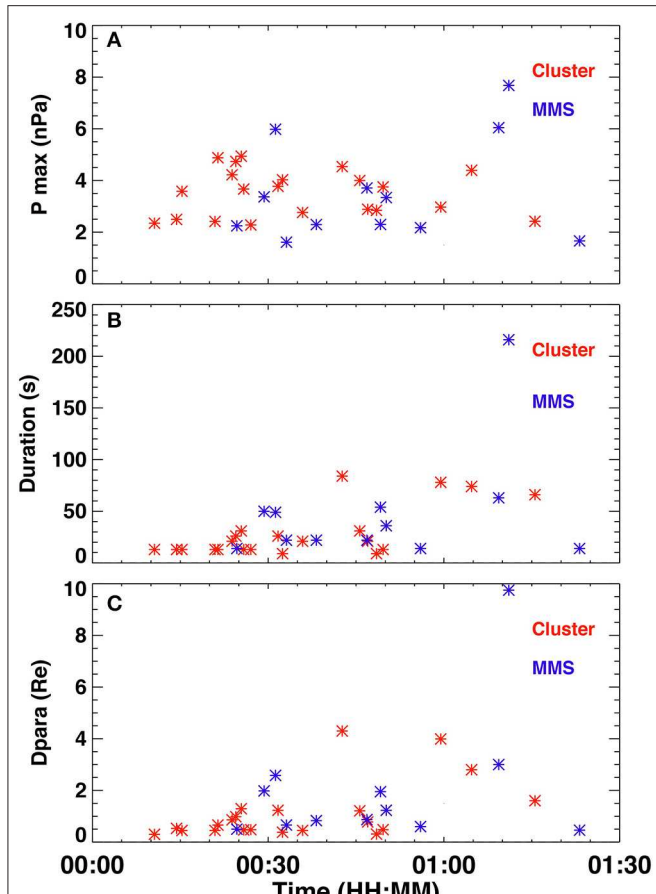


FIGURE 7 | HSJs dynamic pressure P_{vx} (**A**), duration (**B**), parallel size D_{para} (**C**). HSJs observed by Cluster are marked with a red star and the ones observed by MMS are shown in blue stars.

keV. A sharp change of magnetic field is also observed at the magnetopause with the B_z component varying from -17 nT up to $+25$ nT at 00:39:44 UT and from $+32$ nT down to $+5$ nT at 00:44:45 UT (Figure 8H). The first magnetopause crossing shows a short negative V_z flow of -245 km s $^{-1}$ at 00:39:46 (Figure 8F, blue line), which was larger in absolute terms than the velocity components ($V_x = -94$ km s $^{-1}$ and $V_y = -110$ km s $^{-1}$). This may be an indication of reconnection taking place at the magnetopause between the southward magnetic field in the magnetosheath and the northward magnetic field in the magnetosphere. This aspect will however not be further studied in this paper.

The MMS four-spacecraft analysis on the inbound magnetopause crossing at 00:39:44 UT gave a magnetopause normal equal to $(0.30, 0.91, 0.27)$ GSE and a speed of -177 km s $^{-1}$ along the normal (see Table 2). Since the four spacecraft are very close to each other, such parameters are only valid within the very short time interval of the measurements and may not represent properly the magnetopause crossing. For comparison, we have used two other methods based on single spacecraft magnetic field and ion measurements: minimum variance analysis on

B (MVAB) (Sonnerup and Scheible, 1998) and a combination of minimum Faraday residue analysis (MFR) and minimum variance analysis on V (MVAV) (Haaland et al., 2006; Sonnerup et al., 2006). For the crossing at 00:39:44 UT, the magnetopause normal with the timing analysis is mainly directed toward dusk (n_y positive) while it is directed toward dawn (n_y negative) with the MVAB and MFR+MVAV methods. Given the limitation of the timing method due to small spacecraft separations, we believe that the two other methods give, for this crossing, a better estimate of the normal and speed of the magnetopause. The magnetopause would be mainly directed toward dawn (as expected from the position of MMS in the dawn sector) and its speed would vary between 26 and 109 km s $^{-1}$.

For the second outbound crossing at 00:44:45 UT, the direction of the normal obtained by the timing analysis was $(0.93, 0.32, -0.20)$ with a speed of -139 km s $^{-1}$. For this crossing the other two methods (MVAB and MFR+MVAV) give similar orientation of the normal, mainly along X_{GSE} , with a speed ranging between 39 and 94 km s $^{-1}$. The inbound and outbound crossings show a very different normal with an angle of 62 and 84° between them, using MVAB and MFR+MVAV, respectively. The normal to the magnetopause model from Roelof and Sibeck (1993) at 00:39:44 UT was $(0.79, -0.62, 0.05)$ GSE and $(0.79, -0.61, 0.06)$ at 00:44:45 UT (Table 2, 6th column). This is quite different from the MMS observations with an angle between MVAB and MFR+MVAV normals and the model in the range 31 – 52° at 00:39:44 UT and 36 – 44° at 00:44:45 UT. All magnetopause crossings observed during the HSJ period (6 by MMS and 2 by Cluster) are listed on Table 2. They all show a significant deviation from the Roelof and Sibeck (1993) magnetopause model, ranging from a minimum of 11° up to a maximum of 114° . Most likely HSJs indented the magnetopause and then the magnetopause rebounded, as observed previously by Shue et al. (2009). The indentation would explain the outbound crossings and the rebound would produce the inbound crossings. Since such deformation would be local, over around the size of the HSJ, the magnetopause on the sides of the indentation would have a normal making a significant angle with respect to the magnetopause model. Archer et al. (2019) showed THEMIS inbound and outbound magnetopause crossings with large deviation of their normal with respect to the model. They showed that an HSJ produced an indentation of the magnetopause and the subsequent formation of a standing surface wave.

The second largest HSJ was observed by MMS at 01:11:05 UT. Its estimated perpendicular size was 19.5 RE. Similar to the previous one, Cluster entered the magnetosphere a few minutes before 01:11:05 UT and exit again in the magnetosheath a few minutes after. Figure 9 shows 10 min of data from Cluster 4 and MMS 1 (Cluster 4 was used since the ion instrument on C1 was switched off before the end of the interval). The HSJ observed by MMS (four bottom panels) is the longest observed during that day, 5 min long. P_{vx} goes slightly below the threshold of 0.5 Psw and therefore could be split into two HSJs of 1 and 3.5 min, respectively. This is supported by the change in the direction of the flow which is predominantly in $-Y$ direction in the first one

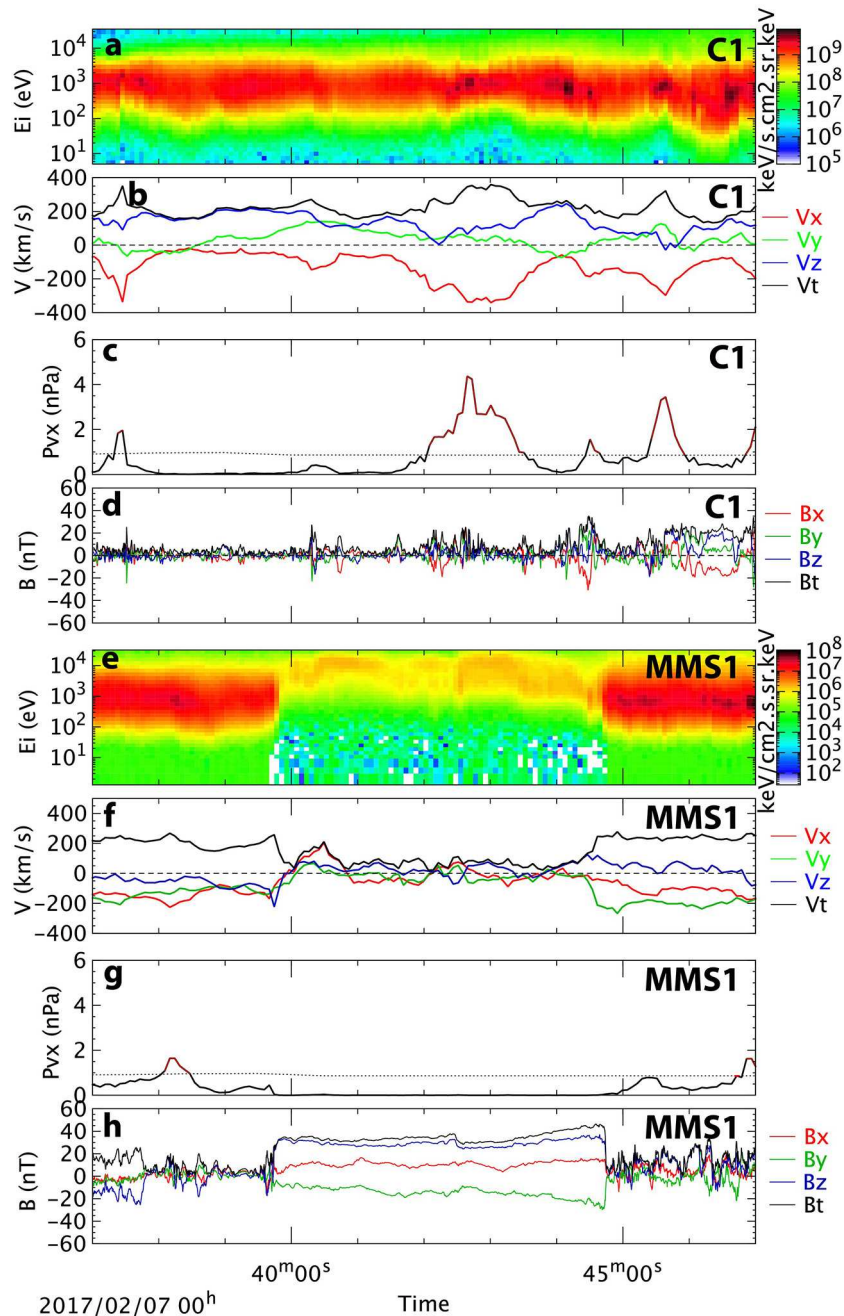


FIGURE 8 | C1 and MMS1 ion and magnetic field data between 00:37 UT and 00:47 UT (same format as **Figure 4**). Red lines on **(C)** and **(G)** show HSJs.

($-V_y$ dominant in 3rd panel from bottom) and $-X$ in the second one ($-V_x$ dominant).

Cluster went into the magnetosphere at 01:06:24 UT and exit in the magnetosheath at 01:14:47 (**Figures 9A–D**). Similar to MMS data, using the four spacecraft we computed the characteristics of the magnetopause. The normal direction given by the timing analysis during the first inbound crossing was $(0.53, 0.23, 0.82)_{\text{GSE}}$ and the magnetopause speed around 142 km s^{-1} along the normal. The second outbound crossing normal

using the timing analysis was $(0.85, -0.28, 0.44)_{\text{GSE}}$ and the magnetopause speed around -143 km s^{-1} . For Cluster the spacecraft being at larger separation (70 times) than MMS, the timing analysis is expected to be more accurate. Indeed, the two other methods, MVAB and MFR+MVAV give similar results. The B_z component of the magnetic field during these crossings is shown on **Figures 10A,B**. The inbound and outbound normals obtained from timing are different with about 42° between the two vectors. The normal to the magnetopause model at 01:06:24

TABLE 2 | Magnetopause crossing characteristics obtained with four-spacecraft analysis.

SAT	Time (UT) inbound/ outbound	Method	Speed (km s ⁻¹)	Normal X,Y,Z _(GSE)	Normal model X,Y,Z _(GSE)	Angle data-model (°)
MMS	00:39:44 I	4 S/C timing MMS124 MVAB	-177	0.30, 0.91, 0.27	0.79, -0.62, 0.05	108
			105	0.05, -0.97, -0.26	"	52
			109	0.07, -0.96, -0.26	"	51
			105	0.05, -0.96, -0.27	"	52
		MMS124 MFR+MVAV	31	0.36, -0.93, -0.07	"	32
			62	0.37, -0.91, -0.21	"	33
			26	0.39, -0.91, -0.15	"	31
		MMS124 MVAB	-139	0.93, 0.32, -0.20	0.79, -0.61, 0.06	59
			-85	0.93, 0.03, -0.36	"	42
			-90	0.94, 0.06, -0.34	"	44
			-94	0.94, 0.02, -0.35	"	41
			-57	0.86, -0.15, -0.49	"	37
			-39	0.81, -0.22, -0.54	"	36
MMS	00:44:45 O	4 S/C timing MMS124 MVAB	-42	0.91, -0.05, -0.42	"	39
			-115	0.32, 0.88, 0.36	"	105
			-103	0.74, 0.64, 0.20	"	80
			-75	0.69, 0.68, 0.23	"	83
		MMS124 MFR+MVAV	-80	0.73, 0.65, 0.21	"	80
			-12	0.44, 0.87, 0.23	"	101
			-12	0.23, 0.96, 0.12	"	114
		MMS124 MVAB	-16	0.31, 0.91, 0.27	"	109
			-65	0.92, -0.28, -0.27	"	28
			-34	0.90, -0.35, -0.25	"	20
			-34	0.90, -0.35, -0.26	"	20
			-34	0.91, -0.34, -0.25	"	20
			-7	0.78, -0.57, -0.26	"	12
MMS	01:01:45 O	MMS124 MFR+MVAV	-10	0.78, -0.56, -0.29	"	13
			-11	0.79, -0.55, -0.27	"	13
			68	0.57, -0.77, -0.28	"	20
		MMS124 MVAB	7	0.16, -0.70, -0.69	"	54
			22	0.38, -0.70, -0.60	"	40
			15	0.27, -0.71, -0.65	"	47
			13	0.56, -0.72, -0.41	"	25
			26	0.54, -0.74, -0.41	"	26
			9	0.51, -0.73, -0.46	"	29
MMS	01:02:30 I	4 S/C timing MMS124 MVAB	-83	0.99, -0.03, 0.10	"	35
			-37	0.95, -0.30, 0.11	"	22
			-43	0.95, -0.27, 0.14	"	25
			-42	0.95, -0.27, 0.13	"	25
		MMS124 MFR+MVAV	21	0.27, -0.94, -0.22	"	37
			2	0.15, -0.95, 0.27	"	47
			36	0.00, -0.89, -0.45	"	55
CL	01:06:24 I	4 S/C timing CL14 MVAB	142	0.53, 0.23, 0.82	0.84, 0.02, 0.53	28
			41	0.76, -0.04, 0.65	"	11
			120	0.54, -0.03, 0.84	"	26
		CL14 MFR+MVAV	36	0.75, 0.54, 0.39	"	32
			108	0.59, 0.17, 0.79	"	23
			-143	0.85, -0.28, 0.44	0.84, 0.01, 0.54	17
			-128	0.93, -0.05, 0.37	"	12

The time of the crossing, if it is inbound or outbound, its speed along the normal, the normal method used, the normal from the Roelof and Sibeck (1993) magnetopause model and the angle between magnetopause computed from data and the model ($\text{acos}(\mathbf{n}_{\text{mp}} \cdot \mathbf{n}_{\text{mod}})$). The methods used are the from timing analysis with four spacecraft, the minimum variance analysis on B (MVAB) (Sonnerup and Scheible, 1998) and a combination of minimum Faraday residue analysis (MFR) and minimum variance analysis on V (MVAV) (Haaland et al., 2006; Sonnerup et al., 2006).

UT was (0.84, 0.02, 0.53)_{GSE} and (0.84, 0.01, 0.54) GSE at 01:14:47 UT. This is different from the Cluster observations with an angle between Cluster normals and the model of 28° at 01:06:24 UT and 17° at 01:14:47 UT. The MVAB and MFR+MVAV methods

give an angle with the model normal between 11 and 32°. In these crossings the magnetopause was less deformed than in MMS crossings at 00:39:44 UT. Although this very large HSJ may have been extended over the Cluster-MMS constellation, there is no

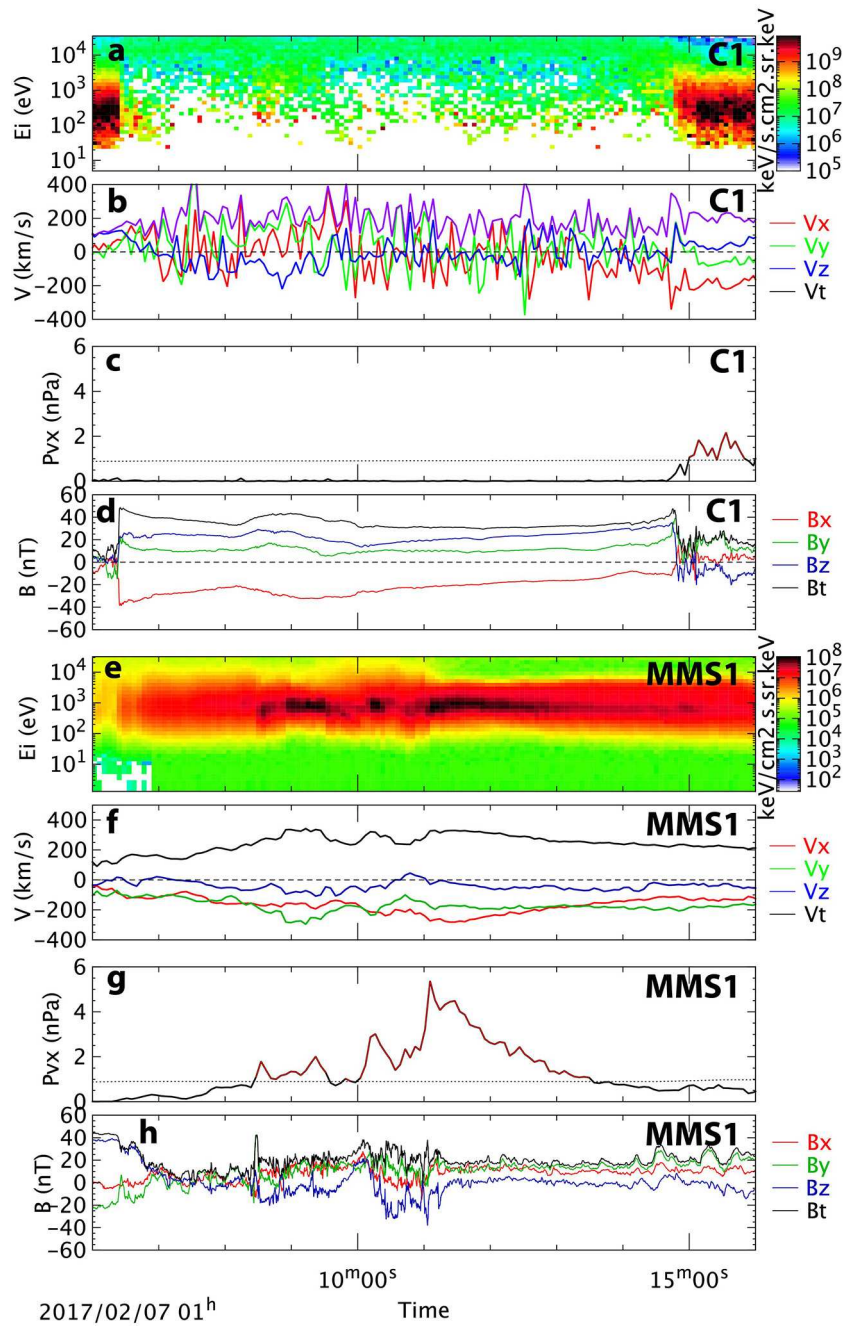


FIGURE 9 | C1 and MMS1 ion and magnetic field data between 01:06 UT and 01:16 UT (same format as Figure 4). Red lines on (c) and (g) show HSJs.

evidence that this was the case since the Cluster constellation was in the magnetosphere a few minutes around the HSJ.

An interesting aspect of the first inbound crossing of Cluster at 01:06:24 UT is that MMS also crossed the magnetopause at exactly the same time. The magnetopause crossing is shown in detail in Figure 10C with the same scale as the Cluster magnetopause crossing in Figure 10A. The Cluster and MMS magnetopause crossings are totally different (see Table 2 for detailed characteristics):

- Cluster crossing is inbound going from the magnetosheath to the magnetosphere and MMS is outbound going from the magnetosphere to the magnetosheath;
- Cluster crossings are sharp lasting on average 4 s while MMS crossings last 40 s;
- MMS crossing shows small structures within the magnetopause most likely due to back and forth motion of the magnetopause, while Cluster crossings are sharp;

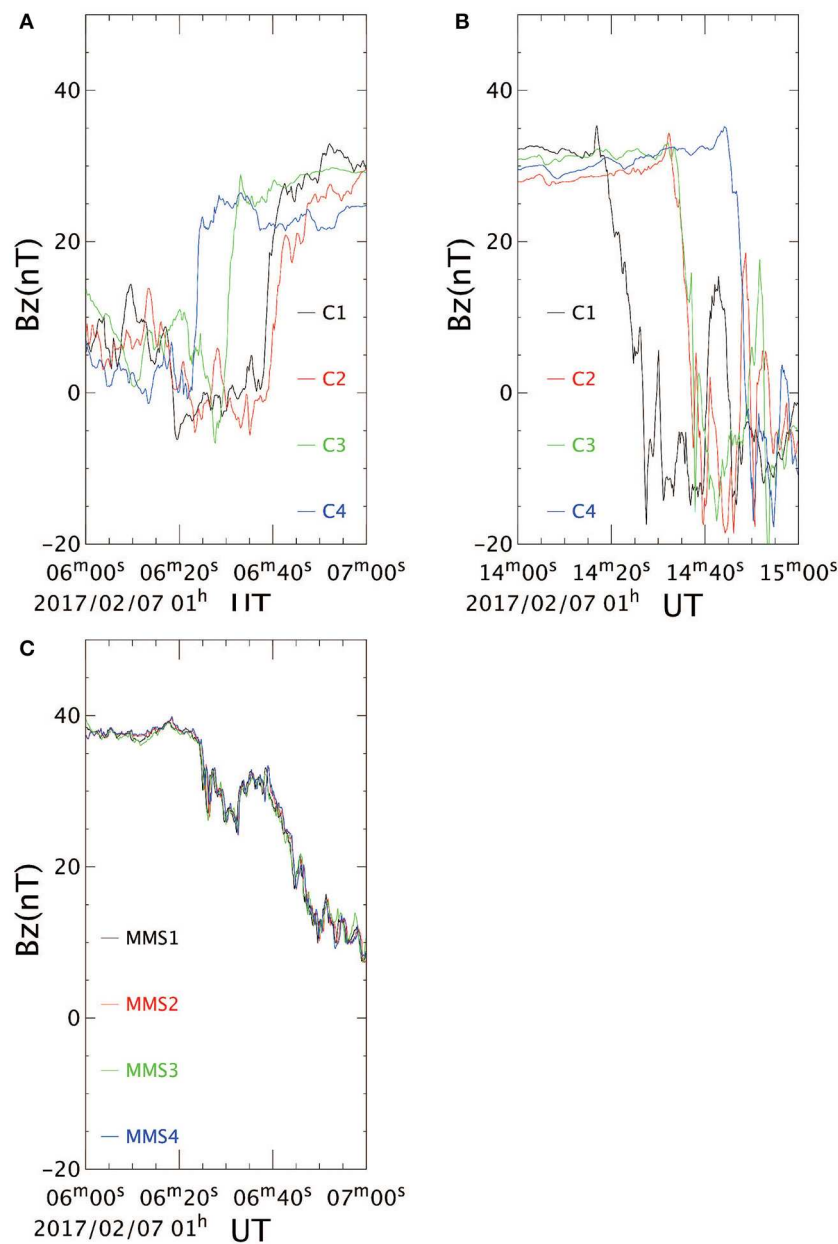


FIGURE 10 | C4 and MMS1 magnetopause crossings on 7 February 2017. Magnetic field from Cluster at 01:06–01:07 UT **(A)** and at 01:14–01:15 UT **(B)** in GSE. Magnetic field from MMS at 01:06–01:07 UT **(C)** (same as **A**) in GSE.

- Since the MMS spacecraft separations are more than 70 times smaller than those between the Cluster spacecraft, the four MMS spacecraft are all in the magnetopause at the same time while Cluster crossings of the magnetopause are separated by about 6 s;
- The magnetopause normal at Cluster is mainly toward the Z and X direction, while MMS magnetopause normal is mainly along X (**Table 2**).

This shows that under the continuous impacts of HSJs, the magnetopause is deformed significantly and can even move in

opposite directions at different places. It can therefore not be considered as a smooth surface anymore but more as surface full of local indentations.

NANODUST INVESTIGATION

We investigate whether nanodust clouds were detected during some of these events. Solar wind data (**Figure 2**) do not show a cusp-like increase of magnetic field (Russell et al., 1983; Lai and Russell, 2018). At the beginning and at the end of the interval

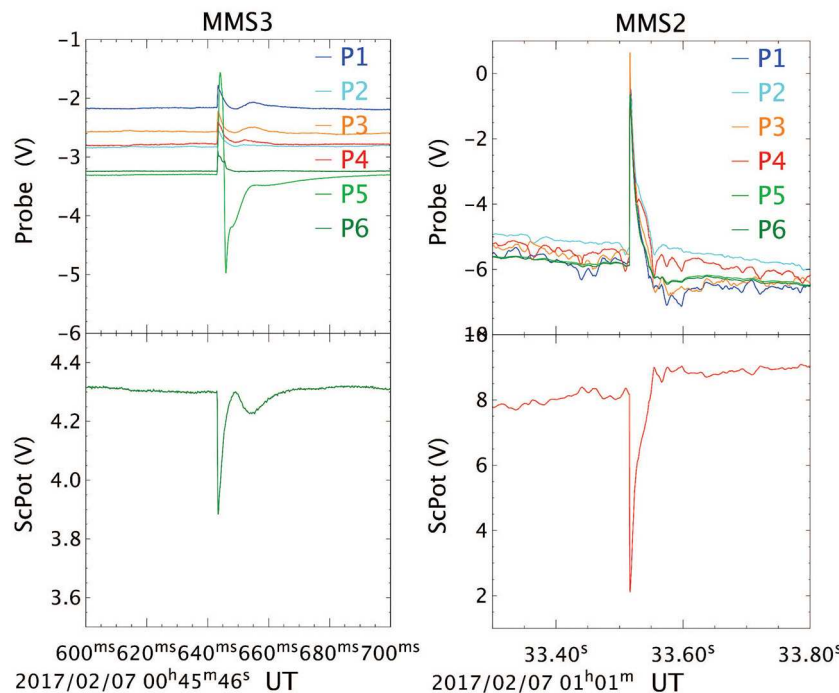


FIGURE 11 | Dust impact observed on MMS3 (**Left**) and MMS2 (**Right**) at 00:45:46.645 UT and 01:01:33.520 UT, respectively. The top panels show the difference of potential between the 6 probes and the spacecraft (called probe potential). P1–P4 are the spin plane probes and P5 and P6 the spin axis probes. The bottom panels show the spacecraft potential calculated using the four spin probes (P1–P4), and corrected from the probe-plasma potential and other effects. Note that the scales are quite different in the two events.

the IMF shows a total field around 4 nT and stable. In the middle of the event, the magnetic field decreases below 2 nT with some variability including some spikes at 00:37 UT and 01:26 UT. These were, however, below the 10 min minimum duration defined for IFEs by Lai and Russell (2018).

We then investigated if impacts of nanodust could be detected on the spacecraft. Dust impacts were detected in the past with electric field antenna as a short (a few ms) pulse of the spacecraft potential on Cluster (Vaverka et al., 2017) and MMS (Vaverka et al., 2018). Some large micro-meteorites/space debris were also detected on MMS with the accelerometers, attitude sensors, and electric field probes (Williams et al., 2016; Vaverka et al., 2018). In such case, the spacecraft potential pulse was lasting up to 1 s. We have looked for spacecraft potential pulses in the Cluster and MMS data during the 1 h 15 s when we see HSJs. To identify such pulses, we need wide band data on Cluster and burst mode data on MMS. Cluster recorded burst mode data, which was excluding wide band data acquisition, and therefore did not include probe potentials at a sufficiently high time resolution to investigate it. MMS, on the other hand, collected 3 intervals of about 10 min between 00:35 and 01:11, mainly centered on the magnetopause crossings (black bars on **Figure 3h**).

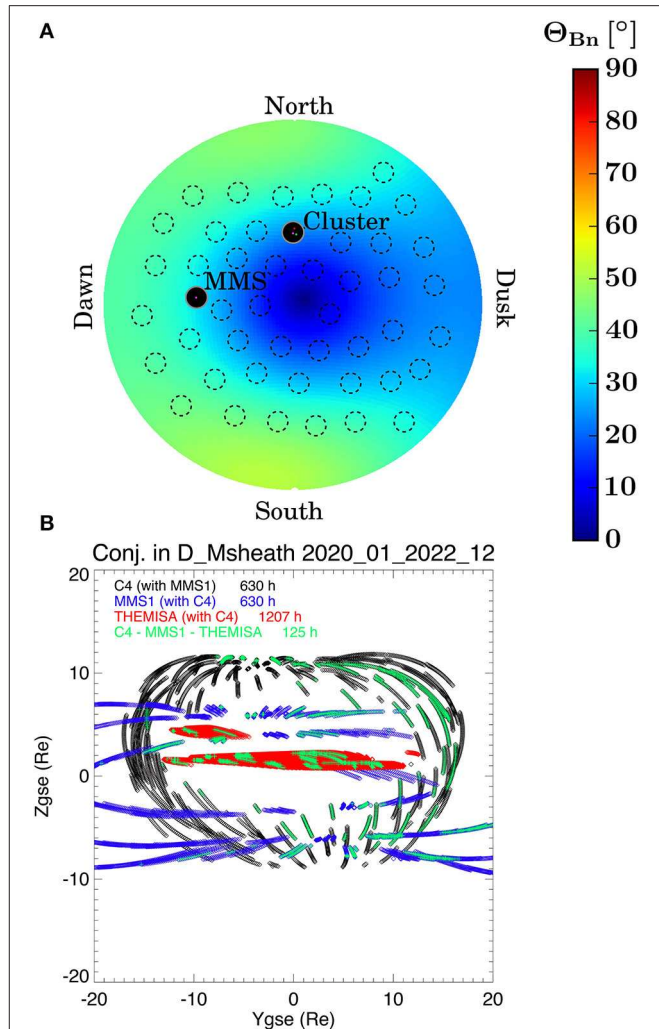
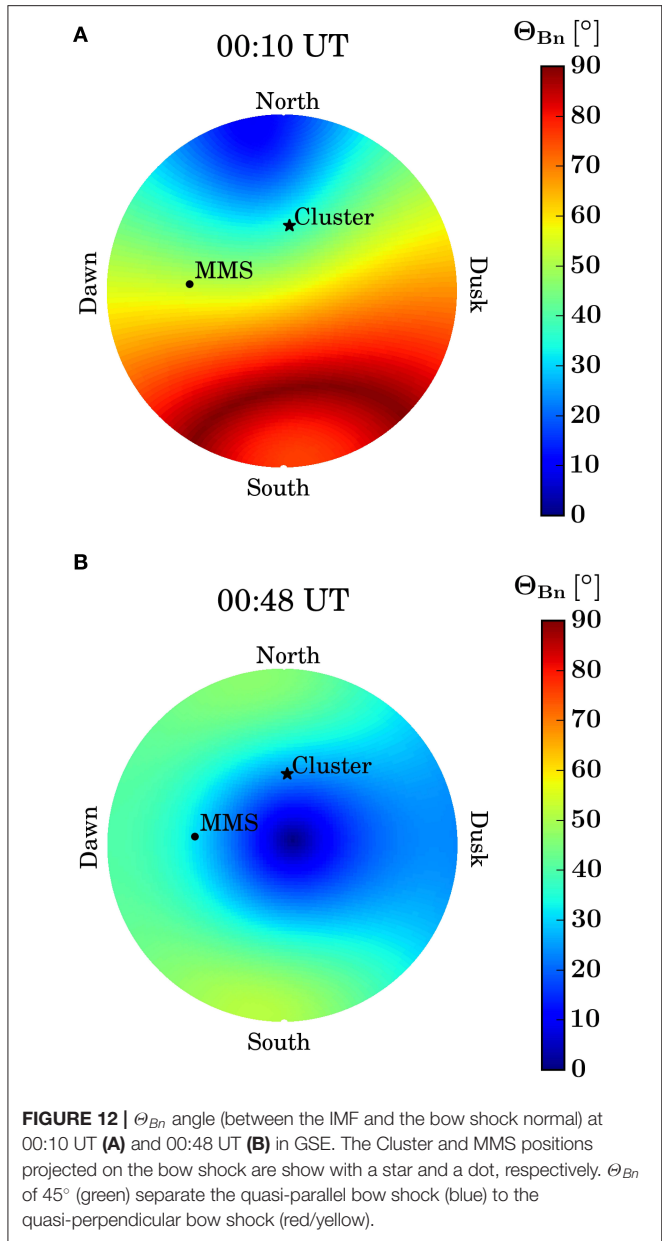
We analyzed the high-resolution spacecraft potential data (150 μ s time resolution) and could identify four possible dust impacts. Two of these are shown on **Figure 11**. Left panel shows the event at 00:45:46.645 UT on MMS3 and right panel shows the second event was detected at 01:01:33.520 UT on MMS2.

Both events are characterized by a sharp increase of the probe to spacecraft potential (top panels) of all 6 probes and then the slow decrease quickly after. The spacecraft potential (bottom panels) is calculated using the four spin probes (P1–P4), and corrected from the probe-plasma potential and other effects. Both events are characterized by a decrease of the spacecraft potential which is explained by a hypervelocity dust impact on the spacecraft body and subsequent reconnection of impact cloud particles (e.g., Vaverka et al., 2018). The plasma around the spacecraft will then become denser and the spacecraft potential will decrease. Note that the scales of both events are very different with a change of spacecraft potential around 0.4 V at 00:45:46.645 UT and around 6 V at 01:01:33.520 UT. These events are very similar to Vaverka et al. (2018) dust impact identification on MMS data. A third and fourth events were detected at 01:06:16.580 UT on MMS3 with a spacecraft potential decrease of 1.5 V and at 01:07:36.906 UT on MMS2 with a spacecraft potential decrease of 0.15 V (not shown). The time of all four dust impacts are shown as dotted lines on **Figure 3h**.

DISCUSSION AND CONCLUSION

We have studied HSJs characteristics and their impact on the magnetopause at two widely separated points (10 R_E) across the dayside magnetosheath, using the Cluster and MMS constellations.

Our main observations can be summarized in the following:



- Many HSJs were observed at two very large separation over the dayside of the magnetosheath;
- IMF was radial with a low cone angle at the center of the event;
- HSJs were observed at Cluster 25 min before MMS;
- HSJs were characterized by a dominant V_x component with strong V_y at $-Y$ position (MMS) and strong V_z components at $-Z$ position (Cluster);
- 21 and 12 HJSs were observed by Cluster and MMS, respectively;
- Two HJSs were observed simultaneously at Cluster and MMS and given their characteristics and size, they would most likely be two separated HSJs;
- The largest HSJs observed, respectively, by Cluster and MMS had a computed size along the flow of 4.3 and 9.8 R_E

and an estimated size of 8.6 and 19.6 R_E perpendicular to the flow;

- During these largest HSJs, when observed by one constellation, the other constellation had entered the magnetosphere a few minutes before and had left again a few minutes after;
- 6 and 2 magnetopause crossings were observed by MMS and Cluster during this interval with a significant angle, from 11° to 114°, between the normal given by the constellations and the normal given by the magnetopause model;

- One inbound magnetopause crossing observed by Cluster was observed simultaneous to an outbound magnetopause crossing of MMS;
- Four dust impacts were observed as a short pulse of the spacecraft potential between 00:45 UT and 01:10 UT on MM2 and MMS3 and no signature of dust cloud (IFE) was observed in the solar wind.

Cluster observed 7 HSJs before MMS observed its first one at 00:25 UT, 24 min later than the first one on Cluster. It has been shown previously that HSJs are predominantly observed behind a quasi-parallel shock (Hietala et al., 2009; Archer and Horbury, 2013; Plaschke et al., 2016), when the IMF makes an angle less than 45° with the shock normal. **Figure 12A** shows the Θ_{Bn} angle (between the IMF and the perpendicular to the bow shock surface) at 00:10 UT (before the IMF becomes radial) and at 00:48 UT (IMF radial). This shows that Cluster was behind the quasi-parallel shock ($\Theta_{Bn} < 45^\circ$) while MMS was behind a quasi-perpendicular shock (Θ_{Bn} larger than 45°) at 00:10 UT. This could explain why Cluster observe HSJs 24 min earlier than MMS. At 00:48 UT (**Figure 12B**), both Cluster and MMS are behind the quasi-parallel shock and both see HSJs around the same time. Under such IMF, the quasi-parallel shock would extend over the whole dayside of the magnetosphere, and it is expected to see HSJs on both Cluster and MMS although they are separated by $10 R_E$. This shows that under such circumstances HSJs may cover a wide area of the front side magnetosphere as observed statistically by Plaschke et al. (2016).

The first MMS HSJ was observed at 00:24 UT. The first IMF cone angle (and therefore Θ_{Bn}) change was observed at 00:32 UT (THEMIS-B) 00:34 UT (OMNI). THEMIS-B timing may be more accurate than OMNI, since it was closer to the bow shock along X. THEMIS was, however, quite far away from the Sun-Earth line ($Y_{GSE} = 48 R_E$) and may also have some inaccuracy of a few minutes. We know that the IMF propagation from L1 to the bow shock can have inaccuracy of up to 20 min (Case and Wild, 2012), specially under radial IMF (Jelínek et al., 2010; Suvorova and Dmitriev, 2015). Such change in OMNI data may have therefore occurred 10–15 min before and could explain that MMS was behind a quasi-parallel bow shock and observing the first HSJ at 00:24 UT. The first turning of the Θ_{Bn} close to 0 may then have occurred a few minutes before the first MMS HSJ observation at 00:24 UT. MMS would then be connected to the parallel bow shock similar to 00:48 UT (**Figure 12B**).

The fact that a string of HSJs are observed at two points of the magnetosheath separated by $10 R_E$ shows that a large portion of the dayside magnetosphere may be impacted quasi-simultaneously by HSJs. Plaschke et al. (2016) assumed a circular surface of $5.7 R_E$ of radius centered around the Sun Earth line in his statistics. Our observations cover a wider area with Cluster at $XYZ_{GSE} = [9.9, 0.3, 7.1] R_E$ and MMS at $XYZ_{GSE} = [7.7, -8.0, 0.7] R_E$. Enlarging the HSJs region, may increase the impact rates of 9 HSJs per hour obtained by Plaschke et al. (2016) for low cone angle. In our observations we detected 33 HSJs (adding Cluster and MMS) in 1 h 15 s and assuming that most of them are distinct, we get up to 26 per hour. This may also be underestimated if HSJs were also present in between Cluster and MMS and in other parts of the dayside magnetosphere.

Plaschke et al. (2017) observed 18 HSJs with MMS in 58 min during low cone angle conditions, which is also higher than in his statistical analysis results. This shows that maybe other criteria such as high Mach number may need to be fulfilled, together with low IMF cone angle, for HSJs to be produced and in such cases, their frequency increases significantly when both criteria are met. Under the continuous impacts of HSJs, the magnetopause is deformed significantly and can even move in opposite directions at different places. It can therefore not be considered as a smooth surface anymore but more as surface full of local indentations.

Figure 13A shows the HSJs observed by Cluster and MMS (black spots using median size of the observations) and Θ_{Bn} at 00:48 UT as background. Since we observed many HSJs at both Cluster and MMS, separated by $10 R_E$, during 1.5 h, it is fair to assume that HSJs would be observed at other locations behind the quasi-parallel shock. Possible additional HSJs, with similar size as the ones observed at MMS and Cluster are sketched as spots in dashed line. The number of HSJs and the space in between is a pure assumption, but it illustrates that we may expect to see HSJs over the whole region of low Θ_{Bn} . Further investigation of other conjunctions between Cluster and MMS will be conducted to collect more events that may help to shed light on the spatial distribution of HSJ. New observations will also come in a few years when the THEMIS spacecraft will have their apogee aligned with Cluster and MMS. **Figure 13B** shows Cluster, MMS and THEMIS predicted simultaneous observations of the magnetosheath in 2020–2022. Double conjunctions will occur during many 100s of hours while triple conjunction with all three constellations at the same time in the magnetosheath would occur around 125 h.

Could the magnetopause crossings by one constellation be related to the HSJ observed by the other? The inbound crossing observed by one constellation (00:39:44 UT with MMS and 01:06:24 UT with Cluster) would not be related to the HSJ observed by Cluster at 00:42 UT and by MMS at 01:11:05 UT since these are observed a few minutes after the magnetopause crossing and they would still need a few additional 10s of second to reach the magnetopause. The outbound crossing however at 00:44:45 UT with MMS and at 01:14:47 UT with Cluster could be related. Both of these crossings are fast -139 and -143 km s^{-1} and show a deviation from the model magnetopause of 59° and 17° , respectively. The large size of these HSJs ($D_\perp = 8.6$ and $19.5 R_E$) would compress a large part of the dayside magnetosphere and the magnetopause may be pushed through a spacecraft even at $10 R_E$ away.

The main possible source of HSJs could be either solar wind discontinuities, solar wind dust cloud or bow shock ripples. Solar wind discontinuities would not explain all the HSJs observed, especially the ones between 00:10 UT and 00:30 UT which occur under stable solar wind IMF. Dust clouds signatures (IFE) were not observed in the solar wind, however, smaller clouds passing through the spacecraft in <10 min cannot be excluded. On the other hand, four signatures of dust impact were observed on MMS. These dust impacts could only be observed in burst data that was limited to three periods of 10 min. These burst intervals are around magnetopause crossing and not in the magnetosheath proper. None of these impacts are occurring simultaneously

with the observation of HSJs, although we observed strong flows in the Y direction for three of them (see **Figure 3**). Four HSJs however have been observed in burst mode (00:38:14 UT, 00:50:10 UT, 00:56:01 UT, 01:09:22 UT, part of 01:11:05 UT) and did not show impact of dust on the spacecraft potential within 10s of seconds or few minutes of their duration. To draw a conclusion on the causality of dust on HSJs would require more events. However, the number of dust impact is still low and we would need more dust impacts and HSJs to exclude the dust clouds from the source of HSJs. Such investigation is however beyond of the scope of the current study. To our knowledge, however, this is the first time that dust impacts are indeed observed around the time of the HSJs observations. It is difficult to compare to statistics of nanodust impacts observed in the solar wind, on average 13 per day (Kellogg et al., 2016), with so few events but if we consider 2 events on MMS3 or MMS2 in 30 min, by extrapolation we would obtain 96/day. This is higher than the maximum rate of 62/day observed by Kellogg et al. (2016), however given the low number of events and the short interval of the MMS observation, it may not be significantly higher than the dust impacts observed in the solar wind.

The last process that would produce HSJs is bow shock ripples (Hietala et al., 2009) when the IMF is radial and the solar wind Mach number is above 10. Our event shows a radial IMF in the center of the event and the Alfvén Mach number was above 10 throughout the interval considered (**Figure 2G**), therefore it would fulfill Hietala et al. (2009) criteria for bow shock ripples and the subsequent penetration of HSJs in the magnetosheath. There is no spacecraft however in our event that could confirm the bow shock ripples. The fact that the HSJs have a -Y velocity component on the dawnside (MMS observations) and a +Z velocity component at mid latitude in the north hemisphere (Cluster observations) may indicate a link with the bow shock. It may also be a signature of the large scale magnetosheath flow diversion around the magnetopause. The fact that Cluster observed HSJs 25 min before MMS, which seems to be linked to the extent of the quasi-parallel bow shock (**Figure 12**), would also favor this process. Future conjunctions should however help to better constraint the HSJs source process by having spacecraft measuring at the same time the region upstream and downstream of the bow shock, the bow shock itself, magnetosheath HSJs and their impact on the magnetopause (**Figure 13B**).

DATA AVAILABILITY STATEMENT

The Cluster, MMS, and THEMIS/OMNI datasets for this study can be found in the Cluster science Archive at <http://csa.esac.esa.int>, the MMS science data center at <https://lasp.colorado.edu/mms/sdc/public/> and the NASA Space Physics Data Facility at <https://omniweb.sci.gsfc.nasa.gov>, respectively.

REFERENCES

- Amata, E., Savin, S. P., Ambrosino, D., Bogdanova, Y. V., Marcucci, M. F., Romanov, S., et al. (2011). High kinetic energy density jets in

AUTHOR CONTRIBUTIONS

CE did the data analysis and wrote the manuscript. K-JH and ST-R co-chair the ISSI working group where this study was conducted and provided comments. LT provided **Figure 12** and part of **Figure 13** and comments on the paper. SH provided support for the magnetopause normal computations and comments on the paper. NA, JD, JE, RF, HF, KG, DG, YK, GL, BL, CN, DS, and AV participated to the ISSI working group. JB, AD, GP, MD, YB, OR, HL, AM, MT, and PK provided comments to the manuscript. CC, ID, AF, RN, JB, BG, CP, CR, and RT provided the Cluster and MMS data through the Cluster archive and MMS data center.

FUNDING

The work of LT is supported by the Academy of Finland (Grant No. 322544). This research was supported by the NASA Magnetospheric Multiscale Mission in association with NASA contract NNG04EB99C. The work at UCLA was supported through subcontract 06-001 with the University of New Hampshire. RF was supported by STFC Consolidated Grant ST/R000719/1. MD was supported by NSFC grants 41874193 and 41821003. ST-R acknowledges support of the Ministry of Economy and Competitiveness (MINECO), Spain, Grant No. FIS2017-90102-R. PK's work was supported by PAPIIT grant IA101118. K-JH was, in part, supported by NSF AGS-1834451, NASA 80NSSC18K1534, 80NSSC18K0570, 80NSSC18K0693, and 80NSSC18K1337. ID thanks CNES for its support. JE acknowledges UKRI/STFC grant ST/N000692/1. YB was supported by the STFC RAL Space in House Research funding. Work of YK was supported by the Swedish National Space Board.

ACKNOWLEDGMENTS

We acknowledge the Cluster and MMS PIs, the Cluster Science archive (<https://csa.esac.esa.int>) and the MMS data center (<https://lasp.colorado.edu/mms/sdc/public/>) for making the Cluster and MMS best calibrated data available. The Space Physics data Facility at NASA/GSFC is also acknowledged for providing the OMNI data set and V. Angelopoulos and the THEMIS team for providing the THEMIS B data. Data analysis was done with the QSAS science analysis system provided by the United Kingdom Cluster Science Center (Imperial College London and Queen Mary, University of London) supported by The Science and Technology Facilities Council (STFC), specially T. Allen and S. Schwartz, and SH for the magnetopause normal analysis plug-ins. The OVT team (<https://ovt.irfu.se>) is greatly acknowledged. We finally acknowledge the International Space Science Institute (ISSI) for supporting the team called MMS and Cluster observations of magnetic reconnection led by two authors of this paper (K-JH and ST-R).

the earth's magnetosheath: a case study. *Planet. Space Sci.* 59, 482–494.
doi: 10.1016/j.pss.2010.07.021

Archer, M. O., Hietala, H., Hartinger, M. D., Plaschke, F., and Angelopoulos, V. (2019). Direct observations of a surface eigenmode of the dayside

- magnetopause. *Nat. Commun.* 10:615. doi: 10.1038/s41467-018-0134-5
- Archer, M. O., and Horbury, T. S. (2013). Magnetosheath dynamic pressure enhancements: occurrence and typical properties. *Annal. Geophys.* 31, 319–331. doi: 10.5194/angeo-31-319-2013
- Archer, M. O., Horbury, T. S., and Eastwood, J. P. (2012). Magnetosheath pressure pulses: generation downstream of the bow shock from solar wind discontinuities. *J. Geophys. Res.* 117:A05228. doi: 10.1029/2011JA017468
- Axford, W. I., and Hines, C. O. (1961). A unifying theory of high-latitude geophysical phenomena and geomagnetic storms. *Can. J. Phys.* 39, 1433–1464. doi: 10.1139/p61-172
- Baker, D. N., Riesberg, L., Pankratz, C. K., Panneton, R. S., Giles, B. L., Wilder, F. D., et al. (2016). Magnetospheric multiscale instrument suite operations and data system. *Space Sci. Rev.* 199, 545–575. doi: 10.1007/s11214-014-0128-5
- Balogh, A., Carr, C. M., Acuña, M. H., Dunlop, M. W., Beek, T. J., Brown, P., et al. (2001). The cluster magnetic field investigation: overview of in-flight performance and initial results. *Ann. Geophys.* 19:1207. doi: 10.5194/angeo-19-1207-2001
- Burch, J. L., Moore, T. E., Torbert, R. B., and Giles, B. L. (2016). Magnetospheric multiscale overview and science objectives. *Space Sci. Rev.* 199, 5–21. doi: 10.1007/s11214-015-0164-9
- Cahill, L. J., and Amazeen, P. G. (1963). The boundary of the geomagnetic field. *J. Geo. phys. Res.* 68, 1835–1843. doi: 10.1029/JZ068i007p01835
- Case, N. A., and Wild, J. A. (2012). A statistical comparison of solar wind propagation delays derived from multispacecraft techniques. *J. Geophys. Res.* 117:A02101. doi: 10.1029/2011JA016946
- Dungey, J. W. (1961). Interplanetary magnetic field and the auroral zone. *Phys. Res. Lett.* 6:47. doi: 10.1103/PhysRevLett.6.47
- Ergun, R. E., Tucker, S., Westfall, J., Goodrich, K. A., Malaspina, D. M., Summers, D., et al. (2016). The axial double probe and fields signal processing for the MMS mission. *Space Sci. Rev.* 199, 167–188. doi: 10.1007/s11214-014-0115-x
- Escoubet, C. P., Fehringer, M., and Goldstein, M. (2001). The cluster mission. *Ann. Geophys.* 19, 1197–1200. doi: 10.5194/angeo-19-1197-2001
- Gunell, H., Stenberg Wieser, G., Mella, M., Maggiolo, R., Nilsson, H., and Darrouzet, F. (2014). Waves in high-speed plasmoids in the magnetosheath and at the magnetopause. *Ann. Geophys.* 32, 991–1009. doi: 10.5194/angeo-32-991-2014
- Haaland, S., Sonnerup, B. U. O., Paschmann, G., Georgescu, E., Dunlop, M. W., Balogh, A., et al. (2006). *Discontinuity Analysis with Cluster, in Cluster and Double Star Symposium, ESA SP-598*. Noordwijk: ESA Publications Division.
- Heikkila, W. J. (1982). Impulsive plasma transport through the magnetopause. *Geophys. Res. Lett.* 9, 159–162. doi: 10.1029/GL009i002p00159
- Hietala, H., Laitinen, T. V., Andreœvá, K., Vainio, R., Vaivads, A., and Palmroth, M. (2009). Supermagnetosonic jets behind a collisionless quasiparallel shock. *Phys. Rev. Lett.* 103:245001. doi: 10.1103/PhysRevLett.103.245001
- Hietala, H., and Plaschke, F. (2013). On the generation of magnetosheath high-speed jets by bow shock ripples. *J. Geophys. Res.* 118, 7237–7245. doi: 10.1002/2013JA019172
- Jelinek, K., Němcéck, Z., Šafránková, J., Shue, J.-H., Suvorova, A. V., and Sibeck, D. G. (2010). Thin magnetosheath as a consequence of the magnetopause deformation: THEMIS observations. *J. Geophys. Res.* 115:A10203. doi: 10.1029/2010JA015345
- Johnstone, A. D., Alsop, C., Burge, S., Carter, P. J., Coates, A. J., Coker, A. J., et al. (1997). PEACE: a plasma electron and current experiment. *Space Sci. Rev.* 79, 351–398. doi: 10.1007/978-94-011-5666-0_13
- Karlsson, T., Brenning, N., Nilsson, H., Trotignon, J.-G., Vallières, X., and Fácsko, G. (2012). Localized density enhancements in the magnetosheath: three-dimensional morphology and possible importance for impulsive penetration. *J. Geophys. Res.* 117:A03227. doi: 10.1029/2011JA017059
- Kellogg, P. J., Goetz, K., and Monson, S. J. (2016). Dust impact signals on the wind spacecraft. *J. Geophys. Res. Space Phys.* 121, 966–991. doi: 10.1002/2015JA021124
- King, J. H., and Papitashvili, N. E. (2005). Solar wind spatial scales in and comparisons of hourly wind and ACE plasma and magnetic field data. *J. Geophys. Res.* 110:A02104. doi: 10.1029/2004JA010649
- Laakso, H., Taylor, M., and Escoubet, C. P. (eds.) (2010). “The cluster active archive,” in *Astrophysics and Space Science Proceedings* (New York, NY: Springer).
- Lai, H. R., and Russell, C. T. (2018). Nanodust released in interplanetary collisions. *Planet. Space Sci.* 156, 2–6. doi: 10.1016/j.pss.2017.10.003
- Lemaire, J., and Roth, M. (1978). Penetration of solar wind plasma elements into the magnetosphere. *J. Atmos. Terr. Phys.* 40, 331–335. doi: 10.1016/0021-9169(78)90049-1
- Lindqvist, P., Olsson, G., Torbert, R. B., King, B., Granoff, M., Rau, D., et al. (2016). The spin-plane double probe electric field instrument for MMS. *Space Sci. Rev.* 199, 137–165. doi: 10.1007/s11214-014-0116-9
- Liu, Y. Y., Fu, H. S., Liu, C. M., Wang, Z., Escoubet, P., Hwang, K.-J., et al. (2019). Parallel electron heating by tangential discontinuity in turbulent magnetosheath. *Astrophys. J. Lett.* 877:L16. doi: 10.3847/2041-8213/ab1fe6
- Malaspina, D., and Wilson, L. B. (2016). A database of interplanetary and interstellar dust detected by the wind spacecraft. *J. Geophys. Res. Space Phys.* 121, 9369–9377. doi: 10.1002/2016JA023209
- Meyer-Vernet, N., Maksimovic, M., Czechowski, A., Mann, I., Zouganelis, I., Goetz, K., et al. (2009). Dust detection by the wave instrument on STEREO: nanoparticles picked up by the solar wind? *Sol. Phys.* 256, 463–474. doi: 10.1007/s11207-009-9349-2
- Miura, A. (1984). Anomalous transport by magnetohydrodynamic kelvin-helmholtz instabilities in the solar wind-magnetosphere interaction. *J. Geophys. Res.* 89, 801–818. doi: 10.1029/JA089iA02p00801
- Moore, T. W., Nykyri, K., and Dimmock, A. P. (2016). Cross-scale energy transport in space plasmas. *Nat. Phys.* 12, 1164–1169. doi: 10.1038/nphys3869
- Nemecék, Z., Šafránková, J. M., Prech, L., Sibeck, D. G., Kokubun, S., Mukai, T., et al. (1998). Transient flux enhancements in the magnetosheath. *Geophys. Res. Lett.* 25, 1273–1276. doi: 10.1029/98GL50873
- Plaschke, F., Hietala, H., and Angelopoulos, V. (2013). Anti-sunward high-speed jets in the subsolar magnetosheath. *Annal. Geophys.* 31, 1877–1889. doi: 10.5194/angeo-31-1877-2013
- Plaschke, F., Hietala, H., Angelopoulos, V., and Nakamura, R. (2016). Geoeffective jets impacting the magnetopause are very common. *J. Geophys. Res. Space Phys.* 121, 3240–3253. doi: 10.1002/2016JA022534
- Plaschke, F., Hietala, H., Archer, M., Blanco-Cano, X., Kajdič, P., Karlsson, T., et al. (2018). Jets downstream of collisionless shocks. *Space Sci. Rev.* 214:81. doi: 10.1007/s11214-018-0516-3
- Plaschke, F., Karlsson, T., Hietala, H., Archer, M., Vörös, Z., Nakamura, R., et al. (2017). Magnetosheath high-speed jets: internal structure and interaction with ambient plasma. *J. Geophys. Res.* 122, 10157–10175. doi: 10.1002/2017JA024471
- Pollock, C., Moore, T., Jacques, A., Burch, J., Gliese, U., Saito, Y., et al. (2016). Fast plasma investigation for magnetospheric multiscale. *Space Sci. Rev.* 199, 331–406. doi: 10.1007/s11214-016-0245-4
- Rème, H., Aoustin, C., Bosqued, J. M., Dandouras, I., Lavraud, B., Sauvaud, J. A., et al. (2001). First multispacecraft ion measurements in and near the earth's magnetosphere with the identical cluster ion spectrometry (CIS) experiment. *Ann. Geophys.* 19, 1303–1354. doi: 10.5194/angeo-19-1303-2001
- Roelof, E.-C., and Sibeck, D. G. (1993). Magnetopause shape as a bivariate function of interplanetary magnetic field Bz and solar wind dynamic pressure. *J. Geophys. Res.* 98, 21421–21450. doi: 10.1029/93J02362
- Russell, C. T., Anderson, B. J., Baumjohann, W., Bromund, K. R., Dearborn, D., Fischer, D., et al. (2016). The magnetospheric multiscale magnetometers. *Space Sci. Rev.* 199, 189–256. doi: 10.1007/s11214-014-0057-3
- Russell, C. T., Luhmann, J. G., Barnes, A., Mihalov, J. D., and Elphic, R. C. (1983). An unusual interplanetary event: encounter with a comet? *Nature* 305, 612–615. doi: 10.1038/305612a0
- Savin, S., Amata, E., Zelenyi, L., Budaev, V., Consolini, G., Treumann, R., et al. (2008). High kinetic energy jets in the earth's magnetosheath: implications for plasma dynamics and anomalous transport. *JETP Lett.* 87, 593–599. doi: 10.1134/S0021364008110015
- Savin, S. P., Zelenyi, L. M., Amata, E., Buechner, J., Blecki, J., Klimov, S. I., et al. (2004). Dynamic interaction of plasma flow with the hot boundary layer of a geomagnetic trap. *JETP Lett.* 79, 368–371. doi: 10.1134/1.172433

- Shue, J.-H., Chao, J.-K., Song, P., McFadden, J. P., Suvorova, A., Angelopoulos, V., et al. (2009). Anomalous magnetosheath flows and distorted subsolar magnetopause for radial interplanetary magnetic fields. *Geophys. Res. Lett.* 36:L18112. doi: 10.1029/2009GL039842
- Sonnerup, B. U. O., Haaland, S., Paschmann, G., Dunlop, M. W., Réme, H., and Balogh, A. (2006). Orientation and motion of a plasma discontinuity from single-spacecraft measurements: generic residue analysis of cluster data. *J. Geophys. Res.* 111:A05203. doi: 10.1029/2005JA011538
- Sonnerup, B. U. O., and Scheible, M. (1998). "Minimum and maximum variance analysis," in *Analysis Methods for Multi-Spacecraft Data*, eds G. Paschmann and P. W. Daly (Noordwijk: ESA Publications Division), 185–220.
- Suvorova, A. V., and Dmitriev, A. V. (2015). Magnetopause inflation under radial IMF: comparison of models. *Earth Space Sci.* 2, 107–114. doi: 10.1002/2014EA000084
- Torbert, R. B., Russell, C. T., Magnes, W., Ergun, R. E., Lindqvist, P.-A., LeContel, O., et al. (2016). The FIELDS instrument suite on MMS: scientific objectives, measurements, and data products. *Space Sci. Rev.* 199, 105–135. doi: 10.1007/s11214-014-0109-8
- Vaverka, J., Nakamura, T., Kero, J., Mann, I. B., De Spiegeleer, A., Hamrin, M., et al. (2018). Comparison of dust impact and solitary wave signatures detected by multiple electric field antennas onboard the MMS spacecraft. *Space Phys. Space Phys.* 123, 6119–6129. doi: 10.1029/2018JA025380
- Vaverka, J., Pellinen-Wannberg, A., Kero, J., Mann, I., De Spiegeleer, A., Hamrin, M., et al. (2017). Detection of meteoroid hypervelocity impacts on the cluster spacecraft: first results. *J. Geophys. Res. Space Phys.* 122, 6485–6494. doi: 10.1002/2016JA023755
- Williams, T., Sulman, S., Sedlak, J., Ottenstein, N. and Lounsbury, B. (2016). Magnetospheric Multiscale Mission Attitude Dynamics: Observations from Flight Data. doi: 10.2514/6.2016-5675.
- Wing, S., Johnson, J. R., Chaston, C. C., Echim, M., Escoubet, C. P., Lavraud, B., et al. (2014). Review of solar wind entry into and transport within the plasma sheet. *Space Sci. Rev.* 184, 33–86. doi: 10.1007/s11214-014-0108-9
- Conflict of Interest:** The authors declare that the research was conducted in the absence of any commercial or financial relationships that could be construed as a potential conflict of interest.
- The handling editor declared a past co-authorship with one of the authors GL.
- Copyright © 2020 Escoubet, Hwang, Toledo-Redondo, Turc, Haaland, Aunai, Dargent, Eastwood, Fear, Fu, Genestreti, Graham, Khotyaintsev, Lapenta, Lavraud, Norgren, Sibeck, Varsani, Berchem, Dimmock, Paschmann, Dunlop, Bogdanova, Roberts, Laakso, Masson, Taylor, Kajdič, Carr, Dandouras, Fazakerley, Nakamura, Burch, Giles, Pollock, Russell and Torbert. This is an open-access article distributed under the terms of the Creative Commons Attribution License (CC BY). The use, distribution or reproduction in other forums is permitted, provided the original author(s) and the copyright owner(s) are credited and that the original publication in this journal is cited, in accordance with accepted academic practice. No use, distribution or reproduction is permitted which does not comply with these terms.



Current Sheet Statistics in the Magnetosheath

Emiliya Yordanova^{1*}, Zoltán Vörös^{2,3}, Savvas Raptis⁴ and Tomas Karlsson⁴

¹ Swedish Institute of Space Physics, Uppsala, Sweden, ² Space Research Institute, Austrian Academy of Sciences, Graz, Austria, ³ Geodetic and Geophysical Institute, Research Centre for Astronomy and Earth Sciences (RCAES), Sopron, Hungary, ⁴ Space and Plasma Physics, Royal Institute of Technology, Stockholm, Sweden

OPEN ACCESS

Edited by:

Benoit Lavraud,
UMR5277 Institut de Recherche en
Astrophysique et Planétologie (IRAP),
France

Reviewed by:

Jiansen He,
Peking University, China
Luca Franci,
Queen Mary University of London,
United Kingdom
Vincenzo Carbone,
Dipartimento di Fisica, Università della
Calabria, Italy

*Correspondence:

Emiliya Yordanova
eya@irfu.se

Specialty section:

This article was submitted to
Space Physics,
a section of the journal
*Frontiers in Astronomy and Space
Sciences*

Received: 02 August 2019

Accepted: 20 January 2020

Published: 07 February 2020

Citation:

Yordanova E, Vörös Z, Raptis S and
Karlsson T (2020) Current Sheet
Statistics in the Magnetosheath.
Front. Astron. Space Sci. 7:2.
doi: 10.3389/fspas.2020.00002

The magnetosheath (MSH) plasma turbulence depends on the structure and properties of the bow shock (BS). Under quasi-parallel ($Q_{||}$) and quasi-perpendicular (Q_{\perp}) BS configurations the electromagnetic field and plasma quantities possess quite distinct behavior, e.g., being highly variable and structured in the $Q_{||}$ case. Previous studies have reported abundance of thin current sheets (with typical scales of the order of the plasma kinetic scales) in the $Q_{||}$ MSH, associated with magnetic reconnection, plasma heating, and acceleration. Here we use multipoint observations from Magnetospheric MultiScale (MMS) mission, where for the first time a comparative study of discontinuities and current sheets in both MSH geometries at very small spacecraft separation (of the order of the ion inertial length) is performed. In $Q_{||}$ MSH the current density distribution is characterized by a heavy tail, populated by strong currents. There is high correlation between these currents and the discontinuities associated with large magnetic shears. Whilst, this seems not to be the case in Q_{\perp} MSH, where current sheets are virtually absent. We also investigate the effect of the discontinuities on the scaling of electromagnetic fluctuations in the MHD range and in the beginning of the kinetic range. There are two (one) orders of magnitude higher power in the magnetic (electric) field fluctuations in the $Q_{||}$ MSH, as well as different spectral scaling, in comparison to the Q_{\perp} MSH configuration. This is an indication that the incoming solar wind turbulence is completely locally reorganized behind Q_{\perp} BS while even though modified by $Q_{||}$ BS geometry, the downstream turbulence properties are still reminiscent to the ones upstream, the latter confirming previous observations. We show also that the two geometries are associated with different temperature anisotropies, plasma beta, and compressibility, where the Q_{\perp} MSH is unstable to mostly mirror mode plasma instability, while the $Q_{||}$ MSH is unstable also to oblique and parallel fire-hose, and ion-cyclotron instabilities.

Keywords: magnetosheath, bow shock, PVI, discontinuities, current sheets, plasma turbulence

1. INTRODUCTION

The interaction between the supersonic and superalfvénic solar wind with the Earth's magnetic field results in the formation of the terrestrial bow shock (BS). The BS geometry depends on the local orientation of the interplanetary magnetic field (IMF) and the shock normal, i.e., on the angle θ_{BN} . When θ_{BN} is smaller than 45° , the configuration of the BS and the adjacent downstream magnetosheath (MSH) is called—quasi-parallel ($Q_{||}$); when the angle is larger than 45° , it is called

quasi-perpendicular (Q_{\perp}). The plasma dynamics of the two geometries is quite different. The Q_{\parallel} MSH being magnetically connected to the solar wind strongly interacts with the upstream transients and discontinuities hitting the bow shock (BS). The MSH turbulence is also influenced by the various instabilities generated by the reflected at the BS ions in the upstream foreshock region. An example is high-speed magnetosheath jets (e.g., Archer and Horbury, 2013; Hietala and Plaschke, 2013; Plaschke et al., 2013) that are believed to be connected to ripples on the BS, created by downstream-convected foreshock fluctuations, triggered by the counterstreaming ions (Hao et al., 2016). Such ripples can allow the solar wind plasma to cross the BS with only weak deceleration, resulting in the high-speed flows in the magnetosheath (Franci et al., 2016). It should be noted, however, that the bow shock ripples are intrinsic and may possibly be created by other mechanisms as well (Sundberg et al., 2016), even in the case of Q_{\perp} BS (Fuselier, 2013). Another product of upstream-downstream interaction is the Hot Flow Anomaly (HFA) (Zhang et al., 2013)—when a solar wind tangential discontinuity with appropriate orientation intersects the BS, a hot core of the back-streaming ions with lower ram pressure, and compressed plasma edges associated with weak shock waves develop, which eventually deform the magnetopause.

In difference, to the Q_{\parallel} MSH geometry, there is a sharp increase of the magnetic field magnitude and abrupt deceleration of the plasma in Q_{\perp} MSH. Also, the fluctuations of the plasma parameters characterizing the MSH region with Q_{\perp} geometry have lower amplitude. Particle energization is mainly caused by the adiabatic and non-adiabatic compressions across the shock. Typical for the Q_{\perp} MSH is the ion temperature anisotropy (with respect to the magnetic field), arising from ion reflection and adiabatic compression of ions transmitted at the shock (Johlander et al., 2018). In turn, the temperature anisotropy give rise to the Alfvén ion cyclotron (AIC) instability, for the case of proton plasma $\beta_p < 1$, and mirror mode (MM) instability, for $\beta_p > 1$. Various simulations have shown the importance of AIC waves at and near the BS (Burgess et al., 2016 and references therein). On the other hand, MM are often observed closer to the magnetopause where the temperature anisotropy is higher (Dimmock et al., 2015). The resulted waves from AIC and MM instabilities, together with the magnetic compressibility, affect the fluctuation anisotropy and their spectral properties (Breuillard et al., 2018).

Most of our observational knowledge about incompressible collisionless magnetohydrodynamic (MHD) turbulence comes from the solar wind (Bruno and Carbone, 2013). It agrees with the classical view of turbulent cascade developing due to non-linear interactions from the large scales where the energy is injected, then being transferred without any loses in the inertial range, and finally being dissipated at the smaller than the ion and electron scales via wave-particle interactions and magnetic reconnection. The inertial range appears as a power law in the power spectral density (PSD) of the fluctuations with Kolmogorov slope $-5/3$. However, an intrinsic feature of solar wind turbulence is the coexistence of intermittent spatio-temporal structures (e.g., discontinuities and current

sheets) along with the turbulent fluctuations. The intermittency is identified as the departure of the probability distribution functions (PDFs) of magnetic field increments from Gaussian statistics (Marsch and Tu, 1994) and it is associated with the formation of sharp gradients. The gradients are important at the small scale end of the MHD range and they reflect the available energy in the turbulent energy cascade which can potentially generate various structures such as current sheets (CSs), (Karimabadi et al., 2014; Matthaeus et al., 2015 and references there in) and magnetic reconnection, (Karimabadi et al., 2014; Matthaeus et al., 2015; Treumann and Baumjohann, 2015). On the other hand again, such coherent structures are of fundamental importance because they become the focal place where energy is dissipated.

Solar wind discontinuities are broadly studied in the past years (Matthaeus et al., 2015 and reference there in). However, their origin is still debated: they are seen either as the boundaries of small scale flux ropes produced in the solar corona (Borovsky, 2008), or alternatively as being locally generated by the turbulent cascade (Carbone et al., 1990). It is worth noting, that both views do not exclude each other. Similarly to the solar wind, the magnetosheath turbulence is also intermittent (Yordanova et al., 2008). The discontinuities can be locally generated or convected from the solar wind to the MSH. Cluster observations showed that turbulence generated thin proton-scale CSs are ubiquitous in the magnetosheath downstream of a Q_{\parallel} bow shock (Vörös et al., 2016). In recent numerical (Wan et al., 2015) and other observational studies in the Q_{\parallel} MSH, it was evidenced that dissipation, plasma acceleration, plasma heating, and magnetic reconnection occurs at such narrow CSs (Sundqvist et al., 2007; Chasapis et al., 2015, 2018; Eriksson et al., 2016; Yordanova et al., 2016; Phan et al., 2018; Vörös et al., 2019).

As a whole, independently on its geometry, the MSH is a unique plasma laboratory because the turbulence there is high plasma beta (β) and it is compressional, i.e., a type of turbulence which does not occur often in the solar wind, except during short time transient CME sheaths, and we know very little about. In addition, the occurrence and origin of discontinuities in Q_{\perp} MSH is largely unknown. Therefore, we aim here to assess the differences in the magnetosheath turbulence properties and structure in an event where MMS measurements are available from the two configurations. This paper is organized as follows: in section 2 we present the determination of the magnetosheath configuration and the discontinuity detection tool; in section 3 the investigated data set is described; in section 4 the results from the comparison are shown, which are finally discussed in the last section 5.

2. METHODS

In order to verify and distinguish between the Q_{\perp} and Q_{\parallel} MSH, we apply a set of criteria based on the magnetic field variance, the temperature anisotropy, and the high energy ion flux. The classification algorithm is based on the local magnetosheath MMS data rather than the associated solar wind upstream measurements. This was done for several reasons. Available solar

TABLE 1 | Averaged parameters and the respective variance (gray) for quasi-perpendicular (Q_{\perp}) and (Q_{\parallel}) MSH.

MSH	$\langle v_{bulk} \rangle$	$\langle v_A \rangle$	$\langle B \rangle$	$\delta B/B_0$	$\langle N_i \rangle$	$\langle T_i \rangle$	$\langle T_{\perp}/T_{\parallel} \rangle$	$\langle \beta_i \rangle$	$\langle J_{curl} \rangle$
Q_{\perp}	136(326)	145(466)	31(16)	0.2(0.02)	22(3)	326(1240)	1.5(0.01)	3(2)	38(590)
Q_{\parallel}	150(2609)	92(1086)	21(58)	0.9(0.2)	26(29)	349(3738)	1(0.03)	16(2648)	172(17735)

Dimensional values are given in the following units: $\langle v_{bulk} \rangle$, $\langle v_A \rangle$: km/s; $\langle B \rangle$: nT; $\langle N_i \rangle$: cm $^{-3}$; $\langle T_i \rangle$: eV; $\langle J_{curl} \rangle$: nA/m 2 .

wind data is usually artificially propagated to the BS from L1, producing an uncertainty regarding the exact time. This is due to the fact that the propagating models are not fully accurate and the BS shape and position are dynamically changing. Additionally, the MMS orbit does not have a constant distance from the BS, which makes the associated upstream values require further propagation inside the MSH depending on the MMS position, providing further uncertainty to the associated solar wind values. Finally, there are several cases where there is no solar wind data available that can be associated to MMS measurements.

Initially, the Partial Variance of Increments (PVI) method was proposed for detection of coherent structures in the solar wind turbulence from single point observations and MHD numerical simulations (Greco et al., 2008, 2009). Later, it was also adapted to multipoint measurements for the magnetosheath region (Chasapis et al., 2015; Vörös et al., 2016). PVI is by definition the partial variance of magnetic field increments ($\Delta \mathbf{B}_{ij}(t) = \mathbf{B}_i(t) - \mathbf{B}_j(t)$), estimated between two points of measurements, in our case—by pairs of spacecraft:

$$PVI_{ij}(t) = \sqrt{\frac{|\Delta \mathbf{B}_{ij}(t)|^2}{\langle |\Delta \mathbf{B}_{ij}|^2 \rangle}}, \quad (1)$$

where the average $\langle \cdot \rangle$ is taken over the whole interval, and $i,j = 1,2,3,4$ is the MMS spacecraft number. It is worth noting that the PVI method from multipoint measurement will be sensitive to structures with size comparable to the distance between spacecraft.

In addition, the rotation of the magnetic field between two spacecraft, i.e., magnetic field shear angle, can be estimated as:

$$\alpha_{ij}(t) = \cos^{-1} \frac{\mathbf{B}_i(t) \cdot \mathbf{B}_j(t)}{|\mathbf{B}_i(t)| \cdot |\mathbf{B}_j(t)|}. \quad (2)$$

Previously was reported that a correlation between PVI and α exists—high PVI and high magnetic shears are indication that the detected discontinuity is a current sheet (Chasapis et al., 2015). It was also shown that such current sheets are associated with local increase of electron temperature and energy dissipation at electron scales (Chasapis et al., 2018). On the contrary, when the PVIs and the magnetic shear angles are small, these parameters measure a stochastic noise.

We note that simulations (Zhang et al., 2015) and observations (Wang et al., 2013) of the discontinuities in the solar wind has revealed that plasma heating is more significant around tangential discontinuities than rotational discontinuities. However, in our case, the PVI (Equation 1) as an identifier of current sheets, together with the magnetic shear angle (Equation

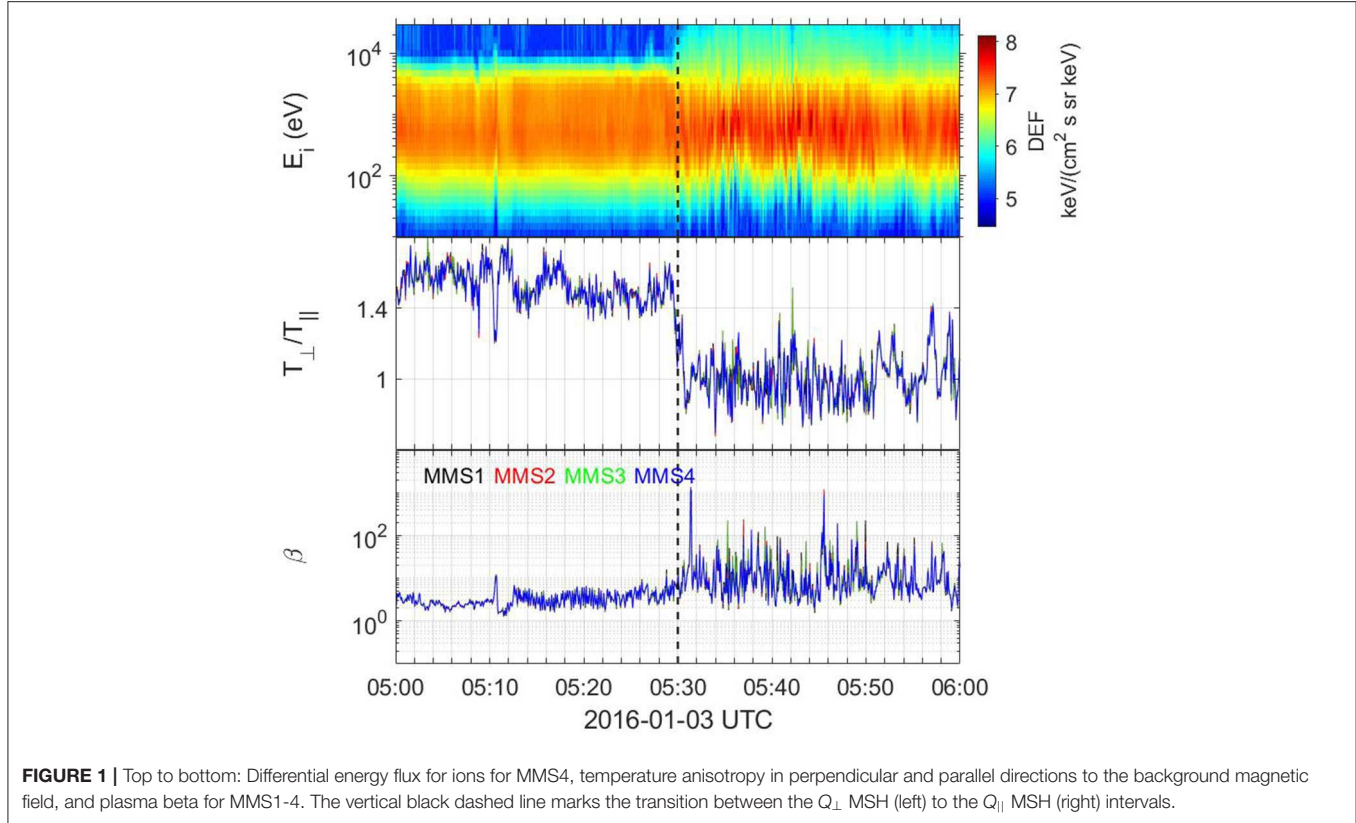
2), were calculated between the spacecraft pairs with separation distances between the electron and ion gyroradius scales. In such a case, the small-scale sub-gyro-scale current sheets found for the given spacecraft separations do not necessarily correspond to discontinuities existing in magnetohydrodynamics (Balikhin et al., 2014).

3. DATA

In this work, we use measurements from the four identical spacecraft of the MMS mission, whose objective is to investigate the plasma processes at kinetic scales in the Earth's magnetosphere. The magnetic field data, sampled at 16 Hz were obtained by the Flux Gate Magnetometer (FGM) instrument (Russell et al., 2014). The Electric field Double Probe (EDP) instrument provides the electric field data with sampling of 32 Hz (Lindqvist et al., 2016). Finally, the electron and ion moments were available from the Fast Plasma Investigation (FPI) instrument (Pollock et al., 2016), sampled with spacecraft spin frequency of 4.5 s. During 2016-01-03/05:00-06:00 UTC, the spacecraft were in the magnetosheath region close to the subsolar region at $(9, -7, -1)$ R_E in GSE coordinates. The fleet was in tetrahedron formation with separation between spacecraft of ~ 36 km. For the sake of comparison, the interval under investigation was selected such that MMS consequently passed through Q_{\perp} and then through Q_{\parallel} BS geometry, so that both cases are subjected to similar upstream plasma conditions. Four minutes (05:28–05:32 UTC) in the transition from one region to the other are excluded from the analysis to ensure that the parameters we compare are typical for the respective MSH configuration. The average plasma parameters are shown in Table 1. The difference between the four spacecraft are insignificant therefore, we choose the values corresponding to MMS4.

4. RESULTS

Figure 1 (top to bottom) shows the spectrogram of the ion differential energy flux, the ion temperature anisotropy with respect to the magnetic field, and the ion plasma beta during the selected event. It is clearly seen that in the interval 05:30–06:00 UTC, there are much larger fluctuations than the ones observed in the period 05:00–05:30 UTC, indicating that the magnetosheath is subjected to a different bow shock geometry: first MMS was sampling a Q_{\perp} MSH and then got immersed in a Q_{\parallel} MSH (the border between the two configurations is marked with the black dash line in Figure 1). We distinguish between the two cases, according to the criteria described in



the section 2, based on the magnetic field variance, temperature anisotropy, and high ion differential energy flux (DEF). It is known, that the temperature anisotropy is typically higher in Q_{\perp} MSH compared to Q_{\parallel} one (Fuselier et al., 1994), which is supported by our estimation in **Figure 1 (middle panel)**, where the ion temperature (T_{\perp}) perpendicular to the magnetic field is higher than the one in the parallel direction (T_{\parallel}) for all spacecraft. In the Q_{\parallel} MSH (to the right of the black vertical line) the temperature anisotropy is small, and fluctuates around 1. Further, the variance of the magnetic field components is also higher in the Q_{\parallel} configuration. This is true for the other plasma parameters (see **Table 1**), e.g., plasma density, resulting in the ion plasma beta (β) shown in **Figure 1 (bottom panel)**. Note that despite the different variability (with β occasionally reaching values from tens to hundreds in Q_{\parallel} MSH), $\beta > 1$ in both geometries, which is characteristic for the magnetosheath, and shows that in general, the plasma pressure dominates the magnetic one. This is opposite to the case of the low plasma β of the upstream solar wind. The most striking difference between the two configurations, however, is the ion differential energy flux that is observed in Q_{\parallel} MSH, while being completely absent in Q_{\perp} MSH (Fuselier, 2013) (**Figure 1, top panel**). One can see also much more discrete structure in the energy band in the Q_{\parallel} MSH vs. the smooth featureless energy spectrum in the Q_{\perp} case.

The visual inspection of the wave forms of the magnetic field (**Figure 2, top panels**) shows that in the Q_{\perp} MSH (*left*) the fluctuations of the components are small, the field intensity

is strong, the components are well-separated and there are no directional changes. On the other hand, in the Q_{\parallel} MSH (*right*), the variability of the magnetic field is very high (see also **Table 1**), the components nearly overlap with sudden changes of sign, and the field magnitude is lower. The "turbulence" level $\delta B/B_0 \approx 0.9$ (for $\delta B > 0.001$ Hz), i.e., the fluctuations are of the order of the background magnetic field. This is opposite to $\delta B/B_0 \approx 0.2$ for Q_{\perp} MSH, meaning that we can assume the validity of mean-field approximation since the fluctuations are quite small. The described behavior is typical for the respective geometries (Lucek et al., 2005).

Next, we search for coherent structures by calculating PVI from the magnetic field increments for all pairs of spacecraft. **Figure 2** presents the PVI (annotated as PVI₄₂) in the plot and the magnetic vector rotations for the example of MMS 4 and 2 pair (**Figure 2, middle panels**). The results from the other pairs of spacecraft are very similar. Over the time scale of 0.25 s (defined by the spacecraft separation and the plasma bulk speed), the PVI in the Q_{\parallel} MSH is characterized by abundance of strong peaks (PVI > 3). Some of the strongest PVI values are also associated with large magnetic field shear angles ($\alpha > 100$), implying that the detected structures are current sheets. On the contrary, in the Q_{\perp} MSH, however, there is a complete absence of any such activity—PVI hardly reaches 1.5 and the magnetic shear is less than 10°. Thanks to the multipoint MMS measurements and the availability of both plasma components (electrons and ions), we can estimate the current density in

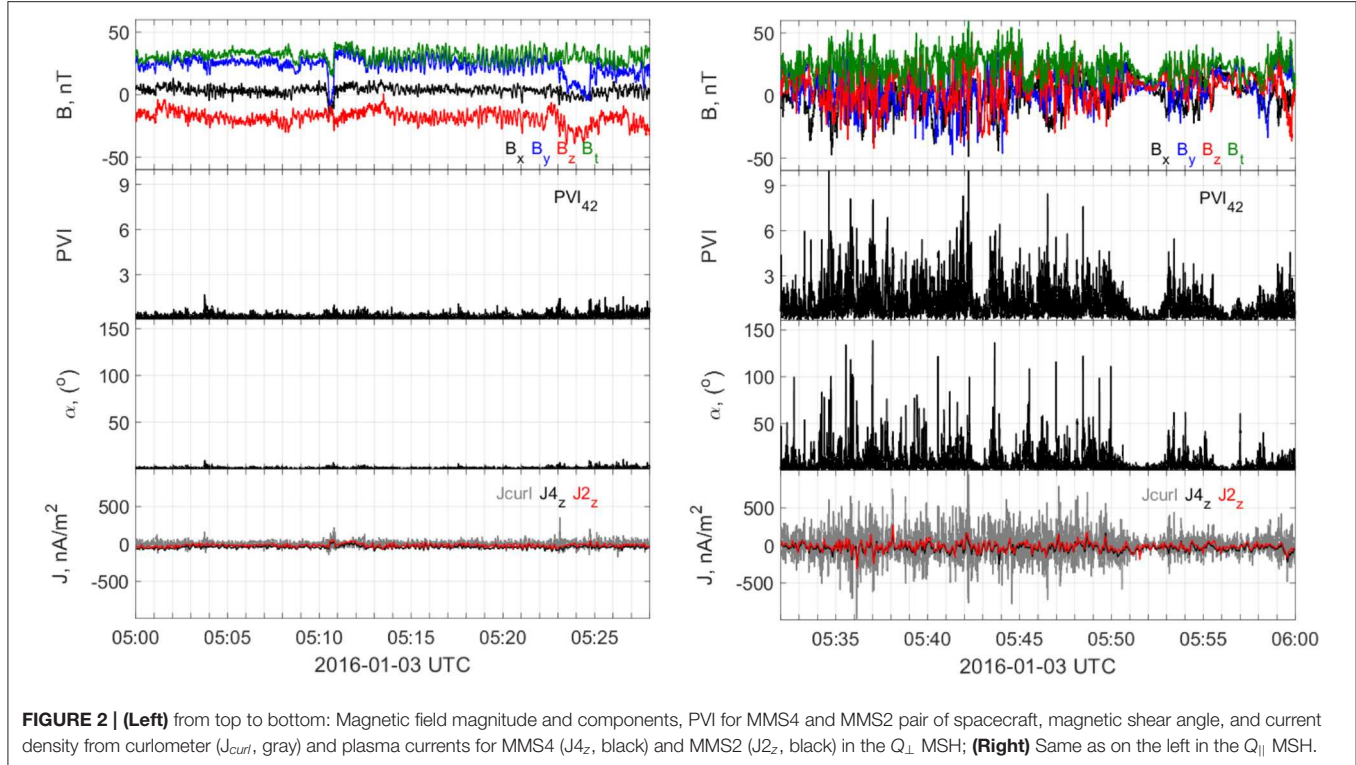


FIGURE 2 | (Left) from top to bottom: Magnetic field magnitude and components, PVI for MMS4 and MMS2 pair of spacecraft, magnetic shear angle, and current density from curlometer (J_{curl} , gray) and plasma currents for MMS4 (J_{4z} , black) and MMS2 (J_{2z} , black) in the Q_{\perp} MSH; **(Right)** Same as on the left in the Q_{\parallel} MSH.

two ways: from the curlometer technique ($J_{curl} = (\nabla \times B)/\mu_0$, μ_0 —the magnetic constant, Dunlop et al., 2002), and from the plasma measurements, and then relate it to the PVI and magnetic shear. **Figure 2 (bottom panels)**, shows the J_z component of the plasma current and the same component of the current from the curlometer. It is worth noting that in this comparison, we cannot benefit from the highest particle resolution because it is not available for such long intervals as the one in hand. However, the spacecraft are so close to each other that the curlometer current is better resolved, and we can see the presence of strong small-scale currents throughout the Q_{\parallel} MSH, where they are also well-correlated with the PVI peaks and large magnetic rotations. Despite the low (spin) resolution, the plasma current follows closely the curlometer current. Previously, such very good correlation between the PVI and the high intensity curlometer current has also been demonstrated on the basis of Cluster multipoint measurements (Chasapis et al., 2017).

Further, we compare the distribution of $PVI > 3$ as a function of the magnetic shear α for the two MSH geometries (**Figure 3, left panel**). The distribution is obtained by combining the PVIs from all pairs of spacecraft. The threshold is chosen such that the statistics represents the stronger discontinuities that may be related to current sheets. Note again that, PVI detection here is limited to the time scale of the spacecraft separation (~ 0.25 s). In the Q_{\perp} MSH, the PVI is concentrated mostly at magnetic rotation under 10° , and there is no PVI values above 20° . At the same time, the PVI histogram for Q_{\parallel} case has counts in the entire range of angles. The distribution maximum is $\sim 30^{\circ}$ and has heavy tail for $\alpha > 90^{\circ}$. It is known from MHD simulations

(Greco et al., 2009) and observations (Vörös et al., 2016) that the heavy tail belongs to the presence of current currents. This is also confirmed here by the histogram of the current density shown in **Figure 3 (right panel)**. Similar to the PVI histogram, the current distribution has heavy tail due to strong currents in Q_{\parallel} MSH extending up to 1000 nA/m², while J has mostly values < 200 nA/m² in the Q_{\perp} . In fact, we performed a single test (not shown) and deduced that the few counts of the maximum current in Q_{\perp} MSH belong to the two structures at 05:11 and 05:22–05:25 UTC (**Figure 2, top and bottom panels** and the isolated light blue bar at ~ 370 nA/m² in **Figure 3, right panel**). Alternative possibility for the current sheets origin, is that they have very likely been convected from the solar wind into the magnetosheath since WIND observations (not shown) reveal non-stationary solar wind at the times corresponding to our event. It is difficult to attribute in the plasma moments an indication that these discontinuities are locally generated, due to the low sampling resolution at the spacecraft spin.

Further, we investigate the correlation between the current intensity from the curlometer and the PVI (**Figure 4**). We consider here only the Q_{\parallel} MSH interval, given the very small PVI activity and current intensity in the Q_{\perp} MSH. In gray are plotted all PVI values, showing wide spread. Since, as described earlier, PVI is proportional to the current, we look at the correlation between the current and only those PVI values that are associated with magnetic rotation angles larger than 100° (black dots). The obtained correlation with this conditioning is quite good with coefficient of 0.7. The large current densities or PVI's (Servidio et al., 2011), associated with large magnetic shear angles (Vörös

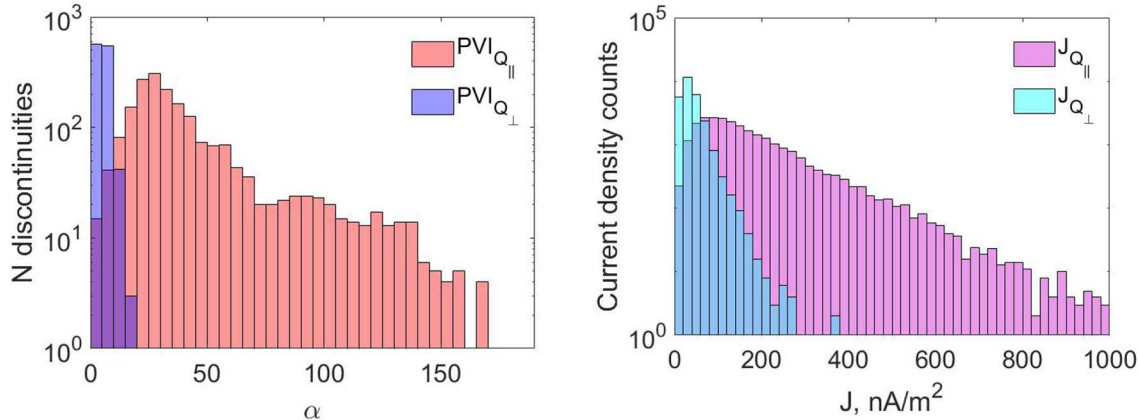


FIGURE 3 | (Left) PVI calculated from magnetic field increments, in bins of 5 degrees shear angle for all pairs of MMS for threshold PVI > 3; **(Right)** Current density from curlometer method in bins of 20 nA/m². Note, the shorter Y range in the left panel.

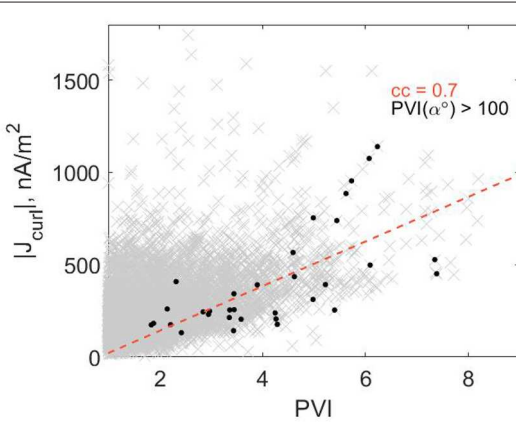


FIGURE 4 | Current magnitude from curlometer vs all PVI values (gray) in the case of Q_{\parallel} MSH. The black dots correspond to PVI conditioned for magnetic shear larger than 100°. The red dashed line represents the correlation with coefficient 0.7, between the current and the conditioned PVI.

et al., 2016; Yordanova et al., 2016) can correspond to potentially reconnecting current sheets.

To characterize further the magnetosheath fluctuations and make a comparison between the two MSH geometries, we compute the PSD of the magnetic and electric field fluctuations for Q_{\perp} in **Figure 5 (left panel)** and Q_{\parallel} MSH (**right panel**). The PSD is calculated from FFT using Welch method with Hanning window and 75% overlap between the data segments. The annotated spectral indices are obtained by linear fitting over certain frequency ranges of the averaged from all spacecraft PSD. Since, the observed PSD is obtained in frequency domain, to interpret the spectral scaling in terms of turbulence regimes we need to transform the temporal scales into spacial scales. This is done by assuming the Taylor hypothesis, where the intrinsic plasma fluctuations evolve much slower than the bulk plasma speed, therefore they are considered frozen-in in the flow (Taylor, 1938). Taylor hypothesis is usually well-satisfied in the solar wind (Perri et al., 2017). In our event, the bulk flow and the Alfvén

velocity have close magnitude (see **Table 1**), which potentially could invalidate this assumption. Recent numerical simulation however, demonstrated that even for high beta cases the spectral slopes are preserved but shifted in fluctuation level (Perri et al., 2017). Also, the presence of zero-frequency structures, such as current sheets, do not violate the Taylor hypothesis. This has been confirmed by MMS observations, where the assumption was successfully applied in a case of electron reconnection in the MSH (Stawarz et al., 2019). Considering our results, we are mindful that the validity of the Taylor hypothesis may be uncertain for our event.

In both MSH configurations the PSD shows power law behavior. However, the spectral shape and the power content are distinctly different between the two geometries. In the Q_{\perp} MSH, the PSD has single power law for the magnetic field (-2.8), extending over one decade (0.1–6 Hz) with the ion gyrofrequency $f_c \sim 0.5$ Hz. The electric field power law at the low frequency is rather short (0.1–0.8 Hz), with close spectral slope -2.6 close to the magnetic field one. A second shallower regime can be recognized starting at 0.8 Hz in the electric fluctuations above 0.8 Hz with spectral index -1 in the range 0.8–6 Hz. There is a bump at 0.05–0.1 Hz in the spectra, probably due to the presence of mirror modes (MM) commonly occurring in the Q_{\perp} MSH at such frequencies. Their typical appearance as wave-train of dips in the magnetic field observations can be distinguished in the period 05:12–05:28 UTC (**Figure 2, top left panel**). MM are characterized by anticorrelation between the magnetic field and plasma density and can also appear as trains of peaks in the magnetic field magnitude. From a large statistical study (Dimmock et al., 2015), it has been shown that the upstream Alfvén Mach number M_A controls the MM formation as dips, when M_A is small, or peaks when M_A is large. A possible scenario has been proposed recently in a numerical study for the development of turbulent cascade in the absence of inertial range, i.e., without Kolmogorov scaling (Franci et al., 2017). It was attributed to the interplay between magnetic reconnection and plasma turbulence. However, this scenario cannot explain the same power law in the MHD and sub-ion regimes in the

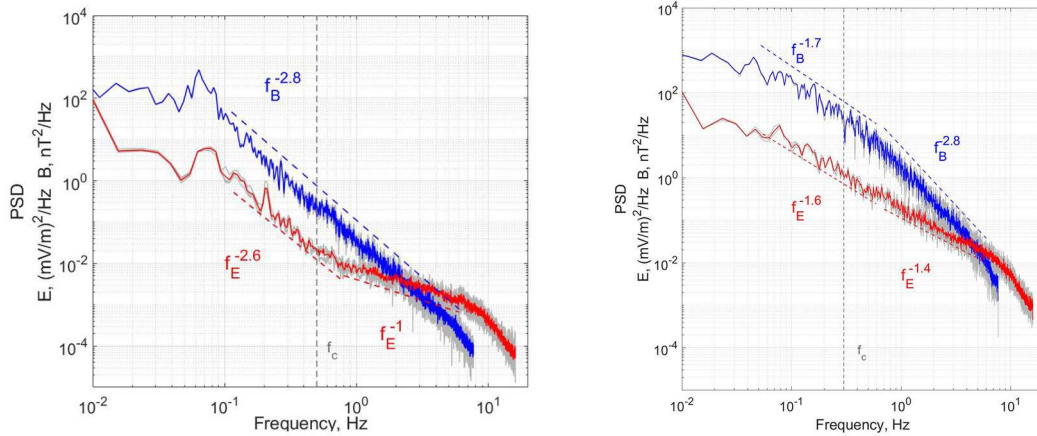


FIGURE 5 | (Left) PSD of the average over the four MMS spacecraft magnitudes of the electric (red) and magnetic (blue) fields over-plotted on the spectrum from each spacecraft (gray) for the Q_{\perp} MSH; **(Right)** Same as on the left in the $Q_{||}$ MSH. The vertical gray dashed line marks the respective gyrofrequency f_c for each MSH geometry. The error in the spectral slopes are very small and are reported in the text.

reported here Q_{\perp} MSH, because there are no strong current sheets and large magnetic field rotations observed that could serve as possible reconnection sites, thus this issue still remains an open question.

In the $Q_{||}$ MSH, on the other hand, there are nearly two orders of magnitude higher spectral content in the magnetic field and one order higher power in the electric field. At the lower frequencies (0.05–0.6 Hz), the spectral index of the magnetic fluctuations is -1.7 , which is close to theoretical Kolmogorov one of fully developed turbulence in the inertial range. A spectral break is observed at 0.6 Hz (near $f_c \sim 0.3$ Hz), followed by a second steeper power law (-2.8) in the higher frequency domain up to 6 Hz. The electric field scaling in the inertial range is -1.6 , which is slightly shallower than the magnetic field spectral slope, but also close to the Kolmogorov one. Above the break at 0.6 Hz at higher frequency, the power law becomes somewhat shallower (-1.4). All of these differences imply that the plasma turbulence in the $Q_{||}$ MSH must be substantially different from the one in the Q_{\perp} MSH. This will be discussed in more details in the next section. For the sake of completeness, we have estimated the uncertainty in the estimation of the spectral slope by considering each individual MMS spacecraft and by varying the frequency ranges over which the spectral fit is performed. We found that the slopes are rather stable with very small errors—for Q_{\perp} MSH, the electric field spectral slope in the MHD domain is -2.61 ± 0.03 , in the kinetic range it is -0.97 ± 0.08 ; and the magnetic field one is -2.79 ± 0.01 . In the case of $Q_{||}$ MSH the electric field scales as -1.59 ± 0.03 in the MHD domain, and -1.38 ± 0.03 in the kinetic range; respectively, the magnetic field index in the MHD range is -1.79 ± 0.02 , and in the kinetic one it is -2.77 ± 0.04 .

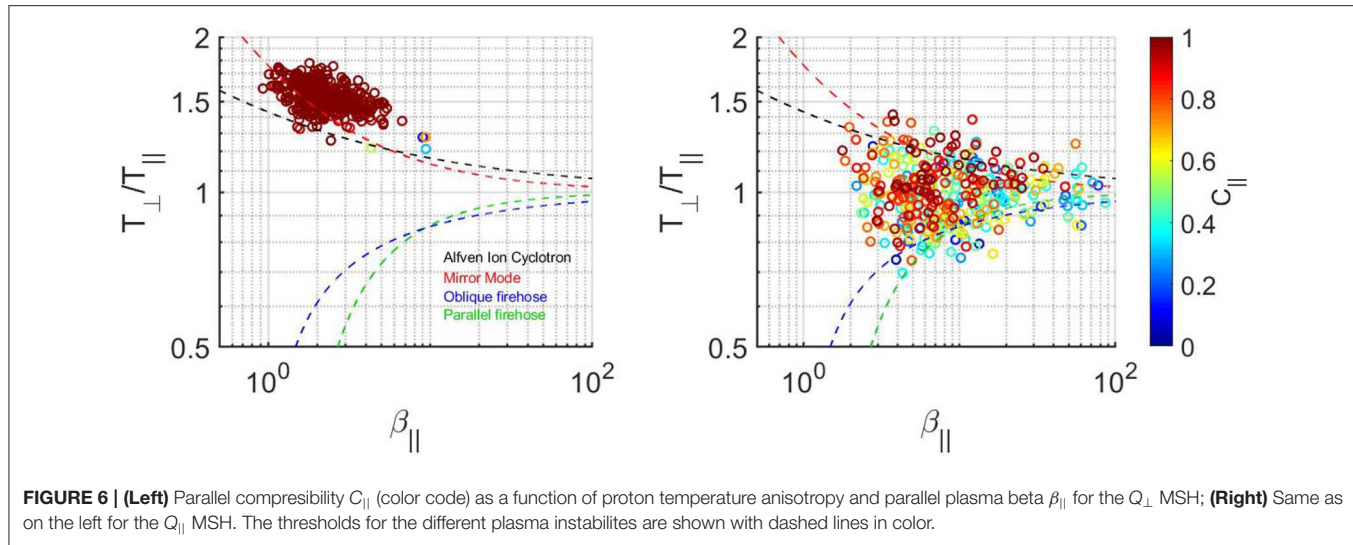
The $Q_{||}$ and Q_{\perp} MSH configurations are clearly associated with different ion temperature anisotropies, plasma β and compressibility distributions. Figure 6 shows the scatterplots for $\beta_{||}$ vs. ion temperature anisotropy ratio $T_{\perp}/T_{||}$, with color coded parallel compressibility $C_{||} = \delta B_{||}^2/(\delta B_{||}^2 + \delta B_{\perp}^2)$. The colored dashed lines correspond to the thresholds of ion cyclotron

(black), mirror mode (red), oblique (magenta) and parallel fire-hose (green) plasma instabilities (Hellinger et al., 2006), respectively. In the Q_{\perp} MSH (Figure 6, left), $C_{||}$ falls in the range of $T_{\perp}/T_{||}$ values between 1.2 and 2, and for $\beta_{||}$ roughly between 1 and 10, being at and over the ion cyclotron threshold and mostly concentrated around mirror mode threshold. $C_{||}$ is also larger in the Q_{\perp} MSH than in the $Q_{||}$ one (Figure 6, right). In the latter case $\beta_{||}$ is roughly between 2 and 100 and $T_{\perp}/T_{||}$ is between 0.7 and 1.5, being over the instability thresholds for larger values of $\beta_{||}$.

5. DISCUSSION

The PVI method provides a relatively simple tool to find in the data small volumes of concentrated field gradients that are linked to coherent structures, i.e., to intermittency. This was demonstrated for the first time by Greco et al. (2008) on the basis of 3D Hall MHD numerical simulation. In a more recent simulation, it was predicted that the large current density corresponds to strong PVI peaks in reconnecting current sheets (Donato et al., 2013). This correspondence was confirmed experimentally in the $Q_{||}$ MSH with the high resolution Cluster (Vörös et al., 2016; Chasapis et al., 2017) and MMS (Yordanova et al., 2016) data.

In the $Q_{||}$ MSH presented here, the intermittency and the related current sheets appear in the burstiness of the PVI (Figure 2, middle panel), and the non-Gaussian PVI and current distributions (Figure 3). Although there is a clear statistical difference in the current distribution between the two geometries, there can exist a few current sheets reaching 200 nA/m^2 also in the Q_{\perp} case. Our results demonstrate that perhaps it is not the mean values or medians of distributions which are important, but the large current values in the tail, which correspond to the strongest current sheets and probably have the largest influence on dissipation during a time interval. In a recent study, based on MMS magnetosheath data (Stawarz et al., 2019), it has also



been shown that the distributions of magnetic field increments and currents are highly non-Gaussian with heavy tails due to reconnecting electron-scale current sheets. The authors have demonstrated that a link exist between the power law spectrum and magnetic reconnection, where below the ion gyroradius, the magnetic field PSD exhibits higher steepening the more current sheets are evidenced to reconnect. In Q_{\parallel} MSH this may be one mechanism for dissipating energy. It is worth noting that it is hard to speculate whether the current sheets are generated by turbulence in the MSH. For example, some current sheets can be generated in the solar wind or by the upstream BS, then convected downstream. When current sheets are generated by turbulence, they are obviously part of the turbulence, perhaps being associated with some additional self-organizing processes in the turbulent cascade, and this is not fully understood yet. Nevertheless, in both cases (current sheets as part of turbulence or generated by some other mechanisms), the study of these structures can be helpful in understanding the different nature of fluctuations in Q_{\perp} and Q_{\parallel} MSH.

While, as discussed already, there is abundance of small-scale current sheets in Q_{\parallel} MSH (Retinò et al., 2007; Vörös et al., 2016), associated with magnetic reconnection (Vörös et al., 2016; Yordanova et al., 2016; Phan et al., 2018) and energy dissipation (Sundqvist et al., 2007; Chasapis et al., 2018), in the Q_{\perp} MSH the fluctuations do not contain strong currents and the magnetic field is not changing directions (Figure 2). Given that current sheets are not present in Q_{\perp} , another dissipation mechanism might be at play. It was suggested that the kinetic processes are driven by electrostatic solitary waves at frequency > 100 Hz (Breuillard et al., 2018), which is unfortunately way outside the range available in our data set. Recently the damping of waves due to wave-particle interactions and the dissipation of ion-cyclotron waves in the Q_{\perp} MSH has been studied by He et al. (2019). They have found that the dissipation of ion-cyclotron wave energy occurs preferentially in the direction perpendicular to the mean magnetic field. This could partially explain the observed perpendicular temperature anisotropy seen in the Q_{\perp} MSH (Figure 1, bottom panel and Figure 6, left plot).

The power of the electromagnetic fluctuations in the Q_{\perp} MSH is much lower seemingly mostly concentrated near a low frequency bump, followed by steep (-2.8) slope at higher frequency (Figure 5, left panel). Similar bump was reported in Breuillard et al. (2018) and it was attributed to mirror modes, below which they also observe the same scaling. Such steep power law extended over the two frequency decades was reported in another Q_{\perp} MSH case study from INTERBALL-1 measurements (Shevrev and Zastenker, 2005), where the authors attributed the steeper PSD at low frequency to the mixture of MHD waves, including MM.

A statistical study of magnetosheath data from Cluster spacecraft revealed that the spectral slope in the MHD domain changes from -1 to -1.6 from the BS toward the flanks close to the magnetopause (Huang et al., 2017). Thus, the upstream solar wind turbulence is modified by the BS serving as a generator of additional fluctuations downstream in the magnetosheath. However, no significant dependence on θ_{BN} of the spectra have been found. On the contrary, they have found that the scaling in sub-ion range is independent on the distance from the BS. The MMS data studied here show similar trend—the spectral index in the frequency range around and above the ion gyro frequency have similar to -2.8 spectral slope for both BS geometries. The same scaling in the kinetic range was observed in another MMS magnetosheath comparison between Q_{\perp} MSH and Q_{\parallel} MSH (Breuillard et al., 2018). However, they also detected an additional range with Kolmogorov-like scaling (-1.6) in the Q_{\parallel} case at 0.02 – 0.2 Hz, similarly to our results of slope close to Kolmogorov -1.7 at 0.05 – 0.6 Hz.

The spectra of the electric field show that in the MHD frequency range the power law follows closely the one of the magnetic field (Figure 5), in the respective MSH geometry. Previous comparison of magnetic and electric field fluctuations from Cluster measurements in the case of high plasma $\beta \geq 1$ solar wind (Bale et al., 2005) and in the magnetosheath (Matteini et al., 2017) have also reported similar scaling in the MHD range. It was also found that, below the ion scales and before the electron scales are reached, the magnetic field PSD steepens

while the electric field one becomes shallower. Another feature is that the electric field power dominates the magnetic field one in the kinetic range. The theoretical prediction is that at sub-ion scales the magnetic and electric field decouple and the relation between their spectral slopes is: $\alpha_E = \alpha_B - 2$ (Sahraoui et al., 2009; Franci et al., 2018). We see similar trend in our results even though not exact - the shallower electric spectral slope leads to -1.8 difference in the fields scaling in the Q_{\perp} MSH, while in the Q_{\parallel} the relation is -1.4 . The reason for the non-exact relation in our case is probably due to the rather short frequency range of the power laws estimation. Another possibility is that, the relation between the slope is specifically valid for perpendicular component of the electric field and the parallel component of the magnetic field and not for the field magnitudes as in our case (Franci et al., 2018). The flattening of the electric field spectrum at high frequency could also explained by the high level noise at the small scales.

Further, as in the previously discussed high β cases the electric field power is higher than the magnetic field at higher frequency. This has been attributed to the contribution of the non-ideal terms in the Ohm's law (Franci et al., 2018). From a numerical prediction it is expected that in the MHD range the magnetic field power law is the same regardless plasma β (Franci et al., 2016). In the high frequency range, however, the spectral index is expected to become shallower the higher the plasma β : from -3.5 ($\beta \sim 0.01$) to -2.9 ($\beta > 1$), the latter being close to the β conditions in our case. Finally, statistical study based on Cluster (Dwivedi et al., 2019) and case study based on MMS (Breuillard et al., 2018) magnetosheath observations support the idea that the magnetic field turbulence cascade with -2.8 scaling at the high frequency range in the magnetosheath results from the non-linear evolution of KAW.

In summary, in this work we have investigated the magnetosheath turbulence downstream Q_{\perp} and Q_{\parallel} BS geometry by means of multipoint MMS measurements at very small spacecraft separations of the order of ion scales. In particular, we have focused on the differences in the fluctuations and occurrences of structures downstream of the different BS geometries. We have shown that while in the Q_{\parallel} MSH there is abundance of discontinuities and very strong currents associated with large rotations in the magnetic field (known from previous studies), in the Q_{\perp} MSH these are absent, which has not been reported before. Both regions exhibit high plasma β because of the compression and higher plasma density, however the fluctuations in all plasma variables in Q_{\parallel} are significantly more intense than in Q_{\perp} MSH. The power of the magnetic field is about two orders higher in the Q_{\parallel} than in the Q_{\perp} MSH. The electric field intensity in the Q_{\perp} case is one order weaker. Further, in the Q_{\perp} geometry the Kolmogorov

scaling is missing, which still remains an open question. One possibility suggested in the literature before, is that the turbulence did not have enough time to develop fully due the close proximity of the bow shock and the transit time through the magnetosheath being too short in comparison with the non-linear time of the intrinsic Alfvénic fluctuations in the inertial range. On the contrary, in the Q_{\parallel} MSH we still observed the inertial range, supporting previously suggested interpretation that the solar wind turbulence survives to some extend the transition through the BS. Finally, we have found that for large plasma β the plasma is unstable to AIC and predominantly MM instability in the Q_{\perp} MSH, while in the Q_{\parallel} MSH it is unstable to AIC, MM, and oblique and parallel fire-hose instabilities.

We conclude here that the different scaling and intrinsic turbulence structure would suggest that the plasma heating and dissipation occur by means of different mechanisms in the two magnetosheath configurations. Obviously, in the absence of simultaneous multi-point observations at the locations both of the bow shock and magnetosheath, we were not able to connect the magnetosheath observations directly with the details of shock physics upstream. However, we believe that the statistical investigations in Q_{\perp} and Q_{\parallel} MSH can help us to improve our understanding about dayside solar wind-magnetosphere interactions.

DATA AVAILABILITY STATEMENT

MMS data are available at the MMS Science Data Center (<https://lasp.colorado.edu/mms/sdc>).

AUTHOR CONTRIBUTIONS

EY and ZV designed the study. EY prepared the data and performed the analysis. SR and TK selected the time interval. All authors have contributed to the discussion and writing of the manuscript.

FUNDING

EY was funded by the Swedish Contingency Agency, grant 2016-2102. ZV was supported by the Austrian FWF under contract P28764-N27. SR and TK acknowledge support from SNSA grant 90/17.

ACKNOWLEDGMENTS

The authors acknowledge the MMS team. EY acknowledge A.P. Dimmock for the fruitful discussions.

REFERENCES

- Archer, M. O., and Horbury, T. S. (2013). Magnetosheath dynamic pressure enhancements: occurrence and typical properties. *Ann. Geophys.* 31, 319–331. doi: 10.5194/angeo-31-319-2013
- Bale, S. D., Kellogg, P. J., Mozer, F. S., Horbury, T. S., and Reme, H. (2005). Measurement of the electric fluctuation spectrum of magnetohydrodynamic turbulence. *Phys. Rev. Lett.* 94:215002. doi: 10.1103/PhysRevLett.94.215002
- Balikhin, M. A., Runov, A., Walker, S. N., Gedalin, M., Dandouras, I., Hobara, Y., et al. (2014). On the fine structure of dipolarization fronts. *J. Geophys. Res. Space Phys.* 119, 6367–6385. doi: 10.1002/2014JA019908
- Borovsky, J. E. (2008). Flux tube texture of the solar wind: strands of the magnetic carpet at 1 AU? *J. Geophys. Res.* 113:A08110. doi: 10.1029/2007JA012684

- Breuillard, H., Matteini, L., Argall, M. R., Sahraoui, F., Andriopoulou, M., Le Contel, O., et al. (2018). New insights into the nature of turbulence in the Earth's magnetosheath using magnetospheric multiscale mission data. *Astrophys. J.* 859:127. doi: 10.3847/1538-4357/aabae8
- Bruno, R., and Carbone V. (2013). The solar wind as a turbulence laboratory. *Living Rev. Solar Phys.* 10:2. doi: 10.12942/lrsp-2013-2
- Burgess, D., Hellinger, P., Gingell, I., and Travnicek, P. M. (2016). Microstructure in two- and three-dimensional hybrid simulations of perpendicular collisionless shocks. *J. Plasma Phys.* 82:905820401. doi: 10.1017/S0022377816000660
- Carbone, V., Veltri, P., Mangeney, A. (1990). Coherent structure formation and magnetic field line reconnection in magnetohydrodynamic turbulence. *Phys. Fluids A* 2, 1487–1496. doi: 10.1063/1.857598
- Chasapis, A., Matthaeus, W. H., Parashar, T. N., Le Contel, O., Retinó, A., Breuillard, H., et al. (2017). Electron heating at kinetic scales in magnetosheath turbulence. *Astrophys. J.* 836:247. doi: 10.3847/1538-4357/836/2/247
- Chasapis, A., Matthaeus, W. H., Parashar, T. N., Wan, M., Haggerty, C. C., Pollock, C. J., et al. (2018). *In situ* observation of intermittent dissipation at kinetic scales in the Earth's magnetosheath. *Astrophys. J. Lett.* 856:L19. doi: 10.3847/2041-8213/aaadf8
- Chasapis, A., Retinó, A., Sahraoui, F., Vaivads, A., Khotyaintsev, Yu. V., Sundkvist, D., et al. (2015). Thin current sheets and associated electron heating in turbulent space plasma. *Astrophys. J. Lett.* 804:L1. doi: 10.1088/2041-8205/804/1/L1
- Dimmock, A. P., Osmane, A., Pulkkinen, T. I., and Nykyri, K. (2015). A statistical study of the dawn-dusk asymmetry of ion temperature anisotropy and mirror mode occurrence in the terrestrial dayside magnetosheath using THEMIS data. *J. Geophys. Res. Space Phys.* 120, 5489–5503. doi: 10.1002/2015JA021192
- Donato, S., Greco, A., Matthaeus, W. H., Servidio, S., and Dmitruk, P. (2013). How to identify reconnecting current sheets in incompressible Hall MHD turbulence. *J. Geophys. Res.* 118, 4033–4038. doi: 10.1002/jgra.50442
- Dunlop, M. W., Balogh, A., Glassmeier, K. H., and Robert, P. (2002). Four-point Cluster application of magnetic field analysis tools: the curlometer. *J. Geophys. Res.* 107:A11. doi: 10.1029/2001JA005088
- Dwivedi, N. K., Kumar, S., Kovacs, P., Yordanova, E., Echim, M., Sharma, R. P., et al. (2019). Implication of kinetic Alfvén wave to magnetic field turbulence spectra: Earth's magnetosheath. *Astrophys. Space Sci.* 364:101. doi: 10.1007/s10509-019-3592-2
- Eriksson, E., Vaivads, A., Graham, D. B., Khotyaintsev, Yu. V., Yordanova, E., Hietala, H., et al. (2016). Strong current sheet at a magnetosheath jet: kinetic structure and electron acceleration. *J. Geophys. Res. Space Phys.* 121, 9608–9618. doi: 10.1002/2016JA023146
- Franci, L., Cerri, S. S., Califano, F., Landi, S., Papini, E., Verdini, A., et al. (2017). Magnetic reconnection as a driver for a sub-ion-scale cascade in plasma turbulence. *Astrophys. J. Lett.* 850:L16. doi: 10.3847/2041-8213/aa93fb
- Franci, L., Landi, S., Matteini, L., Verdini, A., and Hellinger, P. (2016). Plasma beta dependence of the ion-scale spectral break of the solar wind turbulence: high resolution 2D hybrid simulations. *Astrophys. J.* 833:91. doi: 10.3847/1538-4357/833/1/91
- Franci, L., Landi, S., Verdini, A., Matteini, L., and Hellinger, P. (2018). Solar wind turbulent cascade from MHD to sub-ion scales: large-size 3D hybrid particle-in-cell simulations. *Astrophys. J.* 853:26. doi: 10.3847/1538-4357/aaa3e8
- Fuselier, S. A. (2013). Suprathermal ions upstream and downstream from the Earth's bow shock. *AGU 81*, 107–119. doi: 10.1029/GM081p0107
- Fuselier, S. A., Anderson, B. J., Gary, S. P., and Denton, R. E. (1994). Inverse correlations between the ion temperature anisotropy and plasma beta in the Earth's quasi-parallel magnetosheath. *J. Geophys. Res.* 99, 14931–14936. doi: 10.1029/94JA00865
- Greco, A., Chuychai, P., Matthaeus, W. H., Servidio, S., and Dmitruk, P. (2008). Intermittent MHD structures and classical discontinuities. *Geophys. Res. Lett.* 35:L19111. doi: 10.1029/2008GL035454
- Greco, A., Matthaeus, W. H., Servidio, S., Chuychai, P., and Dimitruk, P. (2009). Statistical analysis of discontinuities in solar wind ACE data and comparison with intermittent MHD turbulence. *Astrophys. J. Lett.* 691, L111–L114. doi: 10.1088/0004-637X/691/2/L111
- Hao, Y., Lembége, B., Lu, Q., and Guo, F. (2016). Formation of downstream high-speed jets by a rippled nonstationary quasi-parallel shock: 2-D hybrid simulations. *J. Geophys. Res. Space Phys.* 121, 2080–2094. doi: 10.1002/2015JA021419
- He, J., Duan, D., Wang, T., Zhu, Y., Li, W., et al. (2019). Direct measurement of the dissipation rate spectrum around ion kinetic scales in space plasma turbulence. *Astrophys. J.* 880, 121:1–121:10. doi: 10.3847/1538-4357/ab2a79
- Hellinger, P., Travnicek, P., Kasper, J. C., and Lazarus, A. J. (2006). Solar wind proton temperature anisotropy: linear theory and WIND/SWE observations. *Geophys. Res. Lett.* 33:L09101. doi: 10.1029/2006GL025925
- Hietala, H., and Plaschke, F. (2013). On the generation of magnetosheath high-speed jets by bow shock ripples. *J. Geophys. Res.* 118, 7237–7245. doi: 10.1002/2013JA019172
- Huang, S. Y., Hadid, L. Z., Sahraoui, F., Yuan, Z. G., and Deng, X. H. (2017). On the existence of the Kolmogorov inertial range in the terrestrial magnetosheath turbulence. *Astrophys. J. Lett.* 836:L10. doi: 10.3847/2041-8213/836/1/L10
- Johlander, A., Vaivads, A., Khotyaintsev, Yu. V., Gingell, I., Schwartz, S. J., Giles, B. L., et al. (2018). Shock ripples observed by the MMS spacecraft: ion reflection and dispersive properties. *Plasma Phys. Control Fusion* 60:125006. doi: 10.1088/1361-6587/aae920
- Karimabadi, H., Roytershteyn, V., Vu, H. X., Omelchenko, Y. A., Scudder, J., Daughton, W., et al. (2014). The link between shocks, turbulence, and magnetic reconnection in collisionless plasmas. *Phys. Plasmas* 21:062308. doi: 10.1063/1.4882875
- Lindqvist, P. A., Olsson, G., Torbert, R. B., King, B., Granoff, M., Rau, D., et al. (2016). The spin-plane double probe electric field instrument for MMS. *Space Sci. Rev.* 199, 137–165. doi: 10.1007/978-94-024-0861-4_6
- Lucek, E. A., Constantinescu, D., Goldstein, M. L., Pickett, J., Pincon, J. L., Sahraoui, F., et al. (2005). The magnetosheath. *Space Sci. Rev.* 118, 95–152. doi: 10.1007/s11214-005-3825-2
- Marsch, E., and Tu, C. Y. (1994). Non-Gaussian probability distributions of solar wind fluctuations. *Ann. Geophys.* 12, 1127–1138. doi: 10.1007/s00585-994-1127-8
- Matteini, L., Alexandrova, O., Chen, C. H. K., and Lacombe, C. (2017). Electric and magnetic spectra from MHD to electron scales in the magnetosheath. *MNRAS* 466, 945–951. doi: 10.1093/mnras/stw3163
- Matthaeus, W. H., Wan, M., Servidio, S., Greco, A., Osman, K. T., Oughton, S., et al. (2015). Intermittency, nonlinear dynamics and dissipation in the solar wind and astrophysical plasmas. *Philos. Trans. R. Soc. A* 373, 20140154. doi: 10.1098/rsta.2014.0154
- Perri, S., Servidio, S., Vaivads, A., and Valentini, F. (2017). Numerical study on the validity of the Taylor hypothesis in space plasmas. *Astrophys. J. Suppl. Ser.* 231:4. doi: 10.3847/1538-4365/aa755a
- Phan, T. D., Eastwood, J. P., Shay, M. A., Drake, J. F., Sonnerup, B. U. Ö., Fujimoto, M., et al. (2018). Electron magnetic reconnection without ion coupling in Earth's turbulent magnetosheath. *Nat. Lett.* 557, 202–206. doi: 10.1038/s41586-018-0091-5
- Plaschke, F., Hietala, H., and Angelopoulos, V. (2013). Anti-sunward high-speed jets in the subsolar magnetosheath. *Ann. Geophys.* 31, 1877–1889. doi: 10.5194/angeo-31-1877-2013
- Pollock, C., Moore, T., Jacques, A., Burch, J., Gliese, U., Saito, Y., et al. (2016). Fast plasma investigation for magnetospheric multiscale. *Space Sci. Rev.* 199, 1–76. doi: 10.1007/s11214-016-0245-4
- Retinò, A., Sundkvist, D., Vaivads, A., Mozer, F., André, M., and Owen C. J. (2007). *In situ* evidence of magnetic reconnection in turbulent plasma. *Nat. Phys.* 3, 236–238. doi: 10.1038/nphys574
- Russell, C. T., Anderson, B. J., Baumjohann, W., Bromund, K. R., Dearborn, D., Fischer, D., et al. (2014). The magnetospheric multiscale magnetometers. *Space Sci. Rev.* 199:189. doi: 10.1007/s11214-014-0057-3
- Sahraoui, F., Goldstein, M. L., Robert, P., and Khotyaintsev, Yu. V. (2009). Evidence of a cascade and dissipation of solar-wind turbulence at the electron gyroscale. *Phys. Rev. Lett.* 102:231102. doi: 10.1103/PhysRevLett.102.231102
- Servidio, S., Greco, A., Matthaeus, W. H., Osman, K. T., and Dmitruk, P. (2011). Statistical association of discontinuities and reconnection in magnetohydrodynamic turbulence. *J. Geophys. Res.* 116:A09102. doi: 10.1029/2011JA016569

- Shevryev, N. N., and Zastenker, G. N. (2005). Some features of the plasma flow in the magnetosheath behind quasi-parallel and quasi-perpendicular bow shocks. *Planet. Space Sci.* 53, 95–102. doi: 10.1016/j.pss.2004.09.033
- Stawarz, J. E., Eastwood, J. P., Phan, T. D., Gingell, I. L., Shay, M. A., Burch, J. L., et al. (2019). Properties of the turbulence associated with electron-only magnetic reconnection in Earth's magnetosheath. *Astrophys. J. Lett.* 877:L37. doi: 10.3847/2041-8213/ab21c8
- Sundberg, T., Haynes, C. T., Burgess, D., and Mazelle, C. X. (2016). Ion acceleration at the quasi-parallel bow shock: decoding the signature of injection. *Astrophys. J.* 820:21. doi: 10.3847/0004-637X/820/1/21
- Sundqvist, D., Retinó, A., Vaivads, A., and Bale, S. D. (2007). Dissipation in turbulent plasma due to reconnection in thin current sheets. *Phys. Rev. Lett.* 99:025004. doi: 10.1103/PhysRevLett.99.025004
- Taylor, G. I. (1938). The spectrum of turbulence 1938. *Proc. R. Soc. Lond. A* 164:476. doi: 10.1098/rspa.1938.0032
- Treumann, R. A., and Baumjohann, W. (2015). Spontaneous magnetic reconnection: collisionless reconnection and its potential astrophysical relevance. *Astron. Astrophys. Rev.* 23, 1–91. doi: 10.1007/s00159-015-0087-1
- Vörös Z., Yordanova, E., Graham, D., Khotyaintsev Y., and Narita, Y. (2019). MMS observations of whistler and lower hybrid drift waves associated with magnetic reconnection in the turbulent magnetosheath. *JGR* 124, 8551–8563.
- Vörös, Z., Yordanova, E., Echim, M. M., Consolini, G., and Narita, Y. (2016). Turbulence-generated proton-scale structures in the terrestrial magnetosheath. *Astrophys. J. Lett.* 819:L15. doi: 10.3847/2041-8205/819/1/L15
- Wan, M., Matthaeus, W. H., Roytershteyn, V., Karimabadi, H., Parashar, T., Wu, P. (2015). Intermittent dissipation and heating in 3D kinetic plasma turbulence. *Phys. Rev. Lett.* 114:175002. doi: 10.1103/PhysRevLett.114.175002
- Wang, X., Tu, C., He, J., Marsch, E., and Wang, L. (2013). On intermittent turbulence heating of the solar wind: differences between tangential and rotational discontinuities. *Astrophys. J. Lett.* 772:L14. doi: 10.1088/2041-8205/772/2/L14
- Yordanova, E., Vaivads, A., André, M., Buchert, S. C., and Vörös, Z. (2008). Magnetosheath plasma turbulence and its spatiotemporal evolution as observed by the cluster spacecraft *Phys. Rev. Lett.* 100:205003. doi: 10.1103/PhysRevLett.100.205003
- Yordanova, E., Vörös, Z., Varsani, A., Graham, D. B., Norgren, C., Khotyaintsev, Yu. V., et al. (2016). Electron scale structures and magnetic reconnection signatures in the turbulent magnetosheath. *Geophys. Res. Lett.* 43, 5969–5978. doi: 10.1002/2016GL069191
- Zhang, H., Sibeck, D. G., Omidi, N., Turner, D., Clausen, L. B. N. (2013). Spontaneous hot flow anomalies at quasi-parallel shocks: 1. Observations. *J. Geophys. Res.* 118, 3357–3363. doi: 10.1002/jgra.50376
- Zhang, L., He, J., Tu, C., Yang, L., Wang, X., Marsch, E., et al. (2015). Occurrence rates and heating effects of tangential and rotational discontinuities as obtained from three-dimensional simulation of magnetohydrodynamic turbulence. *Astrophys. J. Lett.* 804:L43. doi: 10.1088/2041-8205/804/2/L43

Conflict of Interest: The authors declare that the research was conducted in the absence of any commercial or financial relationships that could be construed as a potential conflict of interest.

Copyright © 2020 Yordanova, Vörös, Raptis and Karlsson. This is an open-access article distributed under the terms of the Creative Commons Attribution License (CC BY). The use, distribution or reproduction in other forums is permitted, provided the original author(s) and the copyright owner(s) are credited and that the original publication in this journal is cited, in accordance with accepted academic practice. No use, distribution or reproduction is permitted which does not comply with these terms.



Magnetic Field Turbulence in the Solar Wind at Sub-ion Scales: *In Situ* Observations and Numerical Simulations

L. Matteini^{1,2,3*}, **L. Franci**^{4,3}, **O. Alexandrova**², **C. Lacombe**², **S. Landi**^{5,3}, **P. Hellinger**⁶,
E. Papini^{5,3} and **A. Verdini**^{5,3}

¹Department of Physics, Imperial College London, London, United Kingdom, ²LESIA, Observatoire de Paris, Université PSL, CNRS, Sorbonne Université, Univ. Paris Diderot, Sorbonne Paris Cité, Paris, France, ³INAF, Osservatorio Astrofisico di Arcetri, Firenze, Italy, ⁴School of Physics and Astronomy, Queen Mary University of London, London, United Kingdom, ⁵Dipartimento di Fisica e Astronomia, Università di Firenze, Florence, Italy, ⁶Astronomical Institute, CAS, Prague, Czech Republic

OPEN ACCESS

Edited by:

Alexandros Chasapis,
University of Delaware, United States

Reviewed by:

Silvio Sergio Cerri,
Princeton University, United States
Kristopher G. Klein,
University of Arizona, United States

*Correspondence:

L. Matteini
l.matteini@imperial.ac.uk

Specialty section:

This article was submitted to
Space Physics,
a section of the journal
Frontiers in Astronomy and Space
Sciences

Received: 17 May 2020

Accepted: 23 September 2020

Published: 08 December 2020

Citation:

Matteini L, Franci L, Alexandrova O, Lacombe C, Landi S, Hellinger P, Papini E and Verdini A (2020) Magnetic Field Turbulence in the Solar Wind at Sub-ion Scales: In Situ Observations and Numerical Simulations. *Front. Astron. Space Sci.* 7:563075.
doi: 10.3389/fspas.2020.563075

We investigate the transition of the solar wind turbulent cascade from MHD to sub-ion range by means of a detailed comparison between *in situ* observations and hybrid numerical simulations. In particular, we focus on the properties of the magnetic field and its component anisotropy in Cluster measurements and hybrid 2D simulations. First, we address the angular distribution of wave vector in the kinetic range between ion and electron scales by studying the variance anisotropy of the magnetic field components. When taking into account a single-direction sampling, like that performed by spacecraft in the solar wind, the main properties of the fluctuations observed *in situ* are also recovered in our numerical description. This result confirms that solar wind turbulence in the sub-ion range is characterized by a quasi-2D gyrotropic distribution of k-vectors around the mean field. We then consider the magnetic compressibility associated with the turbulent cascade and its evolution from large-MHD to sub-ion scales. The ratio of field aligned to perpendicular fluctuations, typically low in the MHD inertial range, increases significantly when crossing ion scales and its value in the sub-ion range is a function of the total plasma beta only, as expected from theoretical predictions, with higher magnetic compressibility for higher beta. Moreover, we observe that this increase has a gradual trend from low to high beta values in the *in situ* data; this behavior is well captured by the numerical simulations. The level of magnetic field compressibility that is observed *in situ* and in the simulations is in fairly good agreement with theoretical predictions, especially at high beta, suggesting that, in the kinetic range explored, the turbulence is supported by low-frequency and highly oblique fluctuations in pressure balance, like kinetic Alfvén waves or other slowly evolving coherent structures. The resulting scaling properties as a function of the plasma beta and the main differences between numerical and theoretical expectations and *in situ* observations are also discussed.

Keywords: solar wind, plasma turbulence, kinetic physics, numerical simulations, *in situ* observation

1. INTRODUCTION

The solar wind constitutes a unique laboratory for plasma turbulence (Bruno and Carbone, 2013). In the last decade, increasing interest has been raised toward the small-scale behavior of the turbulent cascade, i.e., beyond the breakdown of the fluid/MHD description that takes place at ion scales. Spacecraft observations of solar wind and near-Earth plasmas provide unique measurements of the turbulent fluctuations at scales comparable and smaller than the typical particle scales, the Larmor radius ρ (see Appendix for definition of physical quantities used), and the inertial length d (e.g., Alexandrova et al., 2009; Sahraoui et al., 2010; Alexandrova et al., 2012; Chen et al., 2013a). However, the physical processes governing the energy cascade at kinetic scales and those responsible for its final dissipation are not well understood yet.

What is well established is that, in the transition from MHD to the kinetic regime, plasma turbulence modifies its characteristics. Observational and numerical studies over the last few years have highlighted the main differences between large and small-scale properties of solar wind fluctuations (e.g., Chen, 2016; Cerri et al., 2019). The magnetic field spectrum typically steepens when approaching ion scales, leading at sub-ion scales (between ion and electron typical scales) to a power law with spectral index close to -2.8 (Alexandrova et al., 2009, 2012; Kiyani et al., 2009; Chen et al., 2010; Sahraoui et al., 2013), steeper than Kolmogorov $-5/3$ but also than the theoretical prediction $-7/3$ from EMHD (Biskamp et al., 1996) and (kinetic Alfvén waves) KAW/whistler turbulence (Schekochihin et al., 2009; Boldyrev et al., 2013). The origin of such a spectral slope is still unknown and it has been proposed that it could be related to intermittency corrections (Boldyrev and Perez, 2012; Landi et al., 2019), magnetic reconnection (Loureiro and Boldyrev, 2017; Mallet et al., 2017; Cerri et al., 2018), Landau damping (Howes et al., 2008; Schreiner and Saur, 2017), and the role of the nonlinearity parameter (Passot and Sulem, 2015; Sulem et al., 2016).

The change in the magnetic field spectrum is accompanied by a rapid decrease in the power of ion velocity fluctuations (Šafránková et al., 2013; Stawarz et al., 2016) and the onset of the nonideal terms in Ohm's law which governs the electric field associated with the turbulent fluctuations (Stawarz et al., 2020); as a consequence, the electric field spectrum becomes shallower at sub-ion scales (Franci et al., 2015a; Matteini et al., 2017). In this framework, the electric current (mostly carried by electrons) plays a major role, coupling directly with the magnetic field in the cascade and likely affecting the energy cascade rate via the Hall term (Hellinger et al., 2018; Papini et al., 2019; Bandyopadhyay et al., 2020). All these properties depend further on the plasma beta ($\beta = 8\pi n k_B T / B^2$), which controls, among other things, the scale at which the magnetic field spectrum breaks (Chen et al., 2014; Franci et al., 2016; Wang et al., 2018; Woodham et al., 2018).

One of the most significant differences with respect to the turbulent regime observed at large scales however is the role of compressive effects. While in the inertial range fluctuations show a low level of both plasma and magnetic field compressibility and hence can be reasonably well described by incompressible MHD,

at sub-ion scales density and magnetic field intensity fluctuations become significant and comparable to transverse ones (Alexandrova et al., 2008; Sahraoui et al., 2010; Chen et al., 2012b; Salem et al., 2012; Kiyani et al., 2013; Perrone et al., 2017), in agreement with simulations (Franci et al., 2015b; Parashar et al., 2016; Cerri et al., 2017). It is believed that this is related to a change in the properties of the turbulent fluctuations, which become intrinsically compressive at small scales. It is then by studying in detail their properties that it is possible to shed light on the nature of the fluctuations which support the cascade at kinetic scales (Chen et al., 2013b; Grošelj et al., 2019; Pitňa et al., 2019; Alexandrova et al., 2020).

Another important aspect of solar wind turbulence is its spectral anisotropy (Horbury et al., 2008; Chen et al., 2010; Wicks et al., 2010; Roberts et al., 2017b). Studies about the shape of turbulent eddies, both at MHD (Chen et al., 2012a; Verdini et al., 2018, 2019) and at kinetic scales (Wang et al., 2020), reveal the presence of a 3D anisotropy in the structures when described in terms of a local frame. On the other hand, when the analysis is made in a global frame (without tracking the local orientation of the structures), the 3D anisotropy is not captured, and the k -vectors of the fluctuations show a statistical quasi-2D distribution around the magnetic field (Matthaeus et al., 1990; Dasso et al., 2005; Osman and Horbury, 2006). In this work, we address this latter aspect and we investigate the distribution of the k -vectors with respect to the ambient magnetic field at kinetic scales by using the magnetic field variance anisotropy (i.e., the ratio of magnetic field fluctuations in different components). Bieber et al. (1996) and Saur and Bieber (1999) have shown that, also in single spacecraft observations, it is possible to characterize the 3D k -vector distribution by using variance anisotropy. When the sampling occurs only along a preferential direction, like in typical solar wind observations, their model predicts various possible kinds of variance anisotropy as a function of the underlying k -spectrum. In particular, assuming a quasi-2D gyrotrropic distribution of k -vectors (axisymmetric with respect to the magnetic field), the ratio of the power in the two perpendicular magnetic field components is directly related to the local slope of the spectrum, which is assumed to have the same form for all components and a slope independent of the scale within a given regime. Since both quantities, spectral slope and perpendicular power ratio, can be easily measured *in situ*, the Saur and Bieber model constitutes a useful and simple tool to investigate underlying spectral anisotropies. Despite the model was originally developed for MHD scale fluctuations, it basically corresponds to a geometrical description built on the divergence-less condition for B , so it can be applied to any kind of regimes, including the low-frequency turbulence expected at sub-ion scales (Turner et al., 2011). In the work of Lacombe et al. (2017), we investigated the k -vector distribution at sub-ion scales using the technique by Saur and Bieber (1999). Based on the comparison with the predictions, we concluded that the distribution of the k -vectors in the sub-ion range of solar wind turbulence is consistent with a quasi-2D gyrotrropic spectrum, then approaching a more isotropic shape when reaching electron scales (Lacombe et al., 2017). However, such an application has not been benchmarked by kinetic numerical studies yet.

The aim of this work is then to focus on the spectral anisotropy properties and magnetic compressibility at small scales, by exploiting the detailed comparison of *in situ* observations and high-resolution kinetic numerical simulations. The paper is organized as follows: In **Section 2**, we introduce the spacecraft and numerical dataset used, and in **Section 3**, we describe their spectral properties. In **Section 4**, we discuss the spectral anisotropy at sub-ion scales and test, for the first time, the Saur and Bieber model in numerical kinetic simulations; in **Section 5**, we address properties of the magnetic compressibility and its dependence on the plasma beta. Finally, in **Section 6**, we discuss our conclusions and the implications of our findings for the interpretation of solar wind observations and simulations.

2. DATA AND SIMULATIONS

In this study, we compare the properties of magnetic fluctuations measured *in situ* by the Cluster spacecraft with numerical results obtained by means of 2D hybrid particle-in-cell (PIC) simulations.

2.1. Cluster STAFF Spectra

For our analysis, we use the dataset discussed by Alexandrova et al. (2012), when Cluster was in the free solar wind, i.e., not magnetically connected to the Earth's bow shock. Details have been described also in Lacombe et al. (2017) and we recall here the main aspects. Magnetic field fluctuations are measured by the STAFF (Spatiotemporal Analysis of Field Fluctuation) instrument, composed of a waveform unit (SC) and a Spectral Analyzer (SA). Power spectra are computed on board in a magnetic field-aligned system of coordinates (MFA), based on the 4 s magnetic field measured by the FGM (Fluxgate Magnetometer) experiment. A selection of 112 spectra has been performed, retaining in each spectrum only measurements above three times the noise level in every direction x , y , and z (see Appendix in Lacombe et al., 2017). Each sample is a 10 min average of 150 individual 4 s spectral measurements. This provides spectra above 1 Hz up to typically 20–100 Hz, depending on the amplitude of the fluctuations in each interval. When converted into physical length scales, assuming the Taylor hypothesis ($k = 2\pi f/V_{sw}$), this leads to signals that cover the range between $\sim 2d_p$ and $\sim 0.5d_e$ (where d_p and d_e are the proton and electron inertial lengths, respectively), enabling then a good description of the sub-ion regime from proton to electron scales.

The reference frame adopted (MFA) is such that B_z is the component aligned with the mean magnetic field B_0 (relative to the 4 s interval during which an individual spectrum is calculated); B_x is the component orthogonal to B_z in the plane containing both the solar wind velocity V_{sw} and the mean magnetic field B_0 ; and B_y is the third orthogonal component. Note that a selection criterium is imposed on the angle θ_{BV} , the angle between the local 4 s magnetic field, and the flow velocity; i.e., that θ_{BV} is large enough to avoid a connection with the Earth bow shock during the sampled interval; θ_{BV} in the dataset has an

average value of $\sim 80^\circ$. This implies that, for each spectrum, the mean magnetic field makes a big angle with respect to the sampling direction; moreover, we have checked that θ_{BV} does not vary significantly during the 10 min over which spectra are averaged.

As a consequence, this procedure selects intervals in which Cluster observed highly oblique k-vectors and, to a good approximation, the component B_x corresponds also to the sampling direction (radial) and is orthogonal to B_0 ; B_y corresponds to the other perpendicular component; and B_z is identified as the compressive component B_\parallel . As already discussed in Lacombe et al. (2017), although the total trace power measured *in situ* is an invariant observable, the fact that the sampling occurs only in a preferred direction introduces a relative weight between B_x and B_y that is measurement dependent (Saur and Bieber, 1999). To take this into account, we have employed an analogous approach in the analysis of the simulations data, as described in the next section.

2.2. Hybrid 2D Numerical Simulations

In situ observations are directly compared with numerical simulations performed with the hybrid-PIC code CAMELIA (Matthews, 1994; Franci et al., 2018a). Despite the fact that the hybrid model neglects the dynamics of electrons, it captures well the transition from fluid to kinetic regime around ion scales where electron effects do not play an important role. Hybrid simulations reproduce successfully many of the main properties of solar wind turbulence observed by spacecraft at sub-ion scales (e.g., Perrone et al., 2013; Valentini et al., 2014; Franci et al., 2015a; Franci et al., 2015b; Franci et al., 2018b; Cerri et al., 2016; Cerri et al., 2017; Arzamasskiy et al., 2019). It is then a suitable tool to investigate the turbulent regime probed by STAFF/Cluster data. We use here 2D simulations—computationally more affordable than 3D—in order to explore the parameter space observed *in situ*; in particular, we focus on the effects associated with variations in the proton and electron plasma beta β_p and β_e . The restricted 2D geometry clearly cannot fully capture the richness of the turbulent phenomena (e.g., Howes, 2015) and in general, kinetic aspects related to the propagation of the fluctuations along the magnetic field are inhibited, like the presence of parallel propagating ion-scale waves and associated cyclotron resonances or the development of some kinetic instabilities (although some of their aspects can be still described also in 2D, e.g., Hellinger et al., 2015; Hellinger et al., 2017). On the other hand, in the case of the highly anisotropic solar wind turbulence, spectral properties can be captured efficiently (Franci et al., 2015a; Franci et al., 2015b). In particular, for the purpose of this work, Franci et al. (2016) have shown that 2D hybrid simulations are able to reproduce the ion-break scale behavior in different beta regimes observed in solar wind turbulence (Chen et al., 2014). Moreover, 3D hybrid simulations (Franci et al., 2018b) have confirmed the solidity of the reduced 2D results and the good agreement with *in situ* observations. We then exploit the good matching between simulations and *in situ* observations to characterize

further the properties of kinetic plasma turbulence in the sub-ion regime.

In order to make a direct comparison with sub-ion spectra measured by Cluster, we have adopted a similar approach in the computation of spectra in the simulations. This means that numerical spectra are computed along the x direction only, to mimic the radial sampling occurring in the solar wind. This is obtained by integrating along y the Fourier spectrum $P(k_x, y)$ of each i magnetic field component:

$$P_i(k_x) = \int P_i(k_x, y) dy. \quad (1)$$

Therefore, also in the simulation, B_x corresponds to the sampling direction, orthogonal to the out-of-plane magnetic field B_z , and B_y is the most energetic fluctuating component, being orthogonal to both B_0 and $k = k_x$. With this approach and within the observational conditions previously described, we can perform a direct comparison of simulations and *in situ* data.

The numerical dataset used was originally presented in Franci et al. (2016) and is available online. It is constituted by a set of different 2048^2 2D simulations of decaying turbulence, corresponding to a physical simulation box size of $256^2 d_i$, except for the higher beta case, $\beta_p = 8$, where the size is $512^2 d_i$, and for different beta conditions covering the range of variations observed *in situ*, with $\beta_p = \beta_e$. Runs are initiated with random perpendicular Alfvénic fluctuations with vanishing cross-helicity and equipartition in magnetic and kinetic energies. The rms of the in-plane fluctuations is $B^{rms} = 0.24B_0$ and the highest initially excited k-vector is $k^{inj}d_i = 0.2$ ($B^{rms} = 0.48B_0$ and $k^{inj}d_i = 0.05$ for

the $\beta_p = 8$ case). Spectra are computed at the maximum of the turbulent activity.

3. IN SITU DATA ANALYSIS AND SIMULATION RESULTS

Figure 1 shows three examples of Cluster spectra (2003/02/18 04:45–04:55; 2004/02/22 05:40–05:50; 2004/01/22 04:40–04:50), where frequencies have been converted into k-vectors and normalized to d_p (original sampling frequencies are also shown for reference). Observations cover ion and electron scales, with a transition accompanied by a slope change around $kd_p \sim 10$. In this work, we focus on the sub-ion regime highlighted in yellow in the panels, where electron physics effects can be neglected (at least for spectral properties) and a well-defined slope close to -2.8 can be observed (Alexandrova et al., 2012). The three cases, corresponding to different total beta β regimes [0.8, 1.5, 4], show a similar qualitative behavior: as expected, the spectrum P_y of the perpendicular B_y component (blue) is always the most energetic. The power in the other perpendicular component P_x (black dashed) is always slightly smaller; however, its ratio with P_y is roughly independent of beta and close to the local spectral slope (bottom panels); this is related to the 3D distribution of k-vectors (Lacombe et al., 2017) and will be discussed more in detail in **Section 4**.

On the other hand, the power P_z of the field-aligned component B_z (red) is typically less energetic than P_y ; however, its relative contribution is highly variable with beta:

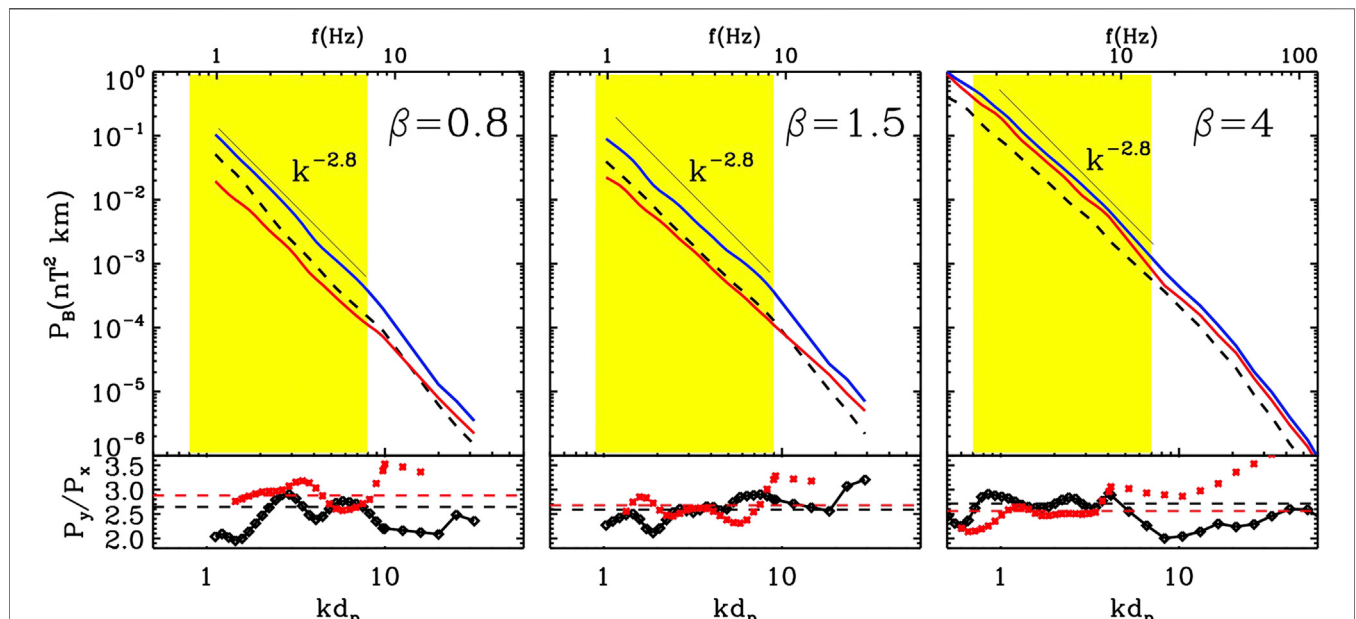


FIGURE 1 | Cluster STAFF spectra for different intervals with $\beta = 0.8, 1.5, 4$ from left to right. Colors encode the magnetic field components B_x (black dashed), B_y (blue), and B_z (red). The region highlighted in yellow corresponds to the sub-ion range investigated in this study. Bottom panels show the ratio of the power in the perpendicular components $P_y(k)/P_x(k)$ (black diamonds) and the value γ of the local slope of the total spectrum $P(k) \sim k^{-\gamma}$ (red stars). The average values of $P_y(k)/P_x(k)$ and γ in the sub-ion range are also shown as horizontal dashed lines.

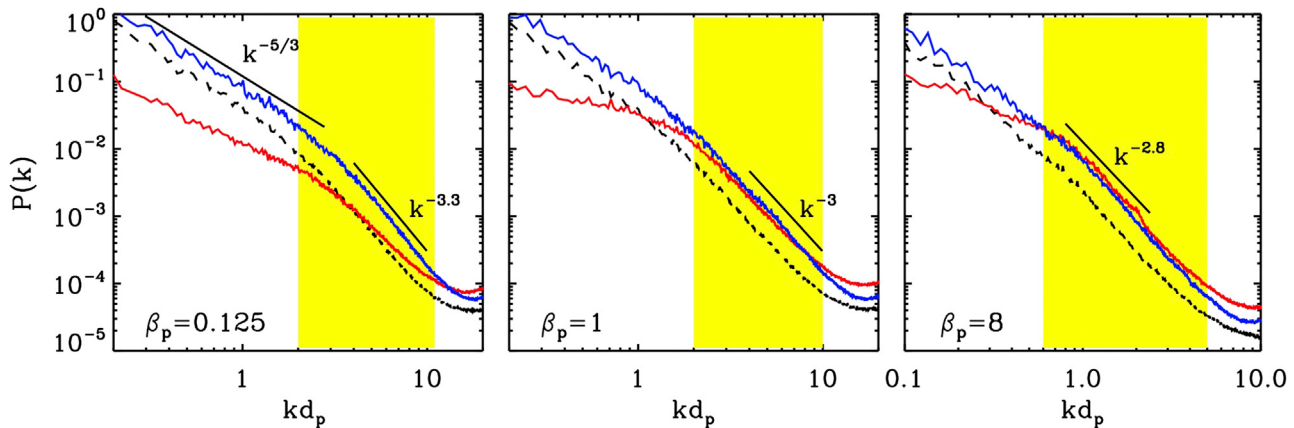


FIGURE 2 | Magnetic field spectra from hybrid simulations for different beta regimes ($\beta_p = 0.125, 1, 10$ and $\beta_e = \beta_p$). Components are encoded as in **Figure 1** and the colored region indicates the sub-ion range that can be directly compared with the analogous region in the observations.

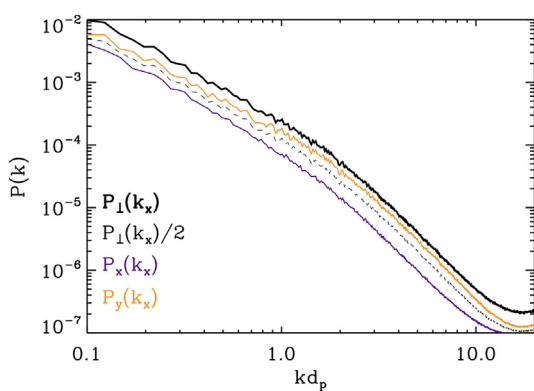


FIGURE 3 | Reduced spectra of the fluctuations of the magnetic field components B_y and B_x defined with respect to a fixed sampling direction k_x for a simulation with $\beta_p = 0.5$. The thick solid black line corresponds to the total perpendicular power $P_{\perp}(k_x)$; the dashed line shows $P_{\perp}(k_x)/2$, also corresponding to the average power in any perpendicular magnetic field component in the axisymmetric case.

P_z is smaller than P_x for $\beta < 1$, comparable to P_x for $\beta \sim 1$, and larger than P_x for $\beta > 1$. This obviously results in variable magnetic compressibility associated with the fluctuations and its functional dependence on beta is the subject of **Section 5**.

Figure 2 shows an analogous selection from numerical simulations; note that, in the simulations, $\beta_e = \beta_p$. In this case, the regime reproduced in the simulation box includes the MHD inertial range and its transition to a sub-ion cascade at smaller scales. The yellow area highlights the region of the spectra—roughly a decade between $k d_p \sim 1$ and $k d_p \sim 10$ —that can be directly compared with the *in situ* data. In this region, the qualitative behavior of the spectra is similar to **Figure 1**: B_y (blue) is always dominant, B_x (black) contributes for a constant fraction of it and is roughly the same at all betas, while B_z (red) varies significantly in the panels and becomes comparable to B_y for large

betas. This confirms that our method of computing spectra in the simulations mimicking satellite observations really captures the main aspects of *in situ* measurements and can then be exploited to investigate further the properties of the turbulent cascade.

4. SPECTRAL ANISOTROPY

4.1. Perpendicular Components Ratio

Bieber et al. (1996) and Saur and Bieber (1999) have investigated how different types of k -vectors distributions can generate a variable anisotropy in the observed magnetic field components, due to sampling effects. In the case of a gyrotropic 2D distribution of k -vectors, the ratio P_y/P_x is expected to coincide with the local slope γ of the spectrum $P(k) \sim k^{-\gamma}$. This applies well to solar wind observations in the physical range of interest here, as it can be appreciated in **Figure 1**, where the ratio P_y/P_x , shown in the bottom panels, is close to the spectral slope observed—typically in the range $[-2.5, -3]$ —and appears roughly independent of the plasma beta. Interestingly, at smaller scales, when the magnetic spectrum steepens as approaching electron scales (Alexandrova et al., 2009), this is not associated with an increase in the perpendicular power ratio P_y/P_x (which on the contrary has a slight decrease); this does not correspond to the expectation for a quasi-2D spectrum according to the model and in fact, Lacombe et al. (2017) have interpreted this signature as the result of a more isotropic distribution of k -vectors close to electron scales.

To validate further this observational conclusion, we verify here the applicability of the Saur and Bieber model to sub-ion scale turbulence. In the simulations, the spectrum is two-dimensional by construction and consistent with the axisymmetric initial conditions imposed in the x - y plane, it is also gyrotropic with respect to the out-of-plane magnetic field B_z .

First, it is instructive to discuss spectra shown in **Figure 3**. These are power spectra of the perpendicular components B_x (purple) and B_y (orange) as a function of k_x , assuming then a fixed

direction of sampling. As expected, $P_y(k_x) > P_x(k_x)$; on the other hand, their sum $P_\perp(k_x)$ (solid black line) is statistically equivalent to the axisymmetric spectrum $P_\perp(k) = P_y(k) + P_x(k)$. The difference is that when calculating the axisymmetric spectrum $P_\perp(k)$, all perpendicular magnetic field directions have equal weight and one can assume that statistically $P_y(k) \sim P_x(k)$; as a consequence, the power associated with any individual perpendicular component corresponds to half of the total perpendicular power $P_\perp(k)/2 \sim P_\perp(k_x)/2$ (thin dashed black line). It is interesting to note that when sampling along a fixed direction (x), as it happens with spacecraft in the solar wind, none of the two measured spectra $P_y(k_x)$ and $P_x(k_x)$ is really representative of the power $P_\perp(k)/2$ of the gyrotrropic description; instead, the component along the sampling (B_x) is significantly reduced due to the solenoidal $\nabla \cdot \mathbf{B} = 0$ condition, while the orthogonal (B_y) is amplified, in order to maintain the same total power $P_\perp(k)$. This means that, in solar wind spectra like in **Figure 1**, neither P_x nor P_y is individually representative of the average power in a perpendicular B component: the individual measurements of P_x or P_y cannot be directly associated with it, but only their sum.

Bearing this in mind, **Figure 4** shows the ratio of the power in the perpendicular components for the three simulations shown in **Figure 2**. The P_y/P_x ratio captures well the transition from MHD to a steeper spectrum at smaller scales; in all cases, the ratio, close to 5/3 at large scales, starts increasing in the vicinity of ion scales and reaches a maximum in the sub-ion regime, where it is saturated close to ~ 3 , in good agreement with the local spectral slope observed in the kinetic range, which is typically close to -3 . At larger k , the ratio then decreases due to the noise. In the framework of the spectral anisotropy, Saur and Bieber model all this indicates a quasi-2D gyrotrropic spectrum of the fluctuations, which corresponds well to the spectrum developed in these simulations. This confirms that the model is valid also at sub-ion scales and reinforces the finding of Lacombe et al. (2017), where is found that solar wind spectra at kinetic scales are described well by a quasi-2D gyrotrropic distribution.

4.2. Beta Dependence

There is another interesting indication suggested by **Figure 4**, namely, the fact that the P_y/P_x ratio in the sub-ion range seems to depend on beta: consistent with this, the sub-ion slope in **Figure 2** is slightly steeper for small β_p and shallower for larger β_p . This behavior is already discussed in Franci et al. (2016) and is found in all simulations for the spectrum of the transverse fluctuations B_\perp ; conversely, the spectrum of the parallel component B_\parallel is almost independent of β_p (see **Figure 4** in Franci et al., 2016). We have then looked for a similar trend also in the *in situ* data. **Figure 5** shows the histogram of the spectral slopes in the kinetic range for B_\perp (top) and B_\parallel (bottom), for larger (red) and smaller (black) total beta. Spectral slopes are calculated between $2 < kd_p < 8$ for $\beta_p < 1$ and between $2 < k\rho_p < 8$ for $\beta_p > 1$, where a quite well-defined power-law scaling is observed. They are then separated into two groups defined by the total beta $\beta < 2$ and $\beta > 2$. The mean of each histogram is indicated by the small vertical line ended with a diamond. For the parallel component (bottom panel), the distribution of the slopes is similar for both beta regimes and centered around a value of approximately -2.65 ± 0.15 ; this is in good agreement with the simulations.

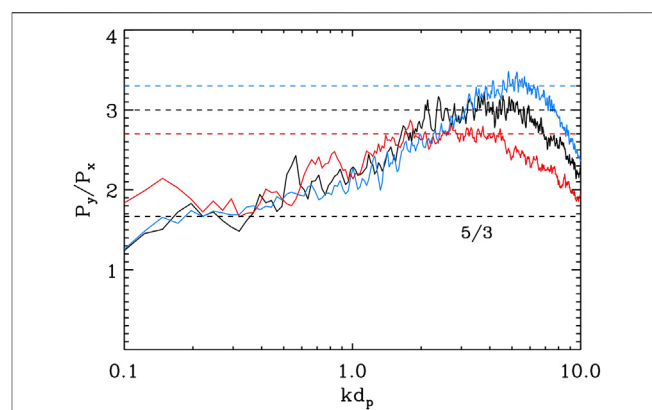


FIGURE 4 | Hybrid simulations: spectra of the ratio of the perpendicular magnetic components $P_y(k_x)/P_x(k_x)$ and corresponding to the local spectral slope. Different colors encode different β_p : 0.125 (cyan), 1 (black), and 8 (red). The horizontal dashed lines show reference spectral slopes observed in the simulations at $kd_p < 1$ ($-5/3$) and at sub-ion scales $kd_p > 1$.

For the dominant perpendicular component (top panel), we observe average values consistent with previous studies based on the total power $\delta B^2 = \delta B_\parallel^2 + \delta B_\perp^2$ of the fluctuations (Alexandrova et al., 2009; Alexandrova et al., 2012; Chen et al., 2013a; Sahraoui et al., 2013). However, in the lower beta case (black), some slightly steeper slopes are observed for B_\perp with respect to the high beta case, with an average of -2.8 ± 0.15 with respect to -2.7 ± 0.15 . We have checked that the difference in the histograms is statistically significant, thus suggesting some β -dependence in the spectral slope. A more detailed investigation is needed to fully identify the role of β_p on the sub-ion spectral slope and is beyond the scope of the present study. This behavior, however, agrees qualitatively with the simulations.

Moreover, a consequence of the behavior in **Figure 5** is that while at high beta, δB_\parallel and δB_\perp have basically the same scaling, so that their ratio remains approximately constant in the sub-ion range, at lower β , their slightly different scaling is expected to result in a slow increase of the $\delta B_\parallel/\delta B_\perp$ ratio between ion and electron scales. These properties are related to the evolution of the magnetic compressibility of the fluctuations in the sub-ion range, which is the main focus of the next section.

5. MAGNETIC COMPRESSIBILITY

We now investigate the role of the third magnetic field component B_z , which is aligned with the local (at 4 s) magnetic field B_0 . In particular, we focus on the magnetic compressibility $C_\parallel = \delta B_\parallel^2/\delta B^2$, where $\delta B^2 = \delta B_\parallel^2 + \delta B_\perp^2$, and its implication for the nature of the cascade at these scales. Note that, in this case, the measurement of B_z is not affected by the sampling direction (provided that this is orthogonal to B_0 to a good approximation) and since we use the total perpendicular power P_\perp , the caution discussed in **Section 4** is not needed here.

Figure 6 shows C_\parallel for three intervals of different total $\beta = 1, 3, 4$ ($\beta_p = 0.3, 1.4, 2.5$) as measured from STAFF (red). For these three cases, we also show the spectrum of the magnetic field

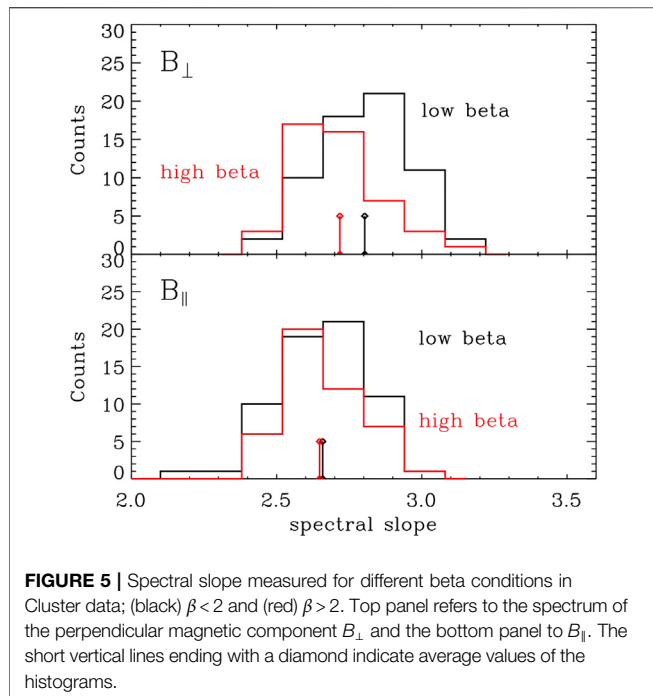


FIGURE 5 | Spectral slope measured for different beta conditions in Cluster data; (black) $\beta < 2$ and (red) $\beta > 2$. Top panel refers to the spectrum of the perpendicular magnetic component B_{\perp} and the bottom panel to B_{\parallel} . The short vertical lines ending with a diamond indicate average values of the histograms.

compressibility as measured at lower frequencies (corresponding to physical scales larger than d_p) by the FGM onboard Cluster (FGM, black). Note that FGM spectra are linearly interpolated between 0.14 and 0.4 Hz to remove artifacts due to spacecraft spin (0.25 Hz). There is a good matching between the two independent measurements at $f \sim 1$ Hz and where data points from both instruments are available for a more extended range, there is also a quite satisfactory overlap between them. The overall behavior agrees well with the expected picture: at a large scale, in the MHD inertial range, the level of compressibility is lower, typically $C_{\parallel} \lesssim 0.1$ (e.g., Horbury and Balogh, 2001; Smith et al., 2006), and starts to increase as approaching ion scales (Alexandrova et al., 2008; Hamilton et al., 2008; Salem et al., 2012; Kiyani et al., 2013; Roberts et al., 2017a), reaching sometimes variance isotropy (indicated by the dashed horizontal line) in the sub-ion range, where the compressibility seems to be saturated. As already shown by Lacombe et al. (2017), the level of magnetic compressibility developed at small scales is larger for high beta than for small beta. Since we focus on the behavior at sub-ion scales, in the following, we restrict our analysis to STAFF measurements only.

To highlight further the β -dependence of the magnetic compressibility, Figure 7 shows C_{\parallel} for a selection of spectra with different β , increasing from red to purple. There is a continuous transition from lower to higher magnetic compressibility as a function of beta, in agreement with linear theory expectations (e.g., Podesta and TenBarge, 2012). Moreover, at high beta, it seems that the fluctuations reach an asymptotic $\delta B_{\parallel}^2 / \delta B^2$ ratio, leading to an extended plateau in the spectrum, while at the lowest beta, a plateau cannot be clearly

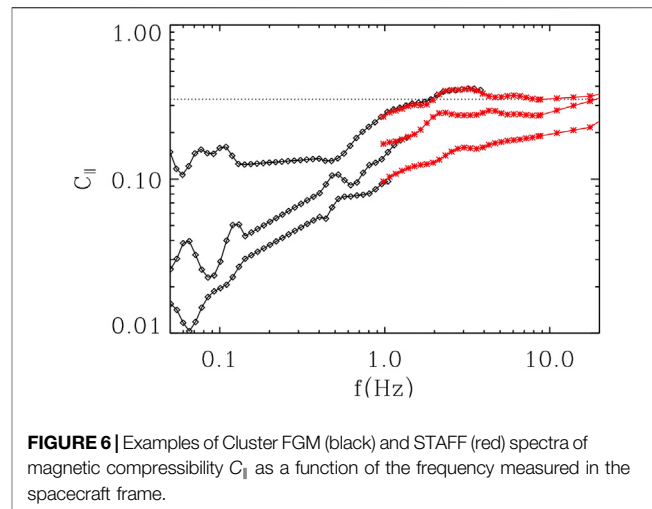


FIGURE 6 | Examples of Cluster FGM (black) and STAFF (red) spectra of magnetic compressibility C_{\parallel} as a function of the frequency measured in the spacecraft frame.

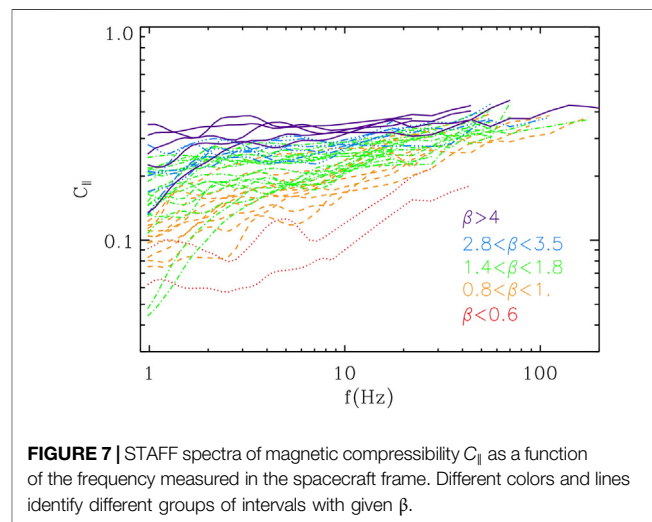


FIGURE 7 | STAFF spectra of magnetic compressibility C_{\parallel} as a function of the frequency measured in the spacecraft frame. Different colors and lines identify different groups of intervals with given β .

identified. We now want to identify more in detail what process and length scale control the level of C_{\parallel} and in solar wind data.

5.1. Beta Dependence and Theoretical Predictions

First, it is useful to go again from frequency to k-vector spectra: in Figure 8, frequencies are converted into k-vectors and normalized with respect to the proton inertial length d_p .

We first identify two big categories such that both proton and electron betas are small, i.e., $\beta_p < 1$ and $\beta_e < 1$, or both are large, i.e., $\beta_p > 1$ and $\beta_e > 1$. We obtain an average total beta $\beta \sim 1$ in the former and $\beta \sim 4$ in the latter. The average spectrum of magnetic compressibility for each of the two families is shown in the top panel of Figure 8 as a function of kd_p ; the thin dotted lines identify the standard deviation around the averages. In the high beta case (solid blue), the compressibility reaches a plateau after $kd_p = 1$ and is saturated at an average level which is very close to isotropy (same power in P_x , P_y , and P_z), while in the low beta case (dashed red), C_{\parallel} remains smaller and there is not a clear plateau at $kd_p > 1$.

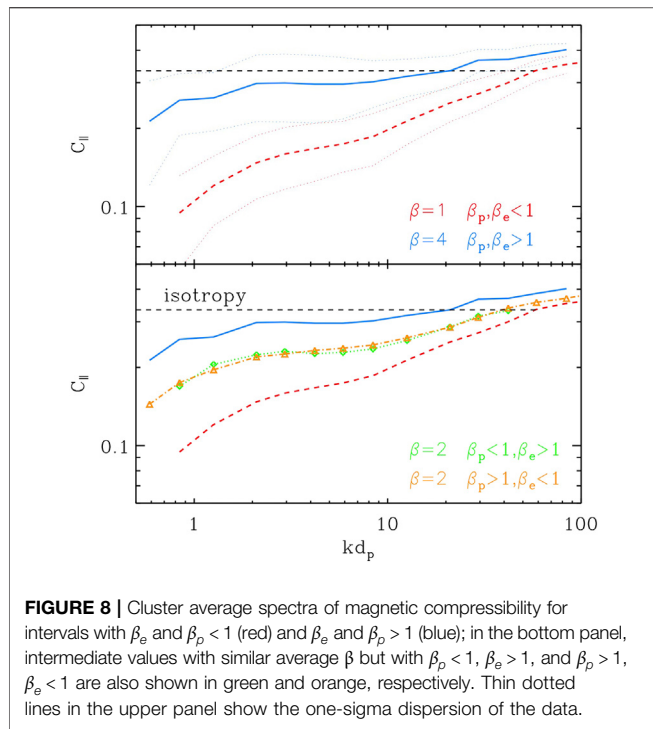


FIGURE 8 | Cluster average spectra of magnetic compressibility for intervals with β_e and $\beta_p < 1$ (red) and β_e and $\beta_p > 1$ (blue); in the bottom panel, intermediate values with similar average β but with $\beta_p < 1$, $\beta_e > 1$, and $\beta_p > 1$, $\beta_e < 1$ are also shown in green and orange, respectively. Thin dotted lines in the upper panel show the one-sigma dispersion of the data.

The remaining spectra are further separated in two other families: the first with $\beta_p < 1$ and $\beta_e > 1$ and the second with $\beta_p > 1$ and $\beta_e < 1$. In this case, the average total betas are very similar, $\beta \sim 1.9$ ($\beta_p \sim 0.75$) and $\beta \sim 2.0$ ($\beta_p \sim 1.5$), respectively, and fall in between the other two groups (small and large β). Consistent with this, the average spectrum of these two families, shown in orange and green in the bottom panel, has a level of compressibility at sub-ion scales that is intermediate with respect to the other two curves. Moreover, they almost precisely fall on top of each other. All this suggests that not only is the total plasma beta a good parameter for ordering the level of compressibility generated at sub-ion scales, but also this level is roughly independent of the individual weights of β_p and β_e , being their sum $\beta = \beta_p + \beta_e$ the only relevant parameter.

This observational finding is in very good agreement with the expectation from the following relation:

$$C_{\parallel} = \frac{\beta_p / 2 (1 + T_e / T_p)}{1 + \beta_p (1 + T_e / T_p)} = \frac{\beta / 2}{1 + \beta}, \quad (2)$$

where T_e and T_p are the electron and proton temperatures.

Eq. 2 can be derived (Schekochihin et al., 2009; Boldyrev et al., 2013) under the assumption of low-frequency magnetic structures in pressure balance at scales where the ion velocity becomes negligible compared to the electron one, or equivalently, the Hall term $J \times B$ becomes dominant over the ideal MHD term $-U \times B$. A special case is the regime of KAW, however, **Eq. 2**, which does not depend explicitly on k and thus on a specific dispersion relation, can be seen as a more general condition for highly oblique fluctuations in the sub-ion range (e.g., ion-scale Alfvénic vortices, Jovanovic et al., 2020), under the assumptions described above (see e.g., Appendix C2 of Schekochihin et al., 2009).

5.2. Comparison with Simulations

To improve our analysis, we focus more in detail on the Cluster observations and compare them with numerical results. Note that, as in the simulations of Franci et al. (2016), it is only considered the case $\beta_p = \beta_e$; we have made a selection of solar wind spectra with similar properties ($\beta_p \sim \beta_e \sim \beta/2$). These have then been divided in five subgroups as a function of β and averaged to obtain a mean C_{\parallel} profile for each β -family. The selection results in 7, 13, 23, 9, and 1 spectra for $\beta = 0.6, 1, 2, 4, 8$, respectively (only one spectrum fulfills the condition for high enough beta). Simulations with approximatively the same β_p (and β) are considered for a direct comparison. In the following analysis, we want to identify the physical scale associated with the changes in the properties of the fluctuations and its possible connection to either the ion Larmor radius ρ_p or the inertial length d_p , as they are related by $\rho_p = \sqrt{\beta_p} d_p$.

The results of this comparison are shown in **Figure 9**, where scales are normalized to both d_p (top) and ρ_p (bottom). Left panels show spectra from *in situ* data and right panels result from simulations, where the colors encode the same range of β . Qualitatively, the global trend seen in the simulations matches well that of the observations. First, the level of magnetic compressibility reached sub-ion scales increases monotonically with β , as expected. Second, we can identify a plateau phase beyond ion scales whose extension is gradually reduced as β decreases; for the smallest betas, the plateau disappears and is replaced by an almost monotonic increase of C_{\parallel} all along the sub-ion range, though with a shallower slope compared to that of the transition from the MHD range.

This seems to suggest a different behavior of the turbulent fluctuations populating the sub-ion cascade as a function of the beta. To investigate further this aspect, horizontal dotted lines in the right panels of **Figure 9** show the theoretical prediction for the asymptotic level of C_{\parallel} between ion and electron scales predicted by **Eq. 2**, with the same color scale. For simulations at large β , when a plateau is clearly observed, the level of magnetic compressibility also agrees well with the one predicted by the theory. In the low beta case, there is a larger discrepancy and the observed level of magnetic compressibility is larger than the constant level predicted by **Eq. 2**. The different behavior of the compressibility in low- and high beta regimes found in our simulations, together with the larger discrepancy with respect to the theoretical predictions observed at low beta, is also consistent with results from previous numerical studies (e.g., Cerri et al., 2016; Cerri et al., 2017; Grošelj et al., 2017).

The situation is somewhat different when comparing predictions to the *in situ* data; in this case, there is a slight difference between the KAW level and the observed one, and this is persistent at all β . In particular, at high beta, it is apparent that while **Eq. 2** predicts compressibility that goes beyond 1/3 (for $\beta \rightarrow \infty$, we have $C_{\parallel} = 0.5$, so $\delta B_{\parallel} = \delta B_{\perp}$), a condition well recovered in the simulations, in Cluster data C_{\parallel} , does not go beyond component isotropy ($\delta B_{\parallel} = \delta B_{\perp}/2$; thus, $C_{\parallel} = 1/3$). However, due to the low statistics in the data (just one spectrum has $\beta \geq 8$), it is hard to draw a firm conclusion here.

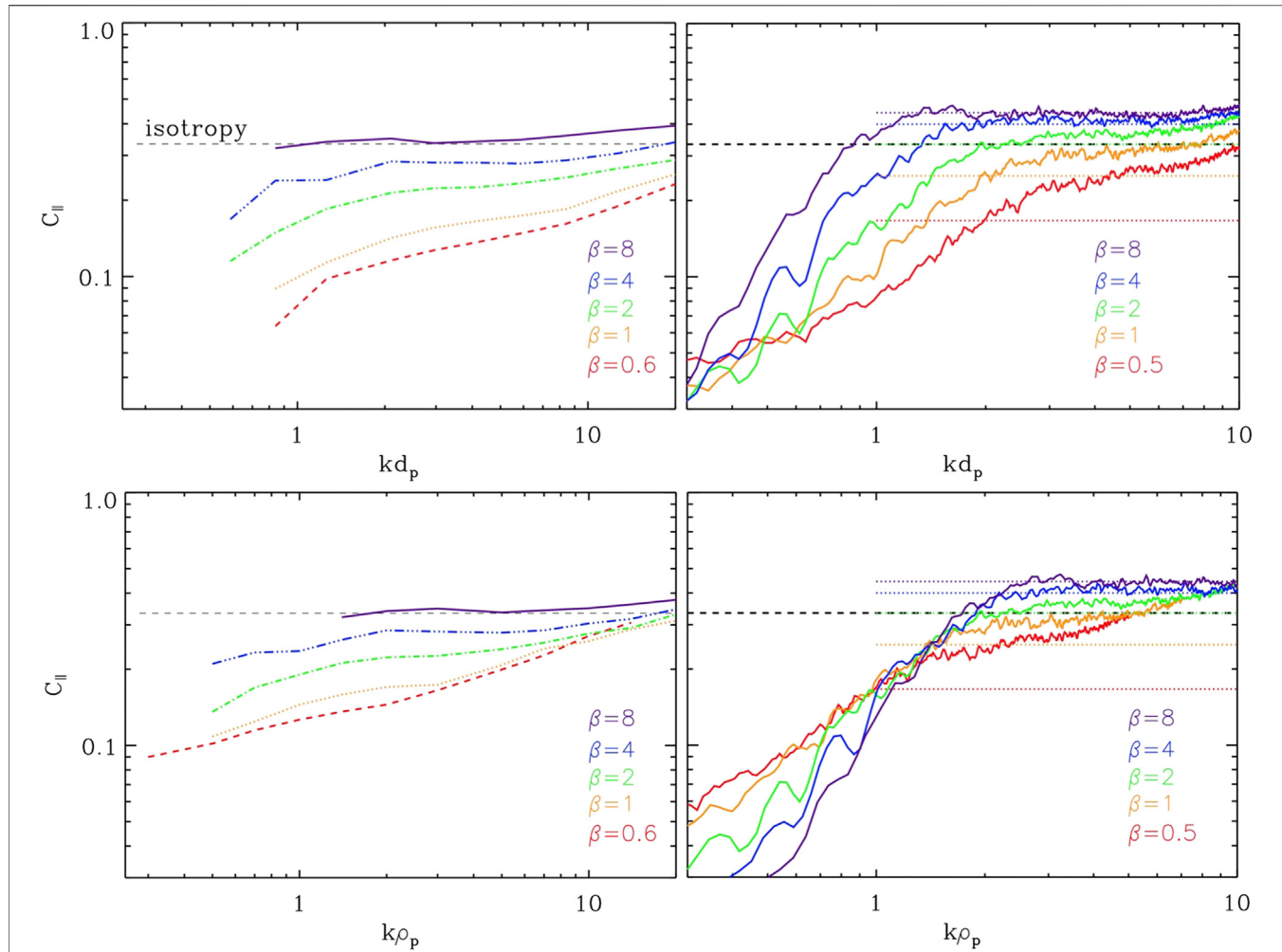
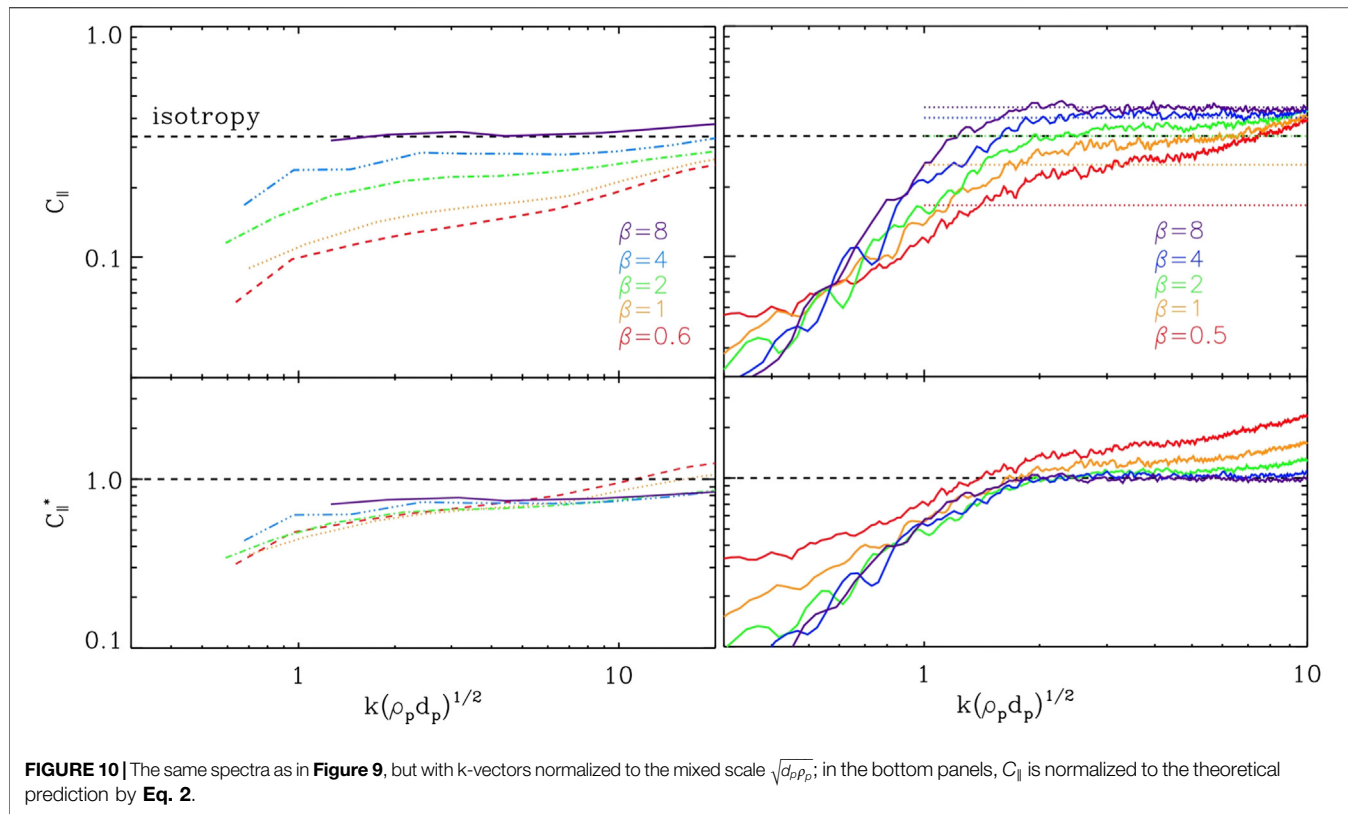


FIGURE 9 | Top panels (left): Cluster spectra of magnetic compressibility for intervals binned on different β , encoded in different styles and colors. Only cases with $\beta_p \sim \beta_e$ have been retained. The horizontal dashed line denotes energy equipartition between components (i.e., isotropy). Right: spectra of magnetic compressibility for simulations with different $\beta_p = \beta_e$, shown with the same style as the left panel. The increase of C_{\parallel} for $kd_i \geq 8$ is due to numerical noise. Bottom: the same as top panels, but with k-vectors normalized with respect to the ion gyroradius ρ_p . Horizontal dotted lines, colored according to their β , are the theoretical prediction of C_{\parallel} from Eq. 2.

Interestingly, from Figure 9, it seems that neither d_p nor ρ_p is able to fully capture and order the change in the spectrum of the magnetic compressibility for different betas; the saturation/plateau phase for low β spectra results more shifted toward high k-vectors compared to the high β ones when normalizing to d_p , while the vice versa is observed when normalizing to ρ_p . This suggests that the behavior can be better captured by an intermediate scale between the two. For this reason, in Figure 10, we have normalized spectra on a mixed scale $\sqrt{d_p \rho_p}$. Note that such a scale, proportional to $d_p \rho_p^{1/4}$, was found to describe well the behavior of the ion-break scale in magnetic field spectra in the range $\beta_p \sim 1$ by Franci et al. (2016), and, although not shown, to describe the variation of the break of the parallel magnetic field spectrum at all betas; this then motivated our choice. When such a mixed scale is used (top right panel), all cases follow the same trend: they grow until they reach $k\sqrt{d_p \rho_p} \sim 2$ and then start flattening, the saturation level depending on the beta. *In situ* observations (top left

panel) seem to follow the same trend, confirming that such an intermediate scale is a good candidate for controlling the variation of the magnetic compressibility spectrum at ion scales.

It is then reasonable to use such a k-vector normalization to better evaluate the agreement with Eq. 2. In the bottom panels of the same figure C_{\parallel}^* , spectra are then normalized to the theoretical prediction for C_{\parallel} . In simulations, as already pointed out, cases with $\beta > 1$ display a good agreement with the sub-ion compressibility level predicted by the theory; as a consequence, when normalized to $\sqrt{d_p \rho_p}$, all spectra collapse on top of each other all along ion and sub-ion scales. A worse agreement is observed at $\beta \leq 1$ when simulations display a slightly higher compressibility level than predicted. Quite differently, the ratio between the *in situ* observations and the theoretical C_{\parallel} is always below one and around 0.7–0.8 for all β groups in the sub-ion range (see also Figure 10 of Lacombe et al., 2017). This behavior is consistent with the results of Pitňa et al. (2019) based



on observations from the wind spacecraft, who find on average $C_{\parallel} \sim 0.9$, without making a distinction among beta regimes and with most of the data displaying a slightly smaller magnetic compressibility than the prediction. Our study confirms this scenario and suggests that the same trend is followed for all spectra, almost independently of the plasma beta. A ratio smaller than one and close to ~ 0.75 is also consistent with similar observational results of the plasma compressibility and based on the ratio between density and perpendicular magnetic fluctuations predicted by linear theory (Chen et al., 2013a; Pit'ia et al., 2019). This was interpreted by Chen et al. (2013a) as a consequence of the nonlinear behavior of the solar wind fluctuations in the sub-ion range, in agreement with simulations of strong KAW-turbulence (Boldyrev et al., 2013). On the other hand, for the magnetic compressibility, our fully nonlinear simulations of sub-ion turbulence do not recover the same effect seen *in situ*, as $C_{\parallel}^* \gtrsim 1$. Other reasons could explain such a discrepancy, e.g., the effect of some electron Landau damping on the fluctuations observed *in situ* (Howes et al., 2011; Passot and Sulem, 2015; Schreiner and Saur, 2017) and not captured by the hybrid model. In order to answer these questions, a more detailed study of the polarization properties of the fluctuations in our simulations is in preparation.

Finally, note that the increase in C_{\parallel} observed at higher k in the *in situ* data could be related to a further change in the properties of the fluctuations as they approach electron scales; as discussed in Lacombe et al. (2017), this also coincides with a change in the estimated spectral

anisotropy. For example, Chen and Boldyrev (2017) have suggested that the increase in the magnetic compressibility beyond the sub-ion range could be related to electron inertia corrections to **Eq. 2**. This effect is then not captured by the hybrid model and we cannot compare any more the observations with the simulations in this range. It is however interesting to note that while the further increase of compressibility at electron scales is predicted for $\beta_e \lesssim 1$ (Chen and Boldyrev, 2017; Passot et al., 2017), in the intervals measured by Cluster, it seems to be observed for all beta ranges for $kd_p \gtrsim 10$ ($kd_e \gtrsim 1/4$). Moreover, it is also interesting to note that spectra for all betas reach isotropy at roughly $k\rho_p \sim 20$, corresponding on average to $k\rho_e \sim 0.5$.

6. CONCLUSION

In summary, we have discussed the properties of magnetic field spectra of turbulent fluctuations in the sub-ion regime and their main dependence on the plasma beta. We have carried out a detailed comparison between *in situ* Cluster magnetic field observations in the frequency range $f(\text{Hz}) = [1, 200]$, corresponding to scales typically between $d_p < l < d_e$, and high-resolution 2D hybrid simulations.

First, we investigated the spectral anisotropy of magnetic fluctuations at sub-ion scales. Our simulations confirm that the model of Saur and Bieber (1999), originally developed for MHD range fluctuations, is valid also at kinetic scales; by applying the model to the numerical spectra obtained mimicking the

sampling along a fixed direction made by spacecraft, we were able to successfully capture original spectral properties as well as their variation with β . This then reinforces the finding of Lacombe et al. (2017) who applied the Saur and Bieber model to kinetic-scale observations for the first time and concluded that fluctuations of the solar wind spectrum in the sub-ion range are quasi-2D and gyrotropic. Moreover, we have shown that the component anisotropy measured *in situ* — leading to an apparent nongyrotropic spectrum from an original gyrotropic one (see also Turner et al., 2011) — is a direct consequence of the solenoidal condition of the magnetic field and the sampling procedure. This is not an effect related to the Doppler-shift of k-vectors swept through the spacecraft by the fast plasma flow and in fact, we were able to reproduce it in simulations just imposing a fixed sampling direction.

Note that our result about the global 2D-symmetry of the k-vectors around the magnetic field is not inconsistent with studies addressing the local shape of the eddies and suggesting the presence of a 3D anisotropy (e.g., Chen et al., 2012a; Verdini and Grappin, 2015; Verdini et al., 2018; Verdini et al., 2019; Wang et al., 2020). In our approach, we do not consider the specific orientation of the turbulent structures in the plane perpendicular to B, and it is reasonable to expect that the local 3D anisotropy is then lost. In other words, despite the 3D anisotropy of the turbulent eddies, their k-vectors can be oriented isotropically around B, leading then—in a frame like the one used here—to the 2D spectrum found in the Cluster observations. This does not exclude that some aspects of the 3D anisotropy could still be captured using a global approach; however, our study suggests that, in this case, one has to also carefully take into account the effects of the component anisotropy introduced by the sampling (Saur and Bieber, 1999, see also Figure 3 in this work).

For the magnetic compressibility C_{\parallel} , we have confirmed that it has a strong dependence on the plasma beta (e.g., Alexandrova et al., 2008; TenBarge et al., 2012; Lacombe et al., 2017). In particular, we have shown that in Cluster observations C_{\parallel} depends on the total beta β only (Figure 8), as expected for low-frequency pressure-balanced fluctuations at highly oblique propagation (e.g., KAW). In the β range explored, we find a good qualitative agreement between the trends observed in the data and in the simulations. The compressibility is observed to increase as a function of β , leading to a plateau at sub-ion scales for high betas and in good agreement with the prediction by Eq. 2. At low beta, a fully developed plateau is not observed beyond ion scales and the compressibility continues to slowly increase along sub-ion scales, in both observations and simulations (see also Grošelj et al., 2019). There is, however, a difference in the asymptotic level of compressibility reached at high β in data and our simulations; in the former, fluctuations seem not to exceed component isotropy ($C_{\parallel} = 1/3$), while in the latter, they approach $C_{\parallel} = 0.5$, which is the limiting value predicted by Eq. 2. This aspect deserves to be explored in future studies, extending the range of β explored, to then establish if the asymptotic condition observed in simulations and predicted by the theory, which implies the same power in the parallel component as in the sum of the perpendicular ones, can be also observed *in situ* for high enough β intervals. As a consequence of the behavior just described, there is a different

quantitative agreement of the magnetic compressibility observed *in situ* and in simulations, with the theoretical prediction by Eq. 2. In simulations, there is very good matching with the predicted level at higher beta, but an excess of C_{\parallel} at low beta; this effect was already observed in Cerri et al. (2017) and is confirmed here on a larger range of β . On the other hand, in solar wind observations, the ratio is always lower than 1 (smaller compressibility than predicted by the theory) and close to ~ 0.75 for all β , in agreement with similar studies on the plasma compressibility (Chen et al., 2013a; Pitňa et al., 2019).

Our analysis also suggests that the increase in the compressibility at ion scales is controlled by an intermediate scale between the Larmor radius ρ_p and the proton inertial length d_p (Figure 9). For simulations, this was already anticipated in Franci et al. (2016), and we could identify it as related to $\sqrt{d_p \rho_p}$, thus proportional to $d_p \beta_p^{1/4}$ (Figure 10). Such a scaling with β_p also corresponds to the scaling observed for the spectral ion break in the range $\beta_p \sim 1$. However, it is worth highlighting that both observations (Chen et al., 2014; Wang et al., 2018; Woodham et al., 2018) and our simulations (Franci et al., 2016) show that the spectral ion-break scale follows the largest of ρ_p and d_p depending on the beta, so that the correction term proportional to $d_p \beta_p^{1/4}$ identified in Franci et al. (2016) is important only around $\beta_p \sim 1$. On the other hand, the present study indicates that a scale proportional to $\sqrt{d_p \rho_p}$ orders well the spectra of compressibility at all betas, for both *in situ* data and simulations, suggesting that such a mixed scale controls the transition in the nature of the fluctuations from MHD to sub-ion range (see also the monotonic scaling with β_p of the ion break in the parallel magnetic field spectrum shown in Figure 4 of Franci et al., 2016). This may imply that the two changes of the regime—the steepening of the magnetic spectrum and the increase in the compressibility—can occur at different scales for more extreme β values. In particular, we expect the spectral break to occur at a larger scale with respect to the plateau in the compressibility when $\beta_p \gg 1$ or $\beta_p \ll 1$, as in these cases, $\sqrt{d_p \rho_p}$ is always smaller than the largest between ρ_p and d_p . A more detailed analysis on this aspect will be the subject of a future study, as well as the possible implications of this behavior for fluctuations in the inner Heliosphere, where the plasma beta is typically lower than at 1AU, which can be observed by the Parker Solar Probe and Solar Obiter.

DATA AVAILABILITY STATEMENT

Publicly available datasets were analyzed in this study. This data can be found here: ESA Cluster archive: <https://csa.esac.esa.int> The numerical data are available at <https://b2share.eudat.eu/records/a58135af9c9d429f92c15ce88bdfddd55>.

AUTHOR CONTRIBUTIONS

LM and LF performed the main analysis and produced figures. OA and CL identified Cluster intervals, provided the *in situ* dataset, and contributed to the observational spectral analysis. PH

provided the hybrid code, LF performed the numerical simulations, and together with LM, SL, AV, and EP, they discussed the use and interpretation of numerical data. All authors contributed to the global interpretation of the results, as well as to their discussion and presentation in the manuscript. All authors revised the manuscript before submission.

FUNDING

This work was supported by the Programme National PNST of CNRS/INSU co-funded by CNES. It has also been funded by Fondazione Cassa di Risparmio di Firenze through the project HYPERCRHEL. LF was supported by Fondazione Cassa di Risparmio di Firenze, through the project Giovani Ricercatori Protagonisti, and by the United Kingdom Science and Technology Facilities Council (STFC) grants ST/P000622/1

REFERENCES

- Alexandrova, O., Krishna Jagarlamudi, V., Rossi, C., Maksimovic, M., Hellinger, P., Shprits, Y., et al. (2020). Kinetic turbulence in space plasmas observed in the near-Earth and near-Sun solar wind. *arXiv e-prints arXiv: 2004.01102*
- Alexandrova, O., Lacombe, C., Mangeney, A., Grappin, R., and Maksimovic, M. (2012). Solar wind turbulent spectrum at plasma kinetic scales. *Astrophys. J.* 760, 121. doi:10.1088/0004-637X/760/2/121
- Alexandrova, O., Lacombe, C., and Mangeney, A. (2008). Spectra and anisotropy of magnetic fluctuations in the Earth's magnetosheath: Cluster observations. *Ann. Geophys.* 26, 3585–3596. doi:10.5194/angeo-26-3585-2008
- Alexandrova, O., Saur, J., Lacombe, C., Mangeney, A., Mitchell, J., Schwartz, S. J., et al. (2009). Universality of solar-wind turbulent spectrum from MHD to electron scales. *Phys. Rev. Lett.* 103, 165003. doi:10.1103/PhysRevLett.103.165003
- Arzamasskiy, L., Kunz, M. W., Chandran, B. D. G., and Quataert, E. (2019). Hybrid-kinetic simulations of ion heating in Alfvénic turbulence. *Astrophys. J.* 879, 53. doi:10.3847/1538-4357/ab20cc
- Bandyopadhyay, R., Sorriso-Valvo, L., Chasapis, A. r., Hellinger, P., Matthaeus, W. H., Verdini, A., et al. (2020). In Situ observation of Hall magnetohydrodynamic cascade in space plasma. *Phys. Rev. Lett.* 124, 225101. doi:10.1103/PhysRevLett.124.225101
- Bieber, J. W., Wanner, W., and Matthaeus, W. H. (1996). Dominant two-dimensional solar wind turbulence with implications for cosmic ray transport. *J. Geophys. Res.* 101, 2511–2522. doi:10.1029/95JA02588
- Biskamp, D., Schwarz, E., and Drake, J. F. (1996). Two-dimensional electron magnetohydrodynamic turbulence. *Phys. Rev. Lett.* 76, 1264–1267. doi:10.1103/PhysRevLett.76.1264
- Boldyrev, S., Horaitas, K., Xia, Q., and Perez, J. C. (2013). Toward a theory of astrophysical plasma turbulence at subproton scales. *Astrophys. J.* 777, 41. doi:10.1088/0004-637X/777/1/41
- Boldyrev, S., and Perez, J. C. (2012). Spectrum of kinetic-Alfvén turbulence. *Astrophys. J. Lett.* 758, L44. doi:10.1088/2041-8205/758/2/L44
- Bruno, R., and Carbone, V. (2013). The solar wind as a turbulence laboratory. *Living Rev. Sol. Phys.* 10, 2. doi:10.12942/lrsp-2013-2
- Cerri, S. S., Califano, F., Jenko, F., Told, D., and Rincon, F. (2016). Subproton-scale cascades in solar wind turbulence: driven hybrid-kinetic simulations. *Astrophys. J. Lett.* 822, L12. doi:10.3847/2041-8205/822/1/L12
- Cerri, S. S., Grošelj, D., and Franci, L. (2019). Kinetic plasma turbulence: recent insights and open questions from 3D3V simulations. *Front. Astron. Space Sci.* 6, 64. doi:10.3389/fspas.2019.00064
- Cerri, S. S., Kunz, M. W., and Califano, F. (2018). Dual phase-space cascades in 3D hybrid-Vlasov-Maxwell turbulence. *Astrophys. J. Lett.* 856, L13. doi:10.3847/2041-8213/aab557
- Cerri, S. S., Servidio, S., and Califano, F. (2017). Kinetic cascade in solar-wind turbulence: 3D3V hybrid-kinetic simulations with electron inertia. *Astrophys. J. Lett.* 846, L18. doi:10.3847/2041-8213/aa87b0
- Chen, C. H. K., Bale, S. D., Salem, C. S., and Maruca, B. A. (2013a). Residual energy spectrum of solar wind turbulence. *Astrophys. J.* 770, 125. doi:10.1088/0004-637X/770/2/125
- Chen, C. H. K., and Boldyrev, S. (2017). Nature of kinetic scale turbulence in the Earth's magnetosheath. *Astrophys. J.* 842, 122. doi:10.3847/1538-4357/aa74e0
- Chen, C. H. K., Boldyrev, S., Xia, Q., and Perez, J. C. (2013b). Nature of subproton scale turbulence in the solar wind. *Phys. Rev. Lett.* 110, 225002. doi:10.1103/PhysRevLett.110.225002
- Chen, C. H. K., Horbury, T. S., Schekochihin, A. A., Wicks, R. T., Alexandrova, O., and Mitchell, J. (2010). Anisotropy of solar wind turbulence between ion and electron scales. *Phys. Rev. Lett.* 104, 255002. doi:10.1103/PhysRevLett.104.255002
- Chen, C. H. K., Leung, L., Boldyrev, S., Maruca, B. A., and Bale, S. D. (2014). Ion-scale spectral break of solar wind turbulence at high and low beta. *Geophys. Res. Lett.* 41, 8081–8088. doi:10.1002/2014GL062009
- Chen, C. H. K., Mallet, A., Schekochihin, A. A., Horbury, T. S., Wicks, R. T., and Bale, S. D. (2012a). Three-dimensional structure of solar wind turbulence. *Astrophys. J.* 758, 120. doi:10.1088/0004-637X/758/2/120
- Chen, C. H. K., Salem, C. S., Bonnell, J. W., Mozer, F. S., and Bale, S. D. (2012b). Density fluctuation spectrum of solar wind turbulence between ion and electron scales. *Phys. Rev. Lett.* 109, 035001. doi:10.1103/PhysRevLett.109.035001
- Chen, C. H. K. (2016). Recent progress in astrophysical plasma turbulence from solar wind observations. *J. Plasma Phys.* 82, 535820602. doi:10.1017/S0022377816001124
- Dasso, S., Milano, L. J., Matthaeus, W. H., and Smith, C. W. (2005). Anisotropy in fast and slow solar wind fluctuations. *Astrophys. J.* 635, L181–L184. doi:10.1086/499559
- Franci, L., Hellinger, P., Guerrasi, M., Chen, C. H. K., Papini, E., Verdini, A., et al. (2018a). Three-dimensional simulations of solar wind turbulence with the hybrid code CAMELIA. *J. Phys. Conf. Ser.* 1031, 012002. doi:10.1088/1742-6596/1031/1/012002
- Franci, L., Landi, S., Verdini, A., Matteini, L., and Hellinger, P. (2018b). Solar wind turbulent cascade from MHD to sub-ion scales: large-size 3D hybrid particle-in-cell simulations. *Astrophys. J.* 853, 26. doi:10.3847/1538-4357/aaa3e8
- Franci, L., Landi, S., Matteini, L., Verdini, A., and Hellinger, P. (2015a). High-resolution hybrid simulations of kinetic plasma turbulence at proton scales. *Astrophys. J.* 812, 21. doi:10.1088/0004-637X/812/1/21
- Franci, L., Verdini, A., Matteini, L., Landi, S., and Hellinger, P. (2015b). Solar wind turbulence from MHD to sub-ion scales: high-resolution hybrid simulations. *Astrophys. J. Lett.* 804, L39. doi:10.1088/2041-8205/804/2/L39
- Franci, L., Landi, S., Matteini, L., Verdini, A., and Hellinger, P. (2016). Plasma beta dependence of the ion-scale spectral break of solar wind turbulence: high-resolution 2D hybrid simulations. *Astrophys. J.* 833, 91. doi:10.3847/1538-4357/833/1/91
- Grošelj, D., Cerri, S. S., Bafón Navarro, A., Willmott, C., Told, D., Loureiro, N. F., et al. (2017). Fully kinetic versus reduced-kinetic modeling of collisionless plasma turbulence. *Astrophys. J.* 847, 28. doi:10.3847/1538-4357/aa894d
- Grošelj, D., Chen, C. H. K., Mallet, A., Samtaney, R., Schneider, K., and Jenko, F. (2019). Kinetic turbulence in astrophysical plasmas: waves and/or structures? *Phys. Rev. X* 9, 031037. doi:10.1103/PhysRevX.9.031037

and ST/T00018X/1. PH acknowledges grant 18-08861S of the Czech Science Foundation. OA and CL are supported by the French Centre National d'Etude Spatiales (CNES).

ACKNOWLEDGMENTS

The authors acknowledge useful discussions with J. Stawarz, G. Howes, and A. Pitna. The authors acknowledge PRACE for awarding them access to resource Cartesius based in the Netherlands at SURFsara through the DECI-13 (Distributed European Computing Initiative) call (project HybTurb3D), and CINECA for the availability of high performance computing resources and support under the ISCRA initiative (grants HP10C877C4 and HP10BUUOJM) and the program Accordo Quadro INAF-CINECA 2017-2019 (grants C4A26 and C3A22a).

- Hamilton, K., Smith, C. W., Vasquez, B. J., and Leamon, R. J. (2008). Anisotropies and helicities in the solar wind inertial and dissipation ranges at 1 AU. *J. Geophys. Res. Space Phys.* 113, A01106. doi:10.1029/2007JA012559
- Hellinger, P., Landi, S., Matteini, L., Verdini, A., and Franci, L. (2017). Mirror instability in the turbulent solar wind. *Astrophys. J.* 838, 158. doi:10.3847/1538-4357/aa67e0
- Hellinger, P., Matteini, L., Landi, S., Verdini, A., Franci, L., and Travnicek, P. M. (2015). Plasma turbulence and kinetic instabilities at ion scales in the expanding solar wind. *Astrophys. J. Lett.* 811, L32
- Hellinger, P., Verdini, A., Landi, S., Franci, L., and Matteini, L. (2018). von Kármán-Howarth equation for Hall magnetohydrodynamics: hybrid simulations. *Astrophys. J. Lett.* 857, L19. doi:10.3847/2041-8213/aabc06
- Horbury, T. S., and Balogh, A. (2001). Evolution of magnetic field fluctuations in high-speed solar wind streams: ulysses and Helios observations. *J. Geophys. Res.* 106, 15929–15940. doi:10.1029/2000JA000108
- Horbury, T. S., Forman, M., and Oughton, S. (2008). Anisotropic scaling of magnetohydrodynamic turbulence. *Phys. Rev. Lett.* 101, 175005. doi:10.1103/PhysRevLett.101.175005
- Howes, G. G., Dorland, W., Cowley, S. C., Hammett, G. W., Quataert, E., Schekochihin, A. A., et al. (2008). Kinetic simulations of magnetized turbulence in astrophysical plasmas. *Phys. Rev. Lett.* 100, 065004. doi:10.1103/PhysRevLett.100.065004
- Howes, G. G., Tenbarge, J. M., Dorland, W., Quataert, E., Schekochihin, A. A., Numata, R., et al. (2011). Gyrokinetic simulations of solar wind turbulence from ion to electron scales. *Phys. Rev. Lett.* 107, 035004. doi:10.1103/PhysRevLett.107.035004
- Howes, G. G. (2015). The inherently three-dimensional nature of magnetized plasma turbulence. *J. Plasma Phys.* 81, 325810203. doi:10.1017/S0022377814001056
- Jovanovic, D., Alexandrova, O., Maksimovic, M., and Belic, M. (2020). Fluid theory of coherent magnetic vortices in high- β space plasmas. *Astrophys. J.* 896 (1), 18. doi:10.3847/1538-4357/ab8a45
- Kiyani, K. H., Chapman, S. C., Khotyaintsev, Y. V., Dunlop, M. W., and Sahraoui, F. (2009). Global scale-invariant dissipation in collisionless plasma turbulence. *Phys. Rev. Lett.* 103, 075006. doi:10.1103/PhysRevLett.103.075006
- Kiyani, K. H., Chapman, S. C., Sahraoui, F., Hnat, B., Fauvarque, O., and Khotyaintsev, Y. V. (2013). Enhanced magnetic compressibility and isotropic scale invariance at sub-ion larmor scales in solar wind turbulence. *Astrophys. J.* 763, 10. doi:10.1088/0004-637X/763/1/10
- Lacombe, C., Alexandrova, O., and Matteini, L. (2017). Anisotropies of the magnetic field fluctuations at kinetic scales in the solar wind: cluster observations. *Astrophys. J.* 848, 45. doi:10.3847/1538-4357/aa8c06
- Landi, S., Franci, L., Papini, E., Verdini, A., Matteini, L., and Hellinger, P. (2019). Spectral anisotropies and intermittency of plasma turbulence at ion kinetic scales. *arXiv* eprint arXiv:1904.03903
- Loureiro, N. F., and Boldyrev, S. (2017). Collisionless reconnection in magnetohydrodynamic and kinetic turbulence. *Astrophys. J.* 850, 182. doi:10.3847/1538-4357/aa9754
- Mallet, A., Schekochihin, A. A., and Chandran, B. D. G. (2017). Disruption of sheet-like structures in Alfvénic turbulence by magnetic reconnection. *Mon. Notices Royal Astron. Soc.* 468, 4862–4871. doi:10.1093/mnras/stx670
- Matteini, L., Alexandrova, O., Chen, C. H. K., and Lacombe, C. (2017). Electric and magnetic spectra from MHD to electron scales in the magnetosheath. *Mon. Notices Royal Astron. Soc.* 466, 945–951. doi:10.1093/mnras/stw3163
- Matthaeus, W. H., Goldstein, M. L., and Roberts, D. A. (1990). Evidence for the presence of quasi-two-dimensional nearly incompressible fluctuations in the solar wind. *J. Geophys. Res.* 95, 20673–20683. doi:10.1029/JA095iA12p20673
- Matthews, A. P. (1994). Current advance method and cyclic leapfrog for 2d multispecies hybrid plasma simulations. *J. Comp. Phys.* 112, 102–116. doi:10.1006/jcph.1994.1084
- Osman, K. T., and Horbury, T. S. (2006). Multispacecraft measurement of anisotropic correlation functions in solar wind turbulence. *Astrophys. J.* 654, L103–L106. doi:10.1086/510906
- Papini, E., Franci, L., Landi, S., Verdini, A., Matteini, L., and Hellinger, P. (2019). Can Hall magnetohydrodynamics explain plasma turbulence at sub-ion scales? *Astrophys. J.* 870, 52. doi:10.3847/1538-4357/aaf003
- Parashar, T. N., Oughton, S., Matthaeus, W. H., and Wan, M. (2016). Variance anisotropy in kinetic plasmas. *Astrophys. J.* 824, 44. doi:10.3847/0004-637X/824/1/44
- Passot, T., and Sulem, P. L. (2015). A model for the non-universal power law of the solar wind sub-ion-scale magnetic spectrum. *Astrophys. J. Lett.* 812, L37. doi:10.1088/2041-8205/812/2/L37
- Passot, T., Sulem, P. L., and Tassi, E. (2017). Electron-scale reduced fluid models with gyroviscous effects. *J. Plasma Phys.* 83, 715830402. doi:10.1017/S0022377817000514
- Perrone, D., Alexandrova, O., Roberts, O. W., Lion, S., Lacombe, C., Walsh, A., et al. (2017). Coherent structures at ion scales in fast solar wind: cluster observations. *Astrophys. J.* 849, 49. doi:10.3847/1538-4357/aa9022
- Perrone, D., Valentini, F., Servidio, S., Dalena, S., and Veltri, P. (2013). Vlasov simulations of multi-ion plasma turbulence in the solar wind. *Astrophys. J.* 762, 99. doi:10.1088/0004-637X/762/2/99
- Pitná, A., Šafránková, J., Němeček, Z., Franci, L., Pi, G., and Montagud Camps, V. (2019). Characteristics of solar wind fluctuations at and below ion scales. *Astrophys. J.* 879, 82. doi:10.3847/1538-4357/ab22b8
- Podesta, J. J., and TenBarge, J. M. (2012). Scale dependence of the variance anisotropy near the proton gyroradius scale: additional evidence for kinetic Alfvén waves in the solar wind at 1 AU. *J. Geophys. Res. Space Phys.* 117, A10106. doi:10.1029/2012JA017724
- Roberts, O. W., Alexandrova, O., Kajdič, P., Turc, L., Perrone, D., Escoubet, C. P., et al. (2017a). Variability of the magnetic field power spectrum in the solar wind at electron scales. *Astrophys. J.* 850, 120. doi:10.3847/1538-4357/aa93e5
- Roberts, O. W., Narita, Y., and Escoubet, C. P. (2017b). Direct measurement of anisotropic and asymmetric wave vector spectrum in ion-scale solar wind turbulence. *Astrophys. J. Lett.* 851, L11. doi:10.3847/2041-8213/aa9bf3
- Šafránková, J., Němeček, Z., Přech, L., and Zastenker, G. N. (2013). Ion kinetic scale in the solar wind observed. *Phys. Rev. Lett.* 110, 025004. doi:10.1103/PhysRevLett.110.025004
- Sahraoui, F., Goldstein, M. L., Belmont, G., Canu, P., and Rezeau, L. (2010). Three dimensional anisotropic k spectra of turbulence at subproton scales in the solar wind. *Phys. Rev. Lett.* 105, 131101. doi:10.1103/PhysRevLett.105.131101
- Sahraoui, F., Huang, S. Y., Belmont, G., Goldstein, M. L., Rétino, A., Robert, P., et al. (2013). Scaling of the electron dissipation range of solar wind turbulence. *Astrophys. J.* 777, 15. doi:10.1088/0004-637X/777/1/15
- Salem, C. S., Howes, G. G., Sundkvist, D., Bale, S. D., Chaston, C. C., Chen, C. H. K., et al. (2012). Identification of kinetic Alfvén wave turbulence in the solar wind. *Astrophys. J. Lett.* 745, L9. doi:10.1088/2041-8205/745/1/L9
- Saur, J., and Bieber, J. W. (1999). Geometry of low-frequency solar wind magnetic turbulence: evidence for radially aligned Alfvénic fluctuations. *J. Geophys. Res.* 104, 9975–9988. doi:10.1029/1998JA900077
- Schekochihin, A. A., Cowley, S. C., Dorland, W., Hammett, G. W., Howes, G. G., Quataert, E., et al. (2009). Astrophysical gyrokinetics: kinetic and fluid turbulent cascades in magnetized weakly collisional plasmas. *Astrophys. J. Suppl.* 182, 310–377. doi:10.1088/0067-0049/182/1/310
- Schreiner, A., and Saur, J. (2017). A model for dissipation of solar wind magnetic turbulence by kinetic Alfvén waves at electron scales: comparison with observations. *Astrophys. J.* 835, 133. doi:10.3847/1538-4357/835/2/133
- Smith, C. W., Vasquez, B. J., and Hamilton, K. (2006). Interplanetary magnetic fluctuation anisotropy in the inertial range. *J. Geophys. Res. Space Phys.* 111, A09111. doi:10.1029/2006JA011651
- Stawarz, J. E., Eriksson, S., Wilder, F. D., Ergun, R. E., Schwartz, S. J., Pouquet, A., et al. (2016). Observations of turbulence in a kelvin-helmholtz event on 8 september 2015 by the magnetospheric multiscale mission. *J. Geophys. Res.* 121 (11), 11021–11034. doi:10.1002/2016JA023458. 2016JA023458
- Stawarz, J. E., Matteini, L., Parashar, T. N., Franci, L., Eastwood, J. P., Gonzalez, C. A., et al. (2020). Generalized ohms law decomposition of the electric field in magnetosheath turbulence: magnetospheric multiscale observations. *Earth and Space Science Open Archive*. 31. doi:10.1002/essoar.10503618.1
- Sulem, P. L., Passot, T., Laveder, D., and Borgogno, D. (2016). Influence of the nonlinearity parameter on the solar wind sub-ion magnetic energy spectrum: FLR-Landau fluid simulations. *Astrophys. J.* 818, 66. doi:10.3847/0004-637X/818/1/66
- TenBarge, J. M., Podesta, J. J., Klein, K. G., and Howes, G. G. (2012). Interpreting magnetic variance anisotropy measurements in the solar wind. *Astrophys. J.* 753, 107. doi:10.1088/0004-637X/753/2/107
- Turner, A. J., Gogoberidze, G., Chapman, S. C., Hnat, B., and Müller, W. C. (2011). Nonaxisymmetric anisotropy of solar wind turbulence. *Phys. Rev. Lett.* 107, 095002. doi:10.1103/PhysRevLett.107.095002

- Valentini, F., Servidio, S., Perrone, D., Califano, F., Matthaeus, W. H., and Veltri, P. (2014). Hybrid Vlasov-Maxwell simulations of two-dimensional turbulence in plasmas. *Phys. Plasmas.* 21, 082307. doi:10.1063/1.4893301
- Verdini, A., and Grappin, R. (2015). Imprints of expansion on the local anisotropy of solar wind turbulence. *Astrophys. J. Lett.* 808, L34. doi:10.1088/2041-8205/808/2/L34
- Verdini, A., Grappin, R., Alexandrova, O., Franci, L., Landi, S., Matteini, L., et al. (2019). Three-dimensional local anisotropy of velocity fluctuations in the solar wind. *Mon. Notices Royal Astron. Soc.* 486, 3006–3018. doi:10.1093/mnras/stz1041
- Verdini, A., Grappin, R., Alexandrova, O., and Lion, S. (2018). 3D anisotropy of solar wind turbulence, tubes, or ribbons? *Astrophys. J.* 853, 85. doi:10.3847/1538-4357/aaa433
- Wang, T., He, J., Alexandrova, O., Dunlop, M., and Perrone, D. (2020). Observational quantification of three-dimensional anisotropies and scalings of space plasma turbulence at kinetic scales. *Astrophys. J.* 898, 91. doi:10.3847/1538-4357/ab99ca
- Wang, X., Tu, C., He, J., and Wang, L. (2018). On the full-range β dependence of ion-scale spectral break in the solar wind turbulence. *Astrophys. J.* 857, 136. doi:10.3847/1538-4357/aab960
- Wicks, R. T., Horbury, T. S., Chen, C. H. K., and Schekochihin, A. A. (2010). Power and spectral index anisotropy of the entire inertial range of turbulence in the fast solar wind. *Mon. Notices Royal Astron. Soc.* 407, L31–L35. doi:10.1111/j.1745-3933.2010.00898.x
- Woodham, L. D., Wicks, R. T., Verscharen, D., and Owen, C. J. (2018). The role of proton cyclotron resonance as a dissipation mechanism in solar wind turbulence: a statistical study at ion-kinetic scales. *Astrophys. J.* 856, 49. doi:10.3847/1538-4357/aab03d
- Conflict of Interest:** The authors declare that the research was conducted in the absence of any commercial or financial relationships that could be construed as a potential conflict of interest.
- The reviewer (SC) declared a past co-authorship with one of the authors (LF) to the handling Editor.

Copyright © 2020 Matteini, Franci, Alexandrova, Lacombe, Landi, Hellinger, Papini and Verdini. This is an open-access article distributed under the terms of the Creative Commons Attribution License (CC BY). The use, distribution or reproduction in other forums is permitted, provided the original author(s) and the copyright owner(s) are credited and that the original publication in this journal is cited, in accordance with accepted academic practice. No use, distribution or reproduction is permitted which does not comply with these terms.

APPENDIX: SYMBOL DEFINITIONS AND NORMALIZED UNITS

The subscripts \perp and \parallel refer to the direction with respect to the ambient magnetic field B_0 and p and e denote, respectively, protons and electrons. All equations are expressed in the c.g.s. unity system. n and T denote the number density and the temperature of a species (we assume also $n_p = n_e = n$). $\beta_{e,p} = 8\pi nk_B T_{e,p}/B_0^2$ are the

electron and proton betas, and $\beta = \beta_p + \beta_e$ is the total plasma beta; here k_B is the Boltzmann constant. For each species of mass m and charge q, the inertial length d is defined as c/ω_p , where $\omega_p = (4\pi nq^2/m)^{1/2}$ is the plasma frequency, and the Larmor radius r is defined as v_{th}/Ω_c , where v_{th} is the thermal speed of each species and $\Omega_c = q_p B_0 / mc$ is the cyclotron frequency. V_{sw} is the solar wind speed and f the frequency of the fluctuations measured by the spacecraft; k denotes the module of the wave vector \mathbf{k} .

Advantages of publishing in Frontiers



OPEN ACCESS

Articles are free to read for greatest visibility and readership



FAST PUBLICATION

Around 90 days from submission to decision



HIGH QUALITY PEER-REVIEW

Rigorous, collaborative, and constructive peer-review



TRANSPARENT PEER-REVIEW

Editors and reviewers acknowledged by name on published articles



REPRODUCIBILITY OF RESEARCH

Support open data and methods to enhance research reproducibility



DIGITAL PUBLISHING

Articles designed for optimal readership across devices



FOLLOW US
@frontiersin



IMPACT METRICS
Advanced article metrics track visibility across digital media



EXTENSIVE PROMOTION
Marketing and promotion of impactful research



LOOP RESEARCH NETWORK
Our network increases your article's readership